Atoms and Molecules in Strong Laser Fields

Dissertation
zur Erlangung des Doktorgrades
an der Fakultät für Mathematik, Informatik und Naturwissenschaften
Fachbereich Physik
der Universität Hamburg

vorgelegt von

René Marcel Leopold Wagner

Hamburg
2022

Gutachter der Dissertation:	Dr. Michael Meyer Prof. Dr. Klaus Sengstock
Zusammensetzung der Prüfungskommision:	Dr. Michael Meyer Prof. Dr. Klaus Sengstock Prof. Dr. Markus Drescher Dr. Michael Martins Prof. Dr. Michael Potthoff
Vorsitzender der Prüfungskomission:	Prof. Dr. Michael Potthoff
Datum der Disputation:	16.08.2022
Vorsitzender Fach-Promotionsausschuss PHYSIK:	Prof. Dr. Wolfgang J. Parak
Leiter des Fachbereichs PHYSIK:	Prof. Dr. Günter H. W. Sigl
Dekan der Fakultät MIN:	Prof. Dr. Heinrich Graener

ABSTRACT

The interaction of light with atoms and molecules is universal and relevant to everyday life. With the advent of light sources such as femtosecond laser oscillators and free-electron lasers (FELs), intense and ultra-short light pulses with well-characterized properties are available, which allow to study the interaction of light and matter in extreme regimes. Applying a two-color pump-probe approach, involving two light pulses, matter can be prepared in a well-defined state by the first pulse and then probed by interacting with the second pulse. In this thesis, the non-linear interaction of light pulses with small atoms and molecules in the gas phase is investigated with special emphasis on photoionization. For this purpose a new high harmonic generation (HHG) source has been characterized, that can be used in two-color experiments to either prepare or probe atoms or molecules that undergo non-linear interaction with another intense light pulse. Furthermore the fragmentation of molecular hydrogen was investigated in light fields at 800 nm and 400 nm as a benchmark experiment for a new experimental set-up. Following this, the fragmentation of the greenhouse gas methane in these optical fields of 800 nm and 400 nm was studied at varying intensities regarding the kinetic energies of the fragment ions generated in the non-linear interaction. The aim of this study was to unravel the influence of ionizing methane primarily by tunneling ionization at 800 nm or by multi-photon ionization at 400 nm on the kinetic energy of the photofragments. Finally, in a two-color experiment, the circular dichroism in multi-photon ionization of an atomic prototype system, ionic helium, was investigated. Using the intense, circularly polarized extreme ultraviolet (XUV) pulses delivered by the FERMI FEL at the LDM endstation atomic helium was ionized and excited into an oriented state in the same XUV pulse. A subsequent near-infrared (NIR) pulse with the same or the opposite helicity as the XUV pulse then ionized the helium ion from the prepared state via multi-photon ionization. This follow-up experiment improves on a previous one by introducing a temporal delay between the XUV and NIR pulses to avoid a population imbalance in the prepared helium ions, and by covering a wider and more dense range of NIR intensities. The influence of the helicity and intensity of the NIR pulses on the circular dichroism of the multi-photon ionization, observed by multi-photon and above-threshold ionization features in the photoelectron spectrum, is then studied regarding the AC-Stark shift, the Freeman resonances, the photoelectron angular distribution and different NIR wavelengths. The experimental results are compared to results from TDSE (time-dependent Schrödinger equation) calculations, which were done by collaborators.

KURZFASSUNG

Die Wechselwirkung von Licht mit Atomen und Molekülen ist ein Prozess, der ständig stattfindet und für die Existenz von Leben auf der Erde unabdingbar ist. Mit dem Aufkommen von Lichtquellen wie Femtosekunden Lasern und Freie-Elektronen-Lasern (FELs) können intensive, ultra kurze Lichtpulse mit genau definierten Eigenschaften erzeugt werden, mit denen diese Wechselwirkung in extremen Regimen untersucht werden kann. Unter Verwendung eines zwei-Farben „Pump-Probe“ Ansatz, bei dem zwei Laserpulse verwendet werden, kann Materie durch einen ersten Puls in einem genau definierten Zustand präpariert und mit einem zweiten Puls untersucht werden. In dieser Doktorarbeit wird die nicht-lineare Wechselwirkung von Licht mit kleinen Atomen und Molekülen in der Gasphase unter dem Aspekt der Photoionisation untersucht. Zu diesem Zweck wurde eine neue Quelle für Hohe Harmonische ('high harmonic generation' HHG) charakterisiert, die in zwei-Farben Experimenten genutzt werden kann, um Materie definiert anzuregen und zu untersuchen. Des Weiteren wird die Fragmentation von molekularem Wasserstoff durch Lichtpulse mit Wellenlängen von 800 nm und 400 nm untersucht, um zu prüfen, ob ein neues experimentelles Setup die zu erwartenden Ergebnisse liefert. Dem folgend wird die lichtintensitätsabhängige Fragmentation eines der kleinsten organischen Moleküle, dem Treibhausgas Methan, bei denselben Wellenlängen hinsichtlich der kinetischen Energien der geladenen Fragmente untersucht, die in der nicht-linearen Wechselwirkung erzeugt werden. Dabei ist das Ziel zu untersuchen, wie sich verschiedene Mechanismen der Ionisation auf die kinetischen Energien der Methanfragmente auswirken: Tunnelionisation bei 800 nm und Multi-Photonionisation (MPI) bei 400 nm. Abschließend wird der Zirkulardichroismus der Photoelektronen in MPI eines atomaren Modell-Systems, einfach ionisiertes Helium, in einem zwei-Farben Experiment untersucht. Hierzu wurden die intensiven, zirkular polarisierten, extrem ultravioletten (XUV) Pulse des FERMI FEL an der LDM Endstation genutzt, um Helium erst zu ionisieren und dann das Ion im selben XUV Puls durch ein weiteres Photon in einen orientierten Zustand anzuregen. Ein dem XUV Puls folgender nahinfraroter (NIR) intensiver Puls, dessen Helizität gleich oder gegenteilig zur Helizität des XUV Pulses ist, ionisiert dann das orientierte Heliumion mittels MPI. Das Experiment verbessert ein vorausgegangenes, ähnliches Experiment, indem der XUV und NIR Puls nicht zeitgleich mit dem Helium Atom wechselwirken, um ein Ungleichgewicht in der Population des angeregten Zustands für die beiden Helizitäten zu vermeiden. Zusätzlich wurden die Intensitätsabhängigkeit des Zirkulardichroismus für eine größere und dichtere Spanne an NIR Intensitäten gemessen. Untersucht wird der Einfluss der zwei unterschiedlichen Helizitäten und Intensitäten des NIR Pulses hinsichtlich des Zirkular-Dichroismus der MPI, welcher für die Multi-Photon- und Above-Threshold-Ionisations (ATI) Merkmale des Photoelektron-Spektrums bestimmt wurde, der darin auftretenden Freeman Resonanzen und der Winkelverteilung der Photoelektronen untersucht.

CONTENTS

1 INTRODUCTION

There is a fundamental drive in mankind to understand the underlying principles of nature, which every human is bound to live by. This understanding of nature can help to shape natural processes in ways that make life easier. These days mankind has understood the working principles of nature to a degree, which enabled many technologies to be discovered that substantially improve everyday life. Many of these technologies arise from the possibility to manipulate matter in a controlled and precise way to achieve a certain outcome. A very capable method of investigating and controlling matter on a fundamental level is the interaction of light and matter [1–4]. One of the most direct approaches for investigating matter is to access the electronic structure of atoms, molecules, or solids, which is possible through a process called photoionization, which was explained by A. Einstein in 1905 [5]. In photoionization matter absorbs a photon, thereby creating a free electron (photoelectron) and matter in a charged, ionic state, missing an electron. A requirement for photoionization is that the energy gained by the electron is sufficient to overcome the binding energy of the electron. Measuring the properties of the photoelectron created in the photoionization allows to study the electronic structure of matter. If photoionization induces the fragmentation of a molecule, the properties of the fragment-ions carry information about the fragmentation process and the electronic state that leads to fragmentation.
Due to the nature of the process of photoionization, the capabilities of the method are strongly entwined with the capabilities of the available light sources. In photoionization experiments typically either laser or synchrotron-based light sources, or a combination of the two are used. Today, optical lasers can produce light with well-defined properties, enabling a precise investigation into the electronic structure of matter. The technique of chirped-pulse amplification (CPA), first demonstrated by Strickland et. al. [6] in 1985, allowed to further amplify the output of short-pulse lasers, thereby reaching new intensity regimes. These days CPA laser systems easily reach field-strengths that match and even surpass the field strengths that outer electrons of an atom experience in the field of the positively charged nucleus. The pulses produced by these, commercially available, laser systems have pulse durations on the order of tens of femtoseconds (10^{-15} - fs) and can reach intensities around $10^{15}\,\mathrm{W/cm^2}$. The electric field of these light pulses is so intense when focused, that the light can't be viewed as a small perturbation to the electronic system any longer. The density of photons becomes large enough that the atom can absorb multiple photons at once, leading to multi-photon ionization (MPI) [7–10]. At even higher intensities the binding potential of the atom is bent so much by the electric field of the light, that the electron can tunnel out of the atom, leading to tunneling ionization [11, 12].
To understand light-matter interaction on a fundamental level, also small molecules that were readily available like hydrogen and nitrogen were exposed to such intense optical radiation as it became available [13, 14]. In these intense

fields it was observed that molecules could be aligned, ionized and dissociated, enabling the study of molecular dissociation on an ultra-fast timescale [15]. Mechanism describing this ionization and dissociation involves bond-softening, bond-hardening [16, 17], enhanced ionization and Coulomb explosion [18–20]. The dissociation of three-dimensional organic molecules in intense fields revealed that during the dissociation new chemical bonds are formed, which did not exist in the parent molecule [21, 22]. A molecule which also shows formation of new chemical bonds after interacting with intense optical pulses is the methane molecule [23, 24]. In this thesis the dissociation of one of the most simple organic molecules, methane, is investigated. Intense optical fields of up to $1 \cdot 10^{15}\,\mathrm{W/cm^2}$ at two different central wavelengths of the optical laser are used to study the influence of the prevalent ionization mechanism on the dissociation of the molecule, tunneling ionization for 800 nm and multi-photon ionization for 400 nm pulses. Using a time-of-flight (ToF) spectrometer, the laser intensity dependent kinetic energy of the ions formed in the dissociation is investigated for the two wavelengths. Using a velocity map imaging (VMI) spectrometer with a delay-line detector [25], the angular distribution of the fragments is measured and dissociation channels are identified via correlations. The single-hit ToF spectra of the VMI allow to identify newly formed chemical compounds, such as H_3^+, as they are not abundant. To characterize the new experimental setup used for the methane experiment, the dissociation of molecular hydrogen is investigated beforehand. Known kinetic energies of fragments from molecular hydrogen are used to calibrate the kinetic energies in the methane experiment.

To study the dynamics of the molecular dissociation in a controlled way, a two-color approach is necessary. For a controlled interaction it would be ideal to have access to photons with energies in the XUV range interacting with the molecule only via one photon at a time. Generating such radiation in a laser laboratory is possible by making use of high harmonic generation (HHG). To this end, a new HHG source driven by intense optical pulses with wavelengths of 800 nm and 400 nm is characterized. Driving the HHG source with 400 nm pulses limits the available maximum photon energy of the HHG radiation but in turn omits the necessity for a monochromator, as only one harmonic with a photon energy of 21.7 eV is produced. HHG has become a versatile tool in studying the dynamics of electron dynamics in atoms, molecules and solids [26–28]. Photon energies of HHG radiation can reach 1.6 keV in the soft X-ray range [29], the pulses can be as short as attoseconds [30] and can also be circularly polarized [31].

To achieve high laser intensities and ultra-short pulse durations at extreme ultraviolet (XUV) and X-ray photon energies, large-scale facilities are necessary. Synchrotron radiation was initially observed as a by-product emitted by synchrotrons which were designed for particle acceleration[32, 33]. To keep the particles on a circular track, dipole magnets were used, which led to the emission of radiation since accelerated charges radiate. Having seen the potential of this radiation regarding the tunability of the photon energy and the intensity of the radiation, dedicated facilities were built with special devices that allowed for efficient production of this radiation. To improve the generation of the radiation, sets of magnets with alternating polarity are used, the so-called undulators. A linear accelerator design, the free-electron laser (FEL), allows to create ultra-short,

intense laser pulses in the XUV und X-ray regime by using a principle called self-amplified spontaneous emission (SASE) [34]. XUV FELs can produce radiation with photon energies of up to 310 eV, pulse durations less than 200 fs and pulse energies of 500 µJ [35, 36]. X-ray FELs can generate photon energies from 0.25 keV to 25 keV with pulse energies of up to 10 mJ and pulse durations of 20–30 fs [37, 38]. By seeding a SASE-FELs with a pulsed ultraviolet (UV) laser, coherent and well-defined radiation with a narrow bandwidth can be produced, as it is done for example at FERMI [35]. Using special undulators it recently became possible to create intense XUV pulses that are circularly polarized at FELs [39–41].

Access to sources of intense circularly polarized pulses opens up the possibility to investigate the chirality or handedness of matter in photoionization experiments. If the interaction between matter and light depends on the helicity (left- or right-circular polarization) of the light, then that matter exhibits a circular dichroism (CD). The building blocks of nature themselves possess a handedness [42]. Many organic molecules are chiral, meaning that those molecules can't be superimposed with their mirror image. In MPI experiments using circularly polarized light this asymmetry leads to a photoelectron circular dichroism (PECD) in the photoelectron angular distribution (PAD) in the forward-backward direction regarding the beam propagation direction for the two different forms of the molecule [43–45].

In contrast to this, atomic systems are generally inherently symmetric and thus do not show any sign of a CD when interacting with light of different helicities. To break this symmetry a two-color pump-probe approach can be used, in which the first circularly polarized pulse creates a spatially oriented, ring-current-like electron distribution, corresponding to an electronic state with magnetic quantum number $m = \pm 1$. The second circularly polarized pulse then interacts with this state and, depending on the helicity combination of the pulses, leads to a CD.

For optical pulses with strong fields creating a rotating tunneling barrier, it has been theoretically predicted that the tunneling ionization probability depends on the magnetic quantum number m of the induced ring-current and, counter-intuitively, it has been theoretically predicted and experimentally shown that tunneling-ionization of the ring-current in optical fields is more likely if the tunneling barrier and the ring-current rotate opposite to each other [46, 47].

Complementary to this, the experiment presented within this thesis explores the CD of a spatially oriented electronic state in the intensity regime of multi-photon ionization. For this, the intense circularly polarized XUV pulses of FERMI at the low density matter (LDM) endstation have been used to sequentially ionize and excite helium into the He^+3p_m resonance with $m = 1$. This sequential ionization and excitation are only possible due to the intense XUV pulses having such high photon densities that the interaction of the helium atom and the helium ion with photons from the same pulse within its duration is likely. The probe in this experiment is an intense left- or right-circularly polarized near-infrared (NIR) pulse with wavelengths around 784 nm, which ionizes the prepared helium ions via the absorption of four or more photons. The kinetic energy and the angle of emission of the photoelectrons is measured using a VMI with a phosphorous screen and a camera. Extending on previous studies [40, 48], now a temporal delay of 500 fs between the XUV and NIR pulse is introduced to avoid a population imbalance in the He^+3p_{+1} state due to the helicity-dependent AC-Stark shift of the

He^+3p_{+1} resonance. By varying the intensity of the NIR laser pulses, it is intended to observe the Freeman resonances, which are induced by the AC-Stark shift, and their impact on the intensity dependence of the CD and the angular distribution of the photoelectrons. The results are compared to a similar investigation on lithium by De Silva et. al. [49, 50]. Additionally the results are compared to TDSE and quasi-particle calculations [51]. The AC-Stark shift and the induced transient resonances can also affect the intensity dependent PECD of chiral molecules.

1.1 OUTLINE

In part 1 of the thesis, the theoretical background regarding physical and technical aspects of the presented studies is introduced. In chapters 2 to 5 the fundamentals of photoionization, ultra-short laser pulses, molecules in strong laser fields and the used spectrometers are discussed, respectively.
In part 2 the experiments, which were performed in the laser laboratory at the European XFEL, are presented. In chapters 6 and 7 the experimental setup is demonstrated, then the new design of the high harmonic source is characterized and photoelectron spectroscopy on molecular hydrogen is presented. Chapter 8 contains the investigation of the dissociation of molecular hydrogen. The results of this study are used to characterize the new experimental setup dedicated to studying molecular fragmentation and calibrating the kinetic energies of the fragments. This calibration of the fragments is used to determine the kinetic energy of fragments from methane created in the interaction with intense laser pulses. Using a VMI, the angular distribution of the fragments is investigated and coincidence of the ions are investigated.
Finally, in part 3 and chapter 9, the experiment performed at the LDM endstation of FERMI FEL regarding the circular dichroism of resonantly excited helium ions is presented. First FERMI FEL and the LDM endstation are introduced after which an overview is given of how the measured data is evaluated and how the intensity of the optical laser has been calibrated. Then the AC-Stark shift of the He^+3p_{+1} resonance is demonstrated to highlight the necessity to separate the pump and probe pulse in time to not perturb the measurement of the CD by an unbalanced initial population of the He^+3p_{+1} resonance for the two polarizations of the NIR pulse. Following this, the intensity dependent CD and photoelectron spectra are investigated for temporally overlapped and separated pulses. A slightly different wavelength allowing for higher NIR intensities explores the saturation regime. Lastly, regarding the CD, the intensity dependence for three slightly different central wavelengths of the NIR pulses is investigated. Following this, the intensity dependent angular distribution of the above-threshold ionization (ATI) photoelectrons is discussed for the various scenarios that were also discussed for the CD.

Part I

THEORETICAL BACKGROUND

In this section the theory of the physical processes, which are the most critical to explain the experiment from the set-up to the observed phenomena, is presented. The central topic is the interaction of atoms with ultra-short laser pulses with special emphasis on the photoionization process. Then the generation of higher harmonics of an intense optical laser and of free-electron laser radiation are described. Lastly, the interaction of molecules with strong laser fields is discussed.

2 PHOTOIONIZATION

The interaction of an electromagnetic wave with an atomic or multiatomic system, which results in the removal of an electron from the system, is called photoionization [52]. Photoionization is a powerful tool to investigate the electronic structure of atoms, molecules and solids, as the outgoing electron, the "photoelectron", has certain properties which are directly coupled to the system it left behind. Investigating matter on such a fundamental level brings with it a wide variety of applications. For example one can study the band-structure of solids [53], investigate how light interacts with plasmonic devices [54] and see the influence of circularly polarized light on chiral molecules [55]. Apart from these more applied examples, photoionization is an excellent tool to probe fundamental processes like electron-electron correlations due to the fundamental nature of the process itself [56].
To gather information about the investigated system one needs to measure certain properties of the photoelectron. An important one is its kinetic energy, or how fast it moves away from the atom after being ionized. The kinetic energy is mostly determined by energy conservation involving the energy of the three constituents of the interaction, the atom, the electron and the photon. Before the interaction, the electron is bound to the atom with a certain binding energy. To overcome this binding energy a certain energy is required, which is the ionization potential I_p. The energy of the photon is given by $\hbar\omega$, where $\hbar$ is the Planck constant and ω is the angular frequency of the light. If the photon energy is greater than the ionization potential, the kinetic energy the electron receives by absorbing the photon is big enough to overcome the binding energy of the atom. The difference between the photon energy and the ionization potential I_p is the kinetic energy of the photoelectron E_{kin}, in short: $E_{kin} = \hbar\omega - I_p$ [52]. If the photon energy is lower than the ionization potential and the photon density is not too high, ionization cannot take place, but the atom can still be excited into a higher state. What happens at high photon densities and intense laser fields will be explained in further chapters. In the upcoming chapter, we will discuss how to describe excitation and ionization by means of physical theory and what influences the probability for either of the processes.

2.1 EXCITATION AND IONIZATION

To calculate the probability for excitation or ionization from an initial state i to a final state f one can make use of perturbation theory [57]. The whole system of the atom and the electromagnetic field is described by a Hamiltonian. This Hamiltonian $\hat{H}$ accounts for the kinetic energy of the electrons, the interaction between the electrons and the influence of the electromagnetic field (Eq. 1). In the equation N is the number of electrons, Z is the nuclear charge, c is the speed of light, t is the time, $\mathbf{r}$ is the position of the electron, $\hat{\mathbf{p}}_\mathbf{n}$ is the momentum operator and $\mathbf{A}$ is the vector potential, describing the electromagnetic field. The following

equations are written in the atomic unit convention, so that the Planck constant divided by 2π is $\hbar = 1$, the electron charge is $e = 1$ and the mass of the electron is $m_e = 1$.

$$\hat{H} = \sum_{n=1}^{N} \frac{1}{2}\left(\hat{\mathbf{p}}_n - \frac{1}{c}\mathbf{A}(\mathbf{r}, t)\right)^2 + \frac{1}{2}\sum_{n>q=1}^{N} \frac{1}{|\mathbf{r_n} - \mathbf{r_q}|} \tag{1}$$

Assuming that the electromagnetic field is so weak, that multi-photon processes do not play a role and that the divergence of the vector potential $\mathbf{A}(t)$ is zero, one can separate the Hamiltonian into a time-independent atomic part and a time-dependent part, the so-called 'interaction Hamiltonian' $\hat{H}_{int}$, see equation 3, which describes the influence of the electromagnetic field. By applying perturbation one ends up with an equation 2 to calculate the probability amplitude C_f for the electronic system to be in a certain state f. Here ψ_i, E_i and ψ_f, E_f are the wave functions and energies of the initial and final state, respectively. Furthermore, the x describes the position and spin state of each electron. It is assumed that the electromagnetic wave is monochromatic with a photon energy of ω and that the polarization is perpendicular to the light's propagation direction.

$$i\frac{\partial C_f}{\partial t} = \int \psi_i(x_1 ... x_N)\hat{H}_{int}(r_1 ... r_N, t)\psi_f(x_1 ... x_N)e^{(E_f - E_i)t}dx_1 ... dx_N \tag{2}$$

$$\hat{H}_{int} = -\frac{1}{c}\sum_{n=1}^{N} \mathbf{A}(\mathbf{r_n}, t)\hat{\mathbf{p}}_\mathbf{n} \tag{3}$$

From the probability amplitude, it is possible to calculate a transition probability per unit time, which, when divided by the photon flux density, becomes the cross-section σ. Equation 4 shows how the cross-section can be calculated within the frame of the assumptions that were made until this point. Here c is the speed of light and π is pi.
From this equation, it is already clear that a transition from the state i to the state f is only possible if the photon energy matches the energy difference between the two states. This is a direct consequence of energy conservation. Another final state dependent contributor to the cross-section are the transition-matrix elements M_{if}. The integration is due to the assumption of the final state being in the continuum since one has to take into account the density of states. For bound states the integral is replaced by a sum and the transition is only possible if the photon energy matches the difference in energy of the initial and final state.

$$\sigma(\omega) = \frac{4\pi}{\omega c}\int |M_{if}|^2 \delta(E_f - E_i - \omega)df \tag{4}$$

$$M_{if} = \sum_{q=1}^{N} \int \psi_i^*(x_1 ... x_N)e^{-i\mathbf{k}\mathbf{r_q}}(\mathbf{e}\cdot\mathbf{p_q})\psi_f(x_1 ... x_N)dx_1 ... dx_N \tag{5}$$

Equation 5 defines the transition-matrix elements. In this equation $\mathbf{k}$ is the wave-vector of the electromagnetic wave and $\mathbf{e}$ is its polarization.
To get a better insight into these transition-matrix elements, they are commonly applied to the hydrogen atom with the restriction to only inspect transitions from a bound state to another bound state in an external field. The eigenstates of the hydrogen atom are well known and can be expressed by three quantum numbers, the principal quantum number n, the angular momentum quantum number l and the magnetic quantum number m. The spatial representation of the wave function is then given by equation 6. In this equation $u_{n\ell}(r)$ is the radial part of the wave function and $Y_{\ell m}(\theta, \phi)$ are spherical harmonic functions, which contain the dependency of the wave function on the polar and azimuthal angle, respectively [58].

$$\langle r \,|\, n\ell m\rangle = \frac{u_{n\ell}(r)}{r} Y_{\ell m}(\theta, \phi) \tag{6}$$

Using the commutator relation $[\hat{H}_0, \hat{\mathbf{r}}] = -i\hat{\mathbf{r}}$ and the electric dipole approximation, $e^{i\mathbf{kr}} \approx 1$, one can rewrite equation 5 into the form of equation 7. Quantum numbers with a mark (n', ℓ', m') are the quantum numbers of the final states, quantum numbers without a mark correspond to the initial state.

$$M_{n\ell m}^{n'\ell' m'} \propto \int d\Omega Y^*_{\ell' m'}(\theta, \phi)\, \mathbf{e} \cdot \mathbf{r}\, Y_{\ell' m'}(\theta, \phi) \tag{7}$$

By evaluating the angular part of the transition matrix element, rules for the transition between different eigen-states can be derived [59], which are also known as 'selection rules'. Transitions are only possible if $\Delta\ell = \pm 1$ and $\Delta m = 0$, or if $\Delta\ell = \pm 1$ and $\Delta m = \pm 1$. These transitions correspond to the absorption or emission of a linearly polarized photon for $\Delta m = 0$ and a circularly polarized photon for $\Delta m = \pm 1$ and are a direct consequence of the conservation of angular momentum [60]. Due to the spherical harmonic functions being orthogonal, they determine if a transition is allowed, while the radial part is what determines the magnitude of the transition probability from the initial to the final state, which can be seen in the way the photoionization cross-section is calculated in reference [61].

Transitions between bound and free states are more complicated since the wave function of the final state has to satisfy the condition of the attractive potential close to the nucleus and also has to take the form of a plane wave at distances far away from the attractive potential [59]. A wave function that properly describes the necessary feature is given in equation 8, neglecting spin contributions [57]. In this formula $\mathbf{p}$ is the momentum vector of the electron, ϑ_p and φ_p are the polar and azimuthal angles associated with the $\mathbf{p}$ and $\mathbf{r}$ vectors, respectively. Additionally $P_{\epsilon\ell}$ are the solutions to the radial part of the Hamiltonian in a spherically symmetric potential, like the Coulomb potential.

$$\varphi_{\mathbf{p}}^{(-)}(x) = \sum_{\ell,m} \frac{1}{p^{1/2}} e^{i\delta_\ell(\epsilon)} \frac{i^\ell}{r} P_{\epsilon\ell}(r) Y_{\ell m}(\vartheta_p, \varphi_p) Y_{\ell m}(\vartheta, \varphi) \tag{8}$$

Since this formula is quite complex and not too enlightening just on its own, one can have a look at special cases.
A special case is created by applying the Born approximation, in which one assumes that the final state wave function was that of a free electron, which is not affected by any potential. This assumption is valid for photon energies large compared to the ionization potential but small compared to the energy of the electrons' rest mass [62]. This leads to the well-known result that for photon energies in the x-ray region the cross-section is proportional to the photon energy to the power of -3.5, $\sigma \propto \omega^{-\frac{7}{2}}$, for ionization of atomic hydrogen.
In contrast to this, the situation is quite complex close to the ionization threshold, leading to phenomena like energetically delayed cross-section maxima and Cooper minima [63]. The origin of these phenomena is the overlap of the radial part of the wave function in the initial and final state. As the photon energy increases, the kinetic energy of the photoelectron increases, thereby changing the final state radial wave function. The higher the kinetic energy is, the more the contribution of the in-going wave is influenced by the contribution of the out-going plane wave.
To visualize the wave functions close to the threshold, one can calculate the radial element for a final state with certain ℓ and m but very high n, so that the electron is barely bound. With increasing photon energies the radial function is compressed towards the potentials center, changing the overlap of the initial and final state wave functions [64] and thereby changing the cross-section.

2.2 INTENSE LASER FIELDS

In the previous section, the interaction of an atom with a weak electromagnetic field was discussed. The main mechanism of ionization is that the electron absorbs a photon with a photon energy that is large enough to overcome the ionization potential of the electron in its initial state. As the amplitude of the electromagnetic wave reaches certain magnitudes, additional ionization mechanisms become relevant. To quantify what these magnitudes are, the so-called 'intensity' or 'irradiance' is defined as $I\,[W/cm^2]$. It can be calculated in the wave picture according to $I(r) = \frac{1}{2}c\varepsilon_0|E(\mathbf{r})|^2$, where c is the speed of light and ε_0 is the vacuum permittivity. The assumption is that the electromagnetic wave is a plane wave at a single frequency with an electric field strength of E [65]. Usually one uses the peak power, meaning that one evaluates the intensity at the position $\mathbf{r}$ where the intensity is highest. It is also possible to calculate the intensity in the photon picture by using the relation $I = hf\phi$ with hf being the product of the Planck constant h and the frequency f of the photons and ϕ being the flux density, which gives the number of photons passing through an area per unit time [66].

As the laser intensity increases, ionization can take place even if the photon energy is smaller than the ionization potential in a non-linear process which is called multi-photon ionization (MPI) [67]. The photon density becomes so high that it is probable for the electron to absorb two or more photons at once, leading to ionization, which was first theoretically described by Göppert-Mayer [7]. The process of multi-photon ionization is shown in figure 1 a).
As the laser intensity increases further and becomes comparable to the field

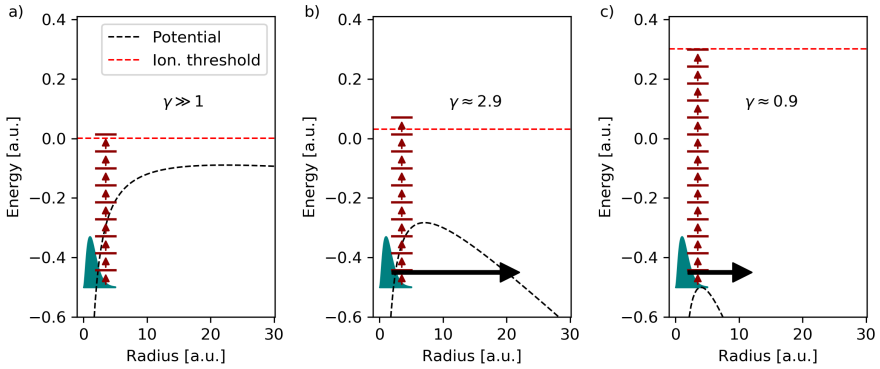

Figure 1: Schematic illustration of strong field ionization mechanisms. The black dotted lines show the potential consisting of the Coulomb potential and the potential created by a static electric field corresponding to the maximum electric field throughout the laser pulse, the red dotted lines show the ionization threshold, including the ponderomotive potential. The hydrogen 1s radial electron probability distribution is shown in teal, with the energy of the state corresponding to the bottom line of the distribution. The red lines show the multi-photon ionization levels and how many photons are necessary to reach the ionization threshold, assuming a wavelength of 800 nm. a) For a Keldysh parameter $\gamma \gg 1$ ($1.4 \cdot 10^{11}\,\mathrm{W/cm^2}$) the ionization is dominated by multi-photon absorption. The potential is not bent enough to allow for tunneling ionization. b) For a Keldysh parameter of $\gamma \approx 2.9$ ($1.4 \cdot 10^{13}\,\mathrm{W/cm^2}$) the potential is bent enough throughout the laser pulse, that the electron wave packet can tunnel through the barrier, which is also called 'tunneling ionization' and is indicated in the figure by the black arrow. Through the increase of the ponderomotive potential, the absorption of another photon is necessary to overcome the ionization potential. c) For a gamma of $\gamma \approx 0.9$ ($1.4 \cdot 10^{14}\,\mathrm{W/cm^2}$), MPI ionization becomes even less probable, showing that now the absorption of 14 photons is necessary for MPI. The probability for tunneling ionization is greatly enhanced, as the tunneling becomes smaller and smaller and vanishes at the given laser intensity. Now the electron wave packet can just move away from the attractive potential of the core without tunneling, which is called over-barrier ionization (OBI). This effect becomes only more relevant, as the laser intensity increases since at the γ given, OBI ionization is only possible at the very maximum of the laser pulse.

strengths that the electron experiences in the Coulomb potential, the Coulomb potential is deformed so much, that the electron can tunnel through the potential barrier (Fig. 1 b).

At even higher laser intensities the potential is bent so much, that the 1s electron in the hydrogen atom is not bound anymore and can freely leave the vicinity of the attractive potential, leading to ionization. This ionization process is called over-barrier ionization (OBI) and is shown in figure 1 c).

To give a quantitative value for the intensity region of the laser field, Keldysh [11] defined an 'adiabatic parameter', see equation 9, which is nowadays called 'Keldysh parameter' [68]. This parameter is the ratio of the angular frequency of the electromagnetic field ω and of ω_t^{-1}, which is the time the electron needs to pass through the tunneling barrier. Furthermore, I is the ionization potential of the electron and F is the electric field strength.

$$\gamma = \omega/\omega_t = \omega\sqrt{2I}/F \tag{9}$$

In a weak electric field, the Coulomb potential is not strongly bent and thus the tunneling barrier is broad, which increases the time the electron needs to tunnel through the barrier, leading to $\gamma \gg 1$. In a strong electric field, the Coulomb potential is heavily influenced by the electric potential of the field and is thus strongly bent. This creates a short tunneling barrier, which implies that the time for tunneling through the barrier is small and $\gamma \ll 1$. An experiment by Landsman et. al. from 2014 showed that this tunneling time is indeed real and can be measured [69]. If $\gamma \approx 1$ the laser intensity is in a mixed regime, where both ionization processes, MPI and tunneling ionization contribute to the overall ionization.
Another aspect becoming relevant in strong field ionization is the shift of the free and bound electronic states in energy within the laser field. This shift is called AC-Stark effect and is the equivalent to the Stark effect in time-independent electric fields. A free electron in a laser field oscillates according to the electric field it is exposed to. Assuming that the electric field is of the form $E(t) = E_0\cos(\omega t)$, then the cycle-averaged energy U_p of the electron in this linearly polarized field is given by equation 10 [70]. Here e is the charge of the electron and m_e is its mass. U_p is also well known as the ponderomotive potential and it appears in figure 1 as a contribution to the ionization threshold, which is shown as the red dotted line. We can see from equation 10 that the ponderomotive potential is proportional to the laser field's intensity. For circularly polarized light of the same peak laser intensity, equation 10 has to be multiplied by a factor of two.

$$U_p = \frac{1}{2}m_e\langle\dot{r}^2\rangle = \frac{e^2E_0^2}{4m_e\omega^2} \tag{10}$$

For bound states, the shift in energy is much more complex and is in general difficult to predict. Already the energy shift of states of the hydrogen atom is very complex [71]. Bound electrons don't follow the electric field in the same way as the free electrons do, as they are affected by the Coulomb potential. A general formula for the AC-Stark shift δE_i of state i in a weak electromagnetic field following perturbation theory is given by equation 11 [72]. Here α_i is the polarizability, F is the field strength, z_{ik} is the dipole matrix element and ω_{ik} is the angular frequency of the atomic transition.

$$\delta E_i = -\alpha_i(\omega)F^2/4 = \frac{F^2}{4}\sum_k |z_{ik}|^2\frac{2\omega_{ik}}{\omega_{ik}^2 - \omega^2} \tag{11}$$

For angular frequencies ω that are small compared to the angular frequencies of transitions ω_{ik}, the equation reduces to the equation for the energy shift in a constant electric field. In the opposite limit, for large angular frequencies, the energy shift becomes the ponderomotive potential for all states, since the electron cannot properly follow the motion of the electric field anymore, if it is bound or not. In general, the energetic shift is lower for states which are more tightly bound. The expressions for the polarizability can be derived by analytically evaluating the

dipole matrix elements. The polarizability for linear polarization is given by equation 12 and for circular polarization it is given by equation 13. In these equations m is the magnetic quantum number and j is the angular momentum of state i. The other parts of the polarizability are the scalar part α^s, the asymmetric part α^a and the tensor part α^T. The $\pm$ sign takes into account if the polarization is left- or right-circularly polarized. Interesting to note here is the fact that the polarizability depends on the magnetic quantum number, which will be relevant later on in the experiment.

$$\alpha_i(m) = \alpha^s + \alpha^T \frac{3m^2 - j(j+1)}{j(2j-1)} \tag{12}$$

$$\alpha_i(m) = \alpha^s + (\pm\alpha^a)\frac{m}{2j} - \alpha^T \frac{3m^2 - j(j+1)}{2j(2j-1)} \tag{13}$$

When measuring the photoelectron spectrum of an atom ionized by strong laser fields, one can actually observe a series of peaks. While the electron is still affected by the Coulomb potential it can absorb more than the number of photons that are necessary for ionization. This leads to a series of peaks in the photoelectron spectrum which are separated by the photon energy, which is known as 'above-threshold ionization' (ATI) [73]. In general, the cross-section for each subsequent ATI peak requiring the absorption of an additional photon is decreasing with each additional photon that has to be absorbed.

Up to now we, assumed in the MPI process that no resonances are involved. Usually, this is not the case, since even the hydrogen atom has many excited states. If several photons are necessary for MPI, there is a manifold of energies where an excited state with energy E_{exc} could be located after the absorption of a certain number of photons n_{res}. The condition $E_{exc} = E_i + n_{res} \cdot \hbar\omega$ has to be fulfilled for resonant ionization and if it is, the ionization is called resonance-enhanced MPI (REMPI) [74]. Resonant MPI enhances the photo-ionization cross-section compared to non-resonant MPI and leads to resonance structures within the MPI and ATI photoelectron peaks, which was first discovered by Freeman et al. [75]. To observe these resonances it was necessary to use sufficiently short laser pulses (400 fs or below), to measure the photoelectron energy at the moment of ionization. If the pulse is too long, the just created photoelectrons will be accelerated by the gradient of the ponderomotive potential in the focal region of the laser pulse, shifting the energy of the photoelectrons by the amount of the ponderomotive potential, so that they end up with the same kinetic energy, rendering the different resonances indistinguishable. Since the AC-Stark shift changes the energy of eigen-states of the system depending on the laser intensity, the fulfillment of a resonance condition will depend on the instantaneous laser intensity throughout the laser pulse. Such an enhancement of the cross-section at resonance with an AC-Stark shifted state, with transient referring to a changing laser intensity, is called a 'Freeman-resonance'.

A schematic depiction of this is shown in figure 2 a) where the intensity dependent multi-photon ionization by three photons is shown. The photons are shown as black arrows and their length corresponds to the photon energy. The black line

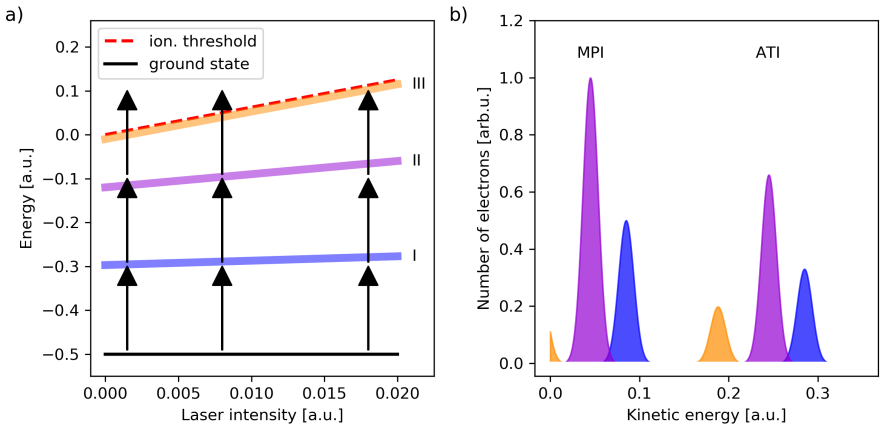

Figure 2: Schematic illustration of Freeman-resonances in MPI. a) Shown is the shift in energy of the ionization potential, the ground state and three different and differently colored excited states depending on the instantaneous laser intensity. The photons are depicted as black arrows and their length corresponds to the photon energy. b) The resulting photoelectron spectrum after the absorption of three photons (MPI) and four photons (ATI). Peaks of MPI and ATI are separated by the photon energy.

is the ground state, the red dotted line is the ionization threshold and the colorful lines show the AC-stark shifted eigen-energies of different excited states. One can see that the excited states are shifted in and out of resonance depending on the laser intensity. The blue excited state (1) is in resonance after absorbing one photon, while the violet excited state (2) is in resonance after the absorption of two photons at a higher laser intensity. The third excited state (3) is weakly bound and therefore shifts similar in energy to the ionization threshold. It is in resonance after the absorption of three photons, which means that this 'Freeman-resonance' only appears in the photoelectron spectrum of the first ATI peak after the absorption of another photon from the excited state.

A schematic of the photoelectron spectrum that would be created if a pulse with an intensity high enough, that all three excited states will be in resonance throughout the laser pulses intensity envelope is shown in figure 2 b). The colors of the peaks correspond to the colors of the excited state that is in resonance. The photoelectron with the highest kinetic energy of the MPI peaks is the blue peak since it corresponds to a resonance that appears at the relatively lowest laser intensity. The violet peak is shifted towards lower kinetic energies since the resonance appears at higher kinetic energies, where the ionization threshold is greater due to the ponderomotive shift. The orange peak only appears in the MPI spectrum due to its width. The center of the distribution is below the ionization threshold due to the ponderomotive shift. In the ATI spectrum this peak appears fully since, with the absorption of another photon, the kinetic energy is large enough to overcome the ionization potential. The other peaks of the MPI also appear in the peaks of the ATI photoelectron peaks after the absorption of another photon. However, the peaks of the ATI photoelectrons are a bit smaller since it is a little bit less likely to absorb yet another photon. These Freeman-resonances have been extensively studied in the case of MPI of xenon [75–78]. In an experiment by M. Li et. al. [79] the

intensity dependent MPI and ATI photoelectron spectrum of xenon in ultra-short laser pulses of 800 nm was recorded. In the resulting 2D plot the photoelectron peaks from Freeman-resonances do not shift in energy with different laser intensities, but different resonances appear and disappear while new resonances appear at lower kinetic energies with increasing laser intensity due to the increasing ponderomotive potential within the same feature (MPI, ATI).

2.3 PHOTOELECTRON ANGULAR DISTRIBUTION

As described in the section about ionization and excitation, the cross-section depends on the transition matrix elements. To get information about the angular distribution of the photoelectron after ionization, it is necessary to calculate the differential cross-section $d\sigma/d\Omega$. Equation 14 shows how to calculate the differential cross-section in the 'length' formulation, which is taken from S. Smith and G. Leuchs [80]. The derivation of formulas for the differential cross-section in the case of one-photon ionization follows the explanations by the aforementioned source.

$$\frac{d\sigma}{d\Omega} = \frac{4\pi^2\omega}{c} k \left(\frac{e^2}{m^2\hbar^2} \right) \left| \hat{\mathbf{e}} \cdot \langle \psi_0 | \sum_{i=1}^{N} \hat{\mathbf{r}}_i | \psi_k^- \rangle \right|^2 \tag{14}$$

Here ω, k and c are the angular frequency, the length of the wave vector and the speed of light, respectively. The squared term contains the transition matrix elements between the initial state wave function ψ_0 and the final state wave function ψ_k^-, which has the form of equation 8. The polarization vector is given by $\hat{\mathbf{e}}$ and the position in space for the i-th electron out of total of N electrons is given by $\hat{\mathbf{r}}_i$. By inserting the wave function of the electron in the continuum and assuming a one-electron system, a different formulation for the matrix element in equation 14 can be found, which is given in equation 15.

$$\hat{\mathbf{e}} \cdot \langle \psi_0 | \sum_{i=1}^{N} \hat{\mathbf{r}}_i | \psi_k^- \rangle \propto \sum_{\ell' m'} a_{n\ell m}^{n'\ell' m'} i^{\ell'} e^{-i\delta_{\ell'}} Y_{\ell' m'}^*(\Theta, \Phi) \tag{15}$$

In this depiction of the matrix element $a_{n\ell m}^{n'\ell' m'}$ are coefficients that include the integration over the radial and angular components in the system of the atom, while $Y_{\ell' m'}^*$ is the spherical harmonic with the angles Θ, Φ corresponding to the direction of the photoelectron relative to the quantization axis. For linear polarization usually the axis of polarization is used as a quantization axis while for circularly polarized light one uses the propagation direction of the light. Using the dipole transition rules for the quantum numbers, the sum over all ℓ' and m' will reduce to only a few terms depending on the polarization and the initial state of the system. For linearly polarized light $\Delta\ell = \pm 1$ and $\Delta m = 0$. This then leads to equation 16.

$$\hat{\mathbf{e}} \cdot \langle \psi_0 | \hat{\mathbf{r}}_i | \psi_k^- \rangle \propto [a_{n\ell m}^{n\ell+1 m} i^{\ell+1} e^{-i\delta_{\ell+1}} Y_{\ell+1 m}^*(\Theta, \Phi) + a_{n\ell m}^{n\ell-1 m} i^{\ell-1} e^{-i\delta_{\ell-1}} Y_{\ell-1 m}^*(\Theta, \Phi)] \tag{16}$$

Since the differential cross-section includes the square of the term one ends up with equation 18 containing the square of the $\ell+1$ and $\ell-1$ contribution and an interference term.

$$\frac{d\sigma}{d\Omega} = |a^{n\ell+1m}_{n\ell m}|^2|Y_{\ell+1m}|^2 + |a^{n\ell-1m}_{n\ell m}|^2|Y_{\ell-1m}|^2 \tag{17}$$

$$- \left[a^{n\ell+1m}_{n\ell m} a^{*n\ell-1m}_{n\ell m} e^{i(\delta_{\ell+1}-\delta_{\ell-1})} Y^*_{\ell+1m} Y_{\ell-1m} + c.c.\right] \tag{18}$$

For a few special cases, it is possible to get a simple form of the differential cross-section. For example, if the initial system is in an s-wave state with $\ell = 0$, because then there is no term with $\Delta\ell = -1$ and the interference term vanishes. The differential cross-section will then always be proportional to $|Y^2_{10}| \propto \cos^2(\Theta)$. This has been observed for photodetachment from negatively charged, atomic hydrogen [81]. The interference of the $\ell+1$ and $\ell-1$ channel could very well be observed in photodetachment from the negative carbon and oxygen ions [82]. At the ionization threshold their angular distributions show s-type symmetry and as the photoelectron energy increases the angular distribution becomes anti-aligned relative to the lasers linear polarization axis, due to interference with the increasing d-wave contribution. The differential cross-section for one-photon ionization by linearly polarized light can be expressed via equation 19 [83].

$$\frac{d\sigma}{d\Omega} = \frac{\sigma_{total}}{4\pi}\left[1 + \beta P_2(\cos(\theta))\right] \tag{19}$$

Here β is the so-called 'asymmetry-parameter', which depends on ℓ and the phase-shifts $\delta_{\ell+1}$ and $\delta_{\ell-1}$ as well as the radial matrix elements. β ranges from -1, in which the angular distribution is perpendicular to the polarization axis of the light, to 2, where the angular distribution is fully aligned along the light's polarization axis. P_2 is the Legendre polynomial of second order. Figure 3 a) shows the angular distributions for different β values. It should be noted that the electron spin is neglected here, which also leads to the neglect of any angular momentum and spin interaction. For circularly polarized light a similar formula can be found, in which $\beta \to -\frac{1}{2}\beta$ [84]. This adaption arises due to a change of the quantization axis. In the case of circularly polarized light, the polarization vector is not a good quantization axis anymore. Instead one chooses the propagation direction of the light, leading to the above change in the formula for the differential cross-section. In figure 3 b) the measured PAD is shown for photoelectrons of helium ionized by circularly polarized XUV pulses. The β parameter is 2 for the different energies.

In multi-photon ionization, the photoelectron angular distribution can be described by the quantum numbers ℓ' and m' in the final state. For every photon absorbed, ℓ and m have to change according to the rules for dipole transitions [85] within the dipole approximation. The angular distribution in the final state can still be described via the superposition of spherical harmonics with all possible quantum number combinations (ℓ, m) and their interference. The following, equation 20 to 25 show how ℓ and m can change for every photon absorbed from a light field with linear polarization.

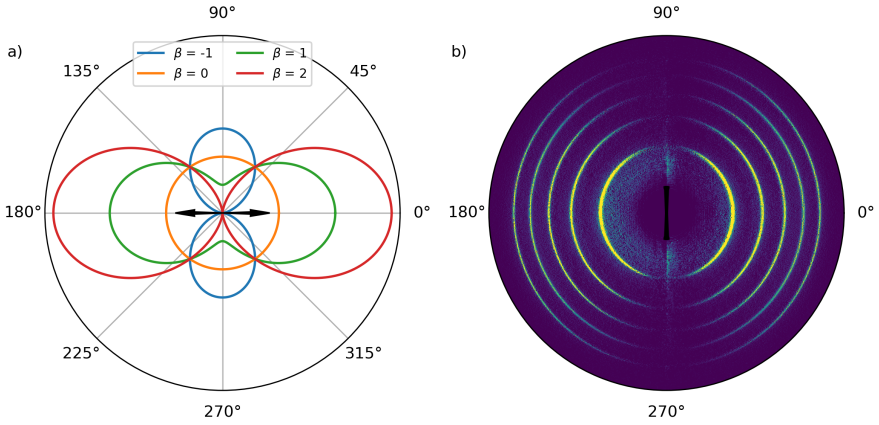

Figure 3: a) Angular distributions of one-photon ionization for different β parameters. The black arrow indicates the polarization direction. b) Photoelectron angular distribution of helium ionized by XUV photons with five different energies. The angular distribution has a β value of 2 for the different energies. Opposite to a), the black arrow indicates the propagation direction of the beam.

$$
\begin{aligned}
1.\,\text{photon}: \quad & (\ell, m) && \rightarrow (\ell+1, m)\,\&\,(\ell-1, m) && (20)\\
2.\,\text{photon}: \quad & (\ell+1, m) && \rightarrow (\ell+2, m)\,\&\,(\ell, m) && (21)\\
& (\ell-1, m) && \rightarrow (\ell, m)\,\&\,(\ell-2, m) && (22)\\
3.\,\text{photon}: \quad & (\ell+2, m) && \rightarrow (\ell+3, m)\,\&\,(\ell+1, m) && (23)\\
& (\ell, m) && \rightarrow (\ell+1, m)\,\&\,(\ell-1, m) && (24)\\
& (\ell-2, m) && \rightarrow (\ell-1, m)\,\&\,(\ell-3, m) && (25)
\end{aligned}
$$

Here one can see how after the absorption of three photons a manifold of final states is available. How many of these final states can be reached depends on the initial values of ℓ and m, due to the condition for the angular momentum quantum number $\ell \geq 0$ and the magnetic quantum number $|m| \leq \ell$ for dipole transitions. Excited states of the system can only be in resonance after the absorption of n photons if the quantum numbers of the excited state match the quantum numbers of the initial state plus the change of those after absorption of n photons. For circularly polarized light the schematic would be similar to the change that for every photon absorbed m would also change by +1 or −1, depending on the helicity.
A general formula to describe the angular distribution in the case of MPI is given in equation 26 [80, 84], which is an expansion of the differential cross-section into spherical harmonics with N being the number of photons absorbed for ionization and $B_{2K,M}$ are the coefficients, which determine the contribution of each partial wave.

$$
I(\Theta, \Phi) = \sum_{K=0}^{N} \sum_{M=-2K}^{2K} B_{2K,M} Y_{2K,M}(\Theta, \Phi) \tag{26}
$$

For linear polarization this description reduces to equation 27 with P_{2K} being Legendre polynomials of order 2K.

$$I(\Theta) = \sum_{K=0}^{N} B_{2K,0} P_{2K}(\Theta) \tag{27}$$

2.4 PHOTOELECTRON CIRCULAR DICHROISM

Circular dichroism (CD) is a measure of how a sample interacts with left or right circularly polarized light. Usually, this interaction is the difference in absorption for the two helicities (left or right circularly polarized) of the light, which is for example used in determining the secondary structure of proteins [86]. A protein consisting mainly of α-helix structures will have a distinctive shape of the wavelength dependent CD between wavelengths from 190 nm to 250 nm, as does a protein consisting mainly of β-sheets. The CD in these studies is usually given in the ellipticity of linearly polarized light after it passed through the sample. Asides from proteins molecules can also have a CD if they are chiral, meaning that they can't be spatially superimposed with their mirror image [87]. Due to differences between the chiral molecule and its mirror image, they behave physically and chemically differently. In biological interactions this difference between the molecule and its mirror image becomes apparent, as for example the taste and smell between the two can be different [88]. In pharmaceuticals this is even more important as the different enantiomers (molecule and mirror image) will have different pharmaceutical effects and can make the difference between a medicine being useful or harmful [89].
The origin of the CD in photo-absorption lies within the electric-dipole-magnetic-dipole terms. The influence of these terms is on the order of 10^{-6} to 10^{-3} relative to the absorption signal, making the difference signal quite weak for small molecules [90]. In a more macroscopic picture, the difference in absorption depends on the pitch of the circularly polarized wave over the dimension of the molecule. Circularly polarized light with a wavelength of 2000 Å (200 nm) only has a small pitch over the dimension of a molecule of about 1 Å[91].
It was predicted theoretically that also the angular distribution of photoelectrons from chiral molecules should exhibit a dichroism [92]. This photoelectron circular dichroism (PECD) arises as the outgoing photoelectron wave scatters differently with the chiral or non-central molecular potential left behind, leading to a difference in the forward and backward angular distribution on the order of 10^{-2} to 10^{-1}, making it much more feasible to use for smaller molecules [90, 91].
Other variants of PECD studies don't ionize the molecule directly via one photon, but rather use a combination of resonant excitation and multiphoton ionization. The forward-backward asymmetry in the PAD has for example been observed in fenchone ionized by one-photon ionization in the XUV region [93]. More recently this asymmetry in the PAD has also been observed in (2+1)-REMPI of fenchone [94] and it could be modeled by theoretical calculations [95]. In REMPI a CD of around 10 % (4 %) was found for a random orientation of the fenchone molecules in the laser pulse in the MPI (ATI) feature. For specifically oriented molecules a CD of up to 33 % could be predicted. It could even be shown that this effect remains when using laser intensities in the tunneling-ionization regime, showing the universality of the PECD in single-photon ionization, MPI, ATI and tunneling ionization [96].

Another emerging very fundamental approach to spatial alignment is to create a polarized atom or ion. This can be achieved by preparing an atom or ion in a magnetic sub-state with $m \neq 0$ by exciting it with circularly polarized light. Ionizing the prepared atom or ion in this polarized state via differently circularly polarized light will lead to a CD, which can be calculated via equation 28 [50]. The calculated circular dichroism is the result of differences in the yield of photoelectrons Y_{++} and Y_{+-} for the different helicities of the light, relative to the helicity of the exciting light.

$$CD = \frac{Y_{++} - Y_{+-}}{Y_{++} + Y_{+-}} \tag{28}$$

In general, for weak light fields in one-photon ionization, the circular dichroism will be positive for these polarized systems, meaning that ionization via pulses with the same helicity is favoured. For a laser intensity in the tunneling regime, the CD becomes negative, meaning that ionization via pulses with opposite helicities is more probable [97]. In multi-photon ionization the circular dichroism will be intensity dependent and is in general not monotonic due to the Freeman resonances which are the result of the intensity dependent AC-Stark shifts. Thus also the used wavelength plays an important role and can induce a sign-change of the CD at similar laser intensities [50]. The study of the CD dependence on the laser intensity and the wavelength in the multi-photon regime is a scientific interest which more recently emerged. It bridges the gap between single-photon and tunneling ionization studies regarding the CD.

3 ULTRA-SHORT LASER PULSES

To study the interaction between light and atoms or molecules in the multi-photon, tunneling, or even over barrier ionization regime, light with a very high intensity is needed. This type of intense light can be provided by chirped-pulse amplification (CPA) laser systems in the optical regime [98], while for the XUV [36] and X-ray regime [99] free-electron lasers (FEL) are typically used. The light provided by these sources is pulsed with pulse lengths down to a few femtoseconds (10^{-15} s, fs) and even lower. This property of the light can be used to study phenomena on a similar time-scale such as the dynamics of molecules upon interaction with a laser pulse. It also enables non-linear interactions of light with matter. Another way of generating very short pulses in the XUV region, although with much lower intensities, is high harmonic generation (HHG). HHG can be used to generate attosecond (10^{-18} s, as) pulses, allowing to investigate electron-dynamics on their intrinsic timescale [100]. The upcoming sections will give a short review of how to generate intense, ultra-short light pulses in the optical and XUV regime.

3.1 OPTICAL LASERS AND NON-LINEAR OPTICS

The basis for generating ultra-short intense laser pulses is the laser, which is an acronym for 'light amplification by stimulated emission of radiation'. The enabling effect of the laser is a phenomenon which is known as 'stimulated emission' [101]. If the photon energy of light interacting with a system of two levels n and m is exactly the energy between the two levels, then the photon can induce a relaxation from the excited to the lower state, thereby emitting a photon with the same energy, phase and propagation direction as the incoming photon. As this process competes with absorption and spontaneous emission, the system needs to be in a state of population inversion, meaning that the excited level is more populated than the lower level, to achieve amplification of the light. To achieve higher levels of amplification, the lasing medium is usually put in a cavity of reflecting concave mirrors to create a feedback. To make use of the light one of the mirrors is semi-transparent, allowing for light to be coupled out. Such a cavity defines which wavelengths can be amplified in the cavity due to the necessity for constructive interference of the light wave after one round-trip in the cavity. The condition can be written as $n\lambda_n = 2L$, with n being a positive integer, λ_n the wavelength and L the length of the cavity, thus allowing only certain wavelengths. In the frequency picture the different wavelengths, or modes, are separated by a frequency of $\Delta f = c/2L$ and the round-trip time t of light in the cavity is $t = 2L/c$.
A first demonstration of lasing in the optical regime in a solid was shown by Maiman in 1960 by pumping ruby [102]. Shortly after lasing was also demonstrated in a gas-mixture of helium and neon [103] and in carbon dioxide [104]. Pulsed laser operation with pulse widths of 2.5 ns was achieved by inserting a loss modulating device into the laser cavity, which could be operated at varying

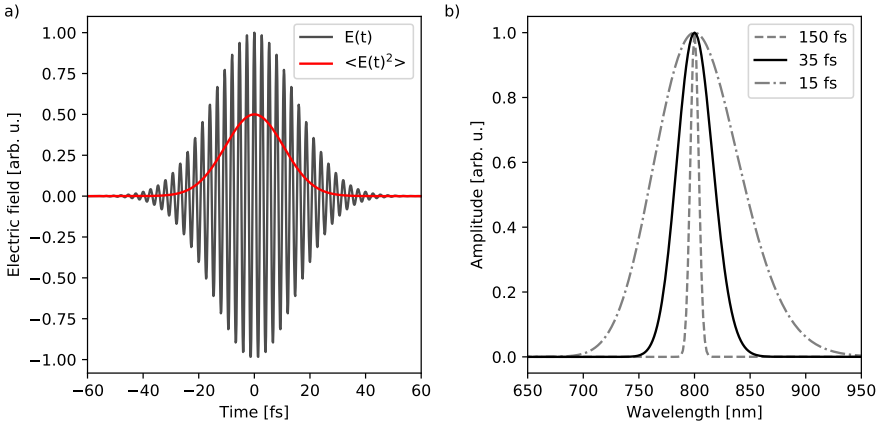

Figure 4: a) Electric field of a laser pulse with a Gaussian envelope (black) and the cycle-averaged laser intensity (red). b) Spectra for laser pulses with different FWHM pulse lengths, showing that shorter pulses require broader spectra.

frequencies [105]. Driving the loss modulating device at the difference frequency between modes leads to 'mode-locking', in which the phases of each of the cavity modes are in a fixed phase relation to all the other modes. For a Gaussian laser pulse the pulse width $\Delta\tau$ is connected to the spectral width $\Delta\nu$, or the number of cavity modes contributing to the pulse, in the following relation $\Delta\tau \cdot \Delta\nu \geq 0.44$ [66]. This shows that to generate shorter and thereby more intense pulses, it is necessary to amplify a large range of frequencies. Much shorter pulses with pulse lengths below picoseconds (10^{-12} s, ps) were generated by using dye molecules as the gain medium due to the broader transitions [106]. Nowadays typically titanium sapphire lasers (Ti:Sa) are used to generate ultra-short laser pulses down to 5 fs [107]. The transitions of the titanium ions in the crystal matrix of sapphire (Al_2O_3) are broadened due to coupling with the crystal field and the vibrations of the crystal lattice, leading to an emission range from 680 nm to 1130 nm [108], which enables the generation of short pulses. The population inversion in the Ti:Sa is created by a continuous-wave (CW) diode laser by pumping the Ti:Sa crystal at a central wavelength of the absorption band around 500 nm. Figure 4 a) shows a laser pulse with a central wavelength of 800 nm and a pulse length of 35 fs full-width half-maximum (FWHM), which is an ideal depiction of the laser pulses that we have access to. In sub-figure b), the spectrum for different pulse lengths is shown. Since the time-bandwidth product holds, longer pulses will have a more narrow spectrum compared to shorter pulses.

Having such short pulses also leads to high laser intensities, reaching the regime of non-linear optics. In non-linear optics, the refractive index is a function of the intensity of the light field due to higher order terms of the electric field in the series expansion of the macroscopic polarization of a material [109]. This leads to a number of effects, one of which is the Kerr-lens effect. A Gaussian beam traveling through a medium with a positive refractive index regarding the non-linear component will self-focus within the medium until linear diffraction balances the focusing through the dimension of the wavelength. This phenomenon is used in

the Ti:Sa laser to achieve mode-locking [110]. The Kerr-lens effect lead to issues when trying to amplify laser pulses, as the self-focusing beam damaged the lasing medium. To circumvent this issue, Strickland et. al. [6] used a technique known from radar, in which the signal is stretched in time before being amplified and compressed after the amplification, to avoid damage to the amplifying circuits. Optically this was achieved by letting the pulse pass through a 1.4 km long fiber, which stretched the pulse due to the different velocities of different spectral components of the laser pulse depending on the refractive index. After the amplification, the pulse was compressed again using a pair of gratings. In modern Ti:Sa amplifiers a pair of gratings is used to temporally stretch and compress the laser pulses. This enabled the generation of laser pulses with several orders higher pulse energy with, when focused, electric field strengths on a similar scale as the electric field that electrons experience in the attractive coulomb-potential of the atom's core.
The availability of laser intensities that enable non-linear optics led to several other useful applications. In non-linear optics light waves can interact with each other, leading to frequency mixing effects. The most straightforward process of this frequency mixing is second-harmonic generation. In this process, two photons with the same angular frequency ω can join together to become one photon of frequency 2ω, which was demonstrated shortly after the appearance of the ruby laser [8]. To efficiently convert the fundamental radiation to the second-harmonic radiation, a birefringent material with an optical axis is necessary to allow for phase-matching between the two frequency components. Usually, the refractive index of a material depends on the frequency of the radiation, which leads to different propagation velocities of fundamental and second-harmonic radiation. To overcome this, a material is used that has an optical axis, meaning that it has different refractive indices depending on the polarization of the radiation relative to the optical axis. This enables phase-matching between the fundamental and second-harmonic radiation by turning the doubling-crystal to a certain angle, leading to an efficient conversion [111]. A typical material used for second-harmonic generation (SHG) of fundamental radiation at 800 nm is β-Bariumborat (β-BBO). In a similar manner also light with different frequencies can add or subtract their frequencies [109]. By focusing an intense laser into a crystal or gas, one can even create a white light continuum, spanning the whole optical spectrum and the near-IR up to wavelengths of a few micron [112, 113].
For gas-phase experiments of atomic systems, usually quite high photon energies in the XUV region are necessary to ionize the system. This unfortunately cannot be provided by solid media, since all materials start to strongly absorb radiation with a photon energy just above the ionization threshold. To overcome this one can use another process of non-linear optics, which is high harmonic generation (HHG) in gases.

3.2 HIGH HARMONIC GENERATION

A few years after the demonstration of second-harmonic generation in a crystal, it was demonstrated that harmonics could also be produced by focusing an intense laser beam in gaseous media [114]. With time more intense laser pulses with a range of wavelengths became available and with these many orders of harmonics

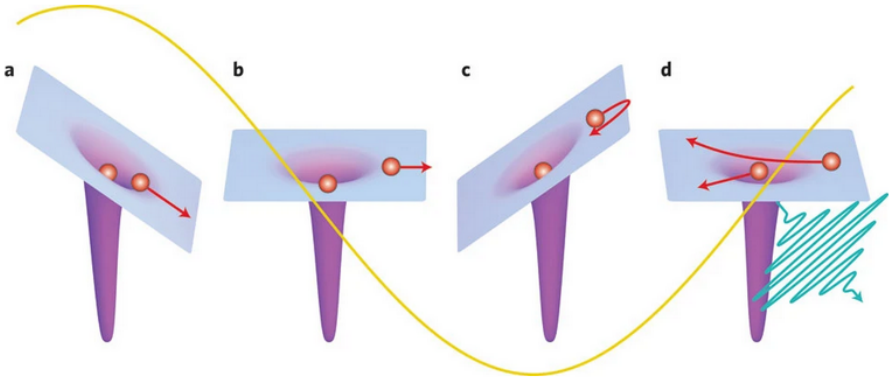

Figure 5: Schematic of the HHG process, taken from [117]. a) At the maximum of the electric field, shown in yellow, the atom is ionized via tunneling ionization. b) The resulting unbound electron is accelerated away from the ion and at some point c) reverses direction and is accelerated back to the ion due to the sign change of the electric field. d) The electron recollides with the ion, thereby emitting high harmonic radiation.

could be generated [115]. This process of generating high harmonics in a gaseous medium is usually referred to as 'high harmonic generation' (HHG). Nowadays high harmonics reach wavelengths up to the soft x-ray region [116] and can have pulse lengths on the attosecond time-scale [100].

The generation of high harmonics can be described in a three-step model [118, 119] for laser intensities I with $\hbar\omega \ll I_p \ll U_p(I)$, shown schematically in figure 5. In the first step, the electron in an atom or molecule is ionized by the laser field, either through tunneling ionization or through multi-photon ionization. Depending on the moment of ionization, the electron will be accelerated away from the ion in the laser field and gain kinetic energy. As the electric field of the laser pulse is periodic, the laser field will reverse at some point, accelerating the electron towards the ion. Upon collision with the ion, the electron can recombine with the ion, leading to the emission of higher energetic radiation. The ionization rate ω_0 of an atom in the tunneling regime, $\gamma \ll 1$, is given in equation 29 in atomic units, following the model of Keldysh [11]. Here I_p is the ionization potential, F is the field strength and $\gamma = \sqrt{\frac{I_p}{2U_p}}$ is the Keldysh parameter with U_p being the ponderomotive potential.

$$\omega_0 = \frac{6\pi}{4}(\sqrt{I_p}F)^{1/2}\exp\left[-\frac{2(2I_p)^{3/2}}{3F}\left(1-\frac{\gamma^2}{10}\right)\right] \tag{29}$$

In the opposite case, for $\gamma \gg 1$, the expression is very different, see equation 30, and accounts for pure multi-photon ionization. In this expression, K_0 is the number of photons at least necessary to ionize the atom at low laser intensities. This expression states the well know fact that multi-photon ionization via K_0 photons is proportional to the laser intensity to the power of K_0.

$$\omega_0 \propto \left(\frac{F}{\omega}\right)^{2K_0} \tag{30}$$

Comparing the two equations it becomes clear that the ionization in the two cases follows different mechanisms, as the ionization rate in the tunneling regime is exponential, while it is to a certain power in the multi-photon regime.
After ionization, the electron will be accelerated by the laser field. The trajectory of the electron is determined by the time of ionization t_i relative to the phase of the oscillating laser field. For some times of ionization, the electron never returns back to the ion, while for other ionization times it does. The maximum photon energy $\hbar\omega$ that can be generated in the high harmonic process depends on the maximum kinetic energy the electron can have at the moment of recollision with the parent ion and is given by equation 31 [118–120], which is also referred to as the high harmonic cutoff. Here U_p is the ponderomotive potential and I_p is the field-free ionization potential.

$$\hbar\omega = 3.17 \cdot U_p + I_p \tag{31}$$

The cutoff is mainly determined by the ponderomotive potential, which itself is proportional to the laser intensity and the wavelength of the radiation squared. Thus high cutoff energies are achieved by using high laser intensities and light with long wavelengths. Using a 3.9 µm driving laser it was possible to generate harmonics with photon energies of up to 1.6 keV, which is in the soft x-ray wavelength range [121].
The electron trajectory which leads to the highest kinetic energy at the moment of recollision is followed if the electron is ionized at a phase angle of 17°, leading to recollision at 234°, assuming that the maximum of the electric field is at 0° [118, 122]. The same trajectory also appears if ionization happens at 197°, since there are two electric field maxima within one cycle. Additionally, there are 'short' and 'long' trajectories, depending on the phase of the field at the moment of ionization, regarding the excursion time, which led to the same kinetic energy of the electron at recollision. This similarity between the trajectories can lead to interference effects in the HHG spectrum [123].
Since the recollision happens twice per laser cycle in opposite spatial directions, assuming linear polarization, the harmonics of the HHG spectrum will be separated by twice the photon energy of the driving laser pulse and only odd harmonics appear in the spectrum, if the pulse is long (multiple cycles) [124]. The HHG radiation produced this way is also called an attosecond pulse train (APT), since twice every laser cycle an attosecond long HHG burst is emitted [125].
Regarding the efficiency of the HHG process, the excursion time of the electron in the laser field plays an important role due to the spatial spreading of the electron wave packet [118]. The larger the electron wave packet is spread out, the less probable the recollision with the parent ion becomes. If the aim is to drive lower harmonics, one can for example use the SHG of the fundamental beam to drive the HHG [126].
Until now we only took the response of a single atom into account, but to actually have a decent HHG yield many atoms are necessary, which involves collective effects. To get a coherent superposition of high harmonics from the atoms at different positions along the beam, the phase-matching condition given by equation

32 needs to be fulfilled [127]. Here q is the order of the harmonic, k is the wave vector and ω_f is the angular frequency of the driving laser.

$$\Delta k = qk(\omega_f) - k(q\omega_f) \tag{32}$$
$$= \Delta k_{disp} + \Delta k_{plasma} + \Delta k_{foc} \tag{33}$$

To maximize the yield, the wave vector mismatch between the fundamental and the harmonic should be minimized and ideally becomes zero. The contributions that need to be balanced are shown in equation 33, with Δk_{disp}, Δk_{plasma} and Δk_{foc} being the wave vector mismatch induced by the dispersion, the plasma and the focusing conditions, respectively. The plasma contribution arises because the laser pulse ionizes the neutral gas atoms as it propagates through them. To achieve $\Delta k = 0$ the plasma contribution needs to balance the contributions from the dispersion and the focusing condition, as it is the only negative contribution, whereas the other two are positive. This balance can be achieved by adjusting the gas pressure of the medium since the plasma frequency and thus the wave vector mismatch of the plasma contribution depends on it.
Having access to a laser-lab based source of XUV and even x-ray radiation is quite handy but it comes at the drawback of having a low conversion rate from the fundamental to the high harmonics. Typical pulse energies of laser-lab based HHG sources range from mJ to μJ depending on the repetition rate, the photon energy of the harmonics and the design of the source [128]. More intense sources in the XUV and x-ray wavelengths are synchrotrons and especially free-electron lasers, which are the topic of the upcoming section.

3.3 FREE-ELECTRON LASER

Free-electron lasers (FELs) provide intense, coherent, short-pulsed radiation over a wide range of photon energies. They are part of the group of fourth generation synchrotron light sources, hinting at the development and the physical principle behind the operation of an FEL. In general, it is known that accelerated charges emit radiation, as for example in an antenna. Synchrotron light is produced in a similar fashion by accelerating electrons to relativistic velocities and passing them through a static magnetic field. This will lead to a deflection of the electrons' beam path and additionally, incoherent light will be emitted since the electrons are accelerated perpendicular to their propagation direction by the magnetic field. The spectrum of the synchrotron radiation is broad around a maximum at a photon energy of ϵ_c, which depends on the electron energy E_e and the magnetic field B [129], see equation 34.

$$\epsilon_c[keV] = 0.665 \cdot E_e^2[GeV]\, B[T] \tag{34}$$

Due to the relativistic velocities, the emission of the light is mainly directed in a cone in the propagation direction of the electrons. Originally this radiation was discovered as a by-product of particle accelerator storage rings, in which these magnets were used to keep the particles on a ring-like trajectory [130].

To enhance the emitted radiation, specific devices were designed to make the electron trajectory bend more often, the so-called 'wigglers' or 'undulators'. These devices consist of permanent magnets which are placed in a row with alternating directions of the magnetic field, forcing the electrons to oscillate perpendicular to their propagation direction with the periodicity of the magnetic field of λ_u. In the resting frame of the electron, the undulator period appears shortened by the Lorentz factor $\gamma = E/(m_0c^2)$, due to the Lorentz-contraction, with E being the electron energy, m_0 being the electrons resting mass, and c being the speed of light. In the laboratory frame, the wavelength of the emitted radiation appears shortened by 2γ, due to the Doppler effect. The combination of these two effects leads to the undulator having a quite short resonant wavelength λ for relativistic electrons, although the dimension of the undulator period is on the order of a few centimeters [131]. A formula to calculate the resonant wavelength is given in equation 35, with K being the so-called undulator strength parameter [132] and Φ being the observation angle relative to the undulator axis. This formula already shows the tunability of the resonant wavelength λ by changing the magnetic field strength. Experimentally this can be realized by changing the gap size between the magnets.

$$\lambda = \frac{\lambda_u}{2\gamma^2}\left(1 + \frac{K^2}{2} + \gamma^2\Phi^2\right) \tag{35}$$

$$K = \frac{eB\lambda_u}{2\pi mc} = 0.934 \cdot B[T]\,\lambda_u[cm] \tag{36}$$

To achieve lasing, very long undulators are used, which led to an effect called self-amplified spontaneous emission (SASE). The electron bunch will start to emit radiation at the resonance frequency λ upon propagating in the undulator. Within the undulator, the combined interaction of the electrons with the magnetic field and the light field, which is emitted by the electrons themselves, will lead to microbunching of the original electron bunch distribution at the wavelength of the undulator period λ_u. The density modulation of the electron bunch leads to some of the emitted wavelengths being emitted coherently, leading to a stronger build-up of the light wave, which in turn leads to a stronger density modulation [34]. At some point after propagating within the undulators saturation is reached and no further amplification takes place.
The spectrum of light generated by the SASE process suffers from shot noise since the amplification process starts from random emissions of radiation. Light pulses from different electron bunches will vary in pulse duration, spectral profile and pulse energy [133]. A way to counteract this is to seed the FEL with an optical/UV laser, which is usually called high-gain harmonic generation (HGHG) [134, 135]. In HGHG a seed laser is overlapped with the electron bunch in the first undulator, which is called a 'modulator', see figure 6. This introduces an energy modulation in the electron bunch, which is converted into a longitudinal density modulation in a dispersive section. The density modulated electron bunch then enters the undulator section dedicated to the lasing, the so-called 'radiator', which can be tuned to harmonics of the seed lasers wavelength. This omits the statistical build-up of the SASE process and leads to more consistent light pulses from different bunches regarding the spectrum, the pulse width, the pulse energy and other properties.
The polarization of light produced by the FEL is dictated by the geometry of the

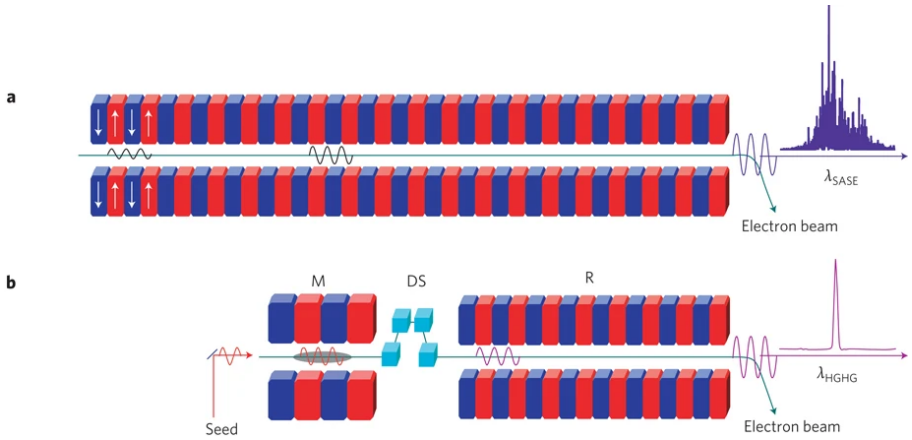

Figure 6: a) Shown is the undulator structure with the SASE build-up of the emitted light wave. At the end, a schematic representation of the spectrum is shown. b) The seed laser and the electron bunch enter the modulator (M), after which the bunch enters the dispersive section (DS) and then lases in the radiator (R). Again a schematic spectrum is shown, which shows one clear main peak, due to the seeding. The figure is taken from [136] and is adapted for the purpose.

magnetic fields within the undulators. One method is to send the electron bunch along a circular trajectory in an APPLE- or DELTA-type undulator [39, 41].
For one of the experiments presented in this thesis the seeded FERMI FEL was used, because of its narrow bandwidth and because it can provide circularly polarized light in the XUV wavelength region, allowing for efficient resonant excitation of selected atomic sub-states.

4 MOLECULES IN STRONG LASER FIELDS

Compared to atoms, molecules can have much more complex interactions with a laser field due to their geometry and multi-atom nature. An electronic excitation or ionization will always be followed by a change of the molecular geometry on a femtosecond scale, which then alters the electronic structure of the molecule and can ultimately end up in the molecule dissociating into smaller fragments [137]. Aside from excitation, ionization and dissociation, molecules can also be spatially aligned in vacuum by laser pulses [138].
The electronic states and energies can be determined by solving the Hamiltonian that accounts for the molecular system of nuclei and electrons. Usually here one makes use of the Born-Oppenheimer approximation [139], which assumes that the time-evolution of the nuclei can be neglected when calculating the electronic eigen-states, since the electrons instantaneously adapt to the new nuclei positions, as they move much faster than the nuclei. It can also be expressed as the separation of the wave functions of the nuclei and the electrons. Calculating the eigen-states for various atomic positions will lead to a potential energy surface (PES). The geometry of a molecule can be found by calculating the PES and then looking for a minimum in the PES of the electronic ground-state. The atomic coordinates at the minimum of the PES are the configuration of the molecule in the ground state. Using density functional theory (DFT) the eigen-energies and the geometry of a molecule can be determined numerically using a computer [140]. Software like ORCA [141] makes these calculations very accessible due to the simple interface and low computational power required, at least if the molecules are not too large. The calculated PES for the ground state of the hydrogen atom and the hydrogen ion are shown in figure 7 a).
To describe the ionization of molecules, only di-atomic molecules are considered for now. Like atoms, molecules have an ionization potential, which is the minimum photon energy required to ionize the molecule. Since the ionization happens quickly relative to the time-scale on which the ions move, one can assume that the ionization happens vertically, with no change of the bond-length of the molecule, in the PES representation of energy levels [142]. This assumption is also called the Franck-Condon principle, which is illustrated in figure 7 a). The bottom figure shows the electronic ground state PES of the hydrogen molecule while the top figure shows the PES of the hydrogen molecular ions electronic ground state. The red region shows how the ground-state wave function of the nuclei of the hydrogen molecule is projected onto the hydrogen molecular ions vibrational states (grey) in the ground-state. Due to the difference in bond-length, ionization can excite the molecular ion into higher vibrational states, depending on the overlap with the initial wave function of the nuclei before ionization. This effect can be well observed for example in photoelectron spectroscopy, as the kinetic energy of the electron after ionization follows from the difference of the photon energy and the ionization potential as well as the energy of the excited vibration,

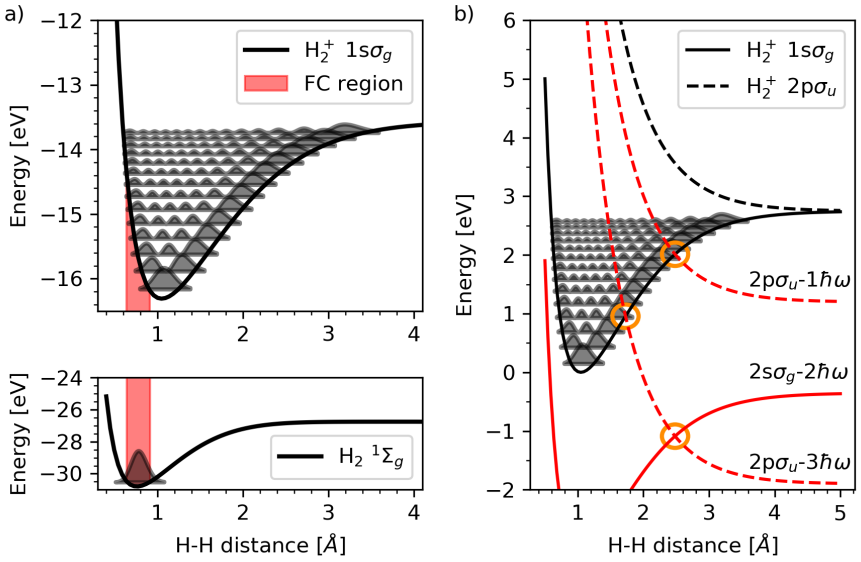

Figure 7: a) The bottom figure shows the PES of the hydrogen molecule in its ground state with the wave function of the nuclei (grey) and a red stripe indicating the Franck-Condon region. The top figure shows the PES of the hydrogen molecular ion and the nuclei wave function for different vibrational levels. b) The PES of the hydrogen molecular ion in the ground state and the dissociative state $2p\sigma_u$. Additionally shown are the relevant dressed PES (red), which appear in a strong laser field. The crossings of the PES and dressed PES are marked with orange circles. Avoided crossings can appear at these positions.

leading to multiple peaks separated by the energy between the vibrational states [143]. The probability for ionization and simultaneous transition between certain vibrational states is given by similar contributions as in the case of an atom, but there is an additional term introduced, the 'Franck-Condon' term, which includes the wave function overlap of the nuclei in the initial and final state [144]. The wave function of the nuclei can be calculated from the shape of the binding potential given by the PES, which can be very different for the ground state of the ion and the ground state of the neutral molecule. Transitions to excited states are also affected by this factor. In general ionization and excitation of a molecule will lead to a change in its geometry.

By absorbing photons, a molecule can be brought into an excited state that can lead to the dissociation of the molecule. The stability of a molecule also depends on its charge state, since the fewer electrons there are, the more the repulsive Coulomb potential of the nuclei plays a role compared to the binding forces. This dissociation can be induced through single-photon interaction and interaction with a strong laser field. A dissociation mechanism that is unique to the interaction with strong laser fields arises through the coupling of the electronic molecular states with the laser field. The periodically oscillating laser field creates replicas of the PES, so-called dressed states, for each electronic molecular state shifted up or down by an integer number of photon energies, which follows from Floquet-theory [145, 146]. Ultimately some of the states will

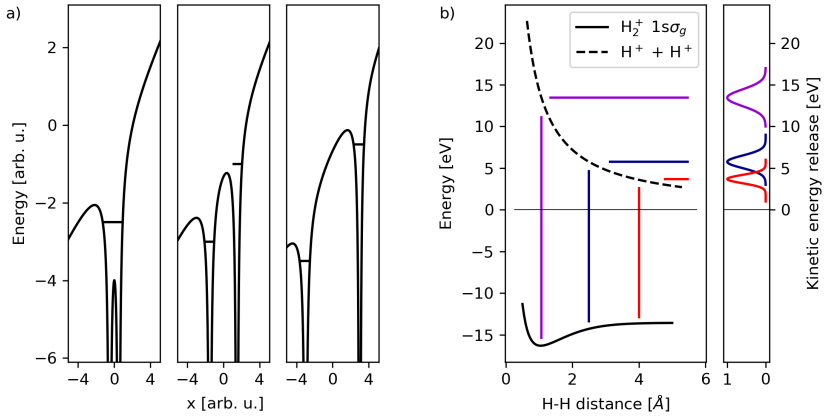

Figure 8: a) Showing the potential of the nuclei and a static electric field for three different internuclear distances. The stark shifted states are shown as black lines. b) The left figure shows the PES of the molecular hydrogen ion as well as the PES of two hydrogen ions. The differently colored lines indicate ionization of the molecular hydrogen ion at different internuclear separations, which leads to different kinetic energies of the fragments, which is shown in the right part of the figure.

cross in energy at a certain bond length, leading to avoided crossings, which appear at the positions marked with orange circles in figure 7 b). If a higher-lying dissociative excited state is down-shifted by the photon energy to cross with the molecular ground-state PES, then some vibrational states (shown in grey) can evolve along the down-shifted dissociative PES ($2p\sigma_u$-$1\hbar\omega$), leading to dissociation. This type of dissociation mechanism is called bond-softening [147]. In contrast to this vibrational states can also be trapped due to this mixing of PES, leading to a phenomenon known as bond-hardening [17]. The molecule can also follow a dissociative PES corresponding to a down-shift in energy by for example three photons ($2p\sigma_u$-$3\hbar\omega$), after which it can follow the original non-dissociative state down-shifted by two times the photon energy ($2s\sigma_g$-$2\hbar\omega$), or continue along the original dissociative trajectory. Depending on the PES that the molecule follows for large internuclear separations, the total kinetic energy of the fragments varies by multiples of the photon energy. This is known as above-threshold dissociation (ATD), with a name that is intentionally chosen to be similar to ATI, as here the kinetic energy of the fragmentation process also depends on the total number of photons absorbed in the dissociation process [148].

Another ionization mechanism that is well known for di-atomic systems is the so-called charge-resonance-enhanced ionization (CREI), which appears at laser intensities in the tunneling and over-barrier regime [19, 149]. This effect manifests itself in an unexpected high ionization rate of di-atomic molecular ions at a special, 'critical', internuclear distance range. This effect can be explained by looking at the static potential created by the laser field and the nuclei for different internuclear separations, shown in figure 8 a). As the molecular ion dissociates, the probability of ionization increases because the binding energy of the electron decreases due to the changing potential, which allows for more efficient tunneling (left figure). As the distance increases a barrier starts to rise between the two atoms and at each

site, the electron is in different states that are separated in energy by the Stark shift. A fraction of the electron density will end up in the higher-lying state, from which the electron can easily tunnel out, which causes a large enhancement in the ionization probability (middle figure). As the distance increases, the barrier between the atoms rises and at some distance becomes so large that it prevents the to higher energies shifted electron to tunnel out, thereby reducing the ionization probability (right figure).

A more universal way in which molecules dissociate is through the accumulation of charge and the subsequent dissociation due to the coulomb-repulsion of the positively charged constituents. This type of dissociation is referred to as coulomb-explosion. The kinetic energy released (KER) in the dissociation can be recovered from the PES that is followed during dissociation. The total KER is given by the difference between the potential energy of the fragments, which are separated by an infinite distance and the potential energy at the internuclear distance that the molecule started along the dissociative PES [150]. This is shown schematically in figure 8 b). The kinetic energy of the fragments also depends on the mass due to the conservation of momentum. The energy of fragments created in the Coulomb-explosion dissociation can be used to determine the internuclear distance at which the ionization took place [151], which is known as coulomb explosion imaging. It can also be used to determine the structure of small molecules by rapidly charging the molecule up via intense and short laser pulses so that the molecule dissociates via coulomb-explosion in the geometry of the ground-state molecule [152]. Overall coulomb-explosion can be used to probe the properties of a molecule and finds many applications, some also outside of pure science as for example in the machining of materials [153].

5 SPECTROMETERS

In this chapter, the spectrometers that were used in the upcoming studies are introduced. Since we want to investigate the interaction of atoms and molecules with intense laser pulses, we need a way to measure how the interaction affected the atoms or molecules. To do this we chose the approach to investigate the charged species that are produced in the interaction of atoms and molecules with strong laser fields. These charged species are photoelectrons and photoions. To detect the charged particles we use high voltage fields which guide them from the interaction region, where the laser and the atoms or molecules interact, to a detector, where they create a signal and the properties of the electron or ion can be determined. To determine kinetic energies or mass-over-charge ratios of the particles, we used a time-of-flight (ToF) spectrometer, while we used a velocity map imaging (VMI) spectrometer to simultaneously determine the kinetic energy, mass-over-charge ratio and angular distribution.

5.1 TIME-OF-FLIGHT

As the name already suggests, a time-of-flight spectrometer measures a time. This time usually refers to the time it takes for a charged particle to fly from the interaction region, where it was created, to the detector, where it is detected. The time of creation is given by a trigger signal, representing the arrival of a laser pulse in the interaction region. A schematic drawing of such a ToF spectrometer is shown in figure 9. To force the charged particles to fly in the direction of the detector, the interaction region is surrounded by two ring-shaped electrodes, so that the charged particles can pass through them [154]. One of these electrodes is positioned so that it can push the charged particles towards the detector and is called the 'repeller'. The other electrode is between the interaction region and the detector and allows to pull the particles towards the detector. This is called the 'extractor'. Another electrode between the extractor and the detector is called the 'lens', which can focus the particle beam. Behind the lens, the charged particles enter the drift tube, which is a section in which the particles propagate towards the detector. Additionally, the tube is covered in μ-metal, to minimize the influence of the earths magnetic field on the trajectory of the charged particles. After having passed the drift tube the particles hit the detector, which consists of a multi-channel plate (MCP). The MCP is a thin disk made out of glass with many holes, or channels, in it. If one applies a large voltage to the MCP and a particle hits it, an electron cascade is created [155]. This will create a large enough voltage drop that can be measured using an oscilloscope. To count single events, it is possible to amplify the voltage drop and use a constant fraction discriminator (CFD) to determine the time-of-flight [156]. Being able to count single events allows to investigate coincidences if multiple particles are created in the interaction [157].
The design of the ToF that we use is of Wiley-McLaren type with a two-stage ac-

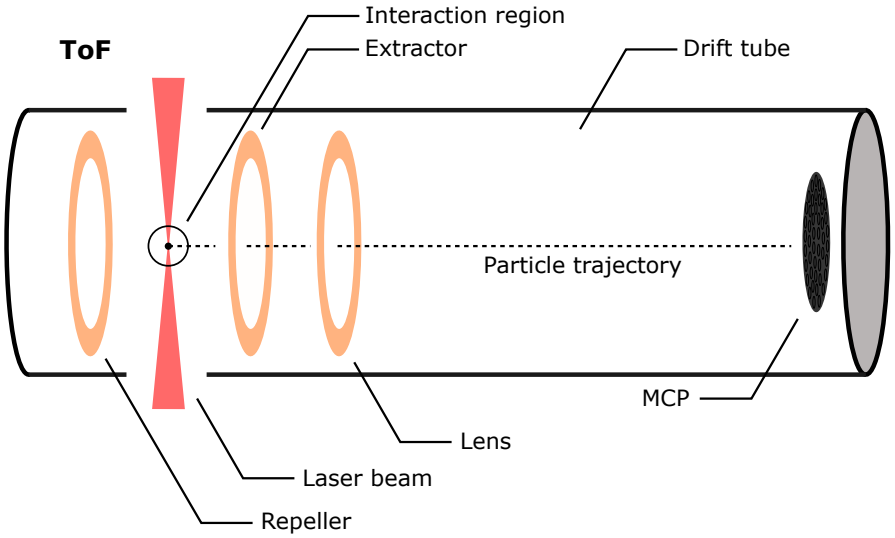

Figure 9: Schematic drawing of a ToF spectrometer.

celeration scheme, which allows to focus particles with the same mass and charge, which originate at different positions in the interaction region, to have the same time-of-flight [158]. The time-of-flight t of ions that is measured in a ToF spectrometer is coupled to their mass(m)-over-charge(q) ratio m/q. Calculating all contributions to the time-of-flight of the source, the acceleration and the drift section, the following relation for the time-of-flight t can be derived:

$$t \propto \sqrt{\frac{m}{q}\frac{1}{2(sE_s + dE_d)}}\,(D + ...)\,. \tag{37}$$

The length that the charged particles have to travel in the source region is s and they are pushed by a field E_s. For the acceleration region the length is d and the accelerating field is E_d. Of course the time-of-flight also depends on the length of the drift section D of the ToF plus factors, which are not shown here, that include the accelerating fields and the origin of the source and the acceleration distance.
As can be seen in equation 37, the time-of-flight of a particle depends on the square-root of the mass-over-charge ratio. A heavier particle has a longer time-of-flight than a lighter particle of the same charge. This dispersion of the mass allows to distinguish ions of different masses. A common use of this capability is found in gas-analyzers, which determine the constituents of a gas and can in general be used to characterize samples that can be brought into the gas-phase.
It is also possible to use the ToF to investigate the kinetic energy of the ions that were created in the source region. If an ion is created with an initial kinetic energy, the ion will have a longer time-of-flight, if the momentum is directed away from the detector and a shorter time-of-flight, if the momentum is directed towards the detector. This will lead to additional peaks in the ToF spectrum with which the fragmentation of molecules can be analyzed. The relation between the added initial kinetic energy E and the change in the time-of-flight Δt for a certain fragment is given by [159]:

$$E = k(\Delta t)^2. \tag{38}$$

Hereby $k = q^2F^2/(8m)$ with F being the applied electric field in the interaction region. With this relation it is possible to derive the ion's kinetic energy from the time-of-flight deviation to ions without any kinetic energy.

Such a ToF is also commonly used to analyze the kinetic energy of electrons. In the electron-mode the extractor and repeller electrodes are on ground level, as they are not necessary to accelerate the electrons. Thus the relation between the photoelectrons kinetic energy E_{kin} and the time-of-flight is simply given by [160]:

$$E_{kin} = \frac{m_e}{2}\frac{L^2}{t^2} \tag{39}$$

Here m_e is the mass of the electrons, L is the distance from the interaction region to the detector and t is the time between the creation of the photoelectron and its impact on the detector. Using this relation one can for example analyze the kinetic energy of photoelectrons and get an insight into the photoionization process.

5.2 VELOCITY MAP IMAGING

Velocity map imaging (VMI) is a technique that can determine the velocity of ions or electrons with the advantage over the ToF spectrometer in that it also reveals the angular distribution of these fragments. In 1987 this technique was first used to determine the angular distribution of photofragments from iodomethane (CH_3I) [161]. By using hollow electrodes instead of mesh electrodes to guide the photofragments, the resolution could be further improved [162]. VMIs are widely used to study the dynamics of gas-phase reactions [163], such as the photodissociation of molecules [164], the reaction kinetics in the collision of two molecules [165], or molecular alignment [166]. Investigating photoelectrons using the VMI allows to retrieve the angular distribution of the outgoing electronic wave function. The additional information can be used for example to determine the polarization of light sources [40], or to see how a specifically designed polarization affects the angular distribution of the photoelectrons [167]. Regarding studies of dichroism, the VMI can for example be used to measure the PECD of chiral molecules [91].

To image the angular distributions of photoions and photoelectrons typically ion optics are used to accelerate the particles towards and onto a 2D detector. A schematic drawing of this is shown in figure 10. Similar to the ToF, the interaction region is surrounded by two electrodes, the extractor and the repeller to which a certain voltage is applied, usually in the kV range. These particles then hit the MCP where they create an electron cascade. This electron cloud then hits the phosphorous screen, where it creates a glow that is recorded by a camera filming the phosphorous screen through a window that allows to use a camera outside of the vacuum within the VMI. Another method to measure the spatial distribution of

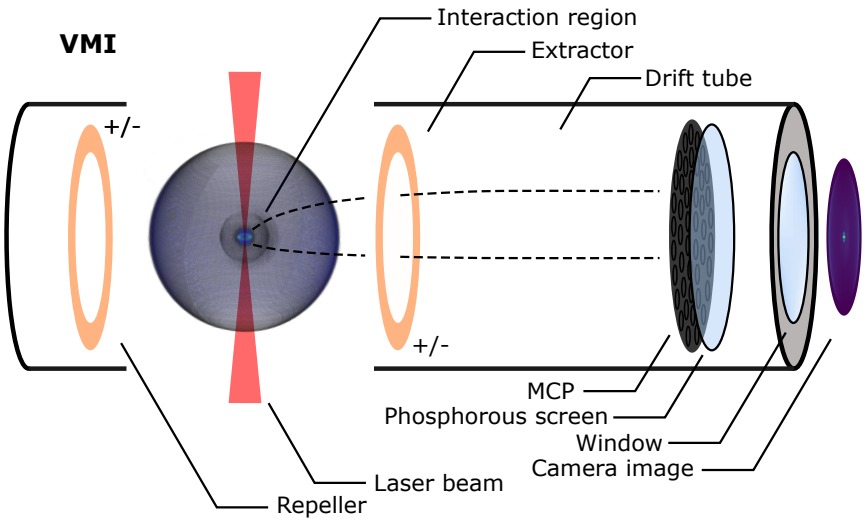

Figure 10: Schematic drawing of a VMI spectrometer. The circle in the interaction represents a 3D distribution of particles emitted due to the interaction with the laser pulse. Dotted lines indicate the path of these particles onto the MCP.

the electrons or ions hitting the MCP screen is to use an array of wires behind the MCP instead of a phosphorous screen. By measuring the time a signal needs to travel through the different wires, the location where the particle hit the MCP can be reconstructed. This type of detector is called a delay-line detector [25, 168].
When a laser beam interacts with atoms or molecules, the resulting photoions and photoelectrons will expand from the interaction region with a certain velocity and angular (azimuthal and polar) distribution. How these photoions and photoelectrons are projected onto the 2D detector is defined by the voltages of the extractor V_E and the repeller V_R. To achieve a mapping of the velocity in the plane parallel to the detectors plane, the voltage ratio has to be set to $V_E/V_R = 0.71$ [162]. Then the radius $R = Nv_{||}t$ at which a photoion or photoelectron hits the detector depends on the time-of-flight t of the particle, its velocity $v_{||}$ parallel to the plane of the detector and the magnification factor N, which can be adjusted by changing the extractor and repeller voltages, while keeping the ratio between the voltages constant. The kinetic energy E_{kin} of the resulting fragment ions or photoelectrons is then given by equation 40:

$$E_{kin||} = \frac{1}{2}mv_{||}^2 = \frac{1}{2}m\left(R/(Nt)\right)^2. \tag{40}$$

Knowing that the time-of-flight depends on the mass m over charge q ratio $t \propto \sqrt{\frac{m}{q}}$, the mass cancels out and it becomes apparent that the radius at which the particles appear on the detector is independent of the particles mass for the same kinetic energy and charge.
To get information about the 3D angular distribution from its projection onto a 2D detector, numerical methods are used. These rely on the definition of a symmetry axis. For linear polarization, this axis is the polarization vector, while for circular polarization it is the light beams propagation direction. If particles are emitted in a plane that is not parallel to the detector, only the velocity component parallel to the

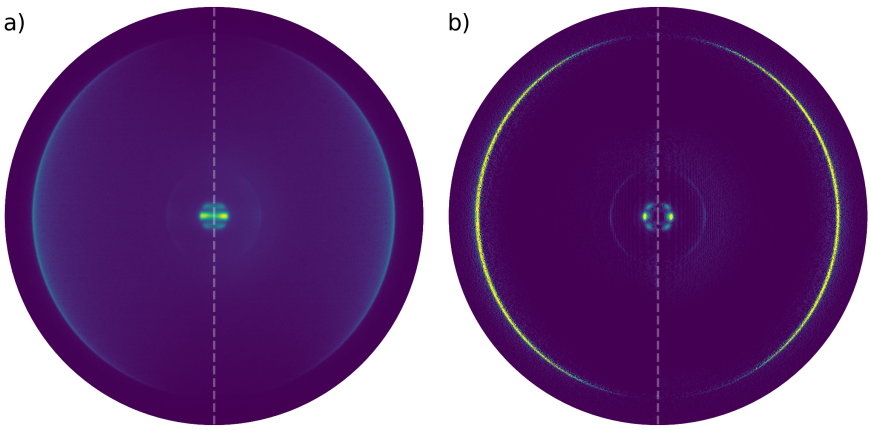

Figure 11: a) VMI detector image of photoelectrons created by circularly polarized light. b) Reconstruction of the 3D angular momentum distribution from the detector image in a) using the Vrakking algorithm. The white broken line shows the propagation direction of the laser beam.

detectors plane will be projected onto the detector. Thus, if the particle contains a velocity component perpendicular to the plane given by the detector, the particle will hit the detector at a shorter radius, although having the same kinetic energy as a particle emitted parallel to the detector. This leads to smearing out, which can be seen in an exemplary detector image in figure 11 a). In this case circularly polarized light was used to create photoelectrons, making the beam propagation axis the axis of symmetry. A reconstruction of the 3D angular momentum distribution is given in figure 11 b) that has been calculated using the Vrakking algorithm [169]. To get the full 3D angular momentum distribution, the retrieved angular distribution has to be rotated around the beam propagation axis (white broken line). The reconstructed image allows to determine the angular distribution of the different photoelectron features and enables to determine the photoelectron spectrum by integrating over all angles.

Part II

THE XUV LASER LABORATORY

This chapter is meant to show experiments that were done in the XUV laser laboratory at the European X-Ray Free-Electron Laser Facility GmbH. The experimental setup is introduced and the XUV source characterized. Results from experiments on hydrogen with two different wavelengths are used as a benchmark for our setup. Further experiments investigate one of the most simple hydro-carbons, the greenhouse gas methane and it's ionization and dissociation in strong laser fields.

6 EXPERIMENTAL SETUP

This chapter is dedicated to describing the experimental setup that we use. There are two main components which are the optical setup and the experimental chamber. The optical setup determines what wavelengths can be used to interact with atoms and molecules, what time scales in dynamics can be resolved and how efficient the setup is in terms of acquiring statistics. The experimental chamber and its spectrometers and sample sources determine what part of the interaction we detect and what type of samples we can investigate, respectively. Together they define the experimental possibilities.

6.1 OPTICAL SETUP

The laser pulses we use are generated by a typical titanium doped sapphire (Ti:Sa) medium. A continuous wave laser drives a Ti:Sa oscillator that gives out 5 nJ laser pulses at a repetition rate of 80 MHz. These laser pulses are fed into a regenerative chirped pulse amplification (CPA) system. Some pulses are picked to be amplified which reduces the repetition rate to 3 kHz with pulse energies of up to 3.6 mJ. The pulses have a central wavelength of 800 nm and a pulse duration of 35 fs which has been measured using a frequency-resolved optical gating (FROG). In the FROG the beam is split and non-collinearly overlapped with itself in a non-linear medium which generates the second harmonic. A spectrometer records the second harmonic spectrum depending on the temporal delay between the two pulses from which a phase retrieval algorithm reconstructs the laser pulse [170].
This is the laser pulse that will be transported to the experiment via numerous optics. A sketch of the beam path is shown in figure 12. The beam from the CPA is reflected by a number of dielectric mirrors and then split by a beam splitter. From here on one part of the beam propagates into an attenuator and an XUV (extreme ultra violet) source. The attenuator consists of a lambda-half wave plate that rotates the polarization of the beam. After this, the beam is reflected by two thin-film polarizers under a shallow angle which filter the horizontal polarization direction. This way the laser power can be attenuated over a wide range of intensities, in our case from 0.1 % to 100 % with a small step size. After this, the beam is focused into the XUV source. A gold-coated toroidal mirror focuses the beam into the interaction region of the experimental chamber. The other part of the split beam passes over a delay-stage for pump-probe experiments. Here a disc with a reflective layer of varying thickness is used to attenuate the beam. This beam is focused by a lens with a focal length of 75 cm. A coated prism with a hole reflects the focused beam into the interaction region while the beam that passed through the XUV source propagates through the hole in the prism. This recombines the beams in the interaction region under a shallow angle. After this, the beams propagate to the exit window after which a beam stopper stops both beams.
This setup allows to do single color experiments with the fundamental beam and

its harmonics and two-color experiments with a combination of fundamental, second harmonic and the XUV. The temporal resolution can be expected to be around 35 fs in an auto-correlation of the fundamental or with a combination of XUV and fundamental.

6.2 EXPERIMENTAL CHAMBER

First, we will present the available spectrometers with which ions and electrons generated in the interaction of a laser pulse with a sample gas are detected. The experimental chamber is fitted with a Wiley-McLaren type time-of-flight (ToF) spectrometer and a velocity map imaging (VMI) spectrometer. The ToF spectrometer is below the interaction region while the VMI is above the interaction region. A set of fast switches would even allow for electron ion coincidence experiments. The sample can be injected with a gas needle or a supersonic jet. A slice through the experimental chamber is shown in figure 13.

The flight distance in the time-of-flight spectrometer is about 50 cm after which the particles hit a multi-channel plate (MCP) which creates an electron cascade upon particle impact resulting in a voltage drop that can be measured with an oscilloscope. For a more sophisticated measurement, the voltage signal from the MCP is fed into an amplifier and a constant fraction discriminator (CFD) which returns a special kind of signal called NIM (Nuclear Instrumentation Standard). This signal is then digitized with an analog-to-digital converter (ADC) and recorded with CoboldPC, a software from RoentDek Handels GmbH. With the voltages of the repeller, the extraction electrodes, the electrostatic lens and the drift tube the transmission of the ToF can be tuned to give the best resolution or the highest amount of detected events. The resolution is important in experiments where dissociation channels should be resolved in ion ToF experiments, while in experiments where photoelectrons created by high harmonics are detected, the interest is greater in a higher yield since resolution regarding the time-of-flight is not the limiting factor.
For the particles to arrive at the MCP of the VMI spectrometer they have to travel a distance of 25 cm. The particles are accelerated to the detector by the extractor and repeller. Varying the sign of the voltages adjusts for positive or negative charges that should be accelerated to the detector. The VMI uses two MCP's to increase the number of electrons generated in the cascade because this time not the voltage drop of the MCP is the signal of interest but spatial information needs to be extracted. The VMI has a hexagonal array of wires to detect the spatial position at which the particles hit the MCP. It works in a way that three wires bent to an alternating shape are mounted on top of each other each with a relative angle of 60° to each other. This way every wire will detect a voltage at different times because the signal needs different times to get to the end of the wire. Using this the first two layers of wire would be sufficient to assign the two arrival times of the signal to an x and a y coordinate. The function of the last layer is to check the consistency. The signals of the wires are fed into an amplifier and a CFD before being digitized and recorded by CoboldPC which does the spatial reconstruction from the signal times of the different layers of wire.
As a way to inject the sample into the interaction region, we mostly use a gas needle which is a pipe with a small inner diameter of 0.5 mm. A valve is adjusted to

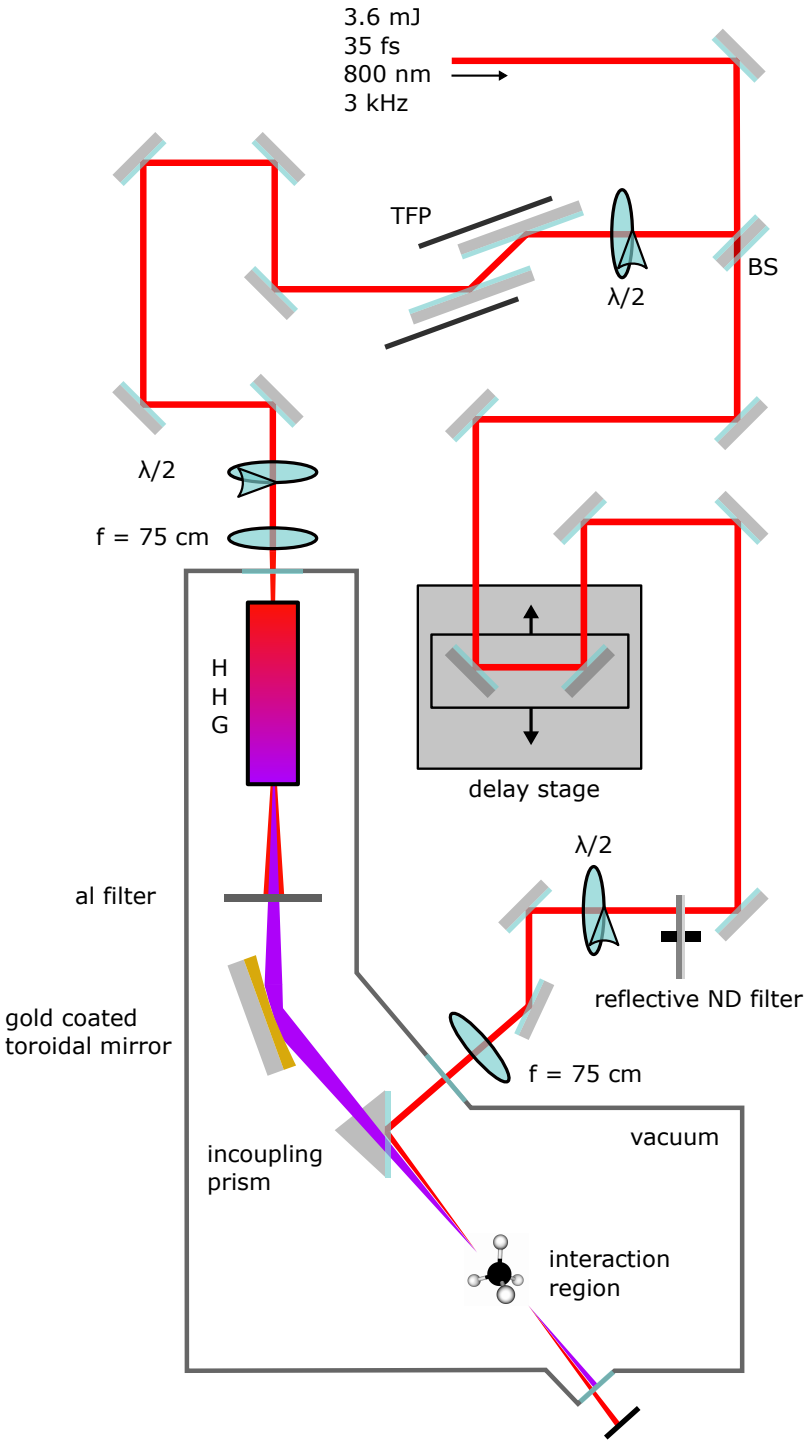

Figure 12: Shown is the path of the beam from the amplifier to the interaction region. (TFP: thin film polarizer, BS: beam splitter)

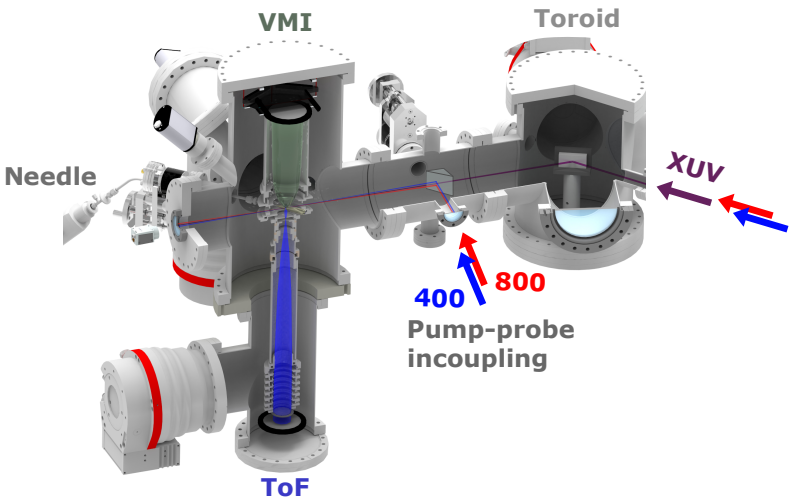

Figure 13: Slice through the experimental chamber with schematic drawings of the beam path of the XUV beam and the optical beam at 800 nm or 400 nm.

put a certain amount of backing pressure on the gas needle. This gas then expands into the vacuum chamber through the needle. The needle is usually moved close to the interaction region, but not so close, that it influences the electric fields guiding the particles to the spectrometers. In general, it is desired to use a low backing pressure since the overall vacuum degrades by using a higher backing pressure and many atoms or molecules are ionized at higher pressures so that the kinetic energy of the photoelectrons and ions are affected by the collectively generated charge distribution, which is known as space-charge.
A more sophisticated but also more complicated way to prepare a gas phase sample is to use a supersonic expansion jet. In this setup, a pulsed valve with a backing pressure of several bars is periodically opened and closed and is synchronized to the laser pulses repetition rate. The gas plume expanding from the pulsed valve hits a skimmer which is a cone of which the top faces the gas plume. This way the more divergent part of the plume is cut and pumped away and only a more narrow and less divergent gas beam remains. After this first differential pumping stage, the thin beam of gas hits another skimmer which makes the beam even less divergent. Again the rest of the gas is pumped. Now only a very fine gas jet remains which is cut vertically left and right to give the beam a narrow expansion so that the laser beam vocal volume only interacts with the gas at a well-defined position along the confocal distance of the focus region. This is very necessary to achieve a high resolution in experiments with the VMI. If the VMI images particles from more points along the focal volume of the laser the picture becomes blurred since ions or electrons with the same momentum from different places along the focal volume are not mapped onto the exact same points on the VMI. By creating a thin slice of gas one can prevent this from happening. Using a molecular jet, the chamber is less flooded with gas, especially when implementing a dump for the jet which removes the gas jet by trapping the gas with a differential pumping section after having passed the interaction region.

7 THE XUV SOURCE

The aim of this chapter is to characterize the new high harmonic generation setup and to show it's capabilities in a benchmark experiment. For this we take a look at the experimental setup and type of high harmonic generating configuration, that we will use for our experiments. The idea is to have a light source that interacts with atoms and molecules with a single photon process, which can act as a probe for often very complex dynamics induced by multi photon interactions in time resolved experiments. To characterize what influences the high harmonic yield and the spectrum, some macroscopic parameters and the driving wavelength are varied. Finally electron spectroscopy on the hydrogen molecule explores the capabilities and limitations of the high harmonic source.

7.1 SEMI-INFINITE GAS CELL SETUP

There are numerous experimental setups to generate high harmonics. One can use pulsed gas jets [171], hollow capillary tubes [172], finite gas cells [116] or semi-infinite gas cells [173] each of which have their own advantages and disadvantages concerning the yield and difficulty of tuning the setup.
Since we conduct gas phase experiments, where the target density is low compared to solids or liquids, a source with a high conversion efficiency would be ideal. With this in mind, the setup we chose is the semi-infinite gas cell (SIGC), which is easy to tune and has a conversion efficiency of 10^{-6} from the fundamental into the high harmonics. This comparatively high conversion efficiency is a result of the long interaction region of the driving beam with the medium and is in turn limited by the re-absorption of harmonics by the medium and the phase matching condition [174]. As the medium, we mostly use argon, since it has a comparable yield to gases, which should have higher conversion efficiencies at lower order harmonics but are less affordable like krypton and xenon.
The previous setup was a finite gas cell and is described and characterized in the Ph.D. thesis of Amir J. Rafipoor [175]. The previous setup followed the finite gas cell design, which consists of a steel confinement with two 1" copper plates. Within this confinement is the gas, which is used to generate the high harmonics. As the laser beam is focused on the copper plates, the laser will burn a hole in them and the beam can pass through the plates and high harmonic radiation is generated in the gas medium. Using a combination of a pressure gauge and a gas flow controller, the gas pressure at the interaction region could be kept constant at a target pressure as the gas is constantly flowing through the holes in the copper plates.
The now new design is a semi-infinite gas cell. The design was chosen to enable higher gas pressures, as in this design, there is only one copper plate with a hole, reducing the gas load flowing into the vacuum. Higher pressures are needed to reach phase-matching of higher harmonics in gases like neon and helium, which allow for higher HHG photon energies through their higher ionization potential.

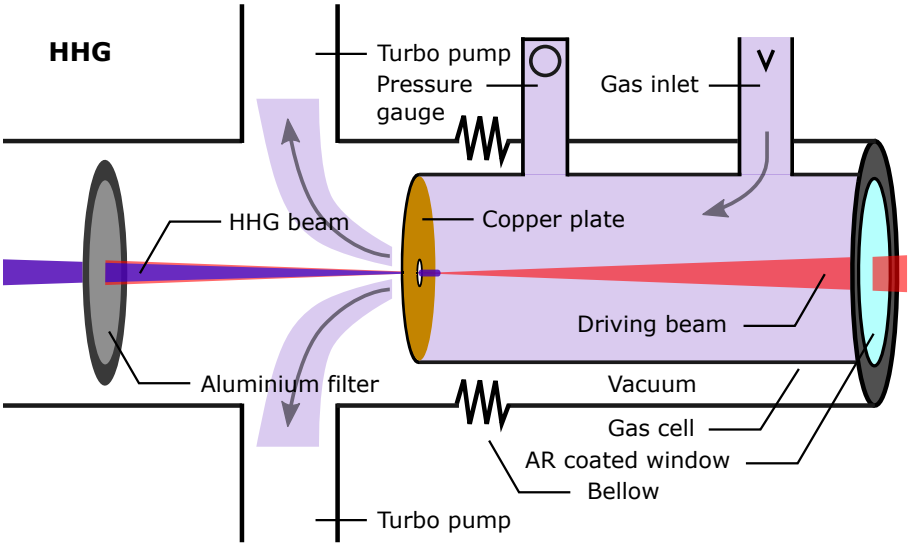

Figure 14: Schematic drawing of the semi-infinite gas cell (SIGC) setup. The beam propagates from the right to the left. Behind the aluminum filter, the beam is focused into the interaction region by a gold-coated toroidal mirror.

Simulations in [172] at a wavelength of 800 nm show that for neon the required pressure to achieve phase-matching is around 400 mbar for a HHG photon energy of 90 eV. Using helium, a pressure of 750 mbar is needed to achieve phase-matching for an HHG photon energy of 140 eV. These pressures are significantly higher, compared to the phase-matching pressure of 30 mbar that we found for argon.

A schematic of the setup of the high harmonic source is shown in figure 14. After the laser beam exits the attenuator, it passes a number of mirrors to align the beam to the experimental chamber. Finally a lens with a focal length of 75 cm focuses the beam at the end of the SIGC. The beam enters the tube of the SIGC through a window with a diameter of 1/2" which is coated to be anti-reflective for short pulses with a central wavelength of about 800 nm. The tube is 70 cm long and has a diameter of 1". At the end of the tube, there is a copper plate that confines the gas within the tube. The tube can be moved relative to the focal plane of the laser and usually, the position of the copper plate is chosen to coincide with the focal plane of the laser beam to get a decent high harmonic yield which is then further optimized. To propagate to the interaction region the laser beam needs to drill a hole in this copper plate which is most effectively done if the copper plate is close to the laser focus. The pressure of the medium in which the high harmonics are generated is measured by a gauge connected to the tube. A needle valve connected to the tube is adjusted to achieve the phase-matching pressure of the medium. For argon, this pressure is roughly around 30 mbar in our configuration. Two turbo pumps remove the gas streaming out of the hole in the copper plate to avoid reabsorption of the high harmonics by the generating medium and a deterioration of the vacuum. The beam then passes through a 1.5 m long tube at the end of which the fundamental beam and the higher harmonics are separated by a 200 µm thin aluminum filter. The ideal transmission of this filter is shown in figure 15 a). Since the higher harmonics can only propagate well in vacuum there is no proper way of focusing that involves transmissive optics like a lens because the high harmonics

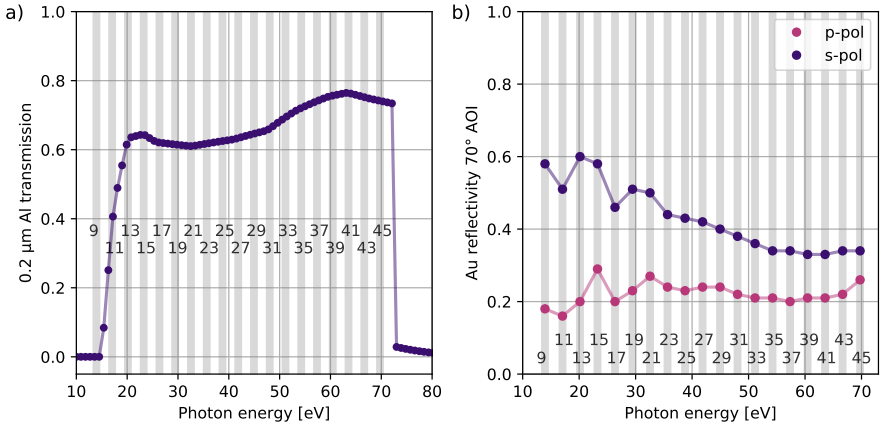

Figure 15: a) Transmission of a 200 µm thin aluminum filter in the XUV. The grey numbers are the odd harmonics of the 800 nm fundamental beam, the data is taken from [176, 177]. b) Photon energy dependent reflectivity of gold for different polarizations at an incidence angle of 70°, the data is taken from [178, 179]. Here s-polarized light is orthogonal to the plane of incidence, which is spanned by the lights propagation vector and the vector normal to the reflecting surface.

would be absorbed by a dense medium. Instead one has to rely on reflective optics to minimize the losses. For this we use a gold-coated toroidal mirror focusing the beam 75 cm downstream into the interaction region. The reflectivity for s-pol and p-pol of high harmonics is shown in figure 15 b). In the end, the higher harmonics hit the exit window of the experimental setup where they are absorbed.

The yield of the harmonics can be optimized by varying parameters of the laser beam and parameters of the SIGC. Laser beam parameters that influence the yield are the pulse energy, which is adjusted by an attenuator and the dispersion of the laser pulse, which is adjusted by the compressor grating in the CPA. Another factor concerning the laser beam is the focal length of the lens which can only be 75 cm or greater. A greater focal length leads to lower laser intensity in the focal region and in turn increases the interaction region since the beam focus is more shallow.

7.2 CHARACTERIZATION OF THE SOURCE

It is practical to find out what influences the high harmonic yield of the XUV source in this configuration and how parameters should be adjusted to achieve the desired HHG output. To measure this output usually an XUV spectrometer is used. In an XUV spectrometer, the generated high harmonic beam passes through a slit and is reflected by a grating separating the different spectral components spatially. The high harmonic beam is then imaged by a 2D detector system giving information about the divergence along the slit axis, the spectral properties and the relative yield between harmonics. To determine the flux, a photodiode can be used[174]. This is the most direct way of characterizing high harmonics but since our experimental setup already has an electron spectrometer we use this instead to characterize the harmonics, albeit having to account for more corrections than in the imaging setup. The instrument we use to characterize the high harmonics is a time-of-flight spectrometer. High harmonics are focused into the interaction region

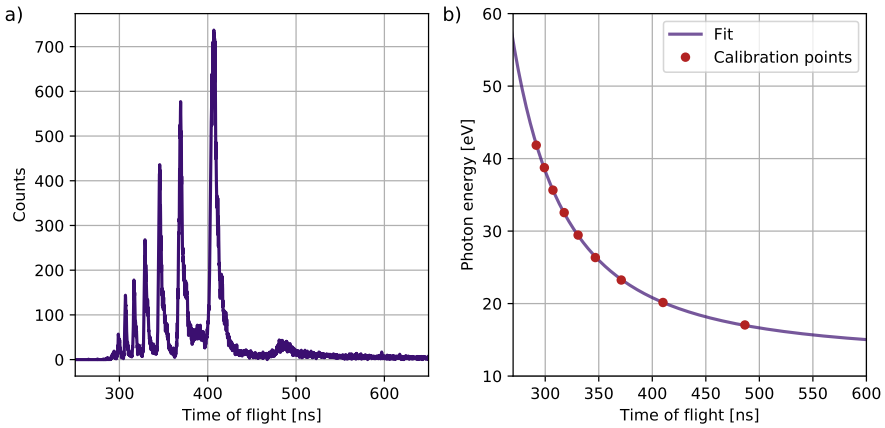

Figure 16: a) Time-of-flight spectrum of electrons from argon ionized by high harmonics generated in argon with laser pulses having a central wavelength of 800 nm and laser intensity of $1.4 \cdot 10^{14}\,\mathrm{W/cm^2}$. The time-of-flight is shown relative to the laser trigger. b) Calibration points of the high harmonic energy and time-of-flight pairs are shown as orange dots. The line through the points is the fit following the relation in equation 41.

by the gold-coated toroidal mirror where the high harmonics, if their energy is high enough, can ionize a gas, for example, argon. This means that high harmonics with photon energies above the ionization potential of argon, which is 15.76 eV [180], are able to free electrons from the argon atom. These electrons are detected by the time-of-flight spectrometer and depending on their energy they will have different times of flight. Faster electrons, with more kinetic energy, will have shorter times of flight, while slower electrons, with less kinetic energy, have longer times of flight. Figure 16 a) shows a time-of-flight spectrum of electrons which were generated by ionizing argon with high harmonics generated in argon with laser pulses centered around 800 nm at a laser intensity of $1.4 \cdot 10^{14}\,\mathrm{W/cm^2}$.

The peak structure reflects the different odd harmonics of the fundamental beam, starting with the 11th harmonic at 17.05 eV with a time-of-flight around 480 ns, which is the first harmonic with sufficient energy to overcome the ionization potential of argon and the transmission barrier of the aluminum filter. Using the second harmonic to generate the high harmonic allows to confirm that the first harmonic is the 11th, as the first harmonic that is able to ionize Argon is the 7th with a photon energy of 21.7 eV (see figure 93 in the appendix). Subsequent peaks in figure 16 a) are further odd harmonics until the cut-off of the high harmonics is reached and no further harmonics appear. Matching the harmonics to their time-of-flight gives a calibration of electron and photon energy to time-of-flight which can be used to turn the time-of-flight axis into an energy axis. The function that is used to interpolate between calibration points is derived from the theoretical relation between the time-of-flight t that a particle of energy E and a mass m needs to travel over a distance s which is the distance between the interaction region of the target and the high harmonics and the point of detection at the end of the time-of-flight spectrometer. This relation is the following (see section 5.1):

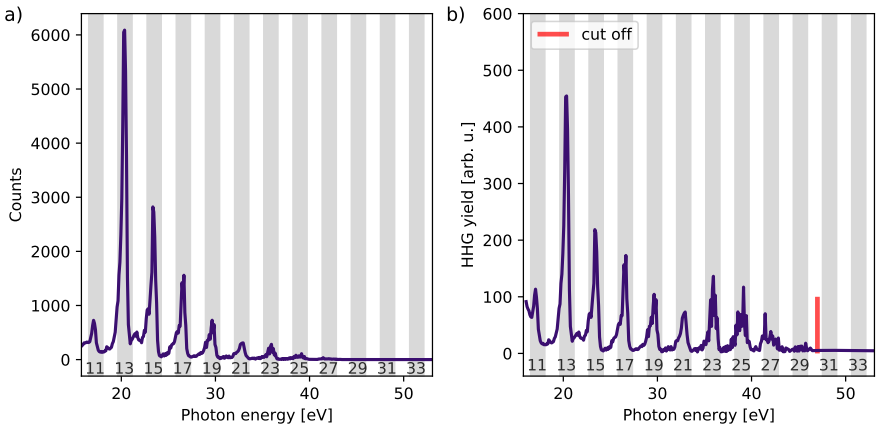

Figure 17: a) Photoelectron yield of argon ionized by XUV pulses from the SIGC. Grey numbers depict the order of the harmonics that correspond to the grey region. b) Approximated high harmonic yield versus the photon energy. The red line shows the high harmonic cutoff, which marks up to which energy high harmonics can be generated and gives information about the laser intensity at the focal point where the high harmonics are generated. The wavelength of the driving laser is centered around 800 nm and the laser intensity is $1.4 \cdot 10^{14}\,\mathrm{W/cm^2}$.

$$E = \frac{ms^2}{2}\frac{1}{(t-t_0)^2} \tag{41}$$

This relation is adapted to allow for a time zero t_0 different from the time-of-flight of 0 ns because the trigger starting the ToF measurement does in general not coincide with the time at which the laser pulse arrives at the center of the interaction region, but can have a constant offset. Furthermore, a shift in energy and a different scaling constant, that is not constrained to the mass and flight distance, are allowed. The result of this function that follows the $1/t^2$ dependence is shown in figure 16 b).

The calibration is applied to the photoelectron time-of-flight spectrum in figure 16 a) which gives the spectrum shown in figure 17 a). In this the photoelectron yield is plotted against the photon energy and the different harmonics can be clearly distinguished. The energy difference between harmonics corresponds to twice the fundamental photon energy of 1.55 eV. The energy axis in figure 17 a) has been binned again to correct for the non-even spacing resulting from the axis transformation from ToF to kinetic energy.

It should be noted that plotting the photoelectron yield against the photon energy can be misleading because the photoelectron yield does not display the high harmonic yield and they are not simply connected by a linear relation. To trace back what factors are relevant in the projection of the high harmonic spectrum onto the photoelectron spectrum, the point where the electron hits the MCP of the time-of-flight spectrometer is considered first. The time-of-flight spectrometer has electrodes, which accelerate and focus particles onto the MCP. The entrance to the time-of-flight spectrometer has an aperture of 7 mm and an acceptance angle of 30° [175]. Because the photoelectrons have a certain energy dependent angu-

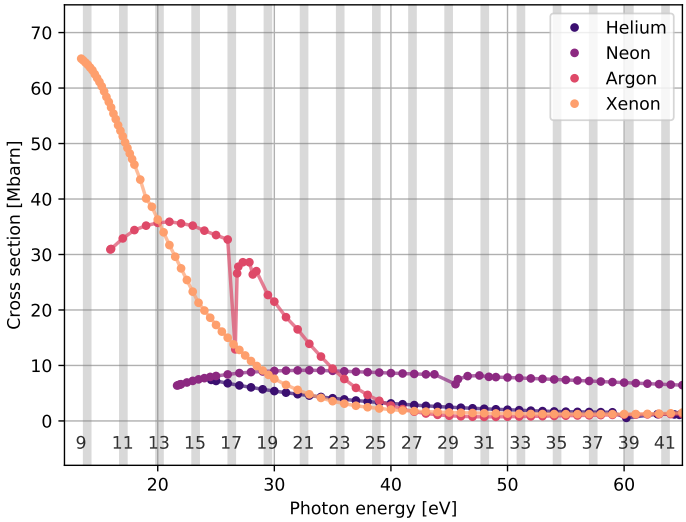

Figure 18: Photoionization cross-sections of different noble gases. Data taken from [184].

lar distribution, the amount of electrons that make it into the time-of-flight spectrometer depends on the energy of the harmonics that created the free electrons. These two factors, which are the angular distribution of the photoelectrons and the transmission of the time-of-flight spectrometer, are not corrected for. Factors that are regarded are the absorption cross-section of the target gas, the reflectivity of the gold-coated toroidal mirror and the transmission of the aluminum filter. Figure 18 shows the photo-ionization cross-section for different photon energies for several target gases. The photoionization cross-section of argon is discussed in detail since it was mostly used as the medium in which the high harmonics were generated. The photo-ionization cross-section of argon exhibits a maximum around 21 eV at a cross section of 35.9 Mbarn from where it drops to 0.74 eV at the energy of the cooper minimum around 49 eV [181]. The dip in the ionization cross-section at 26.65 eV corresponds to the first of the argon 3s auto-ionizing resonances which correspond to the transition $3s^2 3p^6 {}^1S \rightarrow 3s^1 3p^6 np^1 P$ with $n \geq 4$ being the principal quantum number [182]. The photoelectron angular distribution from one-photon ionization of the argon 3p level is given by the interference of the outgoing photoelectron s- and d-wave function. Close to the ionization threshold, the β_2 parameter of the photoelectron angular distribution has a value around 0.0 which resembles the photoelectron being emitted in a spherical wave with no spatial direction being favoured [183]. The main contributor to the outgoing electron wave is the s-part. This changes when the energy of the photoelectron increases. At an electron energy of 7 eV ($h\nu$ = 22.76 eV) the beta parameter has a value of 1.0 and at an electron energy of 20 eV ($h\nu$ = 35.76 eV) the beta parameter approaches a value of 1.8, showing that the d-wave is now the main contributor to the outgoing electron wave, implying that the electron is mainly emitted along the polarization axis of the laser beam.

To estimate the high harmonic yield in arbitrary units, the photoelectron spectrum in 17 a) is divided by the following: the photo-ionization cross-section of

argon excluding the auto-ionizing resonance, the reflectivity of the gold-coated toroidal mirror for s-pol and the transmission of the aluminum filter that blocks the fundamental beam. Applying these corrections gives a high harmonic spectrum, which is shown in figure 17 b), that should be closer to reality than the raw ToF spectrum. The yield is decreasing until the 17^{th} harmonic and then exhibits a plateau, where the yield of subsequent harmonics is similar until the cut-off. That the yield of the 11^{th} harmonic is relatively low can be explained due to the electron angular distribution at that kinetic energy and the low transmission of the ToF. The cutoff of the photoelectron spectrum at 47 eV is given by the intensity of the laser pulse, the ionization potential and the wavelength of the light. With these parameters, one can estimate a laser intensity of at least $1.4 \cdot 10^{14}\,\mathrm{W/cm^2}$.
This back-calculation function from electron yield to high harmonic yield, which considers the photo-ionization cross-section, the reflectivity of the gold-coated toroidal mirror and the transmission of the aluminum filter is applied to all further spectra in this chapter to establish a characterization of the high harmonic generation even without an XUV spectrometer.

7.2.1 *HHG driven by 800 nm laser pulses*

Driving high harmonics with the fundamental of the CPA laser system is the straightforward approach. The aim here is to determine how certain parameters influence the spectrum and the yield of the high harmonics.
The first parameter investigated is the dependence of the high harmonics on the laser intensity. To change the intensity a lambda-half wave-plate in combination with two thin-film polarizer plates is used, which allows to tune the laser intensity from 0.1 % to 100 %. Since some statistic is needed in order to detect a sufficient amount of photoelectrons from the HHG process the available laser intensity we start at is $9.5 \cdot 10^{13}\,\mathrm{W/cm^2}$ corresponding to 20 % of the total available laser intensity. The laser intensity has been estimated from the high harmonic cutoff, giving a maximum available laser intensity of $4.75 \cdot 10^{14}\,\mathrm{W/cm^2}$. The argon pressure in the semi-infinite gas cell has been adjusted to yield the highest rate of photoelectrons at around 30 mbar and the position of the copper plate overlaps with the focus of the driving beam. The power is increased in 10 % steps starting at 20 % up until 100 %. Figure 19 a) shows the high harmonic spectra for increasing laser intensities and in figure 19 b) it can be observed that the harmonic yield increases with increasing laser intensity up to an intensity of $3.8 \cdot 10^{14}\,\mathrm{W/cm^2}$. This is expected since the first step of the HHG process needs an atom to be ionized for which the probability increases with increasing laser intensity. Above a certain laser intensity, the yield does not increase further and even decreases. The reason for this could be due to the depletion of the ground state of the generating medium [185]. At a laser intensity of $2 \cdot 10^{14}\,\mathrm{W/cm^2}$ the electric field of the pulse is sufficiently high to ionize argon by barrier suppression, thereby strongly enhancing the ionization rate. With further increasing intensity barrier suppression will take place before the pulse reached its maximum intensity. Once the medium is completely ionized, the high harmonic yield stagnates as no further ionization can take place. The effect of saturation can also be seen in figure 19 c). At a laser intensity of $9.5 \cdot 10^{13}\,\mathrm{W/cm^2}$ the high harmonic cutoff at 800 nm is 38.8 eV for argon. For a laser intensity of

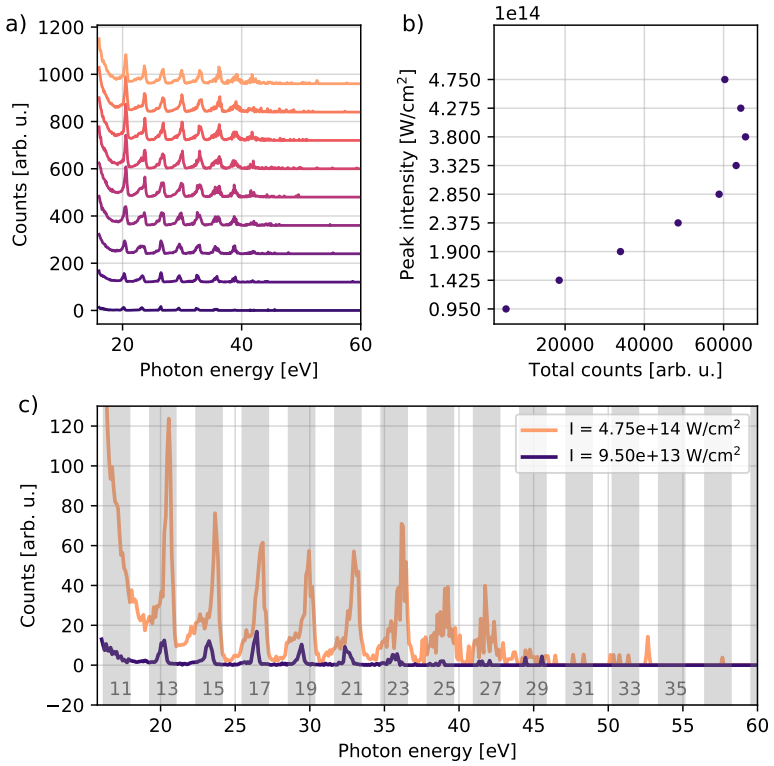

Figure 19: Laser intensity dependence of a) the photoelectron spectrum and b) the integrated yield. c) Comparison of the highest and lowest laser intensity.

$4.75 \cdot 10^{14}\,\mathrm{W/cm^2}$ the cutoff should be at 110 eV for argon, but it appears at 45 eV. This is due to the fact that no ionization happens at the peak electric field of the laser pulse due to saturation at earlier times within the laser pulse.

The effect of ground-state depletion from a certain laser intensity can also be observed, see figure 20 when using different media like neon, argon and xenon at the same driving laser intensity of $3.8 \cdot 10^{14}\,\mathrm{W/cm^2}$ to generate the high harmonics. Here one can see that the high harmonic yield using neon extends until the transmission limit of the aluminum filter at 75 eV, while the spectrum of argon extends until 42 eV. If ground state depletion played no role for argon, the maximum achievable photon energy using neon would be 50 eV. This is not the case and thus ground state depletion is limiting the maximum achievable photon energy using argon. Since neon has a higher ionization potential of 20.18 eV, the barrier suppression intensity is reached only at higher electric fields compared to using argon and hence the photoelectrons can experience greater electric fields leading to high harmonics with more energy. To avoid ground state depletion there are several approaches. These approaches are to use either very short pulses [186], longer driving wavelengths [181] or generating gases with higher ionization potentials. Counterintuitively it is also possible to use even higher laser intensities which makes it possible to ionize atoms multiple times, which effectively avoids ground state depletion [187].

Another effect in the high harmonic generation that we can observe, is the blue shift of the harmonic lines with increasing laser intensity [188]. The 17^{th} harmonic

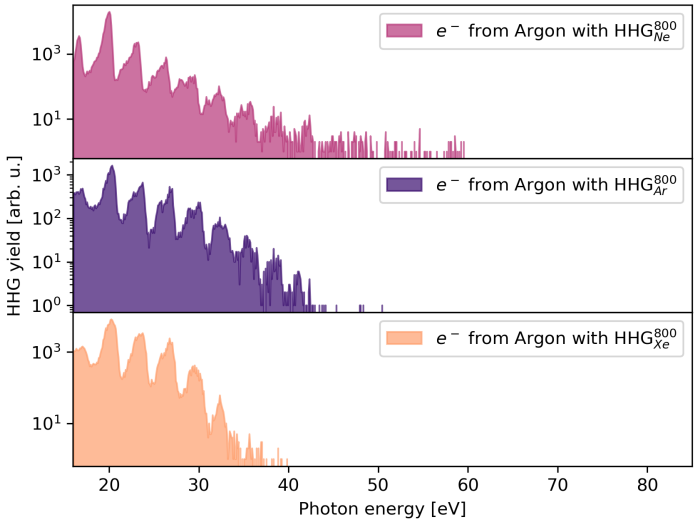

Figure 20: The yield of high harmonics generated in different gases at the same laser intensity. For each gas the pressure has been optimized to achieve the maximum amount of counts over all harmonics.

shifts by 500 meV at the highest intensity, which is shown in figure 21 b). At the same time, there is also a red-shift of 500 meV, but this branch of the harmonic contributes less to the yield of the harmonic. This branching of the harmonic in a lower and higher energetic part is called spectral splitting. The reason for this splitting is a combination of the single-atom response to the intense laser pulse and the propagation of the laser pulse and the harmonics in the generating medium [189]. The atomic response mainly deals with the interplay of different electron trajectories and their phases [123], while the macroscopic picture of the propagation includes aspects like phase matching, and plasma effects acting back on the laser pulse [190]. Recent publications are still investigating what the main contributor to the splitting is [191]. The laser intensity dependence of different harmonics follows a similar trend shown in figure 21 a). The yield increases with increasing laser intensity up until a point of saturation. A very similar behaviour was observed when using the finite gas cell design [175]. Some harmonics show a clear maximum, while the yield of others flattens out. Here we see that higher harmonics tend to form a plateau, while lower harmonics show a maximum in the yield.

The next aspect that we investigate is the influence of the pressure of the generating medium on the high harmonic yield. For this we chose a laser intensity of $3.8 \cdot 10^{14}\,\mathrm{W/cm^2}$, because it leads to the highest yield of high harmonics in the investigation of the intensity. High harmonic spectra for different pressures of the argon gas in the semi-infinite gas cell are shown in figure 22 a). The single harmonics show a maximum in the yield, depending on the pressure, which is shown in figure 22 b). For our setup the optimal pressure for argon is 30 mbar. In principle the more atoms there are to be ionized, the higher the high harmonic yield should be. The reason for there being an optimal pressure is the phase-matching

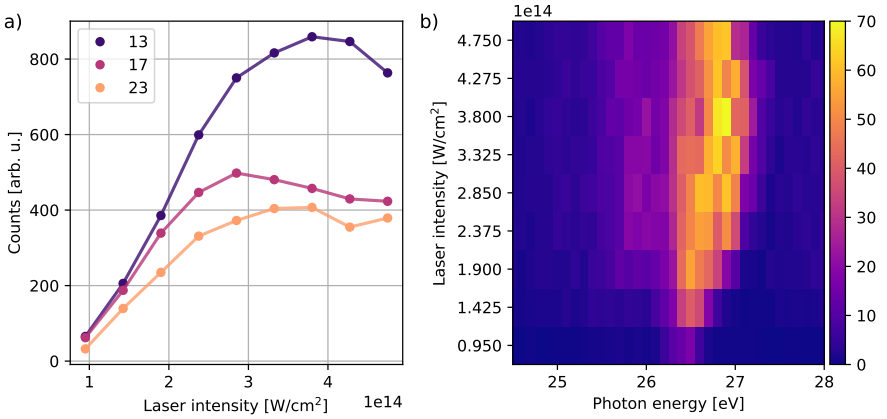

Figure 21: a) Yield of three selected harmonics depending on the laser intensity. b) Intensity dependent yield of the 17^{th} harmonic in detail. The spectral splitting with increasing laser intensity is clearly visible.

condition and absorption. Harmonics generated at different positions in the laser focus should overlap constructively. Therefore the phase velocity of the harmonics and the fundamental beam need to be equal or as close as possible to being equal. This can be achieved by varying the number of atoms, or the pressure, in the focal region of the laser, see section 3.2. The influence of this phase matching can be seen nicely in the split harmonics. At 10 mbar the red-shifted harmonics are favoured or at least equally contributing to the yield. This changes at already 20 mbar where the phase-matching favours the blue-shifted harmonics and does not change with increasing pressure. Another effect that nicely shows the phase-matching can be seen in the shifting of the high harmonic cutoff with increasing pressure. The laser intensity is sufficient to generate harmonics above 45 eV at a pressure of 50 mbar which were not visible at 10 mbar.

The reason for generating high harmonics in vacuum is their short propagation length at atmospheric pressures. At those pressures the attenuation length below 100 eV and above the ionization threshold of argon is less than 500 µm, meaning that after propagating 2.5 mm the remaining intensity is less than 1 % [177, 192]. As the pressure of the generating medium is increased, the attenuation length of the harmonics is shortened. Absorption takes place not only in the cell itself but also in the gas jet which is formed by the gas streaming from the cell through the hole in the copper plate, which is getting denser as the backing pressure is increased. At 70 mbar harmonics in the range from 30 to 40 eV have much less yield than lower and even higher harmonics. This is well explained by the photo-ionization cross-section of argon. At the cooper minimum around 50 eV the cross-section has a minimum which is the reason why harmonics with energies above 40 eV visibly contribute to the spectrum again. This can alternatively be seen in figure 23 a) which shows the integrated yield of the harmonics for every pressure. A comparative view of selected harmonics is shown in figure 23 b), showing that there is not a monotonous trend connecting the optimum phase-matching pressure to the photon energy.

For the finite gas cell design [175], the gas pressure generating the most counts

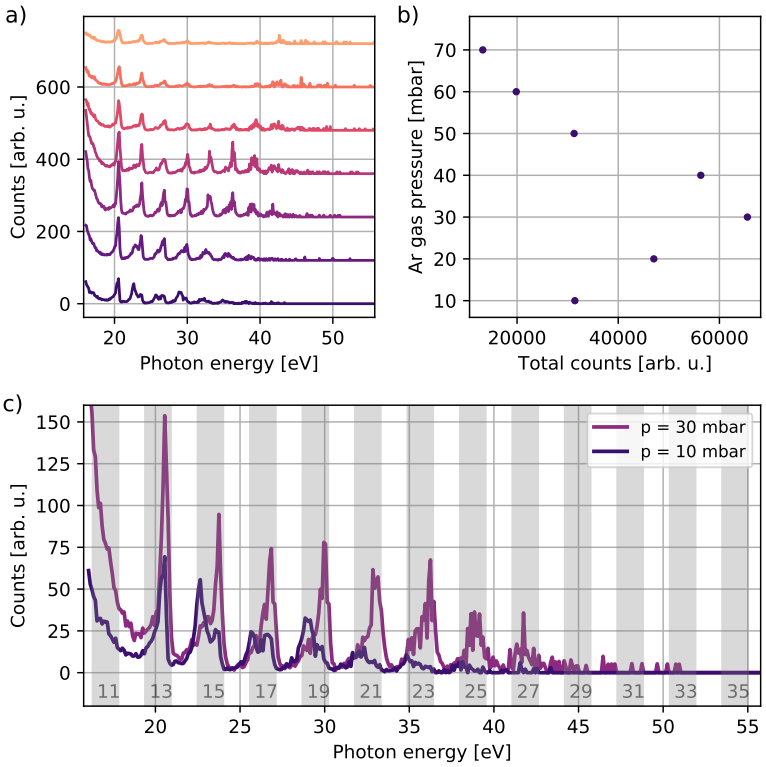

Figure 22: Argon pressure dependence of a) the photoelectron spectrum and b) the total high harmonic counts. c) Comparison between a low pressure and the optimal pressure (30 mbar) photoelectron spectrum.

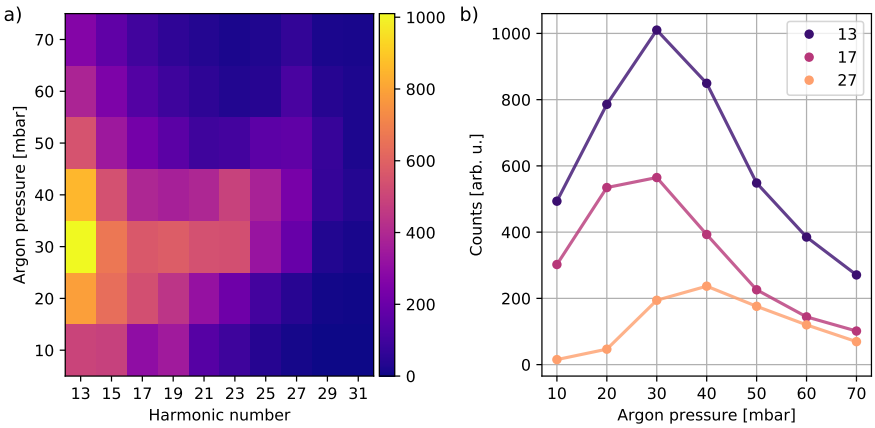

Figure 23: Gas pressure dependence using the semi-infinite gas cell design of a) the yield of the observed harmonics and b) the yield of certain specific harmonics.

was, depending on the harmonic, between 12 mbar and 26 mbar. Having a shorter interaction volume seemed to decrease the pressure required for optimum phase-matching.

The final degree of freedom of the gas cell that we investigated is the position of the copper plate relative to the focal spot position of the laser beam. This influences the length of the medium contributing to the interaction. If the copper plate is before the beginning of the laser focus filament, the interaction length is at its minimum, while it is at its maximum if the laser focus filament is completely inside the semi-infinite gas cell. Changing this position will influence phase matching and absorption of the high harmonics by the medium itself. By propagating more through the dense medium, the medium also acts back on the pulse itself. Even outside of the SIGC the medium plays a role, as the gas streams out of the hole burnt in the copper plate, creating a gas jet co-propagating with the driving laser.
To investigate the influence of the copper plate position relative to the laser focus we connected the SIGC pipe to the vacuum section via a bellow and a translation stage. This lets us move the gas cell relative to the laser focus. The movement is limited by the possible elongation and compression of the bellow and the range of the translation stage. To optimize the position of the copper plate, the plate is put right at the center of the laser filament, which is visible by focusing the beam in the vented HHG chamber. The influence of the copper plate position relative to the laser focus is shown in figure 24. Figure 25 a) shows a 2D colormap image in which the steps in distance between the copper plate and the laser focus position are smaller.

The high harmonic spectra show that the maximum yield over all harmonics is reached when the gas cell is moved 3 mm in direction of the beginning of the SIGC. Thus putting the copper plate roughly at the center of the laser filament is a good starting point for the optimization. To give a better idea of the dimensions figure 25 b) shows a picture of the laser filament that the pulses generate while being focused in nitrogen at atmospheric pressure. Positive cell positions refer to moving the cell in direction of the experimental chamber, while negative numbers refer to the cell being moved further towards the beginning of the SIGC. Striking is the drop-off in the harmonic yield when moving the cell in the positive direction so that more of the filament is within the gas cell, thereby increasing the interaction length. Moving the cell this way leads to a stronger decrease of harmonics in the region from 25 to 40 eV, which could also be induced by increasing the gas pressure to above the optimum.
Changing the cell position influences the splitting of the harmonic. If the copper plate is at the center of the focal plane around 0 mm the harmonics are blue-shifted. This is also the case when the cell is moved so that more of the filament is within the cell. As the cell is moved so that the filament is outside of the cell, the red-shifted harmonic is favoured. This can be explained by a decrease in gas pressure as the intensity for generating harmonics is only sufficient just at the region of the hole in the copper plate, where the pressure drops off due to the gas streaming into the vacuum. This could already be observed in the investigation of the pressure dependence of the harmonics.
The yield of different harmonics for the finite gas cell shows that the harmonics

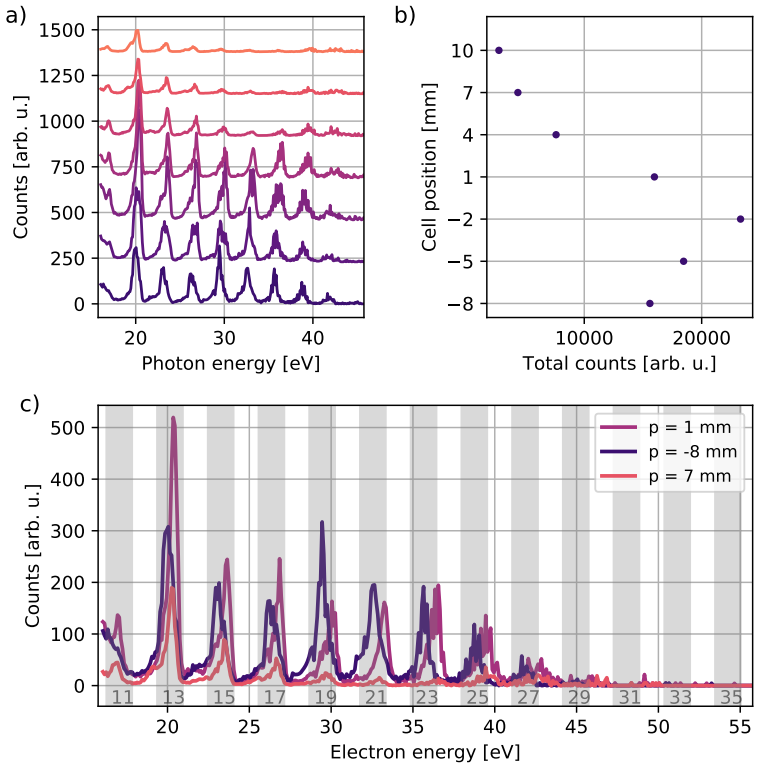

Figure 24: Dependence of a) the photoelectron spectrum and b) the integrated yield on the position of the copper plate relative to the focal point of the driving laser beam. c) Comparison of selected photoelectron spectra for different distances between the copper plate and the focal point.

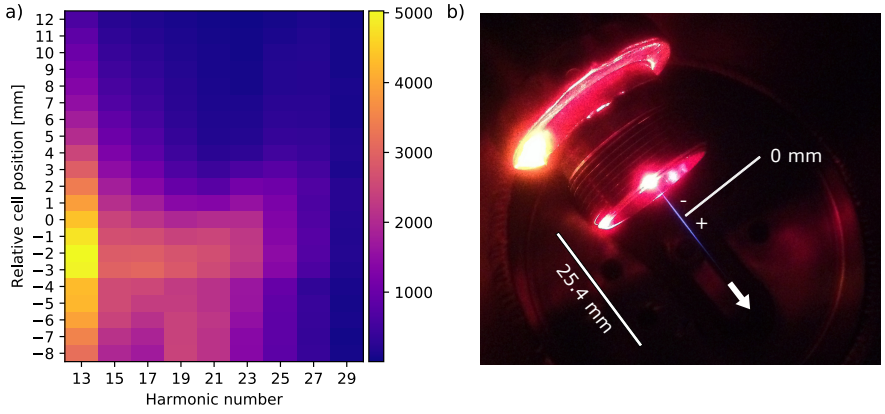

Figure 25: a) High harmonic yield for various distances between the copper plate and the focal plane of the laser. b) End of the semi-infinite gas cell without the copper plate. The filament is created by focusing the laser pulses with a lens of 75 cm focal length into nitrogen at atmospheric pressure. The gas cell is completely extended to see as much of the filament as possible. The arrow indicates the driving beam's propagation direction.

from 13^{th} to 17^{th} have a maximum if the driving beam focus is inside the finite gas cell. For the SIGC this is not true, as the yield of most harmonics peaks between -1 mm and -4 mm, meaning that the driving beam focus is outside of the SIGC. The main cause for this is that in the SIGC design, compared to the finite gas cell design, moving the cell so that the focus is further inside the SIGC leads to re-absorption of the medium. In the finite gas cell, the medium is confined in both directions, limiting re-absorption.

To conclude the harmonic source driven by 800 nm laser pulses with a laser intensity of $3.8 \cdot 10^{14}\,\mathrm{W/cm^2}$ focused by a lens with a focal length of 75 cm allows to generate photons with a maximum photon energy of 44.95 eV, which is the 29^{th} harmonic. A decent flux which is obtained up until the 21^{st} harmonic with a photon energy of 32.55 eV as lower harmonics have in general a higher conversion efficiency. To extend the photon energy range there are numerous approaches. For example, shorter pulses, tighter focusing, longer driving wavelengths, higher pulse energies and media with higher ionization potentials could be used. With higher photon energies inner shells of heavy atoms like xenon become accessible, which could be used to target these atoms in site-specific pump-probe experiments.
Compared to the previous setup using the finite gas cell, the trend of the yield of the harmonics depending on the various parameters is very similar. The biggest difference can be found when looking at the position of the cell, relative to the laser focal plane, which is due to the broken symmetry in the case of using the SIGC.
These findings lead us to pursue a different idea regarding the functionality of the HHG source. Instead of driving the higher harmonics with the fundamental of the laser system, the second harmonic is generated in a β-BBO (bariumborate) crystal and used to drive the high harmonic generation. This will lead to fewer harmonics, due to the lower cutoff energy and a larger gap of 6.2 eV between harmonics. Having a larger gap between harmonics is useful if the aim is to do electron spectroscopy on atomic or molecular systems since features from different harmonics are separated further in energy. By using multi-layer mirrors, or a toroidal grating, instead of a mirror, one could even filter one harmonic, so that the spectrum is not disturbed by other harmonics. In the following section, HHG with the second harmonic is demonstrated and characterized, similar to the characterization using the fundamental wavelength. Lastly, the resolving capabilities of higher harmonics generated by the second harmonic of the laser system are demonstrated in a benchmark experiment on photo-ionization of molecular hydrogen.

7.2.2 *HHG driven by 400 nm laser pulses*

Choosing a shorter driving wavelength of 400 nm for higher harmonics has two implications. The maximum achievable photon energy will be reduced since the ponderomotive potential is smaller than if a driving wavelength of 800 nm is used. Secondly, the conversion efficiency is increased by reducing wave packet spread since the electron spends less time from the time of ionization to the time of recollision [187].
To generate the second harmonic (SHG) of our fundamental beam a lens with

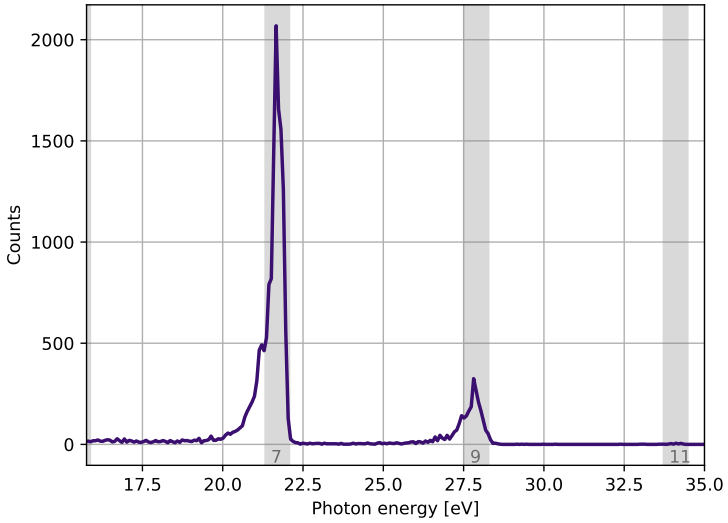

Figure 26: High harmonic spectrum generated by driving argon gas using 400 nm laser pulses with a laser intensity of $2.0 \cdot 10^{13}\,\mathrm{W/cm^2}$. The position of focus is 5 mm inside the gas cell. Compared to driving high harmonics using 800 nm laser pulses, fewer harmonics are visible at 400 nm.

a focal length of 1 m is used, which narrows the fundamental beam size at the position of the 100 µm thick BBO crystal, which is used to convert the fundamental to the second harmonic. The beam is then reflected and directed into the SIGC by two dichroic mirrors, which filter the fundamental beam. This setup has proven to be reliable and easy to set up but only leads to a conversion efficiency (regarding the average power) of roughly 20 % from the fundamental to the second harmonic.

Figure 26 shows a high harmonic spectrum generated with the second harmonic. At first sight one can observe two harmonics, which are the 7^{th} at 21.7 eV and 9^{th} at 27.9 eV. At the position of the 11^{th} harmonic at 34.1 eV a small signal can be observed. The yield of the high harmonics increases linearly with increasing intensity of the SHG, which can be seen in figure 27 a). This is a consequence of the laser intensity regime, which is around $1.0 \cdot 10^{13}\,\mathrm{W/cm^2}$. In this regime, the medium is not strongly ionized which prevents non-linearities introduced by the laser pulse rapidly ionizing the medium.
The pressure dependence has not been investigated in detail since there is a very strong optimum around 10 mbar for argon. The high harmonic conversion efficiency decreases strongly when varying the pressure by 2 mbar in either direction. Varying the distance between the copper cell and the laser focal plane has little effect on the conversion efficiency as can be seen in figure 27 b). Interestingly the behaviour here is opposite to the high harmonics being generated with the fundamental. Moving the cell so that the laser focus is within the cell only influences the conversion efficiency mildly whereas moving the cell so that the laser focus is outside the cell leads to a drop in the conversion efficiency of about 50% in the available translation range of the gas cell. The setup with 400 nm driving laser pulses is less sensitive to the position of the cell and the pressure of the medium.

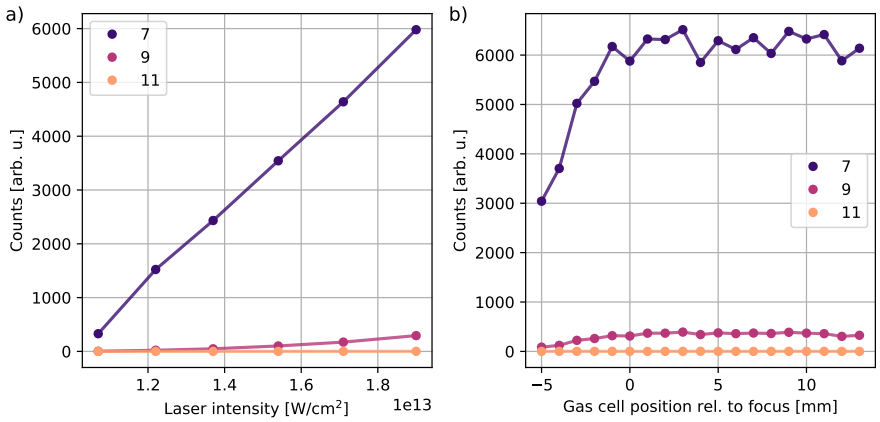

Figure 27: a) Yield of the three observed harmonics for increasing laser intensity. b) Influence of the copper plate position relative to the laser focus on the high harmonic yield. Positive values refer to the focus being further within the SIGC, while negative values refer to the focus being outside of the SIGC.

Driving the high harmonics by the second harmonic generates a similar amount of photoelectrons as when the high harmonics are driven by the fundamental. Since using the SHG creates fewer harmonic orders, the high harmonic yield is concentrated in fewer harmonics, compared to the situation at 800 nm. At comparable laser intensities, the yield using the SHG should surpass the yield using the fundamental [126]. Another difference between the two driving wavelengths is the linewidth. Using 400 nm the spectrum is less affected by splitting of the harmonics as the linewidth with roughly 0.5 eV is much less than for the fundamental with roughly 1 eV in the case of strong splitting.

7.3 PHOTOELECTRON SPECTROSCOPY OF H_2

Using the second harmonic to generate high harmonics has the advantage over using the fundamental, which is the spacing of 6.2 eV between adjacent harmonics. This gives a larger range of energy to separate features in the electronic structure of atoms and molecules and makes interpreting the electron spectra much more straightforward. Also the linewidth at 400 nm is less broadened and does not show spectral splitting as much, making it easier to separate features of the higher harmonics from electronic features of the investigated atom or molecule. As a first example of the spectroscopic performance of the setup, the photoelectron spectrum that arises from ionizing hydrogen with the 7^{th} harmonic with an energy of 21.7 eV is investigated (Fig. 28). Compared to photoelectron spectra of atoms (like argon as previously shown), series of peaks are visible for hydrogen, which correspond to the different vibrational levels of the hydrogen molecular ion. These arise because the hydrogen molecular ion can be excited above the ground state into higher vibrational levels of the potential energy surface of the electronic state. This is a direct result of the Franck-Condon principle, which makes the ionization of vibrational states possible since the ground-state wave function of the hydrogen molecule overlaps not only with the ground-state wave function of the molecular

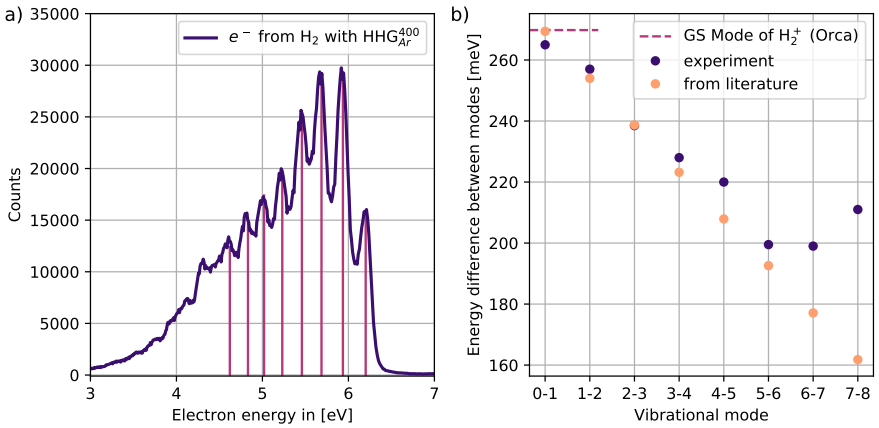

Figure 28: a) Photoelectron spectrum of molecular hydrogen. Lines indicate the central position of the Gaussian fits to the vibrational peaks. b) Energy difference between adjacent vibrational modes compared to literature values [193] and a ground state simulation done with ORCA [141].

ion but also with the wave function of higher excited vibrational states. In this case, the overlap with an excited vibrational state is even more probable than to excite into the lowest energetically possible state, indicating that the bond length of the molecule changes significantly when being ionized, which in this case is from 0.74 Å to 1.04 Å as has been calculated using ORCA [141]. The lower figure shows the energy difference between vibrational modes and also shows values from literature. For the first six vibrational modes, the agreement is quite well until the difference in energy between vibrational modes becomes so small that the linewidth of the higher harmonics leads to strongly overlapping peaks that shift the peak positions resulting in the deviation from literature values. The deviation from the literature values gives an estimate of the spectral resolution of 200 meV when using the high harmonic source. This means that spectral features should be separated by more than 200 meV to just be resolved.

8

SINGLE COLOR EXPERIMENTS

Here we investigate the dissociation of molecular hydrogen (H_2) and methane (CH_4) into charged ions and fragment ions by using either the fundamental (800 nm) or the second harmonic (400 nm) of a Ti:Sa amplifier. Applying these two colors at various intensities will enable us to investigate molecular dissociation in the regime of tunneling ionization up to $1.0 \cdot 10^{15}\,W/cm^2$ with the fundamental and in the regime of multi-photon ionization around $1.0 \cdot 10^{14}\,W/cm^2$ with the second harmonic. Molecular hydrogen acts as a benchmark, while the experiment on methane will shine a light on a more complex, three-dimensional molecule with a specific symmetry.

8.1 DISSOCIATION OF MOLECULAR HYDROGEN

The dissociation of molecular hydrogen is well studied in literature [18, 137, 147, 194, 195]. Due to its simple nature, it acts as a reference for the dissociation of diatomic [137] and more complex molecules. Because of its light constituents, it also serves as a benchmark for ultrafast science and technologies [194]. In the following section, the strong field dissociation of molecular hydrogen in the field of the second harmonic will be investigated. After having established a good understanding of a more simple dissociation, the dissociation induced by the fundamental will be investigated and finally, possible differences between both scenarios are discussed.

8.1.1 *Dissociation of H_2 in 400 nm intense laser fields*

As we observe the dissociation by detecting charged atoms or molecules it would be fairer to say that we actually observe the dissociation of H_2^+. In an intense laser field, the hydrogen can also dissociate without being ionized by excitation to high-lying quasi Rydberg states which will give $H_2 \rightarrow H_2^{**} \rightarrow H + H$ [196]. The corresponding experiment does not show evidence of the hydrogen atoms being ionized during or after dissociating. In the present experiment singly charged hydrogen fragments are detected, which result from the dissociation of $H_2 \rightarrow H_2^+ \rightarrow H + H^+$ and $H_2 \rightarrow H_2^{2+} \rightarrow H^+ + H^+$. For these dissociation channels to occur the hydrogen molecule has to be ionized, i.e. we investigate here the dissociation of molecular hydrogen which undergoes strong field ionization and subsequent dissociation.
A time-of-flight spectrum of the charged species in the interaction of 400 nm laser pulses with hydrogen molecules is shown in figure 29 a). The voltages applied are 0.3 kV at the VMI repeller, 1.0 kV at the VMI extractor and -0.6 kV at the drift tube, while the MCP was at a voltage of 2.0 kV. The spectrum is recorded with an oscilloscope connected to the output of the ToFs MCP. The single peak at a time-of-flight of 2430 ns is the hydrogen molecular ion while the symmetric peak structure around 1900 ns are the charged hydrogen fragments. The effect of kinetic energy release in the dissociation is clearly visible here. As the laser polarization

axis is in line with the axis of the ToF spectrometer, those molecules are favoured to dissociate, which are aligned parallel to the polarization of the light. This is a result of the projected field strength along the molecular axis, which is highest when the molecule is aligned parallel to the polarization of the light. Fragments flying directly into the ToF will have a shorter time-of-flight while fragments that have a momentum directed away from the ToF will need a longer time-of-flight before hitting the MCP of the ToF. The extra or reduced amount of time needed is a measure of the particle's momentum and with that a measure of the kinetic energy released during the dissociation. Because of the symmetry, it is sufficient to analyze one side of the ionic hydrogen fragments. We choose to only look at the particles, which have momentum directed in the opposite direction of the ToF spectrometer.
To track the behaviour of different dissociation channels, a Gaussian is fit to the peaks, before transforming the time-of-flight axis into a kinetic energy release axis. The reason for this is that the shape of the peaks in the ToF spectrum is very close to a Gaussian shape, which changes when transforming the ToF to a kinetic energy axis. The details of this transformation will be explained later on, as it is a result of further analysis of the data. A detailed view of the fragment's kinetic energy release is shown in figure 29 b). As one can see there are two dissociation channels. The channel with lower kinetic energy peaking around 0.5 eV is referred to as the bond-softening (BS) channel (see chapter 4). These fragments result from the dissociation $H_2^+ \rightarrow H + H^+$. The channel peaking around 2.25 eV is referred to as the charge resonance enhanced ionization (CREI) channel (see chapter 4). It is the result of the ionization of the hydrogen molecular ion, leaving behind two protons that repel each other according to the Coulomb force [197]. It should be noted that the KE axis is non-linear in ion KE spectra derived from ToF measurements. The distance between KE points increases with increasing KE. This leads to features at higher KEs having an increased signal compared to features at lower KEs, which is a welcome side effect as it enhances their visibility. The derived yield is not affected by this since it is determined via the ToF spectrum. The kinetic energies of the features are not affected since we calibrate them using values provided by literature. The same is true for the studies using 800 nm pulses.

Bond softening appears if two potential energy surfaces are coupled by a periodically oscillating light field. In the case of the hydrogen molecular ion, these are the ground state $1s\sigma_g$ and the first excited stated $2p\sigma_u$. The coupling of the states in a periodically oscillating laser field generates replicas of the potential energy surfaces shifted up and down by the photon energy. Since the hydrogen molecular ion is initially in the ground state only those shifted excited states which intersect the ground states potential energy surface are of interest to us. In the case of bond softening of the hydrogen molecular ion with a photon energy of 3.1 eV the relevant intersection is between the $2p\sigma_u$ state downshifted by one photon energy and the $1s\sigma_g$ state. At the distance where those two potential energy surfaces intersect an avoided crossing is formed. Figure 30 shows the crossing potential energy surfaces at different laser intensities. The potential energy surfaces have been calculated with ORCA [141]. The internuclear distance of the two protons is changed and a CASSCF calculation with one electron and two active orbitals in the atomic natural orbital basis set with a double zeta basis set is performed [141]. The blue

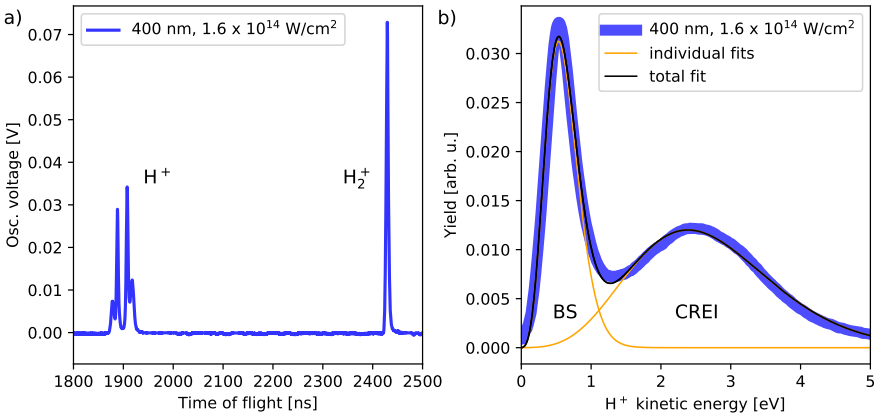

Figure 29: a) ToF spectrum of the strong field dissociation of molecular hydrogen at 400 nm. b) Kinetic energy of hydrogen ion fragments at the same laser intensity. The laser intensity used is $1.6 \cdot 10^{14}\,\mathrm{W/cm^2}$ in a) and b).

curves in figure 30 schematically show the avoided-crossing between the dressed and ground-state PES, leading to vibrational trapping (VT) and bond-softening (BS). Since with increasing laser intensity the gap between the potential energy surfaces gets bigger, the coupled ground state maximum energy shifts more and more below the vibrational state $v = 6$, which is the first vibrational level able to dissociation as the laser intensity increases. The increasing laser intensity allows also lower-lying vibrational states (from $v = 0$ to $v = 5$) to dissociate due to the lowered barrier. The same is true for higher-lying vibrational states ($v = 7$ and further states), which initially cannot dissociate at low laser intensities due to vibrational trapping [17], in which the dressed, coupled PES has a minimum and prevents dissociation (see figure 30). The kinetic energy released depends on the energy of the vibrational level. The higher the vibrational level, the greater the kinetic energy release will be. Table 1 shows the potential energy of the vibrational level above the minimum of the $1s\sigma$ ground state and the corresponding kinetic energy release for each particle which is half of the total kinetic energy release.

The peak in figure 29 b) that was labeled BS channel actually consists of small peaks for each vibrational level but due to the resolution of our experimental setup no contribution of a single vibrational level can be seen. As the gap opens with increasing laser intensity the BS peak will get broader and eventually shift. As the gap opens, more and more vibrational levels contribute to the distribution, leading to the broadening. As the lower levels have higher FC factors, peaking at $v = 2$, the overall BS distribution will have more contributions at lower kinetic energies with increasing laser intensity. This gives the impression of a shift towards lower kinetic energies. Another aspect contributing to the shift towards lower kinetic energy releases is the spacing in energy between vibrational levels, which is getting tighter for higher excited vibrational levels. This shifting can indeed be observed when plotting the kinetic energy of the BS distribution with the highest yield versus the laser intensity, which is shown in figure 31 b). As the laser intensity increases the center of the BS distribution shifts by about 75 meV to lower kinetic energy releases. At this point, the gap between the potential

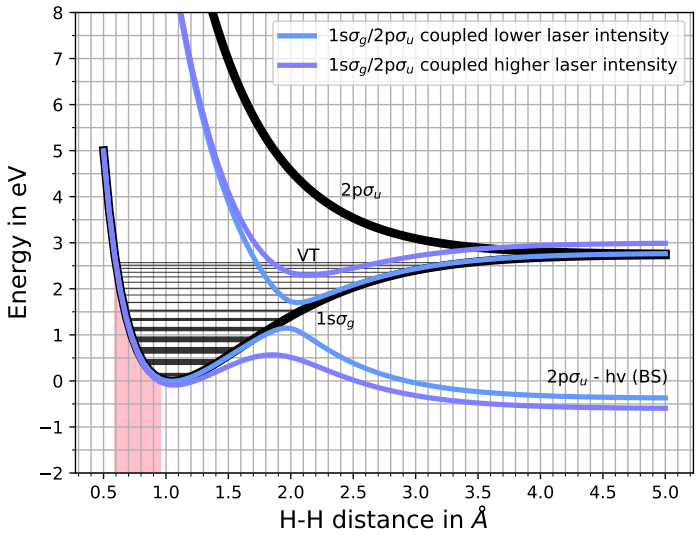

Figure 30: Potential energy surfaces of the coupled $1s\sigma_g$ and $2p\sigma_u$ state of the hydrogen molecular ion for different laser intensities. The rose stripe shows the FC region and the black lines are the vibrational levels. The thickness of the lines corresponds to the FC factors. The field-free PES (black curves) have been calculated using ORCA [141]. The blue curves schematically show the avoided-crossing between the dressed PES, leading to vibrational trapping (VT) and bond-softening (BS).

Vib. level v	FC factors	Pot. energy [eV]	KE [eV]
0	0.0922	0.14	0.25
1	0.1751	0.40	0.38
2	0.1959	0.66	0.50
3	0.1700	0.90	0.62
4	0.1275	1.13	0.74
5	0.0874	1.33	0.84
6	0.0566	1.53	0.94
7	0.0355	1.70	1.02
8	0.0219	1.87	1.10
9	0.0134	2.01	1.18
10	0.0082	2.14	1.24
11	0.0032	2.26	1.30

Table 1: Vibrational levels and their corresponding Franck-Condon factors, potential energies and proton kinetic energy in one photon bond-softening of the hydrogen molecular ion [193].

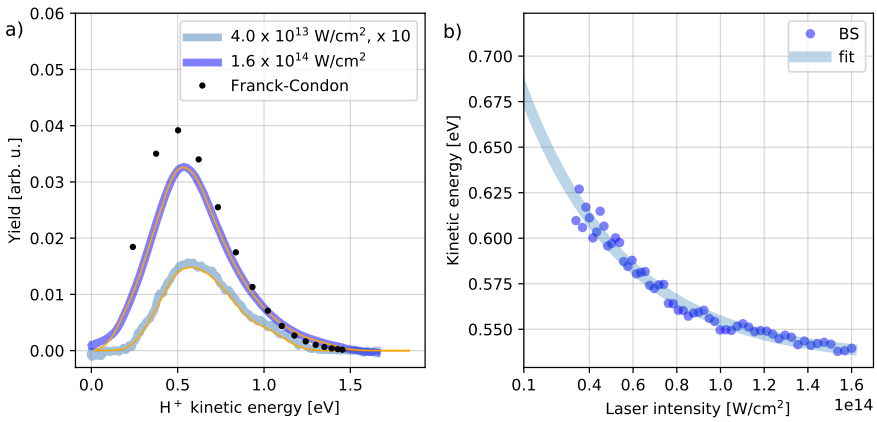

Figure 31: a) Kinetic energy distribution for H^+ at two different laser intensities. The orange curves are the sum of Gaussians for each vibrational level that will lead to the respective kinetic energy. Black dots show the Franck-Condon factors for the different vibrational levels. b) Shift of the kinetic energy center of the BS dissociation channel.

energy surfaces is so large that all vibrational levels contribute to the dissociation and with even further increasing laser intensity the distribution converges to the Franck-Condon (FC) distribution. But this is probably difficult to observe since factors like focal volume averaging and the varying laser intensity during the laser pulse lead to various local laser intensities and therefore to various different KER distributions for different gap widths which contribute to the overall KER distribution.
An interesting side effect of the BS channel is that it can be used to calibrate the time-of-flight to the kinetic energy release. The maximum of the BS distribution is assumed to coincide with the kinetic energy release that is expected for the vibrational level v=2 of the H_2^+ ground state. From thereon it is assumed that the following relation between the kinetic energy (KE) and the time-of-flight (t_{ToF}) holds true: $KE = a \cdot (t_c - t_{ToF})^2$ (see equation 39). Here t_c is the center between the symmetric ion ToF spectrum for H^+ and a is the calibration factor. When overlaying the FC distribution with the spectra of different pulse laser intensities, see figure 31 a), the measured spectrum appears close to the FC distribution, not only in the kinetic energy distribution, but also it's shape. Additionally, the shift of the maximum of the distribution is visible. The difference between the KER and the KE is that KER includes the total kinetic energy of both fragments, while the KE is the kinetic energy of one fragment. In the dissociation of di-atomic molecules the KE is half of the KER of a certain dissociation channel.

The second dissociation channel centered around a kinetic energy of 2.3 eV is the Coulomb explosion channel, more specifically the CREI channel (see chapter 4). To ionize H_2^+ at the equilibrium distance a minimum photon energy of 46.4 eV (from the ORCA calculation) would be required. With the achievable laser intensity of $1.6 \cdot 10^{14}\,W/cm^2$ and this ionization potential we are far in the multi-photon regime at $\gamma = 3.1$. However, ionization would require absorbing more than 15 photons at the same time, which is highly unlikely. The expected single particle

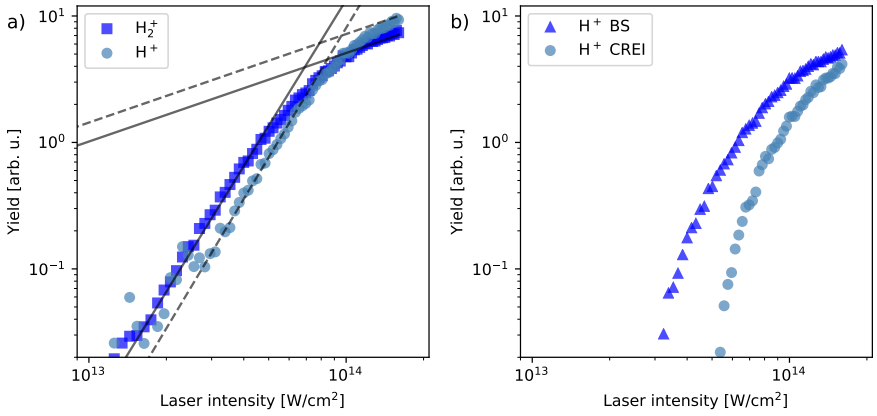

Figure 32: Intensity dependence of the ion yield of a) the molecular hydrogen ion and hydrogen ion and b) the BS and CREI dissociation channel of the hydrogen ion. The grey lines in a) are matched to the flat and more steep section of the yield to estimate the slope and the saturation intensity.

kinetic energy release here would be around 7 eV which is much more than what was measured in the experiment, showing that the dissociation takes place at greater internuclear distances from 2.4 Å (3.5 eV KE) to 14.5 Å (1.0 eV KE). This is calculated using the potential energy surfaces of the doubly charged hydrogen molecule. The maximum ionization probability is reached at an internuclear distance of 4.0 Å, following the maximum of the CREI channel at a KE of 2.3 eV. This leads to the conclusion that the process is enabled by the two nuclei moving apart from each other, which is induced by the BS channel. BS is the precursor to the Coulomb explosion channel [198]. Therefore it has to be considered that the total KE is the sum of the KE of the BS channel up to the point of the ionization and the KE from the Coulomb explosion. The contribution from the BS channel per particle is measured to be 0.5 eV corresponding to the KE of dissociating vibrational level $v = 2$ which has the highest FC factor. The CREI can be explained with a semi-classical model. As the nuclei drift apart and the laser field oscillates, the electron adiabatically follows the laser field and the whole system stays in the ground state. With increasing distance between the nuclei, the central barrier rises so that the electron cannot simply follow the field anymore. Part of the electron distribution is localized at the energetically less favoured site from which the electron can reach a continuum state leading to ionization. For this, the electron has to overcome the outer barrier, which decreases in energy, and the inner barrier, which increases in energy, as the nuclei move apart. The CREI channel is available once the internuclear separation is large enough that part of the electron distribution can be trapped in the energetically higher position (2.4 Å) and is not available anymore once the internal barrier prevents ionization due to the increasing internuclear separation (14.5 Å). This is the reason for the existence of a distinct maximum in the yield of this channel depending on the internuclear separation. In a bit different terms, CREI is a tunneling ionization that is enhanced by a special internuclear separation between two atoms in the case of a di-atom.

Another insightful aspect of laser intensity dependant experiments is the yield of ions and fragments created in the interaction with intense femtosecond laser pulses. The slope of the yield is an indicator of the non-linearity of the processes involved while the change of the slope can be used as a method to calibrate the laser intensity by identifying the saturation intensity. This indirect measurement of the laser intensity is helpful since it is not always straightforward to measure all the necessary parameters such as the spot size in the interaction region, the pulse length and the energy per pulse. If these parameters are known, it is still helpful to have a way of cross-checking the estimated laser intensity. The yield of H_2^+ and H^+ is shown in figure 32 a). As can be seen at lower laser intensities around $3.0 \cdot 10^{13}\,W/cm^2$ the yield of the molecular ion is greater than the hydrogen ion fragments. This is expected at such laser intensities since to generate the hydrogen ions the hydrogen molecule has to be ionized first to then undergo dissociation via the BS or CREI channel. With increasing laser intensity the yields become closer until an intensity of $8.7 \cdot 10^{13}\,W/cm^2$ is reached, where the yields are equal, and from thereon the yield of the hydrogen ion is greater than that of the molecular ion. The reason for this is that the molecule is already ionized earlier in the laser pulse and leaves the molecular ion in a stronger field for a longer time, which increases the probability of dissociation by BS or CREI. Additionally, every molecular ion that dissociates will contribute to the yield of the atomic ion instead. As the laser intensity rises the yield starts to go into saturation. The reason for this is that at the center of the laser focal volume the medium is completely ionized and increasing the laser intensity further will not increase the yield produced in the central spot. But due to the focal volume that is defined by the laser, increasing the intensity further will still increase the yield in the outer shells of the focal volume until they are also saturated. The slope for the molecular ion and the fragment ion is very similar with 3.4 (H_2^+) and 3.5 (H^+) indicating that the non-linearity involved in the generation of both fragments is similar. The saturation intensity at 400 nm for H_2^+ is $6.9 \cdot 10^{13}\,W/cm^2$ and for H^+ it is $7.9 \cdot 10^{13}\,W/cm^2$.
Looking at the yield for the individual dissociation channels one can obtain information about their intensity dependence, which is shown in figure 32 b). The BS channel is the main contributor to the H^+ yield throughout all available laser intensities. As the laser intensity increases, the CREI channel contributes more and more until the contributions are similar at the highest laser intensity.

8.1.2 *Dissociation of H_2 in 800 nm intense laser fields*

The dissociation of the hydrogen molecule in 800 nm laser fields is similar but a bit more complex compared to the dissociation at 400 nm. Figure 33 shows a KER spectrum at a laser intensity of $2.1 \cdot 10^{14}\,W/cm^2$. Here three channels can be identified [18]. The channel with the lowest KER is the BS channel at 800 nm. The channel with a KE around 0.5 eV is the above-threshold dissociation (ATD) channel. The name is related to the phenomenon of above-threshold ionization (ATI) where ionized electrons can absorb more photons than necessary to overcome the ionization potential of the system. In this case, the nuclei follow the three-photon dressed dissociative PES up to the crossing with the two-photon dressed ground-state PES, where it changes to follow the latter. Thus a total of two

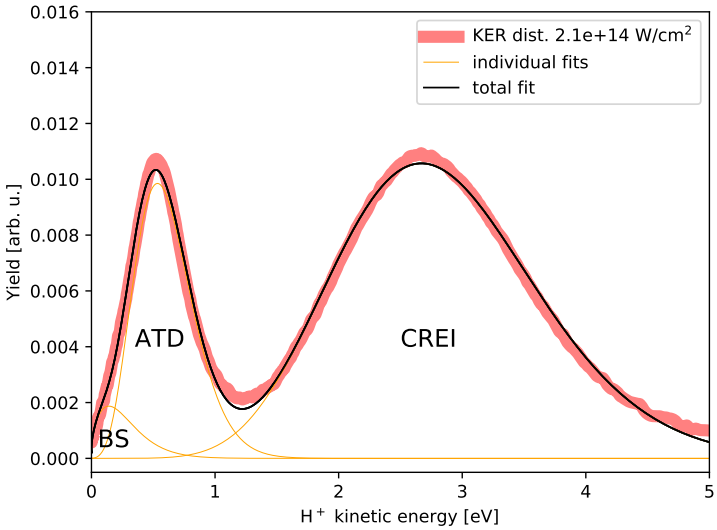

Figure 33: KE spectrum of H^+ fragments from the dissociation of H_2 with 800 nm laser pulses. From left to right the orange curve shows fits to the BS, ATD and CREI channels. The black curve is the total fit as a sum of all orange fits to the individual channels.

photons were absorbed in the ATD process. Similar to the 400 nm KER spectrum the CREI channel is also visible in the dissociation at 800 nm. The KE axis is calibrated with the ATD channel, which is equivalent to the BS channel at 400 nm, as both dressed PES are shifted by 3.1 eV. We can observe a shift in the peak position of the ATD channel with increasing laser intensity, which gets less as the laser intensity increases, indicating that the KE distribution converges to the FC KE distribution, which should peak at 0.5 eV KE, as did the BS channel at 400 nm. The shift is shown in figure 34 a). The exponential fit extends the shift to lower laser intensities, where the statistics are not good enough and which are also out of the range of the attenuator. The exponential fit is chosen since it retraces the measured trend rather well. At very low laser intensities around $10^{10}\,W/cm^2$ only $v = 3$ will contribute to the dissociation (see figure 35), which would lead to a KE of 0.62 eV, which is not reached by the exponential fit. Nonetheless calibrating the KE with the ATD channel leads to a good agreement with literature values of the CREI channels KE which is around 2.8 eV to 3.0 eV [199]. This calibration was also used for the experiment at 400 nm.

To get a better understanding of the BS and ATD channel, figure 35 shows the dressed potential energy surfaces for comparatively low laser intensity. Compared to the 400 nm case also the dressing of the $1s\sigma_g$ state is important to properly describe the ATD channel. The BS channel is opened up by the avoided crossing of the $2p\sigma_u$ state down-shifted by the photon energy ($2p\sigma_u - \hbar\nu$) and the $1s\sigma_g$ state. With increasing laser intensity the gap opens up, but only vibrational states with energies above the $2p\sigma_u - \hbar\nu$ state in the limit of infinite separation between the nuclei can contribute to the dissociation via this channel. At very low laser intensities only v_9 can contribute to the dissociation until the gap is fully opened

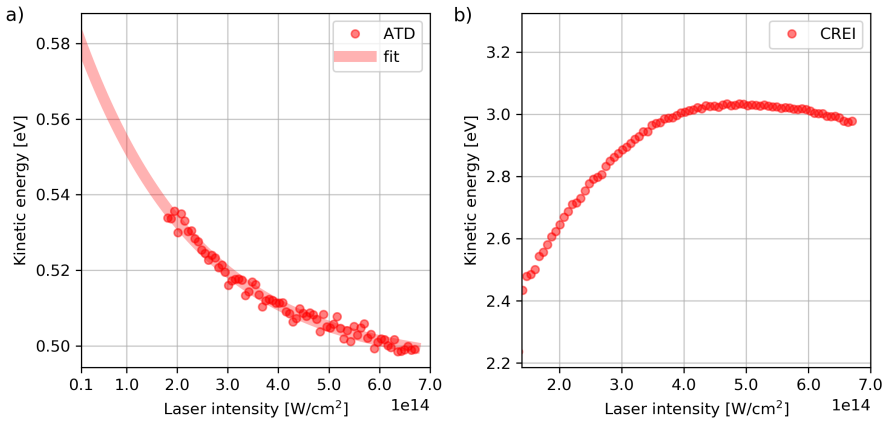

Figure 34: Laser intensity dependence of a) the KE center of the ATD channel and b) the KE center of the CREI channel. The fit in a) extrapolates the ATD KE shift to lower laser intensities.

and vibrational levels higher than $v = 4$ contribute. The dissociation via the ATD channel is initiated by the avoided crossing between the $2p\sigma_u - 3\hbar\nu$ state and the $1s\sigma_g$ state. The molecule then evolves along the dressed $2p\sigma_u - 3\hbar\nu$ state until another crossing between dressed PES is reached at an internuclear distance of 2.5 Å, where the $1s\sigma_g - \hbar\nu$ state forms an avoided crossing with the $2p\sigma_u - 3\hbar\nu$ state. The avoided crossing allows the molecule to follow the $1s\sigma_g - 2\hbar\nu$ PES by emitting a photon, which leads to dissociation by net-absorption of two photons [194]. This absorption of three photons and emission of one photon is the ATD channel, which leads to KEs similar to the one-photon dissociation at 400 nm.

Another interesting effect is the shift of the CREI channel to higher KEs with increasing laser intensity, which has also been observed earlier [200] and is shown in figure 34 b). The mechanism for 800 nm works in the same way as it does for 400 nm, although for the latter no shift to higher KEs could be observed. A shift to higher KE indicates that CREI is initiated at shorter internuclear distances. The reason for this is that, due to the higher field strength, the outer barrier is more strongly suppressed as the laser intensity increases, leading to ionization at shorter internuclear distances. At the lowest laser intensity the CREI channel KE is comparable to the CREI channel KE at 400 nm. Discrepancies could be due to the faster oscillations of the light field, affecting the tunneling time. An influence could also be that the hydrogen molecular ion will be prepared in different states by the two different photon energies.

The yield of H_2^+ and H^+ depending on the laser intensity are shown in figure 36 a). Similar to the dissociation at 400 nm, the yield of the molecular ion is higher than that of the atomic ion up to a certain intensity. Here this intensity is at $2.5 \cdot 10^{14}\,W/cm^2$. With further increasing laser intensity, the yield of the hydrogen ion becomes greater and greater until the maximum available intensity of $1.25 \cdot 10^{15}\,W/cm^2$. At this point, the yield of the atomic ions is one magnitude higher than for the molecular ion. To get access to the non-linearity of the processes involved, the slope of the yield is considered in regions, where saturation effects have no influence. The lines have a slope of 4.5 for the molecular ions and

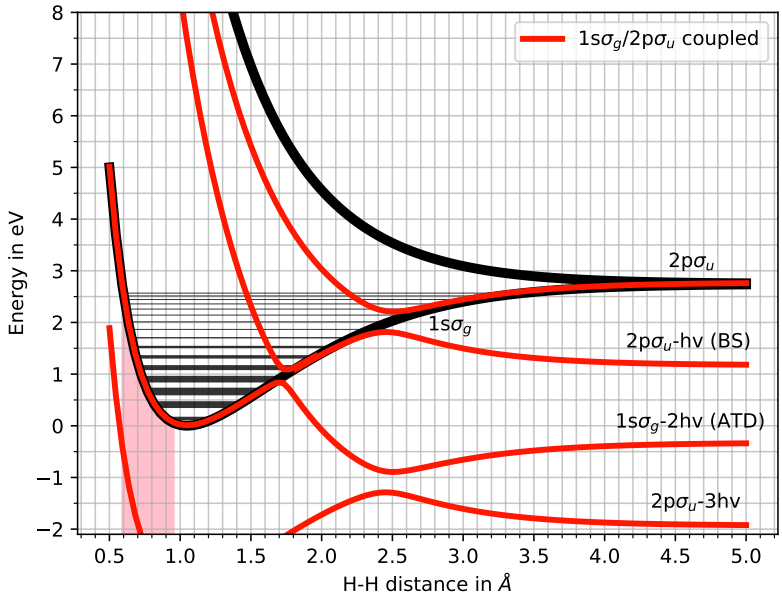

Figure 35: Ground and excited state PES (black curves) of the hydrogen molecular ion in a light field of 800 nm. Red curves are schematics, showing the coupled PES and the avoided crossings that appear.

a slope of 6 for the atomic ions, in contrast to the two similar slopes of about 3.5 for both ions at 400 nm. That the slopes of the two ions are different shows the different degrees of non-linearity which are involved. At 800 nm more photons have to be involved since the photon energy is half of that at 400 nm leading to steeper slopes. Naively one could expect the slopes at 800 nm to be twice the value of the slopes at 400 nm which is roughly the case. Deviations can arise due to the influence of tunneling ionization at increasing laser intensities. Considering the

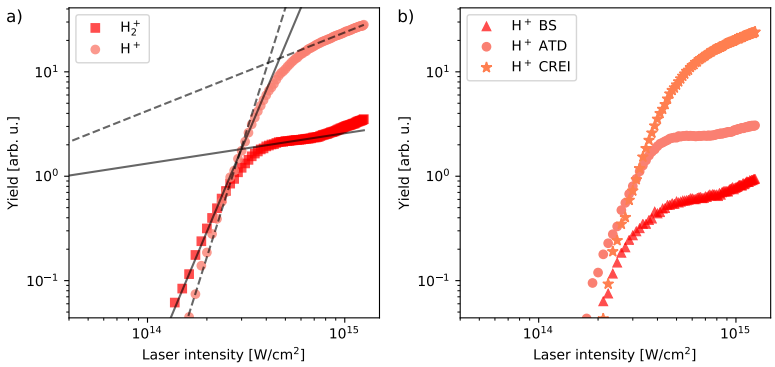

Figure 36: a) Intensity dependent molecular hydrogen and hydrogen ion yield. Grey lines are matched to the flat and steeper part of the yield curves to show the different non-linearities and to derive the saturation intensity at the intersection of the lines. b) Intensity dependent yield of the BS, ATD and CREI dissociation channels.

Keldysh parameter region for 800 nm, values from 1 to 0.32 are found, which respectively extend from the mixed multi-photon/tunneling regime to the tunneling regime. The Keldysh parameter in the case for 400 nm ranges from 6.2 to 1.8, which is in the regime of multi-photon ionization. This could be the explanation for why the slope is less than twice that compared to ionization at 800 nm.
That the slope is steeper for the hydrogen ion compared to the molecular ion shows that a process requiring more photons is involved. This is expected since the atomic ion can only originate from an already ionized hydrogen molecule, which then needs to absorb further photons to evolve along with the BS or ATD channel. The saturation intensities, which can be extracted from the lines fit to the yield curves, are $3.0 \cdot 10^{14}\,\mathrm{W/cm^2}$ for H_2^+ and $4.0 \cdot 10^{14}\,\mathrm{W/cm^2}$ for H^+. Values found in the literature are really close to this with $2.5 \cdot 10^{14}\,\mathrm{W/cm^2}$ for H_2^+ and $3.5 \cdot 10^{14}\,\mathrm{W/cm^2}$ for H^+ [18].
The yield for the different dissociation channels is shown in figure 36 b). The yields are only shown for laser intensities which lead to sufficient statistics. At a laser intensity of $2.5 \cdot 10^{14}\,\mathrm{W/cm^2}$ the ATD and CREI channels have a similar yield while the BS channel goes into saturation. With increasing laser intensity the yields become well separated and at the highest intensity, the CREI channel has a magnitude higher yield compared to the ATD channel. Comparing the BS, ATD and CREI channels there exists a plateau in the yield at around $6.0 \cdot 10^{14}\,\mathrm{W/cm^2}$ that could already be seen in the yield of the hydrogen molecular ion. The interpretation is that with higher laser intensities, more ionized hydrogen molecules also dissociate. Molecules that dissociate along the BS or ATD channel will pass the critical internuclear distances, where CREI takes place, which becomes the most likely dissociation channel at very high laser intensities.

8.2 INTERACTION OF METHANE WITH STRONG LASER FIELDS

Methane is a molecule that is relevant to our society in many ways. As a greenhouse gas, it is an active contributor to the ongoing anthropogenic climate change [201] and as the main constituent of natural gas, it is an important source of energy increasing in relevance in the latest years [202]. Apart from these topics methane plays a role in extraterrestrial observations. It is a contributor to the atmosphere of Titan [203], the moon orbiting Saturn, and can also be found in the atmosphere of Mars [204]. Since large sources of methane on earth are organic processes, this hints at life or former life on these planets.
Looking at methane from the perspective of strong field light-matter interaction has several interesting aspects. Methane is a very simple organic molecule and a building block of larger hydrocarbons. Its chemical formula is CH_4, a carbon atom bound to four hydrogen atoms. The hydrogen atoms have a special arrangement in so far as they are the corners of a tetrahedron. This makes methane part of the T_d symmetry group [205]. The structure makes the dissociation of methane in strong fields much more complex when comparing it to molecular hydrogen. Whereas the shape of molecular hydrogen can be described by one parameter, which is the distance between the two atoms, methane is a three-dimensional molecule with five constituents and thus many more degrees of freedom.
As in the case of the dissociation of hydrogen, we will investigate the dissociation of methane at two different wavelengths. At 800 nm the interaction is relying more on tunneling and electron re-collision, while at 400 nm multi-photon ionization will be the primary ionization mechanism. For the investigation we will use time-of-flight (ToF) and velocity-map-imaging (VMI) photoion spectroscopy. The main new aspect uncovered in this study is the laser intensity dependent kinetic energy (KE) of the photofragments created in the strong field dissociation of methane and the influence of the two wavelengths on this.
In a publication by collaborators, L. Varvarezos et. al. [206], the differences in the ion yields of methane and its fragment ions in strong laser fields of 800 nm and 400 nm have been investigated. Here we revisit these findings and extend the study to the kinetic energy release of the ionic fragments. The experiment was repeated using similar experimental parameters, but this time by measuring the ion ToF spectra for a larger set of laser intensities. This increased resolution regarding the laser intensity enables a more detailed investigation of the intensity dependence of the dissociation process. By using atomic hydrogen ions from molecular hydrogen as a calibration for the KE of the atomic hydrogen ion fragments from methane, we were now able to use simulations to extend the calibration to any other fragments of methane, which allowed us to investigate the intensity dependence of the KE of all fragment ions.
In the following, we will investigate the intensity dependent yield to compare our results to previous studies. Then the intensity dependent kinetic energy of the fragment ions is characterized and investigated. After having done these investigations for both wavelengths, the results are compared. Additional studies using the VMI allowed us to investigate the angular distribution of the fragment ions, especially of the atomic and molecular hydrogen ion as well as the coincidences that appear in the dissociation.

8.2.1 *Dissociation and Fragment Kinetics of Methane at 800 nm*

At first, the dissociation of methane is investigated using a ToF spectrometer. The experimental setup is the same as in the case of the investigation of hydrogen. The laser beam passes through an attenuator and is focused into the interaction region by a toroidal focusing mirror. The attenuator consists of a motorized waveplate and a thin film polarizer. This allows us to investigate the dissociation and ionization of methane at many laser intensity settings. In the interaction region, the methane molecules are ionized and dissociated. The ions and charged fragments of methane are pushed onto the ToF MCP, where they are measured with an oscilloscope. As the particles have different mass-over-charge ratios, they hit the MCP at different times relative to the arrival time of the laser pulse in the interaction region. The resulting spectrum is shown in figure 37 a). The laser intensity of $7.5 \cdot 10^{14}\,\mathrm{W/cm^2}$, which is used to generate this spectrum, is one of the highest used in the experiment. The dissociation and ionization of methane create already many different fragments. Three groups of ions can be distinguished. The first group is visible between 3.2 µs and 4.2 µs. In this group, the peaks are the singly charged fragments of water H_2O^+ and OH^+, which are a result of the water background present even in the ultra-high vacuum. By measuring the background spectrum, it was made sure that the influence of the water dissociation does not significantly influence the spectrum of the hydrogen ions produced from methane. At lower times of flight, the next intense peak is the methane ion, CH_4^+. At further decreasing time-of-flights in this group the fragmented ions CH_3^+, CH_2^+, CH^+ and C^+ can be found. The second group between 2.2 µs and 3.0 µs consists of the doubly charged ions. Here we can find, from right to left, CH_4^{2+}, CH_2^{2+} and C^{2+}.
The last group is between 1.0 µs and 1.8 µs and shows the molecular hydrogen H_2^+ and hydrogen ions H^+. Knowing the mass-over-charge ratio and the respective time-of-flight allows one to convert the time-of-flight spectrum into a mass-over-charge spectrum.

The calibration used to transform the time-of-flight axis into a mass-over-charge axis is shown in figure 37 b). The points shown here are the pairs of a time-of-flight to the mass-over-charge ratio of the specific fragment. To interpolate the points in between a cubic function is used. This extends the simplistic approach given by the theory that the time-of-flight and the mass-over-charge should follow a quadratic relation [207]. However, it was found that a cubic function better interpolates the calibration points.
At the very low laser intensity ($1.5 \cdot 10^{14}\,\mathrm{W/cm^2}$) the lower mass spectrum shown in figure 38 is obtained, while the high laser intensity ($7.5 \cdot 10^{14}\,\mathrm{W/cm^2}$) produces the upper mass spectrum in figure 38. At the lower intensity only the methane ion (CH_4^+), the methyl ion (CH_3^+), the methylene ion (CH_2^+) and the atomic hydrogen ion (H^+) appear. The yield of these ions is much lower compared to their yield at $7.5 \cdot 10^{14}\,\mathrm{W/cm^2}$ and doesn't show any side structures, which is an indication of dissociation involving low kinetic energies. In contrast to that, the high-intensity spectrum shows broad features and additional peaks aside from the central ones.

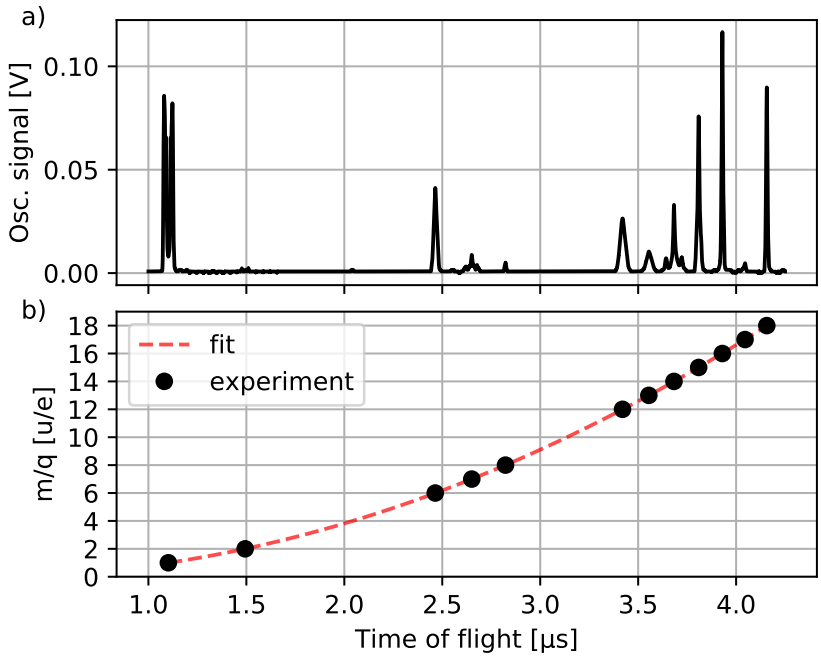

Figure 37: a) Time-of-flight spectrum of methane ionized and dissociated by 800 nm laser pulses at an intensity of $7.5 \cdot 10^{14}$ W/cm^2. b) ToF of certain fragments versus their mass-over-charge ratio. The red line is the fit that allows to transform the ToF axis into a mass-over-charge axis.

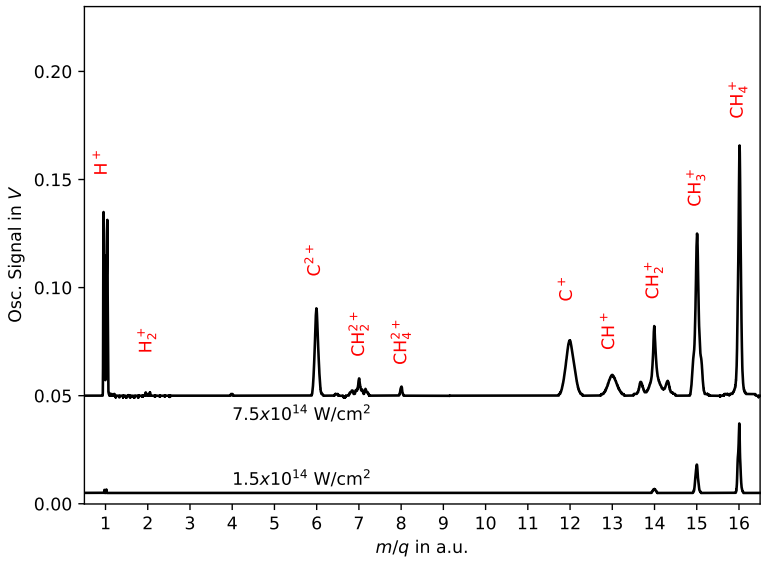

Figure 38: Mass spectrum of methane dissociated at a laser intensity of $1.5 \cdot 10^{14}$ W/cm^2 (lower curve) and $7.5 \cdot 10^{14}$ W/cm^2 (upper curve) at a central wavelength of the laser of 800 nm.

The yield of each ion is calculated by summing up the oscilloscope signal around the corresponding mass-over-charge ratio. The yield of all ions and the intensity dependence thereof is displayed in figure 39. The laser intensity is calibrated by determining the point where the methane ion yield stops increasing, which is where barrier suppression ionization sets in. For methane with an ionization potential of 12.61 eV this happens at a laser intensity of $3.75 \cdot 10^{14}\,\mathrm{W/cm^2}$ [208]. It is important to note that the yield of the ions shown here is above a certain already existing amount, which cannot be accounted for using the oscilloscope. This is due to the oscilloscope only being able to pick up on voltages, which are in the mV range and above. If the amount of particles hitting the MCP is not enough to generate a high enough voltage, they will not be detected by the oscilloscope.
At the lowest laser intensity of $7.5 \cdot 10^{13}\,\mathrm{W/cm^2}$ only two ions are apparent, which are the methane cation and the methyl ion. An ion is defined as apparent if the yield is above 10^{-2}. In a strong laser field, ionization can take place via multi-photon ionization, tunneling/barrier suppression ionization, or electron impact ionization through re-collision. With an ionization potential of 12.61 eV the absorption of nine photons at 1.55 eV is necessary to ionize methane, not including the ponderomotive shift. To quantify which ionization mechanism dominates at which wavelength and laser intensity, the Keldysh parameter is used. The Keldysh parameter γ is a measure of the ratio between the time the electron needs to tunnel out of the binding potential and the oscillation period of the electric field. If γ is small compared to one, the ionization mechanism is dominated by tunneling. If γ is large compared to one, multi-photon ionization dominates. In our case the Keldysh parameter is $\gamma \approx 1.2$, which is in a mixed regime between tunneling and multi-photon ionization. With increasing laser intensity this will shift towards tunneling, as stronger electric fields suppress the binding potential more and more, which decreases the time the electron needs to tunnel through the potential barrier, by decreasing the spatial width of the barrier. As the methane molecule is ionized and left behind in highly excited states, the methane ion dissociates, which can be seen in the abundance of the methyl ion. The dissociation channel responsible for the generation of the methyl ion is

$$\mathrm{CH_4^+} \rightarrow \mathrm{CH_3^+} + \mathrm{H}. \tag{42}$$

The excitation energy required to lead to a certain dissociation pathway can be retraced from Samson et al. [209], which investigates the fragmentation of methane and its dependence on the photon energy in single-photon excitation. While for the ionization of methane a photon energy of 12.61 eV is needed, the methyl ion appears at a photon energy of 14.1 eV. To reach this energy in a multi-photon process, a total number of ten photons is required compared to nine photons necessary to ionize methane. The formation of the methyl ion results from a higher non-linear process compared to the ionization of methane and thus the yield of the methane ion is higher than that of the methyl ion.
Until this point, the discussion relied on the multi-photon aspect of the interaction. But as we are in a mixed regime of multi-photon ionization and tunneling, the electric field of the light also needs to be considered. This aspect has been taken into account by Wang et. al. who propose the field-assisted dissociation (FAD)

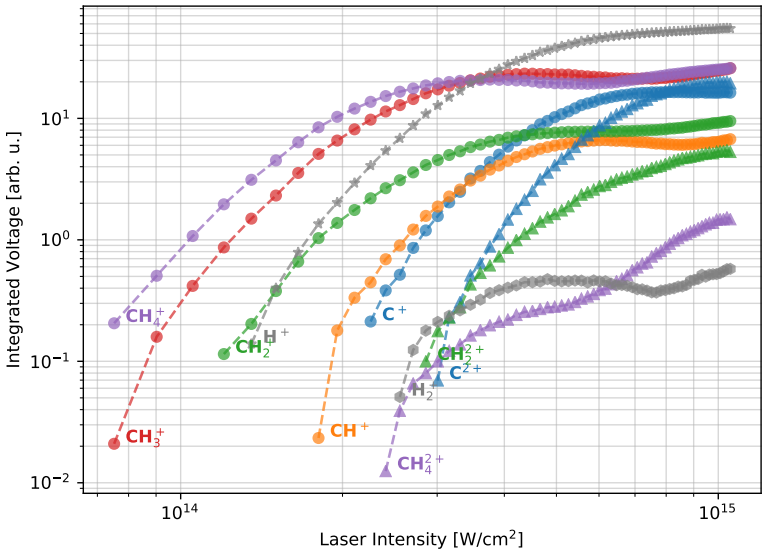

Figure 39: The yield of ions from the ionization and dissociation of methane versus the laser intensity on a double logarithmic scale at a laser wavelength of 800 nm.

model [210]. In this model dressed PESs are generated by adding an electric field to the PES calculation. The result of this is that the favoured dissociation channel should be $CH_4^+ \rightarrow CH_3 + H^+$. Here we observe the opposite. Methyl ions appear before hydrogen ions appear, which indicates that the dissociation into a methyl ion and a hydrogen atom is favoured. This discrepancy could be due to the longer pulse length of 160 fs used in the FAD model, compared to the 35 fs we used in our experiment.

Interestingly the intensity at which the hydrogen ion appears is also similar to the intensity of $1.2 \cdot 10^{14}\,\mathrm{W/cm^2}$ at which the methylene ion (CH_2^+) appears. In the single-photon dissociation [209] this is at a photon energy of 15.2 eV, while the hydrogen ion appears at a much higher photon energy of 22.1 eV. This difference is due to the possibility of further ionizing and exciting fragments from the methane dissociation when using intense laser pulses. With single photons, the whole dissociation is defined by the state of the methane molecule after absorbing a single photon. The intense laser field of optical frequency leads to dressed potential energy surfaces, enhanced ionization and can additionally also excite the methane molecule and its fragments to highly excited states.
The aspect of pulse duration was investigated in a study by Wu et al. where methane was dissociated by intense laser pulses with different pulse lengths of 8 fs, 30 fs (both $0.9 \cdot 10^{13}\,\mathrm{W/cm^2}$) and 110 fs ($1.4 \cdot 10^{14}\,\mathrm{W/cm^2}$) at similar laser intensities [211]. They found that at 110 fs all fragments and ions, that we also observe, appeared. At 30 fs only the singly charged fragments, apart from H_2^+, appear, while at 8 fs only the methane and the methyl ions remain.
Determining which dissociation channel leads to the formation of the methylene ion, is not as simple since there are multiple channels:

$$CH_3^+ \rightarrow CH_2^+ + H \quad (43)$$
$$CH_4^+ \rightarrow CH_2^+ + H_2 \quad (44)$$
$$CH_4^+ \rightarrow CH_2^+ + H + H. \quad (45)$$

Fluorescence studies of the strong field dissociation of methane show clear signs of neutral fragments in excited states like CH and H [212] at a laser intensity of $2.0 \cdot 10^{14}\,W/cm^2$.
The channels for the production of hydrogen ions at a laser intensity of $1.4 \cdot 10^{14}\,W/cm^2$ could be:

$$CH_4^+ \rightarrow CH_3 + H^+ \quad (46)$$
$$CH_3^+ \rightarrow CH_2 + H^+ \quad (47)$$

From the appearance of the hydrogen ion at a similar laser intensity as the methylene ion one could argue in favour of the second channel, as the appearance of the methyl ion might enable the appearance of the hydrogen ion.
As the laser intensity increases to $1.8 \cdot 10^{14}\,W/cm^2$ the methylidyne ion (CH^+) appears. In the single-photon case, it appeared at a photon energy of 22.4 eV, showing the necessity for higher excitation of the methane molecule to dissociate this far. Mechanisms that lead to this fragment could be a higher excitation of the methane ion, or a second excitation and ionization of a fragment, which then fragments again due to an additional interaction with the laser field.
At a laser intensity of $2.3 \cdot 10^{14}\,W/cm^2$ the methane molecule is completely disintegrated as only the carbon ion remains. The single-photon studies in [209] support this, where a photon energy of 25.0 eV was required to generate carbon ions. Mechanisms to get to this fragment could be a step-wise dissociation from CH^+.
By increasing the laser intensity further, a new regime is entered, which is marked by the appearance of doubly charged ions and fragment ions. The methane di-cation appears at a laser intensity of $2.4 \cdot 10^{14}\,W/cm^2$. Another very similar study to this using 50 fs laser pulses finds the methane di-cation at a higher laser intensity of $3.6 \cdot 10^{14}\,W/cm^2$ [24]. Simulations using ORCA show that to ionize the methane ion an energy of 20 eV is necessary. Ionizing methane twice by one photon requires a photon energy of at least 35 eV [213]. A possible mechanism to achieve this energy in a multi-photon process is ionization via electron re-collision. In this scenario, the electron originating from the ionization of methane is accelerated in the laser field and re-collides with the ion, leading to a second ionization. The ponderomotive potential of 21.5 eV would be sufficient for this.
Surprisingly, molecular hydrogen (H_2^+) is created in the strong field dissociation of methane at an intensity of $2.6 \cdot 10^{14}\,W/cm^2$. Apparently, chemical bonds are not only broken during the interaction of methane with an intense laser pulse but also new bonds can be formed. The appearance of the methane di-cation and the molecular hydrogen ion at similar laser intensities shows that one precursor to the molecular hydrogen is the methane di-cation.

$$CH_4^{2+} \rightarrow CH_2^+ + H_2^+ \quad (48)$$
$$CH_3^{2+} \rightarrow CH^+ + H_2^+ \quad (49)$$

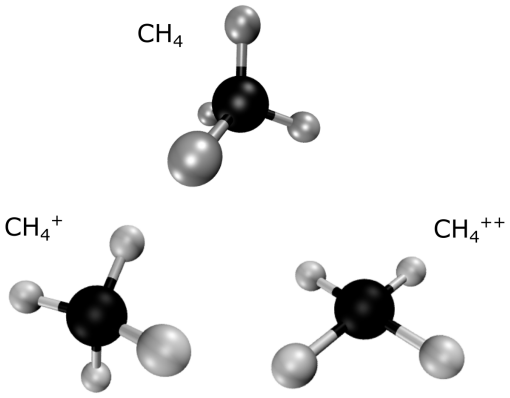

Figure 40: Geometry of methane, the methane ion and the methane di-cation calculated using ORCA [141].

A reason for this might be related to changes in the geometry of methane as it is ionized. While methane has a tetrahedral symmetry, the di-cation is a planar molecule with an angle of 90° between adjacent hydrogen atoms. This flattening of the molecule as it is ionized is depicted in figure 40 and the angles between the hydrogen atoms and bond lengths to the carbon center are given in table 3.
A similar structural change in different stages of ionization can also be observed for the methyl molecule. While methyl is already planar and stays planar, the angle between a pair of the two hydrogen atoms becomes more narrow in the di-cation form. It changes from 120° in the neutral methyl to 80° for the di-cation. Also the bond lengths of these two hydrogen atoms increases. The changes in geometry are shown in figure 94 (see appendix) while the values for the geometry are in the same table already mentioned 3. With respect to the formation of H_2^+, one can exclude the methylene di-cation as a precursor to molecular hydrogen, as the geometry is linear. The carbon atom is in between two hydrogen atoms, which oppose each other, as is shown in figure 95 (see appendix). All the geometries are calculated with ORCA [141].
Other doubly charged ions also appear like the methylene di-cation (CH_2^{2+}) at $2.9 \cdot 10^{14}\,W/cm^2$ and the doubly charged carbon ion (C^{2+}) at $3.0 \cdot 10^{14}\,W/cm^2$.
It is interesting that some doubly charged ions do not appear, like the methyl di-cation (CH_3^{2+}). This is due to the methyl di-cation having a very low dissociation energy of 30 meV when stretching one C-H bond, which is an amount of energy that can already easily be overcome by vibrational excitation [211]. The methylidyne di-cation (CH^{2+}) has a similar dissociation energy of 40 meV, making it similarly unstable.
A tiny peak that appears at a laser intensity of $5.1 \cdot 10^{14}\,W/cm^2$, appears at $m/q = 4$. It could be linked to the triply charged carbon ion (C^{3+}).

After the general overview, the intensity dependent yield of the ions and fragments is discussed (see figure 39). Increasing the laser intensity from the lowest intensity used in the experiment leads to an exponential increase in the yield of the methane and methyl ion, which is expected as the ionization mechanism is non-linear. The yield of these two ions increases, until the barrier suppression intensity of methane is reached ($2 \cdot 10^{14}\,W/cm^2$ in our experiment) and on the way

Ion	Appearance intensity [W/cm^2]
CH_4^+	$7.5 \cdot 10^{13}$
CH_3^+	$7.5 \cdot 10^{13}$
CH_2^+	$1.2 \cdot 10^{14}$
CH^+	$1.8 \cdot 10^{14}$
C^+	$2.3 \cdot 10^{14}$
CH_4^{2+}	$2.4 \cdot 10^{14}$
CH_2^{2+}	$2.9 \cdot 10^{14}$
C^{2+}	$3.0 \cdot 10^{14}$
C^{3+}	$5.1 \cdot 10^{14}$
H_2^+	$2.6 \cdot 10^{14}$
H^+	$1.4 \cdot 10^{14}$

Table 2: Appearance intensities of various ions produced in the dissociation of methane in intense, 800 nm, laser pulses.

different fragments start to appear. Above this intensity the yield of the methane and methyl ion is similar and they follow similar trends. That the yield of these two ions partly decreases at some point can be explained by the increasing probability to dissociate the parent molecule into smaller and smaller fragments. At some point the yield will reach a steady-state, apart from the carbon ion, and the yield will rise according to the volume-integration effect. A study by Strohaber et al. also investigated the yield depending on the laser intensity and they get similar results to ours [24].

The hydrogen ions show a strong increase with laser intensity hinting at a highly non-linear process involved in the generation. Additionally, the hydrogen ions yield is affected by the fact that in principle every methane molecule can lead to the formation of four hydrogen ions. This is also the reason why the hydrogen ion is the most abundant ion at laser intensity greater than $3.5 \cdot 10^{14}\,W/cm^2$. The methylene ion yield always stays below the yield of the methane and the methyl ion. The methylidyne ion is similar as it stays below the yield of all the other precursor fragments.

In sharp contrast to this is the yield of the carbon ion, which is starting below all precursor fragments at its appearance intensity but then rises above the yield of the methylidyne and methylene ion at a laser intensity of $4.3 \cdot 10^{14}\,W/cm^2$. A reason for this is that the carbon ion is the final element of the dissociation chain. While all previous fragments can still lose a hydrogen atom, the carbon ion cannot dissociate any further. This effect is carried on by the doubly charged carbon ion, which surpasses the carbon ion yield at a laser intensity of $8.2 \cdot 10^{14}\,W/cm^2$. When looking at the methylene di-cation the yield only increases further from the appearance intensity, as does the yield of the methane di-cation. The yield of the methylene di-cation above its appearance intensity is greater than the yield of the methane di-cation up to the highest available laser intensity, showing that the methylene di-cation is more stable than the methane di-cation.

Ion	Symmetry	C-H_i Bond lengths [Å]	$\angle H_iCH_j$ [°]
CH_4	T_d	1.09	109.5
CH_4^+	C_{2v}	1.13	96.4 (1,2), 141.1 (1,3)
CH_4^{2+}	D_{4h}	1.19	90.0
CH_3	D_{3h}	1.09	120.0
CH_3^+	D_{3h}	1.11	120.0
CH_3^{2+}	C_S	1.11 (1), 1.30 (2, 3)	80.0 (2,3), 140.0 (1,2)(1,3)
CH_2	C_{2v}	1.12	100.3
CH_2^+	C_{2v}	1.11	141.5
CH_2^{2+}	$D_{\infty h}$	1.20	180.0
CH	$C_{\infty v}$	1.14	180.0
CH^+	$C_{\infty v}$	1.15	180.0

Table 3: Ground state geometry, bond lengths and angles of various fragments and ions created in the dissociation of methane in an intense laser field. The numbering refers to certain hydrogen atoms. If no number is given, the bond length or angle between the closest hydrogen atoms is the same. The symmetries are: T_d (tetrahedral), C_{2v} (see-saw), C_S (mirror plane), $C_{\infty v}$ (linear), D_{3h} (trigonal planar), D_{4h} (square planar), $D_{\infty h}$ (linear with center of inversion).

In conclusion, it was observed that with increasing laser intensity the methane molecule could be dissociated further until only the carbon ion was left. The appearance intensity of the hydrogen ion was comparable to the appearance of the methylene ion, underlining that, in comparison to single-photon dissociation, the laser field enhances dissociation into hydrogen ions. At a higher laser intensity, the doubly charged fragments start to appear. In the same intensity region a new chemical compound, the molecular hydrogen ion, is formed. At even higher laser intensities a small peak started to appear at a mass-over-charge ratio of four, which hints at the triply charged carbon ion. A more detailed view of the dissociation channels and ionization steps is presented in the upcoming section showing investigations of the kinetic energy of the fragment ions.

If a molecule is placed in an intense laser field that is strong enough to initiate dissociation, the molecule will fragment. The fragments of the molecule will move away from each other with a certain velocity and direction according to momentum and energy conservation. The velocity of the fragments is determined by the energy released during the dissociation, which is also called the kinetic energy release (KER). In the experiment, the kinetic energy (KE) of a fragment is measured. If a lot of energy is released, the fragments will have high velocities. Typically the Coulomb-explosion channels, where a molecule breaks up into charged fragments lead to more energetic fragments compared to the dissociation into one charged and one neutral fragment.
The kinetic energy of the fragments can be determined from the ToF spectrum by measuring the width of the main peak, or the position of the side-peaks of

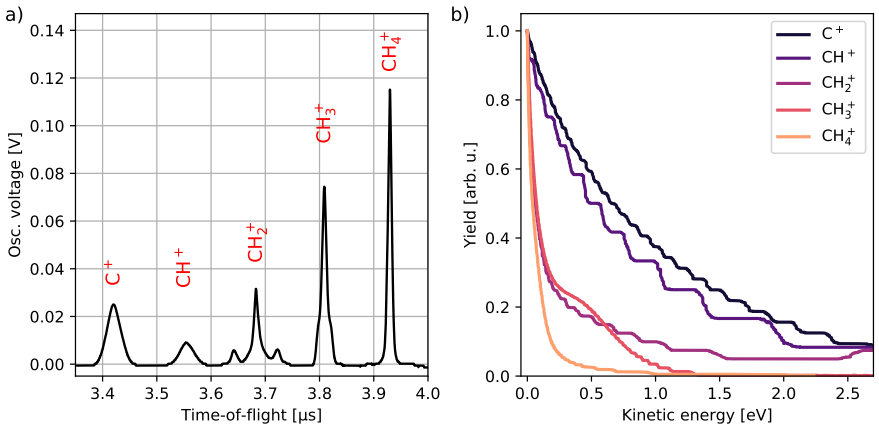

Figure 41: a) ToF spectrum of the methane ion and carbon-containing fragment ions of methane. From left to right the fragments are ions of the following: carbon, methylidyne, methylene, methyl and methane. The laser intensity is $7.5 \cdot 10^{14}$ W/cm^2 and the wavelength 800 nm. b) KE distribution of the methane ion and singly charged carbon-containing fragment ions at a laser intensity of $10.5 \cdot 10^{14}$ W/cm^2 and a wavelength of 800 nm.

the fragment signal. In the extreme case, one fragment will fly directly into the entrance of the ToF, while the other fragment has to fly in the other direction, due to momentum conservation. The fragment flying into the ToF will have a shorter time-of-flight compared to an ion initially at rest. The inverse relation holds true for the fragment flying away from the ToF. Its time-of-flight is longer, as it has to be decelerated before being accelerated back by the electric fields of the ToFs ion optics. Of course, the fragments can also fly apart the other way around, leading to the fragments having peaks with symmetric features. Depending on the KE, one might see just a central peak, a shoulder to the central fragment peak, or even a peak to each side of the central fragment peak, if the KE is high enough. Looking at the ToF spectrum at an intensity of $7.5 \cdot 10^{14}$ W/cm^2 in figure 41 a), the above mentioned distributions can be assigned to the yield of methane and the carbonic fragments. From left to right the ions are the carbon ion, the methylidyne ion, the methylene ion, the methyl ion and the methane ion. Compared to all other carbon-containing fragment ions, the peak of the methane ion is high and narrow. No features should appear, as there is only the comparatively weak recoil from the ionization. This will be used later, as it enables us to estimate the KE resolution of our set-up, at least at the mass of and around the methane ion. Shoulders are observed in the methyl ion distribution, while the methylene yield has shoulders and additionally peaks outside of the central distribution, hinting at an energetic dissociation. The methylidyne distribution is just broad, as is the carbon ion distribution, showing the accumulated KE during the dissociation of methane.

To quantify the KE that is released in certain channels, a relation between the time-of-flight of a certain fragment and its KE needs to be established. For this, a ToF spectrum of hydrogen ions formed in the dissociation of methane was measured and then, without changing the settings of the experiment, the ToF

spectrum of hydrogen ions formed in the dissociation of molecular hydrogen was measured. The result of this is shown in figure 42 a). Using the fact that the KE spectrum of the dissociation of molecular hydrogen is well known (CREI channel center at roughly 2.9 eV KE [195]), we overlap the KE spectra and assign kinetic energies to the peaks of hydrogen ions formed in the methane dissociation, which is shown in figure 42 b). Assuming a quadratic dependence of the KE on the ToF differences provides the relation between the ToF difference and the KE. With this a KE of 5.4 eV for the most prominent hydrogen ion channel in the dissociation of methane is found. The KE calibration for all other ions is obtained by adjusting the distance between the origin of the ions and the detector in a SIMION [214] simulation of the ToF setup to match the observations for the hydrogen ions in the experiment. Then the dependence of the ToF of the other ions on the kinetic energy is simulated. The results of this are parabolas (Fig. 42 c), which allow to calibrate the KE for all other fragments. It should be noted that the KE axis is non-linear in ion KE spectra derived from ToF measurements. The distance between KE points increases with increasing KE. This leads to features at higher KEs having an increased signal compared to features at lower KEs, which is a welcome side effect as it enhances their visibility. The derived yield is not affected by this since it is determined via the ToF spectrum. The kinetic energies of the features are not affected by this, since the ion KE was calibrated using also a non-linear ion KE spectrum of the atomic hydrogen ion fragments from the dissociation of molecular hydrogen. This is also true for the ToF studies using 800 nm pulses.

First we investigate how the KE distribution progresses through the dissociation of the singly charged carbon-containing fragment ions at a fixed laser intensity. A straight-forward assumption about the change of the fragment's KE distribution with further dissociation is that the distribution gets broader, as more hydrogen atoms are dissociated since with every dissociation some recoil momentum will be added. On the other hand, the carbon ion should have a quite narrow KE distribution compared to other fragments because if all hydrogen atoms are dissociated at a similar KE energy while keeping the symmetry of the initial methane molecule, the momentum should add up to a small amount in the end. Figure 41 b) shows the KE distribution of the methane ion and all the singly charged carbon-containing fragment ions at a laser intensity of $10.5 \cdot 10^{14}\,\mathrm{W/cm^2}$. To allow for a better comparison of the KE distibutions, the yield of the fragment ions is normalized to one and only the central peak of the KE distribution is compared. The high KE dissociation channels visible in the methylene ion are omitted for now. As can be seen, the KE distribution only gets broader with each hydrogen atom dissociated. Considering the methane ion peak we can conclude that our resolution in KE at the mass-over-charge ratio of 16 is around 0.1 eV FWHM.
When looking at the differences in KE between the methane ion and the methyl ion, two distinct features can be noticed. The one that stands out is the prominent shoulder centered roughly around 0.3 eV KE, which originates from the coulomb-explosion of the methane di-cation. The other feature is visible as a contribution at low KE and appears as a thin stripe next to the central methane ion peak. This contribution to the KE has to originate from a less energetic process and could be

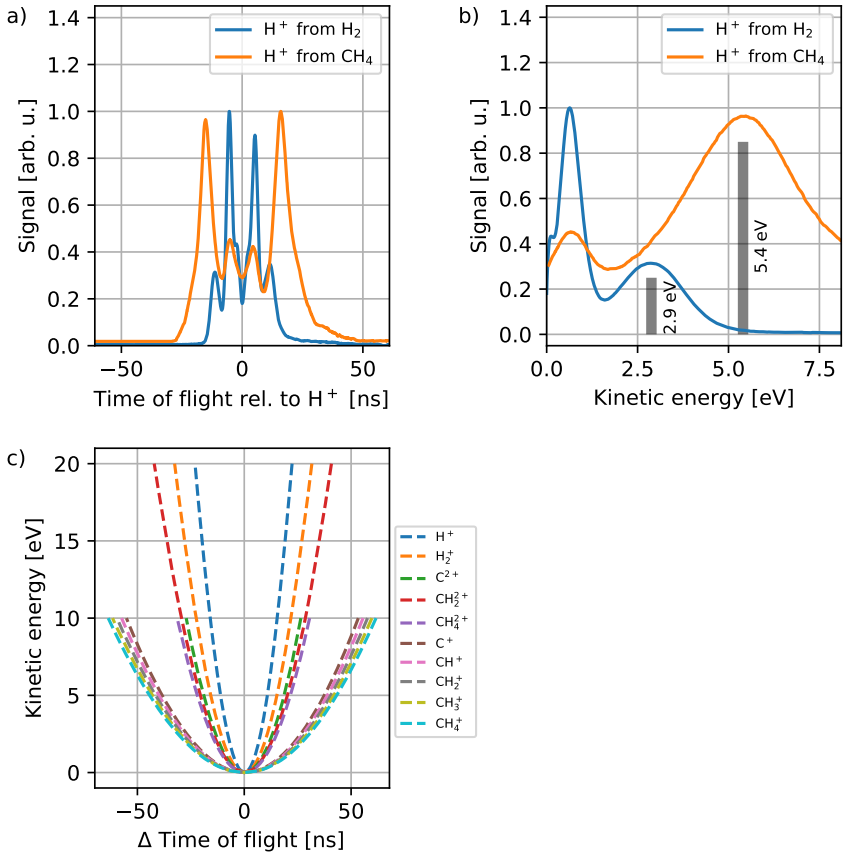

Figure 42: a) Time-of-flight spectra of hydrogen ions from the dissociation of molecular hydrogen and methane. The time-of-flight is shown relative to the center of the distribution. b) KE spectra of hydrogen ions from the dissociation of molecular hydrogen and methane. c) Dependence of the KE on the time-of-flight for various fragments calculated with SIMION.

linked to the dissociation of the methane ion into the methyl ion and a hydrogen atom.

Moving on in the fragmentation chain, the next ion is the methylene ion, which already lost two hydrogen atoms in the dissociation process. Looking at the central part of the methylene ion peak, one can see that it is as broad as the peak of the methyl ion, meaning that there is no noticeable KE pick-up by dissociating a second hydrogen atom. Reasons for this could be a low KE in this dissociation channel or that the momenta of two dissociations don't add. Looking at the shoulder region of the KE spectra, the width of the methylene ions KE distribution is broader compared to the methyl ions KE distribution. One possible dissociation channel, which leads to higher KERs, is the dissociation of the methane di-cation into a molecular hydrogen fragment and the methylene ion.

Continuing the fragmentation path, we can see that the methylidyne ion peak is rather homogenous compared to the other fragments. One can not really observe a shoulder to the central peak or any other significant structure. The same can be seen for the carbon ion. What makes these distributions look so broad is that there are fewer carbon or methylidyne ions, which have a small KE. Most of these

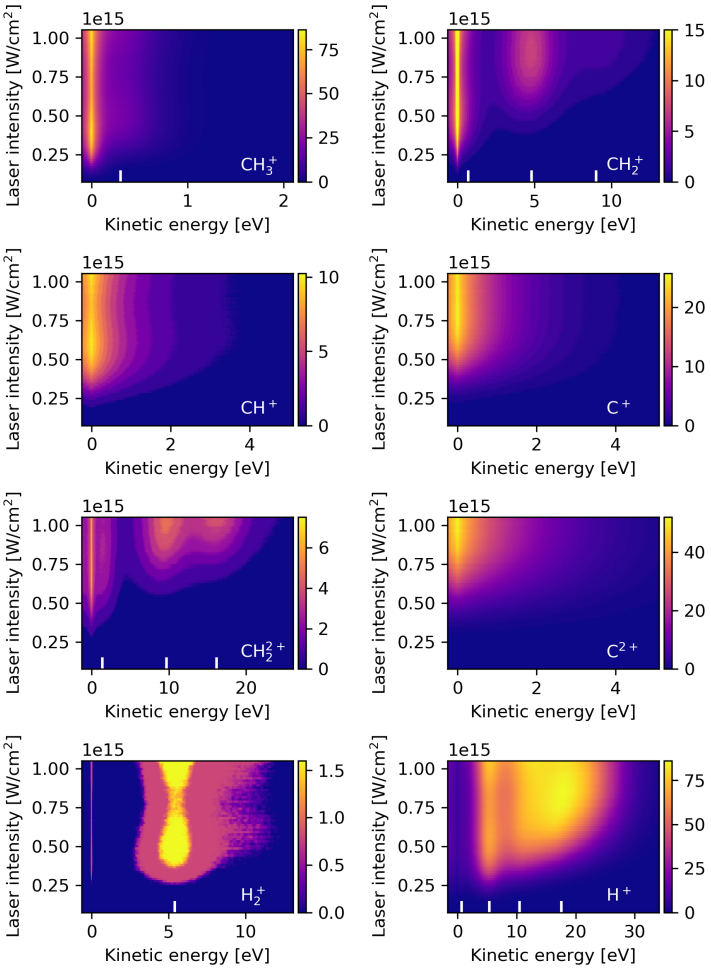

Figure 43: Intensity dependent KE distribution of the ion fragments created in the dissociation of methane in strong laser fields with a central wavelength of 800 nm. From top to right and top to bottom the mass-over-charge ratio decreases. The white text in the intensity dependent KER distribution indicates which fragment is shown. The little white bars indicate the central kinetic energy of certain fragmentation channels.

fragments have picked up KE while following the dissociation channels and only few end up with small KE values. With three to four hydrogen atoms leaving the central carbon atom, all having different KEs and momenta, there will be no significant structure left within the peaks. The broadening of the KE distribution of the methylidyne ion is a consequence of further dissociation. Interestingly the carbon ions KE distribution is nearly identical compared to the methylidyne ions KE distribution, showing that little momentum is gained in the final dissociation step.

Looking at the intensity dependence of the KE, we will identify channels with certain KE, determine the appearance intensity of these channels and try to match KE channels by using momentum and energy conservation.

The shoulder previously visible in the methyl ions KE distribution does not appear at low laser intensities. This can be seen in figure 43, in the top left subplot.

The dissociation channel at 0.3 eV in the methyl ion distribution appears at a laser intensity of $2.0 \cdot 10^{14}$ W/cm^2 and does not change with further increasing laser intensity. That there is no change in the KE distribution as the intensity is increased further is quite interesting, as there are other fragments that show a very different dependency on the laser intensity. By increasing the laser intensity further, excited states and levels of ionization of the methane molecule can be achieved. That there are no additional KE channels appearing for the methyl ion indicates that any excitation of methane above the doubly charged excited state, which leads to the formation of the methyl ion and the hydrogen ion, will lead to dissociation channels, which dissociate further than the methyl ion. This might be due to the methyl ion being generated in higher excited states, which are unstable and dissociate further.

Indications for this can be seen by looking at the intensity dependent KE distribution of the methylene ion in figure 43, in the top right subplot. The part of the distribution, which has higher KE than the methyl ion is centered at around 0.7 eV and appears at a laser intensity of $2.5 \cdot 10^{14}$ W/cm^2. This is the result of the dissociation of doubly charged methane into the methylene ion and a molecular hydrogen ion, which will be discussed in more detail when the KE distribution of the molecular hydrogen ion is discussed. As the laser intensity increases further to about $4.0 \cdot 10^{14}$ W/cm^2 another dissociation channel appears at 4.4 eV KE. The opening of this dissociation channel is a sign of an additional ionization step following the double ionization of methane. Indicative of this is the high difference in KE to the dissociation channel at 0.7 eV, which is connected to the dissociation of doubly charged methane. Signs of the appearance of the triply charged carbon ion at a laser intensity of $5.1 \cdot 10^{14}$ W/cm^2 supports this hypothesis. Another interesting feature of this dissociation channel is a slight change in the center of KE with increasing laser intensity. From the appearance intensity to a laser intensity of $9.0 \cdot 10^{14}$ W/cm^2 the central KE of the channel shifts to 4.8 eV, which is a difference of 0.4 eV of the central KE. Such a shift could be explained by an ionization, which happens as the molecule is already undergoing dissociation. The higher the laser intensity, the earlier during the dissociation process the molecule can be ionized again, leading to more energetic fragments. Another quite weak dissociation channel appears at a higher laser intensity of $6.3 \cdot 10^{14}$ W/cm^2 with a KE of 9.0 eV, requiring even higher excitation or ionization of the precursor molecule.

Next along the dissociation chain is the methylidyne ion, with its intensity dependent KE distribution shown in figure 43, the subplot in the second row on the left. As we have already seen in the discussion about the carbon-containing fragment ions, the KE distribution of the methylidyne ion only consists of one peak. With increasing laser intensity the peak shape does not change a lot, once the whole signal is above the detection threshold of our set-up. The same holds for the intensity dependent KE of the carbon ion, shown in figure 43, in the subplot in the second row on the right. Quite interesting is that neither the methylidyne ion nor the carbon ion show high KE features, which one would expect if the high KE (4.8 eV) methylene fragment ion would dissociate further. But this is apparently not the case.

The next fragment with notable KE is the methylene di-cation. Its intensity dependent KE distribution is displayed in figure 43, in the left subplot of the third row. Similar to the methylene ion there is a central, lower KE, structure and at higher laser intensities, new high KE channels appear, which are well separated from the central feature. The shoulder to the central channel is at a KE of 1.4 eV and appears at a laser intensity of $3.7 \cdot 10^{14}\,\mathrm{W/cm^2}$. The next channel appears at a KE of 9.0 eV at $5.5 \cdot 10^{14}\,\mathrm{W/cm^2}$ and exhibits a shift to higher KE. At the highest laser intensity of $10.5 \cdot 10^{14}\,\mathrm{W/cm^2}$ the KE is centered at 9.7 eV. Such a shift of the KE center of a dissociation channel could be explained by another ionization step during the ongoing dissociation of the molecule, as mentioned before. This was already observed in the coulomb-explosion of hydrogen and can also be seen for example in the coulomb-explosion of nitrogen [159] and is predicted by calculations [215]. The similarity of the KE channels of the methylene ion and the di-cation shows that the additional ionization step might happen in the dissociation that leads to the methylene ion. From the two pairs of KE and intensity a slope of $0.14\,\mathrm{eV}/(10^{14}\,\mathrm{W/cm^2})$ can be calculated. The more energetic dissociation channel shows a similar behaviour. It appears at a KE of 15.4 eV at $6.3 \cdot 10^{14}\,\mathrm{W/cm^2}$ and is centered at a KE of 16.2 eV at $10.5 \cdot 10^{14}\,\mathrm{W/cm^2}$. This gives a slope of $0.19\,\mathrm{eV}/(10^{14}\,\mathrm{W/cm^2})$.
The KE distribution of the doubly charged carbon ion is shown in figure 43, in the right subplot of the third row. It is similar to the KE of the singly charged carbon ion. The fragment starts to appear at a higher laser intensity, but the peak shape and evolution through the increasing laser intensity are quite similar. This means that the main and only feature of the KE distribution is a central peak with a width similar to the carbon ions KE distribution width. Again no features with KEs higher than the central peak appear, showing that high-KE fragments from the methylene di-cation are not dissociating further.

The next fragment, the molecular hydrogen ion is special, as it is a newly formed chemical compound. The appearance is no surprise though, as this has already been observed in other studies [216, 217], and in experiments with other organic molecules like methanol [23]. In the strong field dissociation of acetone, even H_3^+ could be observed [218]. The formation of new hydrogen species is not something exclusive to methane, but rather a common feature in the dissociation of organic molecules in strong laser fields. The intensity dependence of the KE distribution is shown in figure 43, in the left subplot of the bottom row. The molecular hydrogens KE distribution has two features. One is the low KE part in the center, which appears at a laser intensity of $2.7 \cdot 10^{14}\,\mathrm{W/cm^2}$. The other is a channel appearing at a similar laser intensity of $2.5 \cdot 10^{14}\,\mathrm{W/cm^2}$ with a broad KE distribution centered around 5.4 eV, reaching from 2.9 eV up to 11.5 eV. This distribution looks quite edgy, as it is at the voltage limit of what the oscilloscope is able to digitize. It is known that one of the origins of the molecular hydrogen ion is the doubly charged methane molecule, which will dissociate into the methylene ion and the molecular hydrogen ion [219]. The channel with a very low kinetic energy can be attributed to a dissociation of a singly charged precursor molecule into a neutral carbon-containing fragment and the charged molecular hydrogen ion. With increasing laser intensity the KE distribution of molecular hydrogen

does not show any new features, indicating that molecular hydrogen is produced only via a set of specific excited states of the methane di-cation. A publication from Dujardin et. al. using the PIPICO and a single photon to generate the doubly ionized methane method found a value of 5.2 eV for the total KER, which corresponds to a KE of 4.6 eV of the molecular hydrogen ion [213]. In the publication of Strohaber et. al. a KE of 18.9 eV was found, using the same approach to ionize, dissociate and detect ions, as we use in our experiment [24]. Apparently, there still is some uncertainty in what the exact KE value of this dissociation channel is. Our experiment would support the KE found by Dujardin. The decrease in the yield of the high KE channel seen at a laser intensity of around $8.0 \cdot 10^{14}\,\mathrm{W/cm^2}$ appears not only here, but can also be seen in the methyl, methylene (central part) and methylidyne ions KE distribution, while at the same laser intensities other structures start to appear, like the dissociation channel of the methylene ion between 4.4 eV and 4.8 eV. Other fragments like the carbon ion, hydrogen ion and carbon di-cation also show a slight increase in signal around this laser intensity. Apparently, there is a laser intensity region, where fragmentation along the carbon-containing fragments and double ionization is enhanced.

Finally, we investigate the lightest fragment, the hydrogen ion. As it is what mostly dissociates from methane, with the molecular hydrogen being the only exception, it contains a lot of information about the kinetics of the dissociation. The intensity dependence of the KE distribution of the hydrogen ions is shown in figure 43, in the right subplot of the bottom row. The KE of the hydrogen ion fragments is the highest of all the fragments and covers an energy range from 0 eV to 35 eV. That such high KEs appear can be expected after having seen the high KE in the case of the methylene di-cation.

The lowest KE channel visible is defined as channel 1, which can be identified as a thin line appearing from a laser intensity of $1.6 \cdot 10^{14}\,\mathrm{W/cm^2}$ on and which is centered at a KE of 0.7 eV. The yield and KE of this channel do not change with increasing the laser intensity. The next highest dissociation channel, channel 2, is energetically broader and centered around a KE of 5.4 eV. The channel even appears a bit earlier than channel 1 at a laser intensity of $1.4 \cdot 10^{14}\,\mathrm{W/cm^2}$. The origin of this channel can be connected to the dissociation of the methane di-cation into a methyl ion and a hydrogen ion. Following energy and momentum conservation for this dissociation channel, the KE of the methyl ion should be at 0.36 eV, which is close to the shoulder around 0.3 eV in the methyl ions spectrum. Another argument supporting this is that the yield of this channel stays quite constant over the whole laser intensity range, apart from the decrease around a laser intensity of $8.0 \cdot 10^{14}\,\mathrm{W/cm^2}$, which can also be seen in the methyl ions KE spectrum. The next dissociation channels are a bit more difficult to identify, as they show a great broadening and overlap. The next channel, channel 3, appears at a laser intensity of $1.9 \cdot 10^{14}\,\mathrm{W/cm^2}$ and a KE of 10.5 eV. This channel is energetically a bit broader than channel two and shows a slight shift of the maximum of the KE distribution to 13.0 eV at the highest available laser intensity. This corresponds to a slope of $0.29\,\mathrm{eV}/(10^{14}\,\mathrm{W/cm^2})$, assuming a linear shift. The appearance of the next channel, channel 4, can be identified as the shoulder to channel 3, which arises as the laser intensity increases further above the appearance intensity of channel 3. This shoulder starts appearing at a laser intensity of $2.7 \cdot 10^{14}\,\mathrm{W/cm^2}$

at a KE of 17.6 eV. This channel also shows an increase in the KE with increasing laser intensity. At a laser intensity of $10.5 \cdot 10^{14}\,\mathrm{W/cm^2}$ the center of the KE has shifted to 20.0 eV, which gives a slope of $0.32\,\mathrm{eV}/(10^{14}\,\mathrm{W/cm^2})$. Above this laser intensity, the center of this channel's KE distribution does not increase in energy any further.
A study using core-ionization from Williams et. al. finds a maximum in the KE around 5.9 eV for the hydrogen ion [220]. A similar KE of 5.0 eV is predicted by Dujardin et. al. [213]. The KE of 5.4 eV, that we observe, is well in the range of other published findings of the KE of this specific dissociation channel.

The results of the appearance intensity of the dissociation channels, their KE and shift with laser intensity are summarized in table 4. In conclusion, we saw that the dissociation happens along a step-wise process when looking at the yield of the central KE peaks of the ion fragments. While it was still possible for methyl and methylene to distinguish different KE channels as shoulders to the central distribution, this was not possible anymore for the KE distribution of the methylidyne and the carbon ion, which show a significant broadening due to the momentum picked up in the dissociation. With increasing laser intensity double and even triple ionization become available, which could be seen in the appearance of high KE channels in the intensity dependent KE spectra of the methylene ion and di-cation, as well as in the spectrum of the hydrogen ion. Some of these high KE channels show an increase in KE with increasing laser intensity, which was attributed to an ionization step happening as the molecule is undergoing dissociation. This was observed for the triple ionization and there are also hints for a fourth ionization step. Interestingly these high KE channels don't seem to appear as side lobes of any lighter carbon-containing fragments than the methylene ion and di-cation, which indicates that the fragments from these high KE channels don't dissociate further. With the molecular hydrogen ion, a new chemical compound was formed in the strong field dissociation of methane. Overall the hydrogen ions carry the most information about the dissociation, but this information is not easy to extract, due to the strong broadening in kinetic energy of the dissociation channels.

8.2.2 *Angular Distribution and Coincidences in the Dissociation of Methane at 800 nm*

Using a velocity map imaging (VMI) spectrometer we can observe the angular distribution of the fragments and by using a delay-line detector we can also identify coincidences between the ion fragments. Experimentally the set-up is very similar. Here we use the VMI, which is opposed to the ToF, on the other side of the interaction region. We used a repeller voltage of 1.5 kV and an extractor voltage of 1.3 kV. The polarization is changed to be in the plane of the detector so that the molecules most likely dissociate parallel to the detector. For the measurement a fixed laser intensity of $2.5 \cdot 10^{13}\,\mathrm{W/cm^2}$ was used, which is quite low compared to the ToF experiments, where the minimum intensity was twice as high. This is necessary to not flood the detector with too many particles for every laser shot as only a certain number of events per laser shot can be registered by the detector. The laser intensity was adjusted so that statistically not more than one charged particle arrives at the detector for every laser shot. In our case at 3 kHz repetition

Fragment	KE [eV]	App. Int. [10^{14} W/cm^2]	Slope [eV/(10^{14} W/cm^2)]
CH_3^+	0.3	2.0	-
CH_2^+	0.7	2.5	-
	4.4 - 4.8	4.0	0.06
	9.0	6.3	-
CH_2^{2+}	1.4	3.7	-
	9.0 - 9.7	5.5	0.14
	15.4 - 16.2	6.3	0.19
H_2^+	5.4	2.5	-
H^+	0.7	1.6	-
	5.4	1.4	-
	10.5 - 13.0	1.9	0.29
	17.6 - 19.0	2.7	0.31

Table 4: Table noting all the dissociation channels of methane at 800 nm, which can be well-identified, excluding the central peaks. 'App. Int.' is short for appearance intensity.

rate this means 3000 particles per second. The measurement was taken over a time of twenty minutes. For every particle hit, the detector notes three values. The x-coordinate of the hit, the y-coordinate of the hit and the time between the laser trigger and the hit, which corresponds to the time-of-flight. Simultaneously measuring the time-of-flight and the hit on the detector is very practical when looking at ions, as it allows to sort the hits on the detector for their time-of-flight, allowing to easily plot the angular distribution of a certain fragment.
First of all the time-of-flight spectrum is displayed in figure 44. To be able to actually see everything that contributes to the time-of-flight spectrum, the logarithm of the counts is also shown. At the laser intensity used here, further fragmentation becomes less probable for every hydrogen atom dissociated. We can also see hydrogen ions and molecular hydrogen ions, which only appeared at a higher laser intensity in the ToF experiment. What is also interesting to note is that there are molecular hydrogen ions, but we cannot observe any significant amount of doubly charged ions in the spectrum. Apart from this something special can be observed here, which is a peak at a mass-over-charge ratio of 3 which corresponds to the trihydrogen cation. The formation of H_3^+ has also been observed in the strong field dissociation of many other organic molecules [21]. The origin of this is hydrogen migration in the molecule, meaning that three hydrogen atoms come so close that they can form the trihydrogen bond. This study shows also that the formation of H_3^+ is by a factor of 40 less likely compared to the formation of H_2^+. For other molecules, such as C_2H_6, this can be very different with the formation of H_3^+ being nearly as likely as the formation of H_2^+.

To get a deeper insight into the dissociation kinetics, the angular distribution of the fragments is investigated. Having access to the time-of-flight of the ions allows

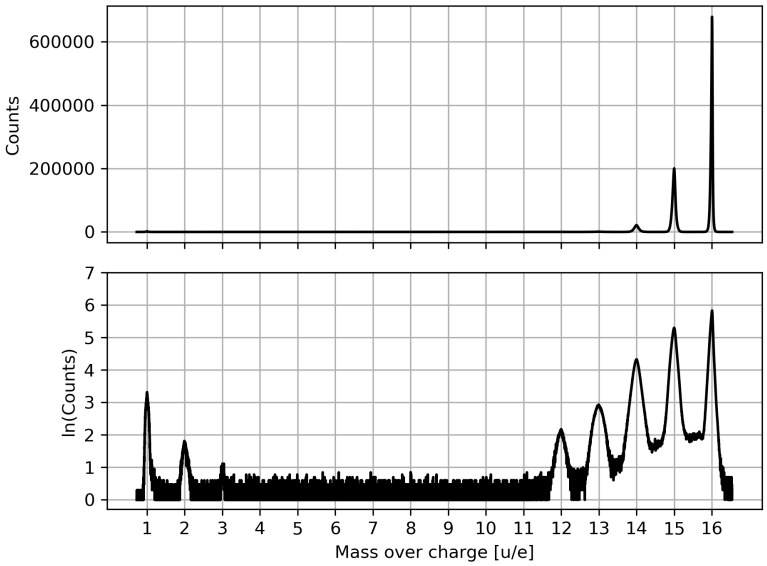

Figure 44: Mass-over-charge spectrum for methane dissociated by 800 nm laser pulses and a laser intensity of $2.5 \cdot 10^{13}\,\mathrm{W/cm^2}$ measured using the VMI. The top figure shows the fragment yield, while the bottom figure shows the logarithm of the fragment yield.

to circumvent the necessity to invert the 2D detector images to recover the 3D angular distribution, see section 5.2. Instead, it is sufficient to select a narrow central slice of certain ions in the ToF spectrum. This selects particles with momentum in the plane parallel to the detector since particles with momentum perpendicular to the plane given by the detector will have shorter or longer times of flight.
The 2D distributions that are obtained this way are shown in figure 45. Each image shows the distribution of ion hits, selected from a narrow time-of-flight slice, for a number of different fragments on the detector. The further outside on the detector a particle hits, the more momentum it had initially. The white double-headed arrow marks the polarization direction of the laser and the laser propagates horizontally through the image.
The detector image of methyl ion hits is shown in figure 45 a). The first aspect visible is that the distribution is elongated at 45° relative to the beam propagation direction, which is most likely due to the gas needle, where the methane gas expands into the chamber, being at an angle of 45°. The distribution does not show any clear features along the polarization axis of the laser and has the highest yield at the center of the detector, which corresponds to vanishing kinetic energies.
From the methylene ion (Fig. 45 b)) to the methylidyne ion (Fig. 45 c)), the distribution exhibits a circular shape with a larger radius and thus higher kinetic energies. From the methylidyne to the carbon ion (Fig. 45 d)) there is no further significant broadening of the distribution visible, which could also be observed in the ToF study. The angular distribution of the methylidyne ion and lighter carbon-containing fragments does not seem to depend on the laser's polarization direction any longer.
In contrast to this are the angular distributions of the molecular and atomic hydrogen ion, shown in figure 45 e) and 45 f), respectively.

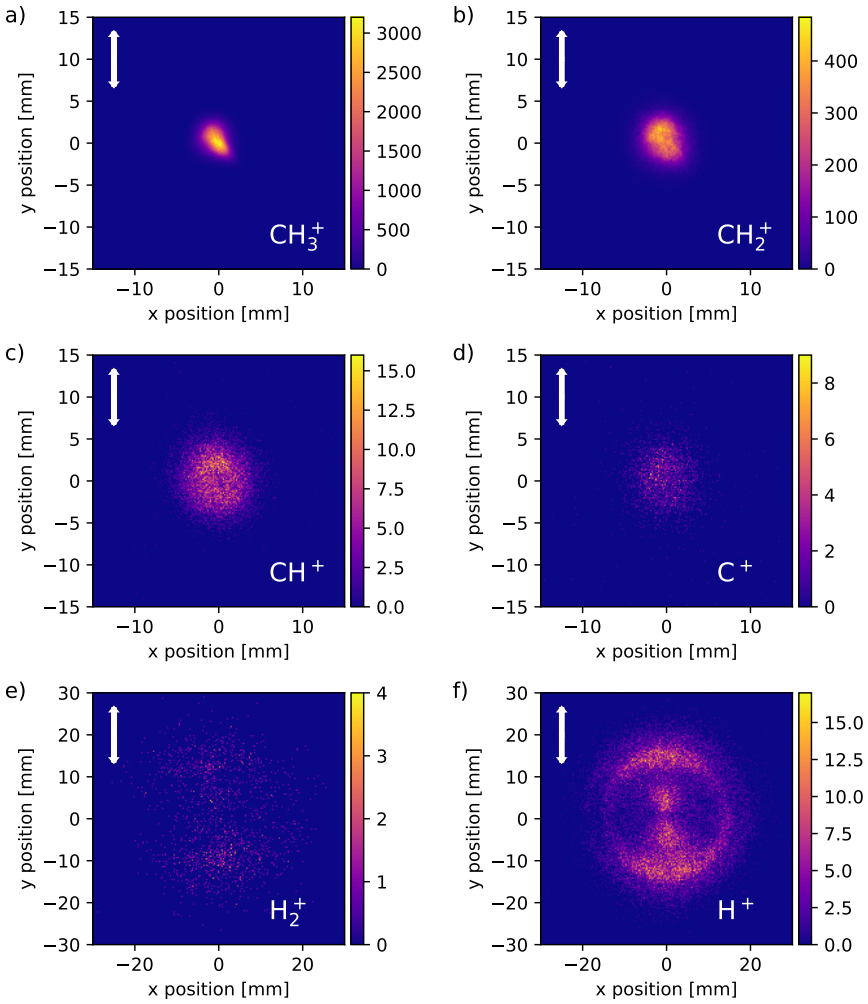

Figure 45: Detector images of different carbon-containing fragments and the molecular hydrogen ion. The double headed arrow marks the laser polarization and the laser beam propagates perpendicular to it. The wavelength used was 800 nm at a laser intensity of $2.5 \cdot 10^{13}$ W/cm^2.

For more insight into which fragmentation steps add KE in the dissociation, the kinetic energy distributions of the carbon-containing fragment ions are compared (Fig. 46 a)). Here the angle integrated yield depending on the kinetic energy is shown. The relation between the radius on the detector where the particle appeared and the particle's kinetic energy have been determined by SIMION simulations.

The methane ions distribution peaks at 10 meV and has an FWHM of 20 meV. The peak at 10 meV is the center of the first KE bin. The kinetic energy of the methane ion would be 34 µeV, if the electron from the ionization had a kinetic energy of 1 eV. So this cannot be the origin of the methane ions KE. Probably the initial momentum from the expansion into the vacuum is the reason for the unexpectedly broad distribution.
The methyl ion yield peaks at a KE of 10 meV and has a FWHM of 25 meV. The methylene ion distribution still peaks at 10 meV but has a larger FWHM of 45 meV.

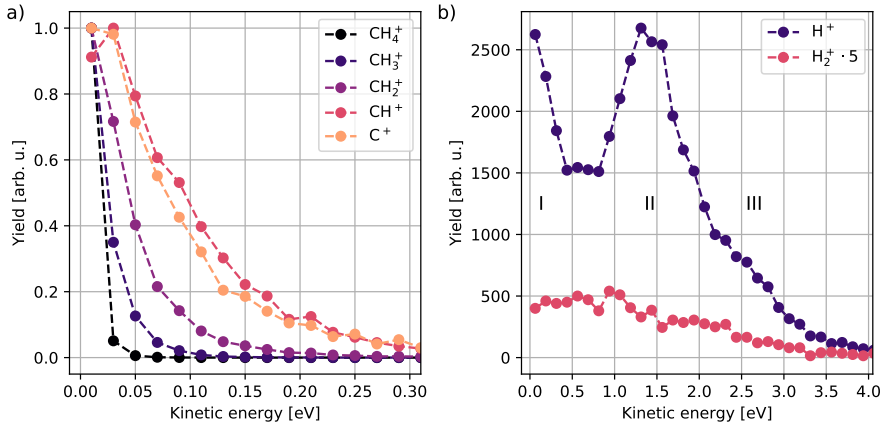

Figure 46: Radially integrated yield plotted against the KE for a) different carbon-containing fragment ions and b) for the molecular and atomic hydrogen ion. In a) the yield of different fragments are all normalized to 1. Roman numbers in b) mark different dissociation channels. The wavelength used was 800 nm at a laser intensity of $2.5 \cdot 10^{13}$ W/cm^2.

Ion	KE at maximum [meV]	FWHM KE [meV]
CH_4^+	10	20
CH_3^+	10	25
CH_2^+	10	45
CH^+	30	95
C^+	30	80

Table 5: KE at the maximum of the distribution and FWHM of the KE for ions and ion fragments of methane measured with the VMI. The laser intensity was $2.5 \cdot 10^{13}$ W/cm^2 with a laser wavelength of 800 nm.

The maximum of the KE of the methylidyne ion is at 30 meV with a FWHM of 95 meV. The carbon ion yield peaks at 10 meV with an FWHM of 80 meV, which is similar to the methylidyne ion.
The main increases in KE take place from the methyl (25 meV) to the methylene ion (45 meV) and from the methylene to the methylidyne ion (95 meV). The results are summed up in table 5.

The detector image of the hydrogen ion is shown in figure 45 f). The distribution shows a correlation between the momentum of the hydrogen ions and the polarization axis of the electric field. By eye, three features can be distinguished. One feature is close to the center of the detector, which shows a strong angular dependence. Further out one can see a clear ring, which corresponds to another dissociation channel with higher kinetic energy. This dissociation channel also shows a strong angular dependence. The last channel lies beyond the feature with the ring-shaped angular distribution. These are even more energetic hydrogen ions showing a weak angular dependence.

A depiction of these channels is shown in figure 46 b), where the angle integrated yield of the atomic and molecular hydrogen ion depending on the KE is displayed. The channels, which were mentioned before, are marked with arrows here. The least energetic channel ranges from 0.1 eV to 0.5 eV, having it's maximum at 0.1 eV. It is quite narrow compared to the next higher energetic channel, which ranges at least from 0.8 eV to 2.0 eV with a maximum around 1.4 eV. The highest energetic channel ranges at least from 2.2 eV up to 3.5 eV and shows no clear maximum, as it heavily overlaps with the channel with lower kinetic energy.
Using the ToF, atomic hydrogen channels could be found at 0.7 eV and 5.4 eV, which does not match the channels found using the VMI. The reason for this might be the different laser intensity regions. Using the ToF the lowest used intensity was $7.5 \cdot 10^{13}\,\mathrm{W/cm^2}$, where only the methane and the methyl ion appear. In the experiment using the VMI the laser intensity was $2.5 \cdot 10^{13}\,\mathrm{W/cm^2}$ and all fragments appeared.

The angular distribution of the hydrogen ion is displayed in the top part of figure 47. The figure below shows the yield of a certain channel integrated over the energy range, marked by the colored lines in the top figure. The color of the integrated yield in the lower part of the figure corresponds to the colored lines in the top part of the figure. To quantify and characterize the angular distribution the molecular alignment parameter $< \cos^2(\theta) >$ is used [166]. If the molecular exclusively fragments in the direction of the polarization axis of the laser beam, the alignment parameter will be 1. In the opposite case, if the molecule fragments exclusively perpendicular to the polarization axis of the laser beam, the alignment parameter will be 0. Usually, the angular distribution will have a certain distribution that does not correspond to either of the extreme cases, for example, a $\cos^2(\theta)$ distribution, with the maxima along the laser polarization direction, has an alignment parameter of 0.75. The alignment parameter of the three different channels are quite close with 0.67 (channel 1, grey), 0.66 (channel 2, red) and 0.61 (channel 3, yellow). The angular distribution of all channels is broader compared to a $\cos^2(\theta)$ distribution, but overall there is no significant difference between the channels.

Additional information about the dissociation of coulomb-explosion channels can be found when looking at the time-of-flight of particles that are being created by the same laser shot. This method of investigating molecular dissociation into charged fragments is called PIPICO (photoion-photoion coincidence) [221]. For every laser pulse, if two particles hit the detector, a time-of-flight pair can be formed consisting of the time-of-flight of the first ion and the time-of-flight of the second ion. Collecting all these pairs for all laser shots and displaying them as a two-dimensional histogram results in figure 48.
The time-of-flight region chosen is where the first particle is a hydrogen, molecular hydrogen, or tri-hydrogen ion and the second particle is a carbon-containing ion. With this, we omit coincidences of carbon-containing ions as one methane molecule can never fragment into two charged carbon-containing fragments. Examples of these coincidences, which are not the result of a single methane molecule's dissociation, are found when looking at the methane ion and its

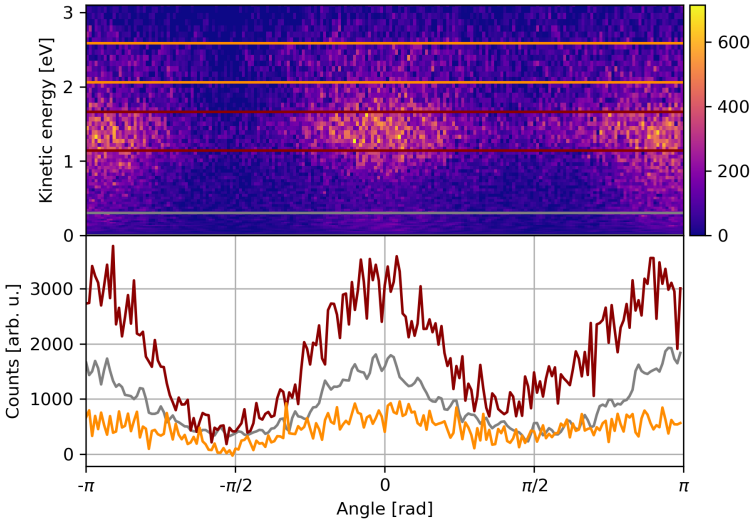

Figure 47: The top part of the figure shows a polar plot of the hydrogen ion kinetic energy distribution on the detector. The colored lines mark the integration region of different dissociation channels. The lower part shows the angular yield integrated between the lines of the top figure. The black dotted line shows the fit with the special function. The wavelength used was 800 nm at a laser intensity of $2.5 \cdot 10^{13}\,\mathrm{W/cm^2}$.

coincidences with a hydrogen, a molecular hydrogen or a tri-hydrogen ion. The methane ion has not even undergone dissociation, so no fragment can be produced. These coincidences arise from the dissociation of at least two methane molecules. Care has to be taken when interpreting the results of these coincidence maps.

Indications for true coincidences where two ions are formed in the fragmentation of one methane molecule appear as diagonal lines in the coincidence spectrum. These diagonal lines are visible in the coincidence of the hydrogen and methyl ion, in the coincidence of the hydrogen and methylene ion and in the coincidence of the molecular hydrogen ion and the methylene ion. The formation of the diagonal line is connected to momentum conservation. Methyl ions on the diagonal line (where the metyl-hydrogen ion coincidences are) with a longer time-of-flight compared to most of the methyl ions had momentum away from the detector. The hydrogen ion from this coincidence has a lower time-of-flight compared to the average hydrogen ion, meaning that it is created with momentum directed towards the detector. Thus this coincidence is actually the dissociation of the methane di-cation into a hydrogen ion and a methyl ion. If the molecule dissociates, only the momentum component perpendicular to the plane that the detector is in will contribute to a change in the time-of-flight spectrum. With these coincidences, the origin of the molecular hydrogen ion is clearly identified to be the dissociation of the doubly charged methane molecule into a molecular hydrogen and a methylene ion.

In a study by Kukk et. al. [222] PEPICO (photoelectron photo-ion coincidence) was used to investigate core-ionized methane by measuring the energy of the auger-electron and measuring the time-of-flight of coinciding ions. This allowed

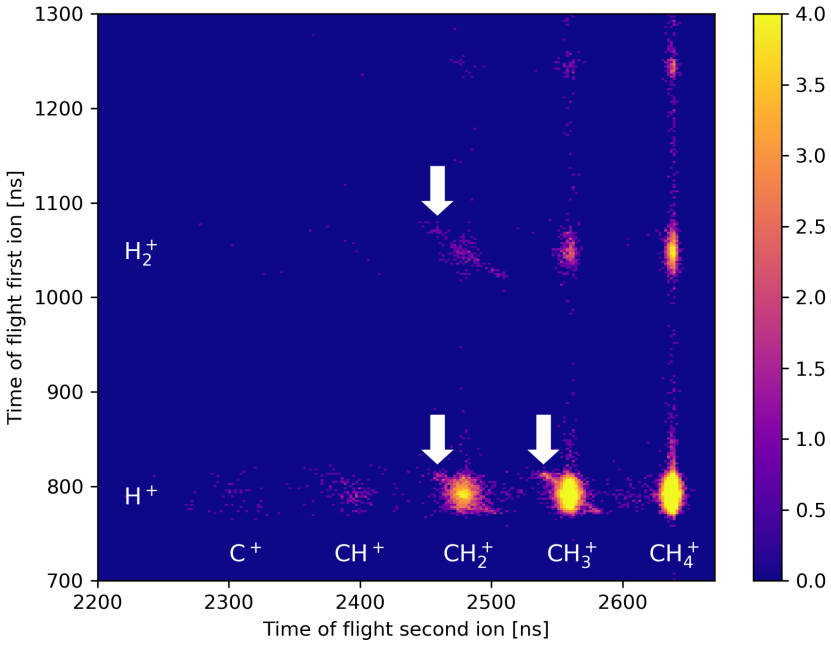

Figure 48: PIPICO spectrum of methane dissociating in an 800 nm laser field at an intensity of $2.5 \cdot 10^{13}\,\mathrm{W/cm^2}$. Here we focus on the region where a hydrogen, a molecular hydrogen, or a tri-hydrogen ion arrives first (first ion) and then a carbon-containing fragment ion arrives (second ion). The colormap displays the logarithm of the yield, limited to 4.0 to ensure visibility of the relevant features. The white arrows mark the diagonal lines indicating coincidences.

them to see which electronic state will lead to what kind of ionic fragments. The core-ionization of methane guarantees that the dissociating ion is at least ionized twice as it fragments. Their observations show that the methyl ion exclusively originates from low excited $1t_2^{-2}$ states. This supports the observation that the shoulder in the ToF KE spectrum of the methyl ion does not change when increasing the laser intensity. Such an exclusive range can also be found for the molecular hydrogen ion. Here the $1t_2^{-2}$ states are again the precursor to the dissociation, but slightly higher excited states of this configuration are required. This supports the findings of the ToF KE distribution of molecular hydrogen ions, which does not significantly change with changing laser intensities. The methylene ion is mostly originating from $1t_2^{-2}$ states, but also from the more energetic $2a_1^{-1}1t_2^{-1}$ states. For the methylidyne and carbon ion, these states are precursor states as is the higher energetic $2a_1^{-2}$ state.

The VMI measurement gave insight into the angular distribution of the methane fragment ions and made it possible to identify coulomb-explosion dissociation channels. We saw that the KE distribution of the carbon-containing fragment ions becomes broader with each hydrogen dissociated, until the methylidyne ion, where the distribution becomes independent of the laser polarization direction. Looking at the hydrogen ion, we could identify three different dissociation channels and noticed that they have different angular distributions. In the PIPICO spectrum, clear signs of three coulomb-explosion channels could be observed,

clarifying the origin of the molecular hydrogen ion.

8.2.3 *Dissociation and Fragment Kinetics of Methane at 400 nm*

Now we will look at how methane behaves when being ionized and dissociated by 400 nm ultra short laser pulses. Having half of the wavelength at 800 nm, the field oscillates with twice the frequency at 400 nm. This has an effect on the mechanism of ionizatio because the faster the field oscillates at the same laser intensity, the less probable tunneling ionization becomes. The re-collision ionization mechanism is also affected by this, as the ponderomotive potential at 400 nm is only a quarter of the ponderomotive potential at 800 nm for the same laser intensity.
To generate the second harmonic we focus the 800 nm beam with a lens with a focal length of 1400 mm, which focuses the beam at the end of the empty semi-infinite gas cell. To achieve a high conversion from 800 nm to 400 nm we put the frequency doubling BBO crystal at 600 mm from the lens in laser propagation direction. After passing the BBO the beam is reflected by two dichroic mirrors, which separate the fundamental and the second harmonic beam. Additionally, they are also used to guide the beam to the toroidal mirror, which focuses the beam in the center of the interaction region. As we have no compression stage for the second harmonic beam, a balance between a high conversion rate of fundamental to second harmonic and high laser intensities at the interaction region has to be found. The achieved conversion rate was roughly 25 %, when measuring the second harmonic power right after the beam passed the harmonic separator mirrors.
To measure the second harmonic yield for the power set-points of the fundamental a photodiode was used. The final intensity calibration is done by comparing the laser intensity dependent yield of the methane ion with the ionization rate given by the PPT model [223]. The result of the PPT calculation is shown in figure 49 for a laser wavelength of 400 nm and 800 nm and additionally the wavelength-independent ADK-model calculation is shown. Adding the ADK model [224] highlights the contributions to the ionization by multi-photon ionization because it is included in the PPT model but not in the ADK model. The PPT model for 400 nm shows a linear slope at lower laser intensities, which corresponds to an exponential increase in the ionization probability due to multi-photon ionization. At around $1.7 \cdot 10^{14}\,\mathrm{W/cm^2}$ there is a characteristic decrease of the slope, which is a feature that we also observe in the intensity dependent yield of the methane ion that is displayed in figure 50 b). This feature is used to calibrate the laser intensity for 400 nm.

To get an overview of the fragmentation of methane in 400 nm laser fields the ToF spectrum at the highest available laser intensity of $4.1 \cdot 10^{14}\,\mathrm{W/cm^2}$ is investigated (Fig. 50 a)). The spectrum at 400 nm mainly shows two groups, the carbon-containing ions and fragments ions and the hydrogen and molecular hydrogen ions. The yield of the doubly charged ions is barely visible. Comparing this spectrum to the spectrum at 800 nm (figure 38) at the highest laser intensity, it becomes clear that the dissociation at 400 nm creates fewer fragments with high

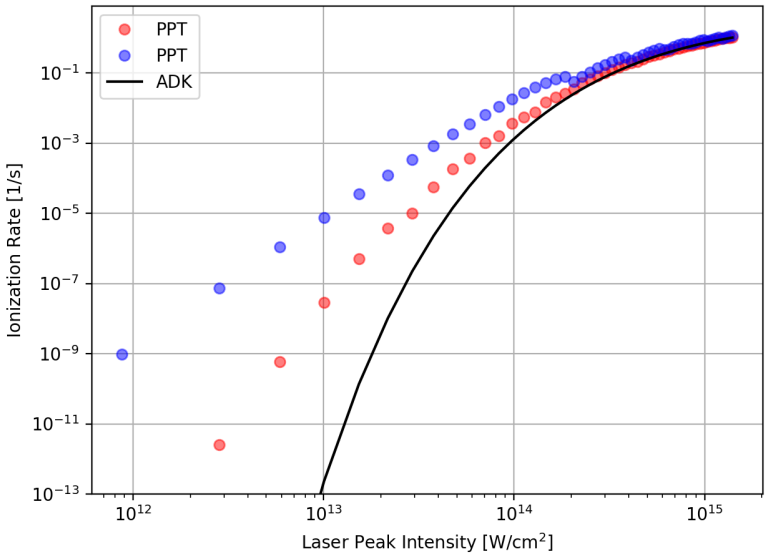

Figure 49: Ionization rates calculated with the PPT model for 400 nm (blue) and 800 nm (red) for an atom with the ionization potential of methane (12.61 eV). The black curve is a calculation of the ionization rate with the ADK model, which does not include multi-photon ionization.

kinetic energies, as there are no peaks to the side of the central peaks for any fragment.

The intensity dependent yield of ions and fragments ions from the dissociation of methane in laser fields of 400 nm is shown in figure 50 b).
At the lowest laser intensity of $4.3 \cdot 10^{13}$ W/cm^2 only the yields of the methane and the methyl ion are above the appearance limit of 0.1. At a slightly higher laser intensity of $4.6 \cdot 10^{13}$ W/cm^2 the methylene ion appears.
The next ion appearing is the hydrogen ion at a laser intensity of $6.1 \cdot 10^{13}$ W/cm^2. At higher intensities, the yield follows the yield of the methylene ion until a laser intensity of $1.0 \cdot 10^{14}$ W/cm^2, at which the yield stagnates due to the competition with the appearance of the molecular hydrogen ion.
Continuing in the dissociation chain, the methylidyne ion follows at a laser intensity of $7.9 \cdot 10^{13}$ W/cm^2. The large gap in intensity to the methylene ion shows that the methylene ion is relatively stable, which is further supported by the stability of the di-cation.
The carbon ion follows together with the hydrogen molecular ion at a laser intensity of $1.3 \cdot 10^{14}$ W/cm^2. The yield of the carbon ion stays below, but close to the methylidyne ion, showing that the barrier to dissociate further from the methylidyne ion to the carbon ion is little.
At even higher laser intensities the group of doubly charged ions appears. As they require higher excitations, they are well separated from the singly charged ions regarding the laser intensity and the yield. The carbon and the methylene di-cation appear at the same laser intensity of $1.9 \cdot 10^{14}$ W/cm^2, the methane di-cation appears at a slightly higher laser intensity of $2.6 \cdot 10^{14}$ W/cm^2. Interestingly the yield of the carbon and methylene di-cation increases similarly and has similar

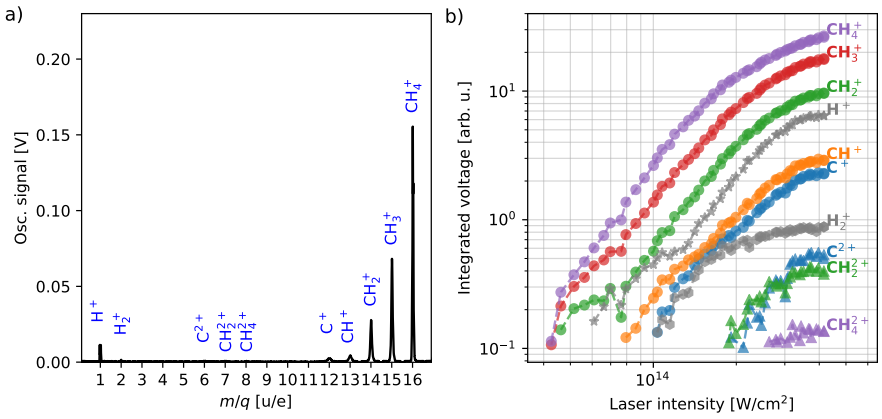

Figure 50: a) Mass-over-charge spectrum of methane dissociated by 400 nm laser pulses at a laser intensity of $4.1 \cdot 10^{14}$ W/cm^2. b) Yield of ions and fragment ions of the methane dissociation in 400 nm laser pulses and their dependence on the laser intensity.

values, while the carbon di-cation yield only increases slightly and is three to four times lower.
Overall the spectrum looks much tidier compared to 800 nm (Fig. 39), because the yields of different ions don't cross and the yield of the doubly charged ions does not surpass the yield of the singly charged ions. Overall double ionization is less probably than at 800 nm, which might be due to the lower ponderomotive potential leading to lower excitations through electron re-collision and the overall lower available laser intensity at 400 nm.

The intensity dependent KE distribution of ions created in the dissociation is shown in figure 51. As the laser intensity increases, the yield of the methyl ions with low KE increases and a faint shoulder is formed at 250 meV. At 800 nm this shoulder was more pronounced.
In the spectrum of the methylene ion the dissociation channels with high KE are missing, which appeared at 800 nm (Fig. 43), showing that double and especially triple ionization is not as likely.
The methylidyne and carbon ions KE distribution are very similar to the distributions at 800 nm in terms of shape and maximum kinetic energy of around 3.5 eV (CH^+) and 4.0 eV (C^+).

The intensity dependent KE distribution of the doubly charged methylene ion is missing the high KE features that were visible at 800 nm. The spectrum of the doubly charged methane ion is not much different to the one at 800 nm.
Moving on to the hydrogen-containing fragment ions a very broad KE distribution can be observed. A slight structure appears in the KE distribution of the molecular hydrogen ion at a laser intensity of $1.3 \cdot 10^{14}$ W/cm^2. Here a central feature with low KE extending up to a KE of 2.0 eV and a second feature appearing from 3.0 eV to 11.0 eV is seen. As the laser intensity increases further, the features become impossible to separate, until at some point the central feature has enough yield to overcome the next voltage binning step of the oscilloscope. The most energetic

Ion	Appearance intensity [W/cm^2]
CH_4^+	$4.3 \cdot 10^{13}$
CH_3^+	$4.3 \cdot 10^{13}$
CH_2^+	$4.6 \cdot 10^{13}$
CH^+	$7.9 \cdot 10^{13}$
C^+	$1.3 \cdot 10^{14}$
CH_4^{2+}	$2.6 \cdot 10^{14}$
CH_2^{2+}	$1.9 \cdot 10^{14}$
C^{2+}	$1.9 \cdot 10^{14}$
H_2^+	$1.3 \cdot 10^{14}$
H^+	$6.1 \cdot 10^{13}$

Table 6: Appearance intensities of various ions produced in the dissociation of methane in an intense, 400 nm, laser pulse. The appearance intensities are heavily reliant on our experimental set-up and will most likely overestimate the appearance intensities.

feature broadens with increasing laser intensity until, at the maximum laser intensity, it extends all the way to 13.0 eV.
The lightest fragment, the hydrogen ion, shows clear signs of different dissociation channels in the intensity dependent KE distribution. Three different dissociation channels can be distinguished. The channel with the lowest kinetic energy is centered around 0.4 eV KE and is likely connected to the dissociation of the methane or methylidyne molecule into a neutral carbon-containing fragment and a hydrogen ion. The second very distinct channel is centered around a KE of 5.1 eV. This channel could also be observed at 5.4 eV in the KE spectrum of hydrogen ions resulting from the dissociation with 800 nm laser pulses. The discrepancy in the KE is probably due to the calibration of the KE. The third channel is centered around 10.5 eV. This channel is relatively broad, compared to the two other dissociation channels. At 800 nm a channel at this KE could also be observed, but due to the large KE broadening it is not easy to clearly identify this channel. A clear difference to the spectrum at 800 nm is that the KE only extends up to 20 eV whereas it extended up to 35 eV at 800 nm.
Figure 52 a) shows the hydrogen ion KE distribution at 800 nm (red) and 400 nm (blue) at a laser intensity of $2.3 \cdot 10^{14}$ W/cm^2 and $4.1 \cdot 10^{14}$ W/cm^2, respectively. By just looking at the two graphs one can see that the difference in the kinetic energy between the two different wavelengths is quite small. The low-KE channel, called channel 1, shows the biggest difference here. Where in the case of 400 nm the kinetic energy of the channel is at 0.4 eV, it is at 0.7 eV for 800 nm. That the KE is different between the two wavelengths is an indicator for bond-softening dissociation, as there the KE depends on the wavelength. The other two channels do not show any differences in the KER between the two wavelengths, indicating that these channels arise due to Coulomb-explosions.

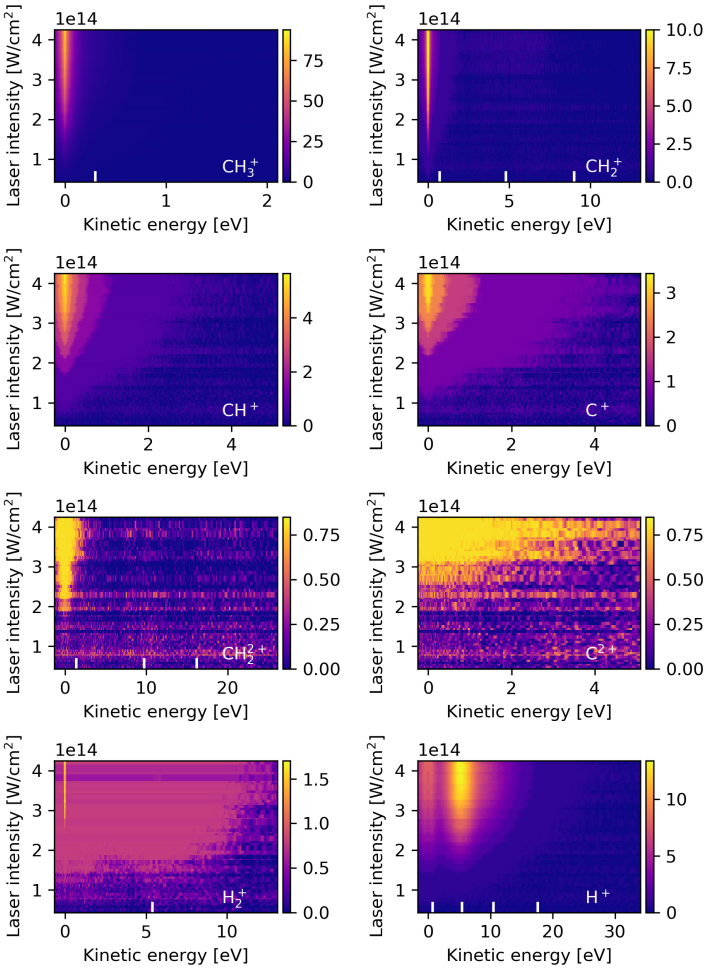

Figure 51: Intensity dependent KE distribution of selected ion fragments created in the dissociation of methane in a strong laser field at a central wavelength of 400 nm. The white text in the intensity dependent KER distribution indicates which fragment is shown.

Lastly we will compare the ion yield of the carbon-containing ion fragments at 800 nm (red) and 400 nm (blue), shown in figure 52 b). Here we can see, what was already observed by our collaborators, who focused on another main aspect [206]. At lower laser intensities, up to $2 \cdot 10^{14}$ W/cm^2, the yield of fragment ions at 400 nm is much greater than at 800 nm. The methyl ion does not appear at 800 nm, until a laser intensity of 10^{14} W/cm^2 is reached. At this laser intensity at 400 nm the methane can already fragment into the methylidyne ion and even the carbon ion appears at a slightly higher laser intensity. One reason they found is connected to the shorter period at 400 nm. A pulse with a wavelength of 400 nm has twice as many oscillations as a laser pulse with a wavelength of 800 nm, if the pulses have the same duration. This way it is more probable for the 400 nm laser pulse to excite higher vibrational modes, which will finally lead to the dissociation. The interpretation was backed-up with calculations of vibrational modes of methane and potential energy surface calculations of dissociating methane. In our experiment, we measured more points in intensity, which we can use to plot the

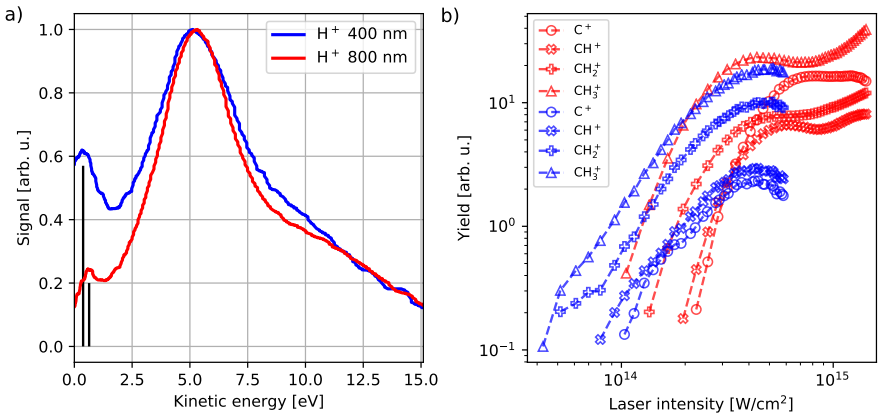

Figure 52: a) Comparison of the KE distribution at 800 nm and 400 nm with laser intensities of $2.3 \cdot 10^{14}\,\mathrm{W/cm^2}$ and $4.1 \cdot 10^{14}\,\mathrm{W/cm^2}$, respectively. b) Yield of carbon-containing ion fragments at 800 nm (red) and 400 nm (blue).

yield of carbon fragment ions against the laser intensity. Here we see, that the slope of the yield of fragment ions at 400 nm is smaller compared to the same fragments at 800 nm. This hints at a difference in non-linearity, which can easily be explained by laser intensities, which are in the multi-photon ionization regime. To ionize methane at 400 nm, one needs at least five photons (neglecting the ponderomotive shift), whereas nine photons are needed at 800 nm. This enhances the ionization probability at lower laser intensities at 400 nm.
Looking at higher laser intensities, this situation reverses. At $5 \cdot 10^{14}\,\mathrm{W/cm^2}$ the yield of the methyl ion, the methylidyne ion and the carbon ion is higher at 800 nm, compared to 400 nm. Interestingly the carbon ion yield at 800 nm is nearly as high, as the methyl ion yield at 400 nm, showing how efficient ionization and dissociation becomes at these laser intensities at 800 nm. Since the laser intensity is higher than the barrier-suppression intensity of $3.7 \cdot 10^{14}\,\mathrm{W/cm^2}$, what was enhancing the ionization and dissociation at lower laser intensities at 400 nm is now hindering ionization at higher laser intensities relative to 800 nm. As the field is oscillating faster at 400 nm, the tunneling time is decreased, leading to a lower ionization probability than at 800 nm. Additionally the ponderomotive potential at 800 nm is 30 eV at $5 \cdot 10^{14}\,\mathrm{W/cm^2}$, while it is only 7.5 eV at 400 nm. This means that at 800 nm the molecule can be highly excited and doubly ionized by re-colliding with an electron accelerated in the laser field. These highly excited states will lead to further fragmentation, as new dissociation channels might be accessible by these states. This effect is visible in the plateau in the yield of the carbon ion. In this region, doubly ionization becomes much more prominent and as we know from figure 39, the yield of the carbon di-cation even surpasses the yield of the carbon ion at 800 nm at the highest laser intensities.

In conclusion, we saw that the dissociation of methane at 400 nm leads to overall lower KER compared to the dissociation at 800 nm. Reasons for this are the overall lower laser intensity available at 400 nm and the lower ponderomotive potential at 400 nm, which prevents high excitations through electron re-collision. Also tunnel-

Fragment	KE [eV]	App. Int. [10^{14} W/cm^2]	Slope [eV/(10^{14} W/cm^2)]
CH_3^+	0.3	1.7	-
CH_2^+	0.7	1.1	-
H_2^+	0 - 12	1.7	-
H^+	0.4	1.4	-
	5.1	1.4	-
	10.5	1.7	-

Table 7: Table noting all the dissociation channels of methane at 400 nm which can be identified. 'App. Int.' is short for appearance intensity.

ing ionization at 400 nm is not as efficient as at 800 nm due to the faster oscillations of the electric field at 400 nm. The difference between the wavelengths also manifested itself in the kinetic energy of a bond-softening dissociation channel and in the ionization rate of carbon fragment ions at low laser intensities.

8.2.4 *Angular Distribution of the Molecular and Atomic Hydrogen Fragments at 400 nm*

Now the angular distribution of the hydrogen fragments from methane is investigated for laser pulses with a central wavelength of 400 nm and a laser intensity of $2 \cdot 10^{13}$ W/cm^2. Again, as before, by choosing ions that arrive in a central time-of-flight slice of the respective fragment or ion, the effective 3D velocity distribution can be recovered. The detector images for the molecular hydrogen ion and the atomic hydrogen ion are shown in figure 53 a) and b), respectively. Overall the angular distribution of the atomic and molecular hydrogen ions is apparently more aligned regarding the polarization direction of the laser at 400 nm. For the atomic hydrogen ion three features appeared at 800 nm, whereas at 400 nm only one feature appears.

To quantify the angular distribution the alignment parameter $< \cos^2(\theta) >$ is used, as it was at 800 nm. Interestingly at 400 nm only one distinguishable channel appears in contrast to the three at 800 nm. This dissociation into this channel mainly happens along the polarization axis of the laser, as is confirmed by the asymmetry parameter of 0.72, meaning that it favours the polarization direction of the laser slightly more than the channels at 800 nm. This is counter-intuitive since usually it is expected that in higher non-linear processes the angular distribution should become more narrow, as the projected field strength and thereby the projected non-linear intensity I^N on the C-H molecular axis drops off faster for higher-nonlinear processes of order N as would be the case for 800 nm compared to 400 nm.

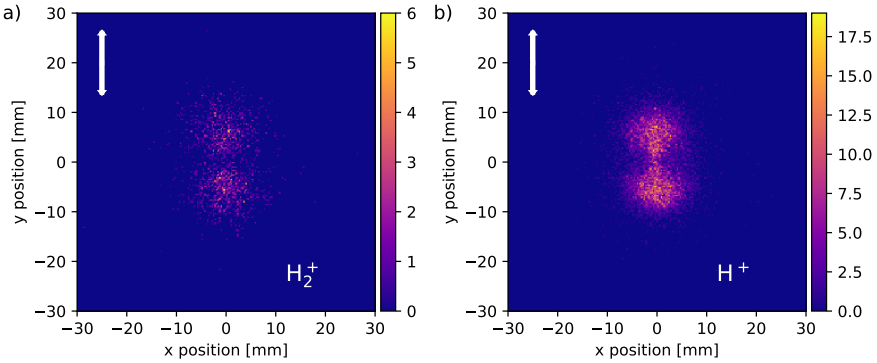

Figure 53: Detector images of the molecular and atomic hydrogen ion. The white arrow in the images indicates the polarization axis of the laser, relative to the detector images. The beam passes through the image horizontally. The wavelength of the laser was 400 nm and the intensity $2 \cdot 10^{13}\,\mathrm{W/cm^2}$.

8.2.5 *Conclusion*

The ToF in combination with a SIMION model of our experimental set-up enabled us to determine the kinetic energy of all fragment ions from methane and their dependence on the laser intensity. With increasing intensity, additional dissociation channels with higher kinetic energies appeared in some fragments like the methylene ion, di-cation, as well as the atomic hydrogen ion, indicating double- and triple-ionization happening in the dissociation of the methane molecule at 800 nm. The kinetic energy of hydrogen ions showed four different dissociation features with the highest kinetic energy being up to 35 eV at the highest laser intensity of about $10^{15}\,\mathrm{W/cm^2}$. At 400 nm no indication of triple-ionization was found, due to the lower ponderomotive potential and an in general lower available maximum laser intensity. Thus fewer dissociation channels appeared at 400 nm, with a maximum kinetic energy of 20 eV of the hydrogen ions. In the intensity dependence of the fragments yield clear differences appeared due to the different degrees of non-linearity involved at lower laser intensities.
With the VMI the angular distribution of the ions could be recovered. From the methane ion to the methyl ion the angular distribution became more circular. At 800 nm the biggest increase in the width of the angular distribution could be found from the methylene to the methylidyne ion (45 meV to 95 meV), while the angular distribution of the carbon ion is more narrow again (80 meV). For 400 nm the observation was similar. The biggest differences between the two wavelengths were visible in the angular distribution of the hydrogen ions. At 800 nm three dissociation features could be discerned with kinetic energies up to 3.5 eV, while at 400 nm only one feature appeared with kinetic energies up to 1.0 eV.
The PIPICO spectrum at 800 nm revealed that one dissociation channel forming the molecular hydrogen ion, which is created in the dissociation of methane, is the dissociation of the doubly charged methane ion. Other dissociation channels for hydrogen ions were found in the dissociation of the methane and the methyl di-

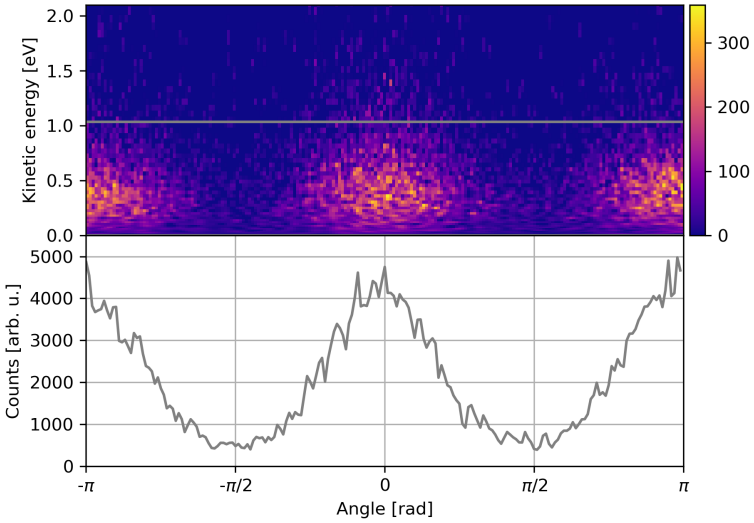

Figure 54: Angular distribution of the hydrogen ion. The top part of the figure shows a polar plot of the KE distribution. The lower part of the figure shows the angular yield integrated between the grey lines at 0 eV and 2.4 eV. The integrated angular yield is fitted by a special function, which is the black striped line. The wavelength of the laser is 400 nm and the intensity $2 \cdot 10^{13}\,\mathrm{W/cm^2}$.

cation. At 400 nm such dissociation channels could not be identified using PIPICO due to the insufficient laser intensity to form doubly charged ions.

Part III

STUDY OF THE CIRCULAR DICHROISM OF STATE-PREPARED HELIUM IONS

In this chapter an experiment on atomic helium is presented which was carried out at the free-electron laser facility FERMI, located in Italy near the city of Trieste. Using the seeded beam of FERMI, helium atoms were first ionized and resonantly excited by circularly polarized XUV radiation. Using then a circularly polarized optical laser, the excited helium ion was further ionized by multi-photon ionization. The circular polarization of the optical light could be adjusted to rotate in the same or the opposite direction relative to that of the XUV light. This led to a circular dichroism (CD) in the yield and in the angular distribution of the photoelectrons. The origin and the details of this dichroism will be discussed in the following chapter.

9 CD IN MPI OF RESONANTLY EXCITED HELIUM-IONS

Circular dichroism (CD) is a phenomenon that appears if a system interacts differently with left- and right-handed circularly polarized light. Its applications cover a wide range of topics, such as identifying protein conformations [225], investigating spin-dependent processes [226, 227], distinguishing molecular conformations in different solutions [228], determine the chirality of molecules in gas phase [229] and studying nano-materials [230]. In this experiment, which was carried out at the FERMI FEL in April of 2019, we aimed to study the circular dichroism in two-color multi-photon ionization on a prototype system, atomic helium. The investigation was a follow-up of an earlier experimental campaign, in which this dichroism was first observed [48].

The prototype system in [48] was a helium ion, which is prepared in the excited and oriented 3p(m = +1) state. A schematic drawing of the preparation (blue arrows) is shown in figure 55. This system has the advantage of having only one electron, which allows to use well-established computational approaches to compare with the experimental results. To prepare the He ion, the intense, circularly polarized XUV laser pulses that are available at FERMI FEL were used. The XUV pulses were tuned to a photon energy of 48.37 eV which is the energy required to excite the helium ion from the ground state He(1s) to the He(3p) state. Due to the high intensity of the XUV pulse ($1 \cdot 10^{13}$ W/cm^2) a first XUV photon ionizes the helium atom, creating the $He^+(1s^1)$ ion and then another XUV photon from the same pulse can interact with this helium ion, exciting it into the $He^+(3p^1)$ state. Since the XUV pulse is circularly polarized, the 3p state is spatially oriented, which can be expressed by the magnetic quantum number $m = +1$. This is a direct consequence of the dipole selection rules ($\Delta\ell = 1$, $\Delta m = +1$) for the absorption of circularly polarized light of positive helicity, see chapter 2.1.

To enable the study of a circular dichroism, an intense ($1 \cdot 10^{12}$ W/cm^2) circularly polarized optical laser, that has the same or opposing helicity to the XUV pulse, with a wavelength of 784 nm (1.58 eV), finally ionizes the prepared helium ions in a multi-photon process via the absorption of at least four optical photons, see chapter 2.2. A schematic drawing of this multi-photon process (red arrows) is shown in figure 55. In case of multi-photon ionization (MPI) by four absorbed photons, the outgoing electron is called the MPI photoelectron. If five or more photons are absorbed, the electrons are formed by above-threshold ionization (ATI) and are hence labeled as ATI (1) (five photons), ATI 2 (six photons), ATI 3 (seven photons), and so forth.

The MPI electrons have different final states in the continuum depending on the helicity of the optical laser. If the optical photons have the same helicity (co-rotating) as the right-handed circularly polarized XUV photons, then due to the selection rules ($\Delta\ell = \pm 1$, $\Delta m = +1$) and the requirement of $\ell \geq |m|$ (see chapter 2.1), the angular momentum and magnetic quantum number have to change each by +1. From the initial He^+(3p, m= +1) state this leads to a final state with ($\ell = 5$, $m = +5$),

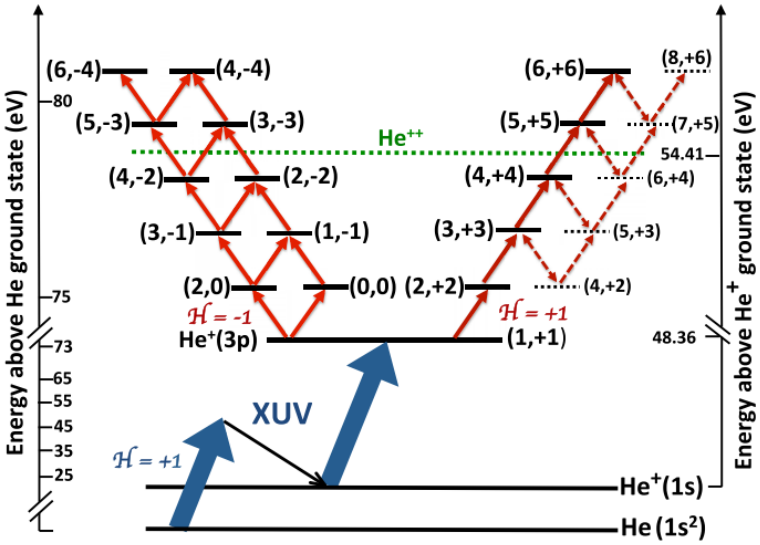

Figure 55: Schematic of the interaction of helium atoms with a bi-chromatic field consisting of an XUV and NIR laser pulse in lowest order perturbation theory (LOPT). The XUV photon energy is tuned to 48.37 eV, which is in resonance with the 3p(m = +1) resonance of the helium ion. This resonance is populated, after sequential excitation by two XUV photons, leading to the ionization of helium and then the excitation into the resonance state. From here NIR photons of 1.58 eV photon energy can ionize the excited helium ion via multi-photon ionization. The left branch corresponds to counter-rotating laser fields, while the right branch corresponds to co-rotating laser fields. Dashed lines show higher-order processes. This figure is taken from [48].

or short $(5, +5)$, after the absorption of four photons. If the helicity of the optical photons is opposed to the helicity (counter-rotating) of the XUV photons, then two final continuum states are available with $(5, -3)$ and $(3, -3)$. For the ATI electrons, the pairs of quantum numbers are $(6, +6)$ for the same helicity and $(6, -4)$ and $(4, -4)$ for opposing helicities.

The main outcome of the previous experiment was the observation of a strongly intensity dependent circular dichroism of the MPI electrons. This is shown in figure 56 a). At low laser intensities the dichroism is nearly 1, favouring ionization of co-rotating XUV and NIR pulses, and with increasing laser intensity the circular dichroism decreases and even changes sign. It was found that one of the reasons for this strong intensity dependence is the helicity dependent AC-Stark shift of the $3p(m = +1)$ resonance. For low laser intensities, this AC-stark shift is small and similar for both helicities. With increasing laser intensity the AC-stark shift becomes much more significant for XUV and NIR photons with the same helicity, which prevents the effective population of the $3p(m = +1)$ resonance. As a consequence, less excited atoms are available for multi-photon ionization in the case of co-rotating pulses. In TDSE simulations this could be shown by calculating the intensity dependent population of the $He^+(1s)$ and $He^+(3p)$ states after the two pulses interacted with the helium atoms, which is shown in figure 56 b).

Recently the AC-Stark shift of the states that are involved in the ionization of the helium ion by the XUV and NIR pulse have been estimated using quasi-particle

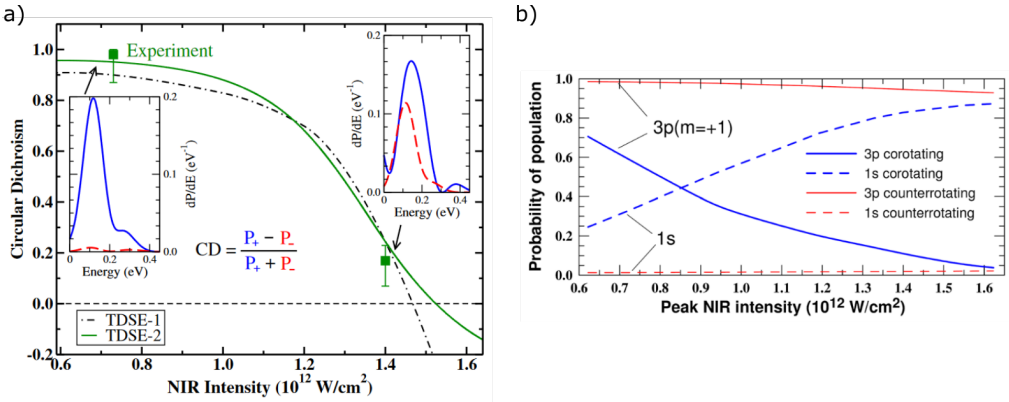

Figure 56: a) Intensity dependence of the CD (green squares) of the MPI electrons at a kinetic energy of 200 meV. The dotted black and solid green lines are results from TDSE calculations. The insets show calculated photoelectron spectra at two laser intensities close to the ones measured in the experiment. b) Calculated population of the $He^+(1s)$ and $He^+(3p)$ states in the co-rotating (blue) and counter-rotating (red) scenario after the interaction with the NIR and XUV pulse. These figures are taken from [48].

calculations [51]. These calculations confirmed the assumption that the intensity dependent $He^+(3p)$ level shift is different for the two helicities. These calculations also show that other intermediate resonances, that lie energetically between the $He^+(3p)$ resonance and the ionization potential, play a role in the intensity dependence of the CD. Depending on the laser intensity the multi-photon ionization might be resonant with a certain intermediate state, depending on the state's AC-Stark shift, which leads to an increase in the photoelectron yield.

With the new experiment, we wanted to actually measure the shift of the $He^+(3p)$ level depending on the intensity of the optical laser. We also recorded photoelectron spectra for a broader range of laser intensities of the optical laser, from $1 \cdot 10^{12}$ W/cm^2 to $3.3 \cdot 10^{13}$ W/cm^2, and with many steps in between. With this fine sampling we want to investigate the trend of the CD of the MPI electron that was foreshadowed by the previous experiment and was predicted by TDSE and quasi-particle simulations [51]. Additionally, we want to specifically observe in how far ionization via transient resonant states affects the intensity dependence of the CD.

To check how the uneven population of the $He^+(3p)$ resonance by the XUV pulse in the co- or counter-rotating scenario affects the CD, we made the optical laser pulse arrive after the XUV pulse (LL, (optical) laser late) so that the helium atom or ion does not interact with the optical and XUV pulses at the same time.

Another similar study on lithium [50] showed that the CD can vary strongly with slightly different wavelengths of the optical laser, even if the central photon energy of the optical laser only changes by tens of meV. To see how tiny variations in the photon energy affect the CD, we used three different wavelengths in the experiment: 784 nm, 793 nm and 800 nm.

Additionally, we investigated how the CD is affected by laser intensities in the barrier-suppression regime, where the predictions from lowest order perturbation

theory (LOPT) might not hold anymore.
Further investigations were done regarding the angular distribution of the photoelectrons. The focus was on the ATI electrons, as the MPI electrons shift below the ionization threshold above a certain laser intensity, which makes it impossible to observe the angular distribution. The aim is to investigate how the transient resonances affect the angular distribution in the continuum.
In the upcoming sections, the experimental setup will be introduced. Afterwards, the experimental data is analyzed regarding the aspects mentioned above.

9.1 FERMI AND THE LDM ENDSTATION

FERMI [231] is a free electron laser facility located near Trieste in Italy. The name FERMI is an acronym for 'Free Electron Laser Radiation for Multidisciplinary Investigations'. The FEL generates light in the XUV and soft x-ray regime in the form of coherent ultrashort laser pulses. A set of special undulators of type 'Apple II' enables variable polarization of the light pulses [39]. FERMI has the advantage over most other FELs that it does not rely on the stochastic SASE process to generate XUV pulses but instead it uses the so-called high-gain harmonic generation (HGHG) mechanism. Usually, this is also called 'seeding', making FERMI a seeded FEL.
As highly relativistic free electrons are the source of the radiation, the first step is to create these free electrons. In the photo-injector, a polycrystalline copper cathode is illuminated by a picosecond UV laser pulse thereby creating electrons. The quantum-efficiency of copper at the UV lasers wavelength of 263 nm is $10^{-5} - 10^{-4}$ which requires the UV laser to have pulse energies of roughly 500 µJ to achieve the necessary bunch charge of around 1 nC. The repetition frequency at which the laser illuminates the cathode is 50 Hz. The UV pulse length can range from 1 ps to 20 ps. The freed electrons are accelerated by a radio frequency gun up to 5 MeV kinetic energy while at the same time being focused by solenoid magnets. In further elements the electrons are accelerated up to 100 MeV after which a laser heater is used to suppress micro-bunching instabilities and to control the energy spread of the electron bunch [232]. In the four upcoming LINAC (linear accelerator) sections the electron bunch is accelerated from 100 MeV up to 1.2 GeV in the FEL-1 branch of FERMI and accelerated up to 1.5 GeV in the FEL-2 branch.
As the electron bunch has reached its desired kinetic energy, it enters the undulator section. In the first short undulator, called the modulator, the electron bunch is co-propagating with the seed laser. The simultaneous interaction of the relativistic electron beam with the magnetic structure of the undulator and the co-propagating seed laser introduces an energy modulation with a period of the seed lasers wavelength. This energy modulation leads to a spatial modulation of the electron bunch at the seed laser's wavelength as the beam propagates further through the modulator and a dispersive section. Now the electron bunch is divided into micro-bunches. If the FEL is not seeded, the electron bunch instead interacts with light emitted from the electrons by spontaneous emission in the undulator structure. Because the spontaneous emission is a statistical process, every laser shot will vary according to the spontaneous emission. Compared to this, seeded FELs have better shot-to-shot reproducibility and longitudinal

coherence.
In the FEL-1 branch, the modulator is followed up by six undulators, called the radiators, which are tuned to a harmonic of the seed laser thereby generating intense XUV FEL radiation. The undulators in the radiator are of APPLE-II type which allows the generation of XUV light of arbitrary polarization. To ensure synchronization between the RF plants, the photoinjector and the seed laser FERMI uses an all-optical system. The FEL-2 functions similarly although it uses a double cascade of HGHG to be able to reach down to a wavelength of 4 nm [35]. After the XUV FEL pulse is generated the electrons are deflected into a beam dump. The wavelength of the light generated ranges from 100 nm (12.4 eV) to 20 nm (62.0 eV) for the FEL-1 branch and from 20 nm to 4 nm (310.0 eV) for the FEL-2 branch. The pulse duration is 30 fs to 100 fs and below 100 fs, respectively, while the pulse energy is up to 50 µJ for the FEL-1 branch and up to 10 µJ for the FEL-2 branch. The light, which is used in the experiments, is guided to the endstations via the beam transport system. This system and the capabilities of the LDM endstation are described by Svetina et. al. [233]. In the case of the LDM beamline, these are mirrors coated with graphite, gold, or graphite-iridium which are hit under a shallow angle as low as 2° to minimize losses. As there are many types of experiments, which all require different spectrometers and sample environments, there are different end-stations addressing specific scientific topics. The end-stations of FERMI are: EIS-TIMEX, EIS-TIMER, DiProl, TeraFERMI, MagneDyn and LDM. The experiment on helium was performed at the 'low density matter', LDM, end-station, which is specialized in investigating gaseous species. Common topics of research are non-linear light-matter interactions, dichroism and time-resolved experiments.
Before entering the chamber of the end-station the XUV beam is co-propagating with the seed laser. A set of aluminum filters with varying thicknesses can be used to absorb the seed laser at the cost of also slightly attenuating the XUV beam. Additionally, there are slits used to confine the beam or to reduce stray light. A fluorescent screen can be inserted into the FEL beam to observe and accordingly adjust the position of the FEL beam. Through a window perpendicular to the XUV beam, an optical laser can be coupled in to co-propagate with the FEL beam to the sample. This is important for many experiments where the optical laser will trigger a reaction that is probed by the XUV laser. To focus the beam a set of Kirkpatrick-Beaz mirrors is used [234]. After the beam has passed through the experimental chamber it enters the beam dump where it is absorbed and the beam path ends.
The endstation itself is of a modular nature [235]. It is composed of six vacuum chambers, which are aligned perpendicular to the XUV beam. The main purpose of these chambers is to provide a defined, dense sample beam of atoms, molecules, or clusters and to also provide analysis of the sample beam species independently of the XUV beam. The chambers which provide all this are in the order as follows: source chamber, doping chamber, differential pumping chamber, detector chamber, quadrupole mass spectrometer chamber, and surface ionization detector chamber. The latter two were not relevant for the experiment that we performed. A drawing of these chambers is shown in figure 57.
A schematic drawing of the inner parts of the detector chamber is shown in

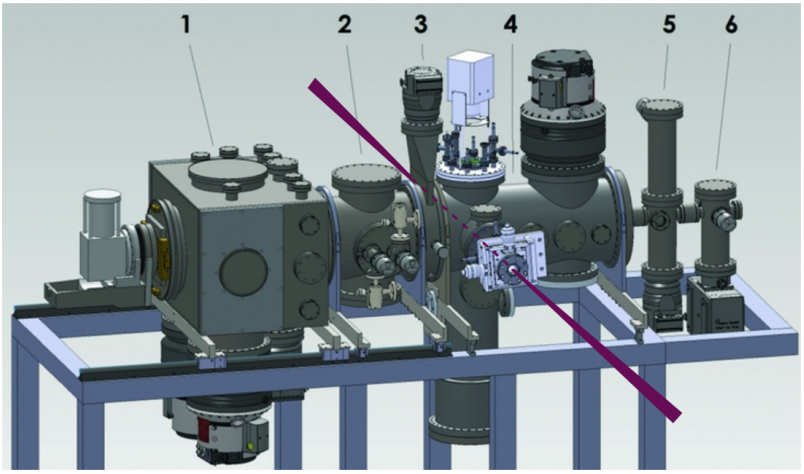

Figure 57: LDM endstation chambers. 1) Source chamber. 2) Doping chamber. 3) Differential pumping chamber. 4) Detector chamber. 5) Quadrupole mass spectrometer chamber. The violet lines show the beam path of the FEL. The figure has been adapted from [235].

figure 58. The source chamber holds a pulsed Even-Lavie valve, which operates at the repetition rate of the FEL and a skimmer that cuts a central part of the gas plume from the pulsed valve. In the doping chamber, clusters can be doped with other elements. After this, a differential pumping section cuts the beam further down via two slits to reduce the sample beam width to about 50 µm at the interaction region and ensures that the vacuum in the experimental chamber is not compromised by the gas which is cut from the sample beam. The detector chamber holds the spectrometers that observe the interaction of the XUV beam with the sample. The sample beam crosses the XUV beam at a right angle right in the center of the spectrometers. One of them is a VMI detector, which can analyse the angular distribution of ions and electrons. The detector used in this VMI is an MCP combined with a phosphorous screen. A camera films the glowing screen which then gives the image of the velocity distribution of the electrons or ions. Opposite to the VMI, on the other side of the interaction region, is a time-of-flight spectrometer that measures the kinetic energy of electrons or the mass of the ions. The voltages on the electrodes can be switched very quickly, within tens of nanoseconds, which allows to detect electrons with the VMI and ions with the ToF, or vice versa, from the same laser shot. Following the sample beam, there is a quadrupole-mass spectrometer, which can analyze the mass and type of particles in the sample beam.

9.2 BEAMTIME PREPARATIONS

To measure the effect of the dichroism, we analyse the kinetic energy and angular distribution of the photoelectrons freed by multi-photon ionization (MPI) and above-threshold ionization (ATI) using a velocity map imaging spectrometer (VMI).
To image electrons with a VMI spectrometer, it is crucial to have a small interac-

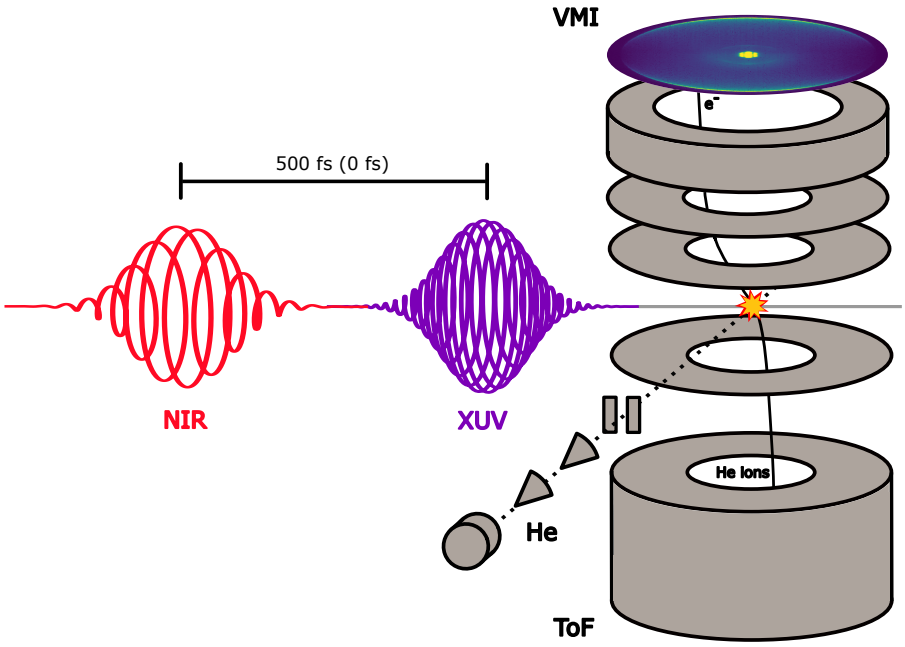

Figure 58: Schematic drawing of the interaction region. The two laser pulses (time delayed by 500 fs or overlapping) interact with the neutral helium atoms in the interaction region. The electrons are pushed onto the VMI detector, while the ions are pushed into the time of flight spectrometer.

tion volume between the sample gas and the laser pulses to ensure good resolution of the velocity distribution for the electrons on the detector. The biggest issue regarding the size of the interaction volume is its dimension along the propagation direction. Any point along the FEL beam acts as a source of photoelectrons, which are pushed onto the detector, where they create a smeared-out distribution. To overcome this issue, a gas jet is used to shape the sample distribution in the interaction region. The jet consists of a nozzle, two skimmers and a pair of blades. With this arrangement, it is possible to create a very narrow (about 2 mm long), dense sheet of gas, which enables a good distribution resolution on the detector. Additionally, the gas jet operates with a pulsed valve, which reduces the amount of gas entering the experimental chamber. The backing pressure of the helium gas at the valve was 20 bar, while the opening time was 140 µs. The temporal overlap of the gas pulse with the laser pulse was optimized by varying the delay of the valve's opening time until the helium ion yield was maximized. Here the ToF spectrometer was used to measure the helium ion yield.
Since we wanted to observe electrons with a kinetic energy of more than 35 eV, the 50 eV voltages setting of the VMI spectrometer was used. The next step is overlapping the NIR and XUV laser pulses spatially and temporally. The spatial overlap is found by comparing the beam positions on a YAG imager. To find the temporal overlap of the XUV laser pulse with the NIR laser pulse, the delay of the NIR laser pulse was changed, while the XUV pulse was tuned to the helium 5p resonance characterized by a lifetime of 7.7 ns [236]. If the pulses overlap or the NIR pulse arrives late, a low-energy electron signal produced by multi-photon ionization of the 5p resonance can be measured and used to minimize the temporal

delay. Finally, to find the precise overlap at the XUV photon energy corresponding to the ionic 3p resonance, the temporal delay was optimized using the signal of the sidebands. These sidebands arise as the photoelectrons from the ionization of the helium atoms are also in interaction with the NIR field, where they can absorb NIR photons to gain more kinetic energy, or emit NIR photons into the NIR field [237]. This leads to additional peaks in the photoelectron spectrum separated by the NIR photon energy. The better the overlap of the pulses is, the greater the yield of the sidebands will be and the more orders of sidebands will appear [238].
The final step is to fine-tune the XUV wavelength to the 3p (m = +1) helium ion resonance, which we want to populate. For this, the helium di-cation yield is measured, while the XUV wavelength is tuned. When the resonance is populated, helium di-cations are created via multi-photon ionization by the NIR laser.

9.3 OVERVIEW AND CALIBRATIONS

To give an overview of what features were observed in the experiment and how the VMI images are analyzed, we start with a simple image, figure 59 a), showing the detector image of helium interacting only with the XUV laser pulse at a photon energy of 48.37 eV, a laser intensity of $1 \cdot 10^{13}$ W/cm^2 at a pulse energy of 70 µJ and a pulse duration of 100 fs (FWHM). The photon energy of 48.37 eV corresponds to the energy required to excite a helium ion from the 1s ground state into the excited 3p state. The corresponding VMI image shows that the photoelectron distribution has a symmetric shape around the beam propagation axis, which is horizontally in the image. The radius at which a photoelectron hits the VMI detector is proportional to its velocity component parallel to the surface of the detector. For the given photon energy and an ionization potential of 25.59 eV for helium [239], this results in a kinetic energy of the photoelectron of 22.87 eV, which also defines the velocity of the photoelectron. Around the atom, the photoelectron is emitted in a certain direction in a three-dimensional space. As it is obvious from the detector image, a large number of photoelectrons are actually emitted with a velocity component perpendicular to the detector. To get from this projected 3D distribution to the original 3D velocity distribution, we use the so-called Vrakking algorithm following a publication by Marc J. J. Vrakking [169]. This algorithm assumes that the 3D photoelectron angular distribution is rotationally symmetric around the beam propagation axis for circularly polarized light, which is justified in our case. The result of this Vrakking algorithm is shown in figure 59 b). This image shows a slice through the 3D angular distribution of the photoelectron. The radius corresponds to the total velocity of the photoelectron and not just the component parallel to the detector. By rotating the distribution around the beam propagation axis, the full 3D angular distribution can be retrieved.

The faint circle in the center part of figure 59 a) arises from stray light hitting the detector. Since this stray light contribution is smaller on the upper detector half, all the reconstructed images were mirrored to only include the top half of the velocity distribution while the lower half was discarded.
To calibrate the relation between the distance from where a particle hit the detector to the detector's center and the kinetic energy of the particle, we need to generate electrons with varying kinetic energies, which was realized by changing

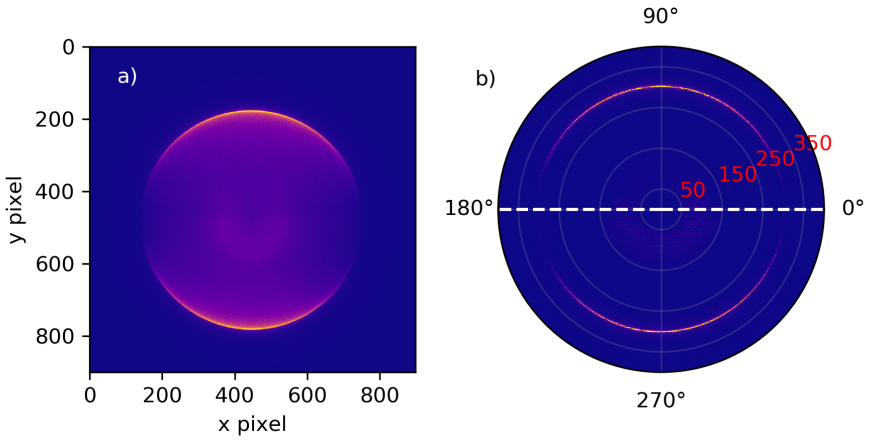

Figure 59: a) Camera image of the phosphorous screen behind the VMI's MCP. The XUV pulse is traveling through the image horizontally. b) Inverted image using the Vrakking algorithm. The dotted white line indicates the beam propagation direction. The red numbers indicate the distance in pixel to the center of the distribution.

the photon energy of the XUV pulses. For this task, a number of harmonics of the seed-lasers photon energy were used, which can be selected by changing the tapering of the undulators. Figure 60 a), shows an overlay of reconstructed photoelectron velocity distributions when ionizing helium with different harmonics of the FERMI FEL. The outermost ring corresponds to the 10th harmonic (48.37 eV) and each ring further corresponds to the next lower harmonic, ending up at the 6th harmonic. From the radial profile of this detector image in figure 60 b), we can assign to each of the peaks a kinetic energy by knowing the photon energy of the FELs harmonics. This mapping of the radial coordinate to electron kinetic energy is shown in 60, c), and a parabolic fit is added, to extend the calibration to other, not measured, kinetic energies. A parabola is chosen since this relation is expected by theoretical considerations [162]. The only fit parameter necessary is an amplitude A scaling, which gives a fit parameter of $2.6144 \cdot 10^{-4}$ eV. This parabola is used in all upcoming figures with a kinetic energy axis. The fact that the calibration is described by a parabola has implications for the energy resolution. In the center of the detector, the spatial separation of evenly spaced kinetic energies is larger than at higher kinetic energies, meaning the kinetic energy resolution will be better at the center of the detector, i. e. at lower kinetic energies, and will get linearly worse at higher kinetic energies and detector radii.

Until now we have only considered spectra of photoelectrons, created by the XUV pulses. Adding now the optical laser (NIR), different features will show up. The NIR laser pulses have a central wavelength of 784 nm with a bandwidth of 13 nm (FWHM), corresponding to a photon energy of 1.58 eV with a bandwidth of 26 meV (FWHM). The pulse duration is 140 fs (FWHM). Different scenarios are realized in the experiment: (a) the polarization vector of the optical laser is co- (↻ ↻) or counter-rotating (↺ ↻) relative to the XUV lasers polarization and (b) the optical laser pulse arrives at the same time as the XUV laser pulse (T0) or with a 500 fs delay (LL) to exclude that the XUV (100 fs FWHM) and

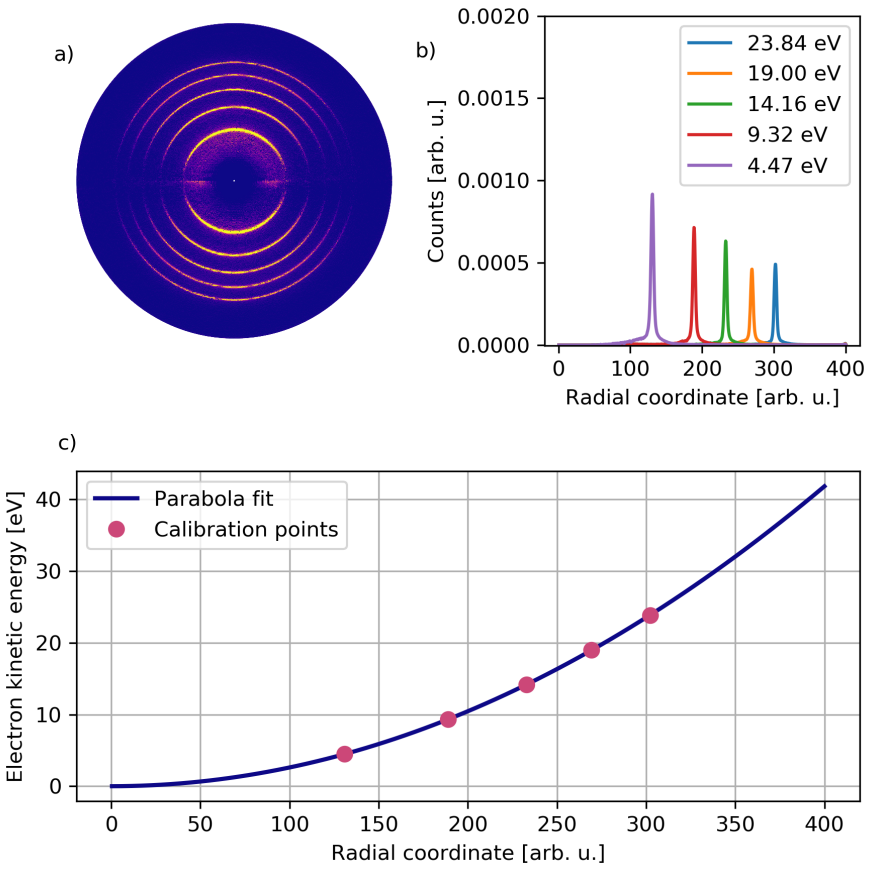

Figure 60: a) Reconstructed 2D velocity distribution of helium ionized with the 10th to the 6th harmonic of the FERMI FEL overlayed. b) Radial profile for each of the photoelectron distributions of the different harmonics. c) Parabola fit through the calibration points.

NIR pulse (140 fs FWHM) overlap significantly in time. How these four possible configurations change the photoelectron angular distribution, is shown in figure 61 for an NIR laser intensity of $3.6 \cdot 10^{12}\,\mathrm{W/cm^2}$. In all four images, additional features are clearly visible at low kinetic energies. These electrons are produced by multi-photon and above-threshold ionization of the populated 3p (m = +1) state of the helium ion. The only possibility without the NIR would be the absorption of another XUV photon after being excited into the 3p (m = +1) resonance, which would correspond to the interaction of three XUV photons with a single helium atom. This would result in photoelectrons with kinetic energies of 42.4 eV, which we cannot observe with the kinetic energy range of the detector.

Another visible effect is the difference in the angular distribution of the MPI electron in the co- (a, c) and counter-rotating (b, d) case. In the co-rotating case, two lobes are visible, while in the counter-rotating case we observe six lobes. As explained earlier, the application of co- and counter-rotating NIR laser pulses leads to the formation of different final states in the continuum with different quantum numbers. The angular distribution of the MPI electron will depend on these quantum numbers and thus is different for the two cases. The difference in the angular

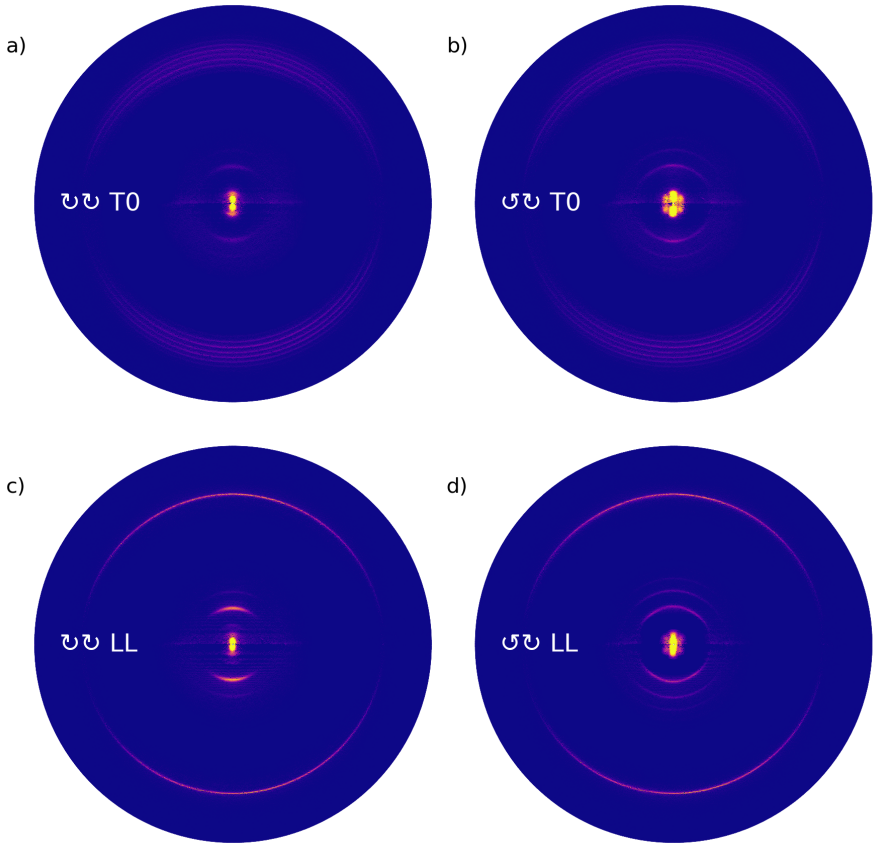

Figure 61: 2D velocity distribution for different combinations of the XUV and NIR pulses a) co-rotating and temporally overlapped b) counter-rotating and temporally overlapped c) co-rotating and NIR 500 fs delayed d) counter-rotating and NIR 500 fs delayed. The peak intensity of the optical laser is $3.6 \cdot 10^{12}$ W/cm^2.

distributions is also already an observation of a circular dichroism.
Another obvious change is related to the kinetic energies of the photoelectron produced by the ionization of the neutral helium atom, i. e. in the outer, high kinetic energy region of the image. In the case of temporally overlapping XUV and NIR pulses, the kinetic energy of the photoelectron starts to split into sidebands. Looking at the 2D distributions in the case of separated XUV and NIR pulses, these structures disappear, since the XUV and NIR pulse don't overlap temporally and thus the photoelectrons from the XUV pulse are never in interaction with both the XUV and the NIR laser field. The features of the MPI electron do not seem to change a lot at first sight, when changing between the time-zero (a, b) or laser late (c, d) configuration.
To derive the kinetic energy distribution of the photoelectrons, the images are integrated over all angles. An example of such a derived spectrum is shown in figure 62. For detector radii up to 200, the peaks correspond to MPI and ATI from the excited 3p state of the helium ion. For detector radii larger than 200, one peak appears for temporally separated pulses which is the photoelectron originating from the ionization of the neutral helium atom via the XUV pulse (XUV photoelectron). In the case of overlapped pulses, the photoelectron can interacts also with the field

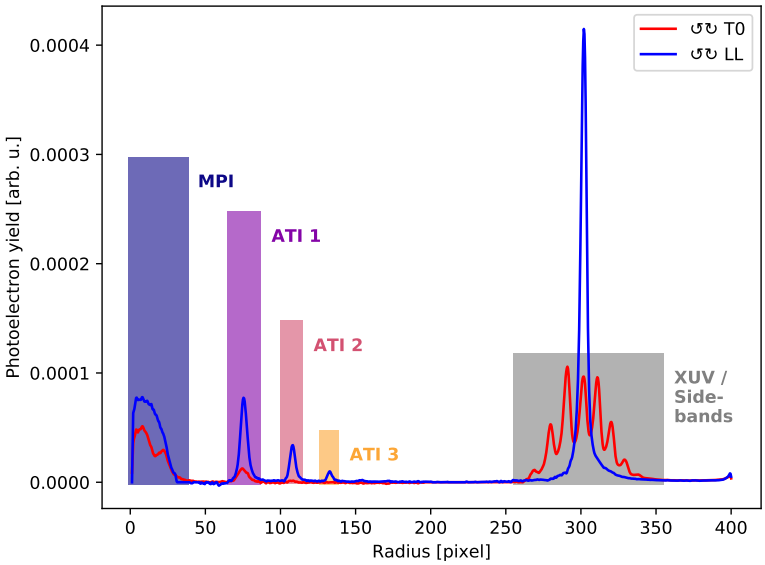

Figure 62: Photoelectron spectra for the counter-rotating case of temporally overlapped pulses (T0) and temporally separated (LL) pulses. The peak intensity of the optical laser is $3.6 \cdot 10^{12}\,\mathrm{W/cm^2}$. The peaks are marked with colored faint regions and labeled accordingly.

of the optical laser, leading to the formation of sidebands, which are visible here as additional peaks. The transformation of a pixel to an energy axis is done using the calibration derived from the mapping of different known kinetic energies to different detector radii, which was previously shown in figure 60.

For investigating the dependence of the photoelectron spectra on different NIR laser intensities, we need a way to convert pulse energies into laser intensities in the interaction volume. Since precise experimental parameters (focus size, diameter of the gas jet, etc.) are often difficult to extract, we have established a procedure to derive the laser intensities from sideband spectra measured in the experiment and compare them to sideband spectra calculated via TDSE simulations. By matching the theoretical spectra to the experimental spectra, it is possible to calibrate the laser intensity used in the experiments. This comparison is done for three different laser wavelengths, 784 nm, 793 nm and 800 nm that were used in the experiment. Figure 63 shows the procedure and the resulting calibration curve. The first four plots show photoelectron sideband spectra of the three different wavelengths. The pulse energies are chosen to match a theoretical sideband spectrum at a fixed intensity. The simulations were performed at a central wavelength of 784 nm of the optical laser and we assume that there is only little difference in the sideband spectra for the three different central wavelengths used in the experiment. We only try to match the most and least energetic sidebands, as additional sideband orders are an indicator for higher laser intensities. The central part of the sidebands does not overlap well with the simulations, which might be due to the neglect of volume integration, which was not included in the simulations, and the longer optical pulse duration of 175 fs used in the simulations compared to 140 fs in the experiment. The resulting four pairs of laser intensity to pulse energy points are then fitted with a line providing the calibration from pulse energy to laser intensity, which is

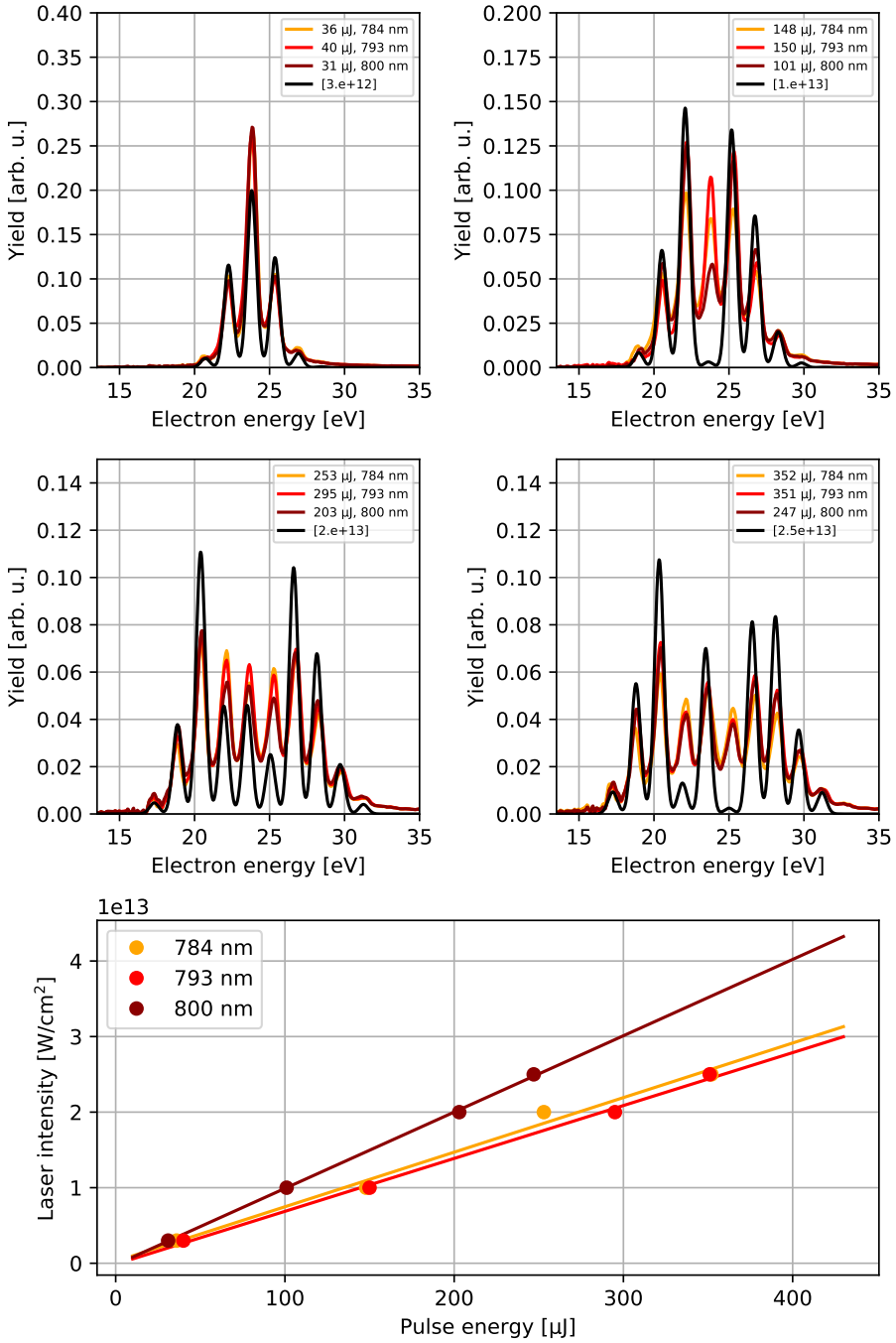

Figure 63: Calibration of the laser intensity using calculated sideband spectra and matching them with measured sideband spectra. The four upper images show the overlay of calculated spectra and experimental spectra, while the lower image shows the best fit of lines to the calibration points obtained.

used as a calibration.
Checking the differences in the sideband spectra between co- and counter-rotating optical laser pulses shows that the difference is on the order of a few percent, see [40], and thereby negligible for our purpose, meaning that we can use the calibration for both polarizations of the optical laser pulse (see figure 63 in the appendix). Later in the evaluation of the data, when comparing the measured and computed circular dichroism, we find discrepancies, which can be resolved by dividing the laser intensity determined using the sidebands by a factor of three. Why the laser intensity is so much higher when using the sidebands to calibrate the laser intensity is not really clear. It might be related to the computations not using a laser pulse with the same properties as the one used in the experiment. For example, the pulse length in the experiment was 140 fs whereas the pulse in the simulations is limited to 60 fs (FWHM). It should also be noted that the calculated sideband spectra do not originate from the same computations as the calculated spectra of the MPI and ATI photoelectrons or the CD, presented in the following sections. The initial intensity calibration using the sidebands is still handy to calibrate the different wavelengths relative to each other since the sideband spectra depend less on small variations of the photon energy than the CD and we only have access to computations performed using a wavelength of 784 nm.

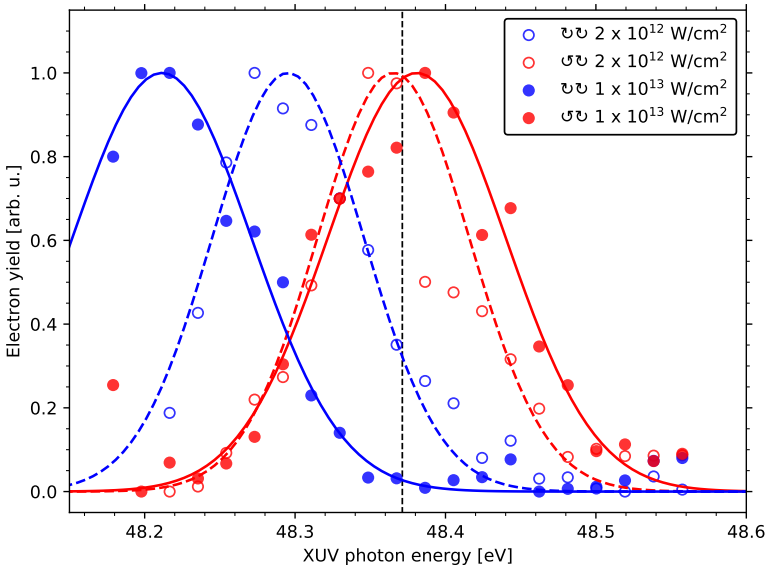

Figure 64: Yields of MPI and ATI (1, 2, 3, ...) photoelectrons for different photon energies of the XUV pulse in the presence of an intense optical laser field (784 nm) with co- (blue curves) or counter-rotating (red curves) polarization relative to the XUV pulse. This yield is shown for two different peak laser intensities of the optical laser. The photon energy at which the unperturbed 3p resonance is, is marked by the dotted line. Gaussians are fitted to the data points.

9.4 AC-STARK SHIFT OF THE 3P RESONANCE

In a first experiment, we were aiming to confirm the shift of the 3p resonance in the helium ion. For this, we chose two intensities of the optical laser, $2 \cdot 10^{12}\,\mathrm{W/cm^2}$ and $1 \cdot 10^{13}\,\mathrm{W/cm^2}$ at the central wavelength of 784 nm, which was also used in the previous experiment [48]. For both of these laser intensities we used the two polarization combinations and scanned the FEL photon energy over the region where one would expect the unperturbed 3p resonance of the helium ion to lie energetically. To observe the shift we measured the yield of the MPI and ATI (1, 2, 3, ...) photoelectrons. The result of this investigation is shown in figure 64. The maximum in the MPI and ATI photoelectron yield in the case of counter-rotating laser pulses is centered around the 3p resonance at $2 \cdot 10^{12}\,\mathrm{W/cm^2}$. At $1 \cdot 10^{13}\,\mathrm{W/cm^2}$ the resonance seems to be shifted towards higher energy by about 10 meV. The calculations in [51], see figure 97, predict that the shift should not exceed 10 meV, at least not up to a laser intensity of $2 \cdot 10^{12}\,\mathrm{W/cm^2}$. For the co-rotating case this is very different, where already at the lower laser intensity the resonance shifts by about 80 meV towards lower XUV photon energies. The calculations predict a shift of 90 meV towards lower XUV photon energies at a laser intensity of $2 \cdot 10^{12}\,\mathrm{W/cm^2}$. At $1 \cdot 10^{13}\,\mathrm{W/cm^2}$ this shift is 160 meV towards lower XUV photon energies. For this laser intensity there are no calculations to compare the results to. Overall the validity of arguments brought forward in earlier studies [48] to explain the strong variation of the CD in the resonant multi-photon ionization process could be confirmed here, one of which is the population asymmetry of the helium ions $3p_{+1}$ state for the two different polarization combinations induced by the AC-Stark shift.

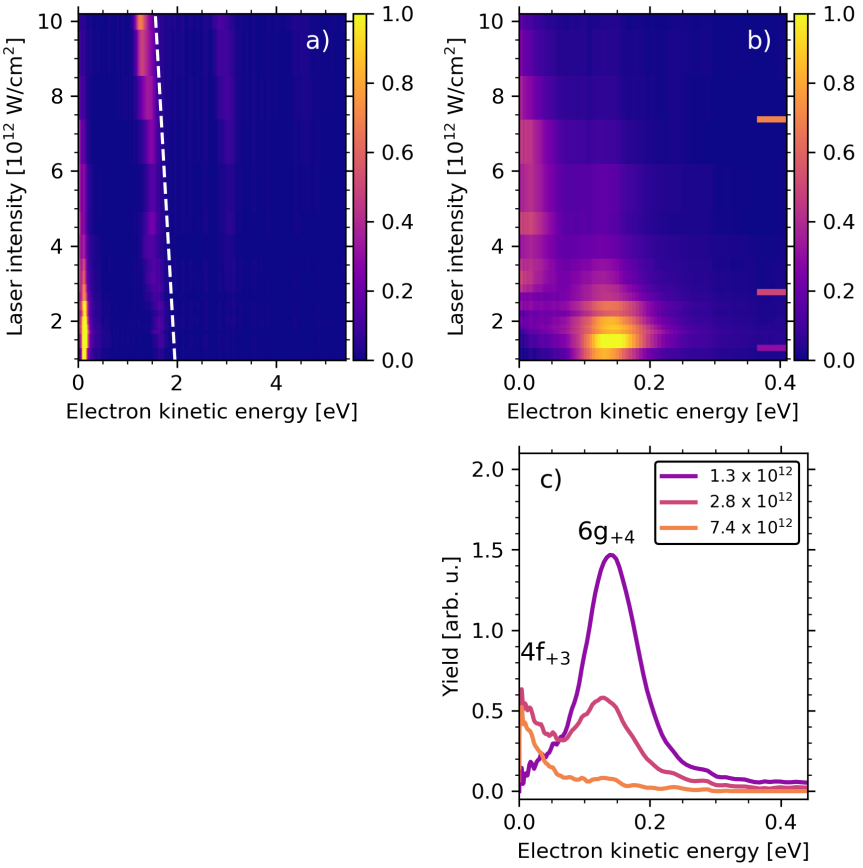

Figure 65: a) Kinetic energy distribution of the low-energy electrons for different laser intensities. b) Same as in a), but focusing on the MPI electron. c) shows line-outs of the 2D plots at different laser intensities. Shown is the counter-rotating case, with the central wavelength of the optical laser at 784 nm. The scale of the colormap in a) and b) is chosen to highlight all the important features. A white line indicating a linear shift of the kinetic energy with the laser intensity is shown in a), next to the ATI feature.

9.5 CIRCULAR DICHROISM WITH POPULATION ASYMMETRY

The first aspect of the experiment that is presented here, is the extension of the studies, which were presented in the paper by M. Ilchen et al. [48]. In the recent experiment, we used a wider range of laser intensities, which provides a more detailed insight into the intensity dependence of the circular dichroism. Before considering the circular dichroism at different laser intensities, the intensity dependence of the electron kinetic energy spectrum is analyzed and interpreted for the two polarization combinations of the XUV and NIR.

As a starting point, we will investigate the scenario of co-rotating pulses. Figure 65 a) shows a 2D map of the laser intensity dependent kinetic energy distribution of the electrons. Different lines are clearly appearing, each corresponding to a different feature of the ionization induced by the optical laser. The peak around 0 eV to 0.4 eV corresponds to MPI electrons and were created by the absorption of four

NIR photons from the populated 3p(m = +1) state. The additional peaks separated by the NIR photon energy or multiples thereof correspond to ATI electrons. With increasing laser intensity, the kinetic energy of the electrons decreases. The cause of this is the NIR field, which leads to the so-called ponderomotive shift, see section 2.2. Electrons in an oscillating light field will have a certain average quiver energy. This energy has to be provided by the photons in addition to the ionization potential. As the laser intensity increases, the average quiver energy of a free electron in the light field increases, shifting the ionized electron's kinetic energy to lower values. In figure 65 a) the ATI electrons show a shift towards lower kinetic energies of about 400 meV. This is of similar value as the expected ponderomotive potential difference of 500 meV between laser intensities of $1 \cdot 10^{12}\,\mathrm{W/cm^2}$ and $1 \cdot 10^{13}\,\mathrm{W/cm^2}$ and thus the main reason for the shift in kinetic energy. For better visualization, a white broken line is introduced, which shows a linear shift in kinetic energy as would be expected by the intensity dependence of the ponderomotive potential. At a laser intensity of $9 \cdot 10^{12}\,\mathrm{W/cm^2}$ most of the MPI feature has shifted below the ionization threshold, which is referred to as 'channel closing'.

The detailed kinetic energy structure of the MPI electrons kinetic energy is shown in figure 65 b) for different laser intensities. Looking at the kinetic energy of the MPI electrons we can see that there are two features. At the lowest laser intensity there is one main feature at 140 meV. With increasing intensity, another feature appears, which has its maximum at the ionization threshold i.e. at vanishing kinetic energies. These are electrons with barely enough energy to escape the attractive potential of the doubly charged helium ion. In figure 65 c) this becomes more clearly visible, as traces recorded at three different laser intensities are shown. The fact that there is more than one feature hints at a phenomenon called resonance-enhanced multi-photon ionization (REMPI). This effect occurs if a higher lying state of, in our case an atom, has an energy, which can be reached by the absorption of an integer amount of photons from the initial state. These resonant excitation processes greatly enhance the ionization probability.

States that enable this resonant ionization can be found when taking integers of the photon energy and compare these energies to the energy difference between the 3p level and excited states with principal quantum numbers $n > 3$. To calculate the energy of the helium ion levels the following formula is used: $E_{ij} = -13.6 \cdot Z^2 \left(\frac{1}{n_i^2} - \frac{1}{n_j^2} \right)$ [60]. It gives the energy difference E_{ij} between two states i, j with principal quantum numbers n_i, n_j for a hydrogen-like atom of charge Z. For example the energy difference between the state with $n = 3$ and the excited state $n = 4$ is 2.64 eV. The combined energy of two photons corresponding to a wavelength of 784 nm is 3.16 eV. Thus the gap between the states with $n = 3$ and $n = 4$ has to increase by 520 meV to allow for a resonant excitation.

For $n = 3$ and $n = 6$ the energy difference is 4.53 eV, which is close to the energy of the sum of three photons with 4.75 eV. If the energy difference between the $n = 3$ and $n = 6$ states increases by 210 meV, resonant excitation can take place via the absorption of three photons.

The energy gaps can and will be bridged by the AC-Stark shift, see section 2.2, which is the energy shift of electronic states in an intense laser field. Since this shift depends on the quantum numbers of the electronic states, the shift is in general different for different states, enabling a closing of the energy gap and resonant

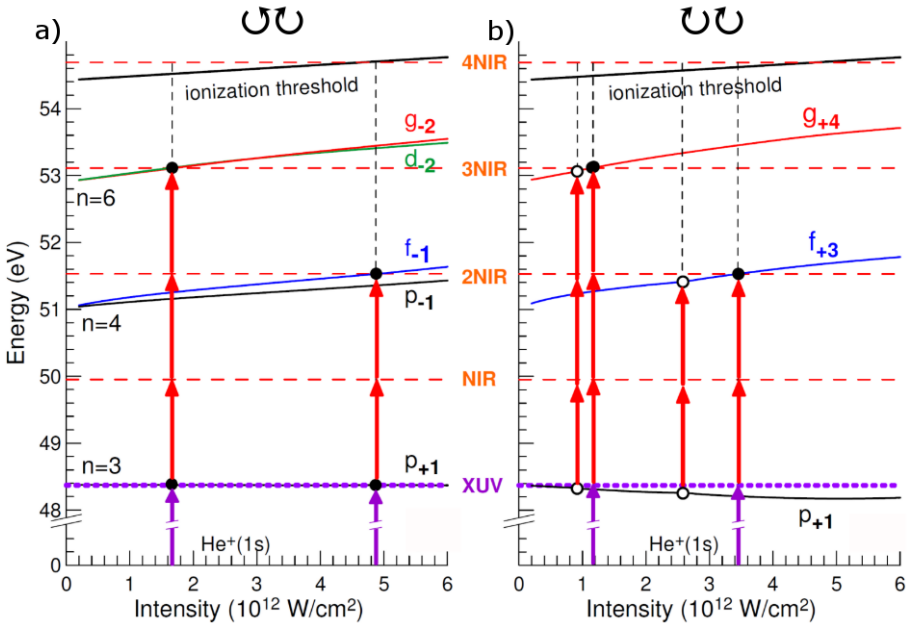

Figure 66: Shown are the quasi-energies of helium ion states depending on the NIR laser intensity relative to the helium ions 1s state for the a), counter-rotating case and b), co-rotating case. The figure is taken from [51] and has been adapted.

excitation at certain laser intensities. The bandwidth of the laser of 26 meV is low enough to identify ionization via a resonant excitation.
States with principal quantum numbers larger than $n = 6$ don't play a role at low laser intensities, since four photons are already enough to reach the continuum from the 3p resonance. At higher laser intensities this changes, when the ponderomotive shift, the AC-Stark shift for unbound electronic states, increases the effective ionization potential so far that states just below the ionization threshold with high $n > 15$ can be resonantly excited via the absorption of four photons.
The requirements of the selection rules in dipole transitions allow the possible excited states to be more precisely defined as $n\ell_m$ with n being the principal quantum number, ℓ being the angular momentum quantum number, expressed by letters ($\ell = 0, 1, 2, 3, 4, ...$ is equivalent to $\ell = s, p, d, f, g, ...$) and m being the magnetic quantum number. For the co-rotating case the relevant excited states are $4f_{+3}$ and $6g_{+4}$. For the counter-rotating case these are $4p_{-1}$, $4f_{-1}$ and $6d_{-2}$, $6g_{-2}$.

A theory-study from 2019 by a collaborator, A. Grum-Grzhimailo [51], investigates the quasi-energies of the helium ions eigenstates in a NIR laser field of varying intensity and different polarizations and solves the time-dependent Schrödinger equation (TDSE) for co- and counter-rotating laser pulses. The findings of the former are presented in figure 66 showing the quasi-energies relative to the 1s ground state of the helium ion for the two polarization combinations. In the calculation of the quasi-energies only the NIR field was taken into account and the light field was assumed to be monochromatic and of infinite duration.
First we consider the results of the calculations for co-rotating pulses in figure 66 b). The states shown are the initial $3p_{+1}$ ionic state and higher lying states with angular and magnetic quantum numbers, which could match the allowed transitions ($\Delta\ell = +1$, $\Delta m = +1$, for each photon absorbed) after absorption of a

certain number of NIR photons from the co-rotating NIR pulse. The length of the red arrows corresponds to the NIR photon energy. As the laser intensity increases, all states will are affected by the AC-Stark shift. The magnitude of the shift is determined by the polarizability of the state, see chapter 2.2. While some states shift up in energy relative to the $1s_0$ state, like the $4f_{+3}$ ($\ell = 3$, $m = +3$) and $6g_{+4}$ ($\ell = 4$, $m = +4$) states, others shift down in energy, like the $3p_{+1}$ ($\ell = 1$, $m = +1$) state. In addition transitions are indicated for the co-rotating case that don't rely on the excitation of the $3p_{+1}$ resonance, but on direct ionization from the ionic $1s_0$ ground state by absorbing one XUV photon and the NIR photons simultaneously. For the counter-rotating case, shown in figure 66 a), the shift of the $4p_{-1}$ ($\ell = 1$, $m = -1$), $4f_{-1}$ ($\ell = 3$, $m = -1$), $6d_{-2}$ ($\ell = 2$, $m = -2$) and $6g_{-2}$ ($\ell = 4$, $m = -2$) states is positive. The energy of the $3p_{+1}$ resonance does not depend on the NIR laser intensity (≤ 10 meV difference).
Different resonant transitions can be identified and related to a well-defined laser intensity. At low laser intensities around $1 \cdot 10^{12}\,\mathrm{W/cm^2}$ for the co-rotating case in figure 66 b), the $6g_{+4}$ state is in resonance after absorption of three NIR photons from the $3p_{+1}$ state. At a slightly higher laser intensity, there is also the possibility for resonant ionization by directly absorbing one XUV and three NIR photons. At a laser intensity of $2.7 \cdot 10^{12}\,\mathrm{W/cm^2}$, resonant ionization via a two NIR photon transition between the $3p_{+1}$ and the $4f_{+3}$ states is possible. At $3.4 \cdot 10^{12}\,\mathrm{W/cm^2}$ the direct $1s_0 - 4f_{+3}$ transition is resonant with the absorption of one XUV and two NIR photons. Since the NIR pulse has a certain pulse-length and varying intensity along the pulse envelope, these resonances occur only at certain times along the laser pulse. Such resonances are called 'transient' or 'Freeman' resonances [75, 77, 240, 241], see section 2.2. They first appeared as a sub-structure to the MPI and ATI peaks in the photoelectron spectrum in strong field ionization of xenon when using laser pulses with pulse durations less than 1 ps. Finally, with further increasing laser intensity, the ionization potential shifts to such high energies, that the absorption of four NIR photons is not sufficient any longer to overcome the ionization threshold from the $3p_{+1}$ state and the MPI feature shifts below the ionization threshold. It should be noted that the nomenclature for unperturbed states is used here, although they are influenced by the electric field of the laser pulses.

Based on these experimental results the distinct features observed in the experimental data (figure 65 c) can be explained by the resonances that occur during different times within the laser pulse. At the lowest laser intensity of $1 \cdot 10^{12}\,\mathrm{W/cm^2}$ up to $2.3 \cdot 10^{12}\,\mathrm{W/cm^2}$, we can only see one larger feature at 140 meV kinetic energy, which corresponds to ionization via the resonant three photon $3p_{+1} - 6g_{+4}$ transition at $1 \cdot 10^{12}\,\mathrm{W/cm^2}$.
The kinetic energy of the MPI photoelectron being created via a resonance is derived from figure 97 b), which is located in the appendix. It shows the quasi-energies of resonant ionization via the relevant states relative to the ionization threshold after the absorption of four photons for a range of laser intensities. That we can still observe resonant ionization via the $6g_{+4}$ transition at higher laser intensities has two reasons. First, once the intensity is above the laser intensity required for resonant transition, the resonant transition can still take place, just

not at the peak of the laser pulse envelope, but at different times within the envelope.
Following figure 97 b), the resonance should be at a kinetic energy of 180 meV instead of the measured 180 meV, indicating that the energy calibration of the detector might not be exact. This might very well be possible due to the calibration points lying in the eV range, whereas the features that we investigate lie in the $100\,meV$ range. The $1s_0 - 6g_{+4}$ resonant transition via one XUV and two NIR photons also contributes to this and should appear at a kinetic energy that is 20 meV higher. Due to the width of the peak centered around 140 meV of 100 meV FWHM, it is not possible to distinguish the two ionization pathways. These two features have the highest kinetic energies since the lower laser intensity at the time of ionization is directly related to a lower ionization potential.
Considering now higher laser intensities of $2.7 \cdot 10^{12}\,W/cm^2$ and above, another feature appears at the ionization threshold, which corresponds to the sequential resonant ionization involving the $3p_{+1} - 4f_{+3}$ transition induced by absorbing two NIR photons. This process should lead to a feature centered around a kinetic energy of 10 meV following figure 97 b), but in our experiment, the feature seems to be already slightly below the ionization threshold. The direct ionization via the $1s_0 - 4f_{+3}$ ($3.4 \cdot 10^{12}\,W/cm^2$) transition might play a role, as the corresponding feature should appear at a kinetic energy of 80 meV, where we indeed see some signal in the low energy tail of the peak centered around 140 meV.

If the NIR pulse polarization is counter-rotating to the XUV pulse, the situation is different. Figure 67 shows the experimental results for this case. The first noticeable aspect is that the higher ATI features are more pronounced compared to the co-rotating case. Looking at the MPI photoelectron spectrum in figure 67 c), three features can be distinguished. The highest energy feature is centered around 130 meV, the next at higher laser intensities around 60 meV. The third feature is visible as a tail to the ionization threshold. Comparing these results to quasi-energy calculation for the counter-rotating case (figure 66 a), it is clear that different resonant transitions play a role here. At a laser intensity of $1.6 \cdot 10^{12}\,W/cm^2$ a three NIR photon resonant transition between the $3p_{+1} - 6g_{-2}$ and $3p_{+1} - 6d_{-2}$ states is possible, leading to the feature centered around 130 meV, which is close to the predicted 170 meV from 97 a). The feature centered around 60 meV cannot be assigned to any resonant transition following the diagram in figure 66 a) or 97 a). It might arise due to an energetic splitting of the $6d_{-2}/6g_{-2}$ resonance which appears due to an avoided crossing, similar to the avoided crossing that appears for co-rotating laser pulses between the helium ions $1s_0$ and the $6g_{+4}$ state, see figure 97 b). The pronounced tail at the ionization threshold can be assigned to the $3p_{+1} - 4f_{-1}$ resonance via absorption of two NIR photons that occurs at a laser intensity of $4.85 \cdot 10^{12}\,W/cm^2$. Channel closing takes place at a similar intensity as it did in the co-rotating case around $1 \cdot 10^{13}\,W/cm^2$.

After having identified the individual lines showing up in the photoelectron spectrum, we will now analyze their intensity dependent yield. The yields have been calculated by summing up the region of kinetic energies for the inspected lines, which is shown in figure 68. Sub-figure a) shows the total yield of all MPI

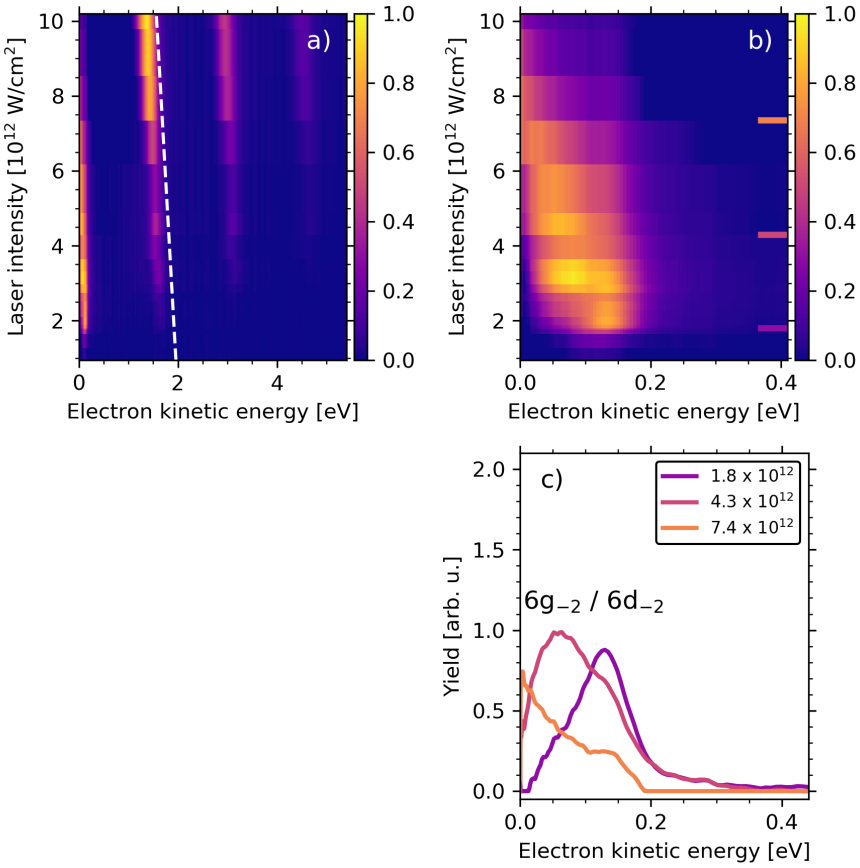

Figure 67: a) Laser intensity dependent kinetic energy distribution of the electrons. b) Same as in a), but focusing on the MPI electron. c) shows line-outs of the 2D plots at different laser intensities. Shown is the counter-rotating case, the wavelength of the optical laser is 784 nm. Brighter colors correspond to higher values. The scale of the colormap is chosen to highlight all the important features. A white line indicating a linear shift in kinetic energy is shown in a), next to the ATI feature.

and ATI electrons for co- (blue curve) and counter-rotating (red curve) pulses. At the lowest laser intensity, the yield in the co-rotating case is higher than in the counter-rotating case. TDSE calculations in reference [48] showed that the MPI ionization probability is roughly 50 times higher in the co-rotating case at a laser intensity of $7.3 \cdot 10^{11}\,\mathrm{W/cm^2}$. At the lowest laser intensity, which was used in the present experiment ($1 \cdot 10^{12}\,\mathrm{W/cm^2}$), a value of 21 was deduced. With increasing laser intensity the ionization in the counter-rotating case becomes more probable compared to the co-rotating case. The reason for this is the polarization dependent AC-stark shift of the $3p_{+1}$ state in the oscillating NIR field. As the wavelength of the XUV is fixed and the difference in energy between the $1s_0$ and $3p_{+1}$ states becomes smaller, the XUV pulses cannot efficiently populate the $3p_{+1}$ state during the whole XUV pulse duration any longer, resulting in a decrease of the ionization probability and is thus limiting the MPI and ATI electron yield. With further increasing NIR laser intensity the time during which the $3p_{+1}$ resonance cannot be efficiently populated increases up to a certain point, from where on the yield

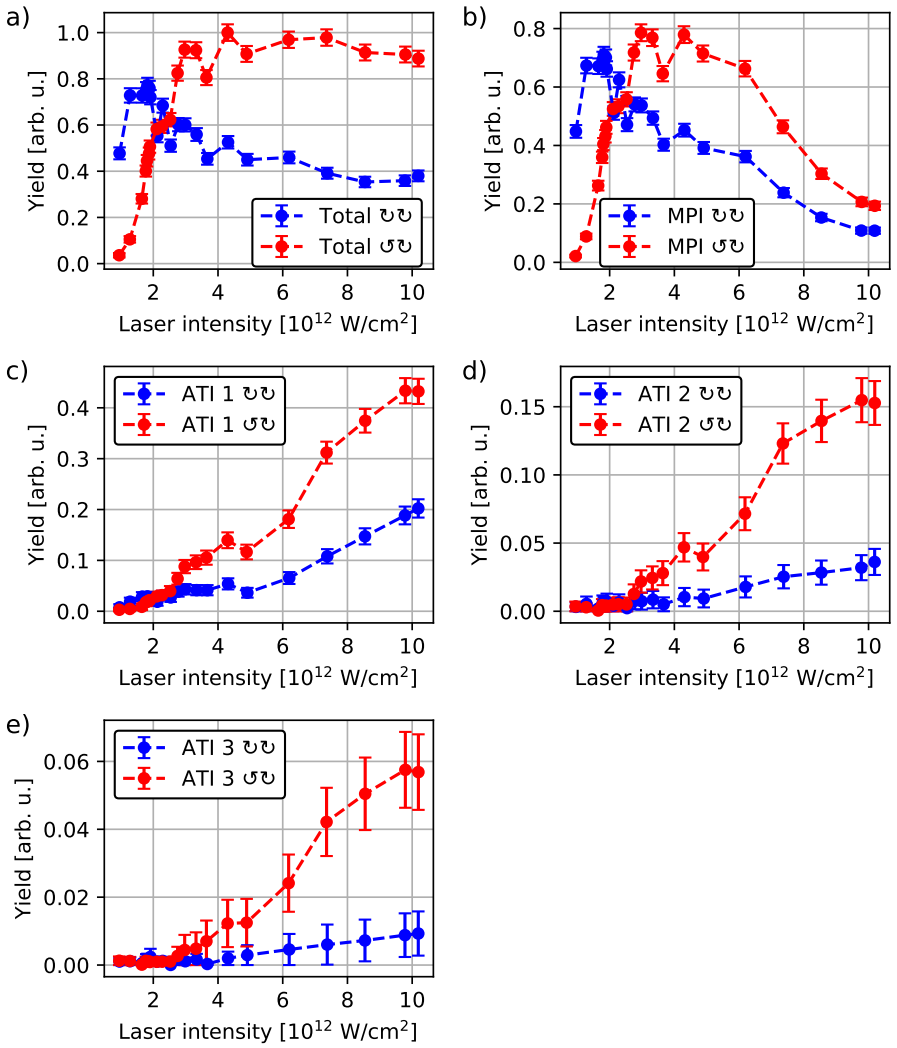

Figure 68: Yields of different electron lines as a function of the NIR intensity for temporally overlapped pulses. The blue curves show the yield in the case of co-rotating pulses, the red curves show the yield in the case of counter-rotating pulses. a) compares the total yield, while other figures focus on a specific line: b) MPI, c) ATI, d) ATI 2, e) ATI 3.

stagnates. Since the NIR pulses and the XUV pulses overlap, some helium ions can always be resonantly excited at relatively low IR intensities and thus there will always be a certain amount of resonantly excited helium ions which can be ionized by the NIR pulse. For the counter-rotating case the $1s_0 - 3p_{+1}$ resonance does not significantly change in energy and thus allows for excitation of the helium ions throughout the whole XUV pulse duration. With increasing laser intensity the yield starts to saturate at $5.0 \cdot 10^{12}\,\mathrm{W/cm^2}$, as all the excited helium ions are ionized even before the whole NIR pulse passed the excited atoms. Although the total yield has saturated, the relative contribution from each of the photoelectron features can still change.

Figure 68 b) shows the yield of the MPI electrons for the co- and counter-rotating case. The traces of the yield look very similar to those for the total yield at low laser intensities since it is the ionization channel with the highest ionization proba-

bility. With increasing laser intensity, the yield in both polarization cases decreases strongly, due to the shift of the MPI feature below the ionization threshold. For the co-rotating case, this shift below the ionization threshold happens at lower laser intensities compared to the counter-rotating case due to the additional shift of the $3p_{+1}$ resonance. For the yield in the co-rotating case, two maxima at laser intensities of $1.7 \cdot 10^{12}\,\mathrm{W/cm^2}$ and $2.7 \cdot 10^{12}\,\mathrm{W/cm^2}$ are observed. The first arises due to the three-photon NIR resonance with the $6g_{+4}$ intermediate state. The second arises when the low energy feature in the electron spectrum appears (Fig. 65 b, c), corresponding to the resonant ionization via the $4f_{+3}$ intermediate state. A similar behaviour is observed for the yield in the counter-rotating case. The strong ramp of the yield at lower laser intensities is due to the resonant three NIR photon ionization from the $3p_{+1}$ state over the $6g_{-2}$ and $6d_{-2}$ states (cf. figure 67). The first maximum at $3 \cdot 10^{12}\,\mathrm{W/cm^2}$ is due to a resonant feature at 80 meV in the photoelectron spectrum. Another maximum at $4.1 \cdot 10^{12}\,\mathrm{W/cm^2}$ is promoted by a two NIR photon resonance with the $4f_{-1}$ state.
Considering now the yields for the ATI lines in figure 68 c), d) and e), they all have a very similar trend and the electron yield in the co-rotating case is in general less than in the counter-rotating case throughout all the ATI features above a certain laser intensity. One of the reasons for this is the lower population of the $3p_{+1}$ resonance in the co-rotating case. In the counter-rotating case the yield of the ATI 1 features is very little up to a laser intensity of $1 \cdot 10^{12}\,\mathrm{W/cm^2}$, from where on the yield increases, before it starts to flatten at the highest laser intensities due to saturation setting in. Saturation appears when the optical laser is intense enough to ionize all the prepared helium ions. The rather sudden increase in yield in both polarization cases arises as the MPI feature shifts below the ionization threshold, as then high-lying Rydberg states lead to additional resonant transitions, thereby increasing the ionization probability.

After discussing how the laser intensity influences the yield of the photoelectrons at different laser intensities, we consider the circular dichroism, which is calculated from the yield. The circular dichroism is shown in figure 69 and is calculated in the following way:

$$\mathrm{CD} = \frac{Y_{co} - Y_{cont}}{Y_{co} + Y_{cont}} \tag{50}$$

with Y_{co} being the yield in the case of co-rotating and Y_{cont} being the yield in the case of counter-rotating laser pulses. What was observed for the yield in the two different cases can now be condensed into the circular dichroism (CD), which compares the yield of the two different polarization combinations. The circular dichroism of the MPI electron is close to unity at the lowest laser intensity and decreases with increasing laser intensity until the dichroism passes the zero at $2 \cdot 10^{12}\,\mathrm{W/cm^2}$, where the yield for both polarization combinations is equivalent. Around a laser intensity of $4 \cdot 10^{12}\,\mathrm{W/cm^2}$ the CD reaches a value of -0.25 and decreases only slightly for higher intensities. Comparing this to the TDSE predictions from the 2017 paper [48], we find a similar behaviour. There the CD starts close to unity and then crosses zero at an intensity of $1.52 \cdot 10^{12}\,\mathrm{W/cm^2}$ and then ends at -0.17 for $1.62 \cdot 10^{12}\,\mathrm{W/cm^2}$, the highest simulated intensity and showing the ten-

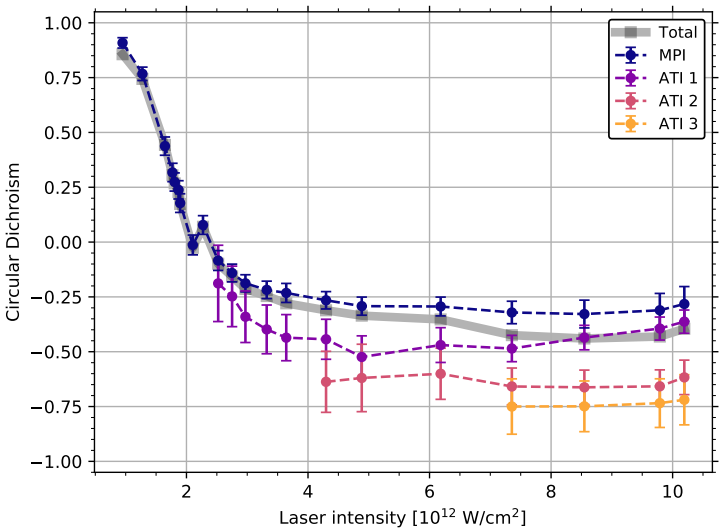

Figure 69: Dichroism of the four different lines of the photoelectron spectrum, MPI, ATI, ATI 2 and ATI 3 for temporally overlapped laser pulses. In grey, the circular dichroism of all photoelectrons ionized by the NIR pulse is shown.

dency to decrease further at higher laser intensities. These observations underline that the interpretation of the results and the model used to predict these results in the previous study seem to be valid.
The CD of the first ATI electron shows a very similar behaviour as the MPI electron. The CD reaches a lower value of -0.5 at a laser intensity of $5 \cdot 10^{12}\,\mathrm{W/cm^2}$. From there on the CD slightly increases up to -0.3. The higher the ATI order, the lower the CD value becomes, showing that ionization in the counter-rotating case is overall more efficient with each increasing order in the non-linear ionization processes as the laser intensity increases towards the saturation regime. The CD of the second ATI is around -0.65 and the CD of the third ATI is around -0.75 at the highest laser intensities.

9.6 CIRCULAR DICHROISM WITH BALANCED INITIAL POPULATION

To exclude effects caused by an imbalance in the $3p_{+1}$ population for the two combinations of polarizations affecting the circular dichroism, the XUV and NIR pulses were separated in time so that the NIR pulse arrives 500 fs after the XUV pulse. This ensures that the pulses don't overlap temporally. The population of the $3p_{+1}$ resonance will not significantly change during this time, as the lifetime of excited states is on the order of nanoseconds [242]. In addition the simultaneous absorption of XUV and multiple NIR photons becomes impossible.
As in the case of temporally overlapped pulses, first, the intensity dependence of the MPI and ATI photoelectrons in the two different polarization combinations is considered. The corresponding results are shown in figure 70 for the co-rotating case. Again the theoretical calculations by A. Grum-Grzhimailo are used to explain the appearance of certain distinct features in the kinetic energy distribution of

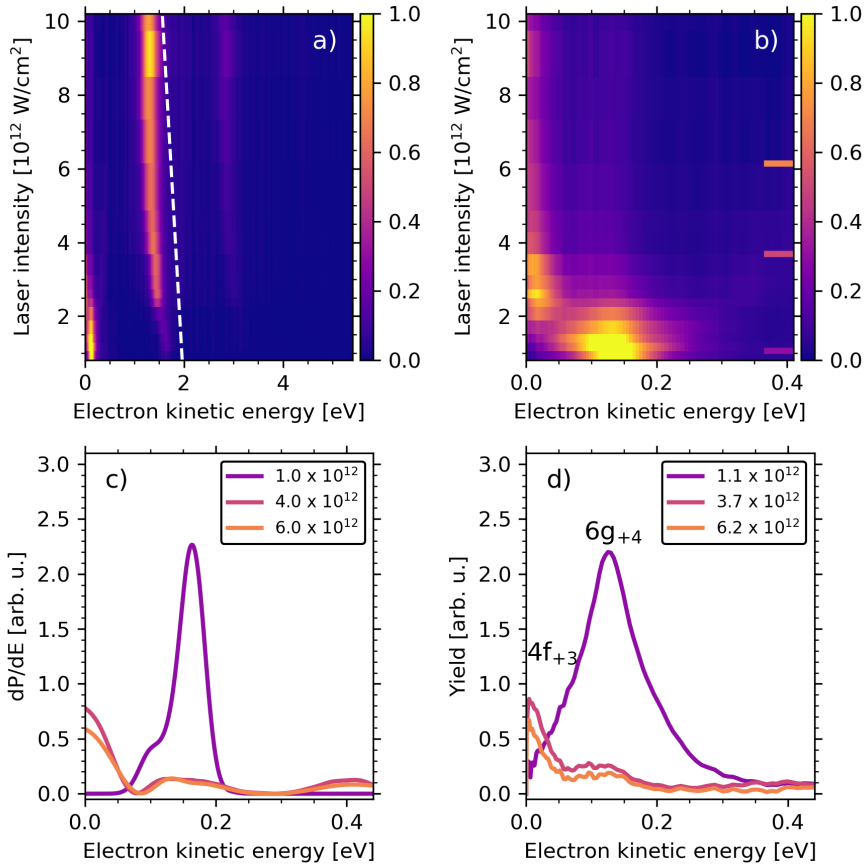

Figure 70: a) Kinetic energy distribution of the low energy electrons as a function of laser intensity. b) Same as in a), but focusing on the MPI electron. d) shows line-outs of the 2D plots at different laser intensities. d) Photoelectron spectra calculated using TDSE. The XUV and NIR are co-rotating and temporally separated. The wavelength of the optical laser is 784 nm. The scale of the color map in a) and b) is chosen to highlight all the important features. A white line indicating a linear shift in kinetic energy is shown in a), next to the ATI feature.

the MPI electrons. The first feature noticeably different is the change in kinetic energy of the ATI electrons compared to the case of overlapping laser pulses (cf. Fig. 65). Here the change to lower kinetic energies is much more gradual. With increasing laser intensity the ATI electrons shift to lower kinetic energies up to a laser intensity of $6.7 \cdot 10^{12}\,\mathrm{W/cm^2}$. The reason for this might be due to saturation, the fact that the XUV pulse prepares a defined number of helium ions in the 3p state. If all of these prepared ions are already ionized by the NIR pulse before it reaches its maximum laser intensity, the electrons don't experience the higher laser intensities throughout the pulse duration and thus they can't shift further towards lower kinetic energies. Details of the MPI electron's kinetic energy are presented in figure 70 b). At the lowest laser intensities, there is only one main feature centered around a kinetic energy of 130 meV, which can be attributed to the three NIR photon resonant $3p_{+1} - 6g_{+4}$ transition (see figure 66 b)). With increasing laser intensity, this feature shifts slightly towards lower kinetic energies and at $2 \cdot 10^{12}\,\mathrm{W/cm^2}$ a low energy feature appears close to the threshold. This

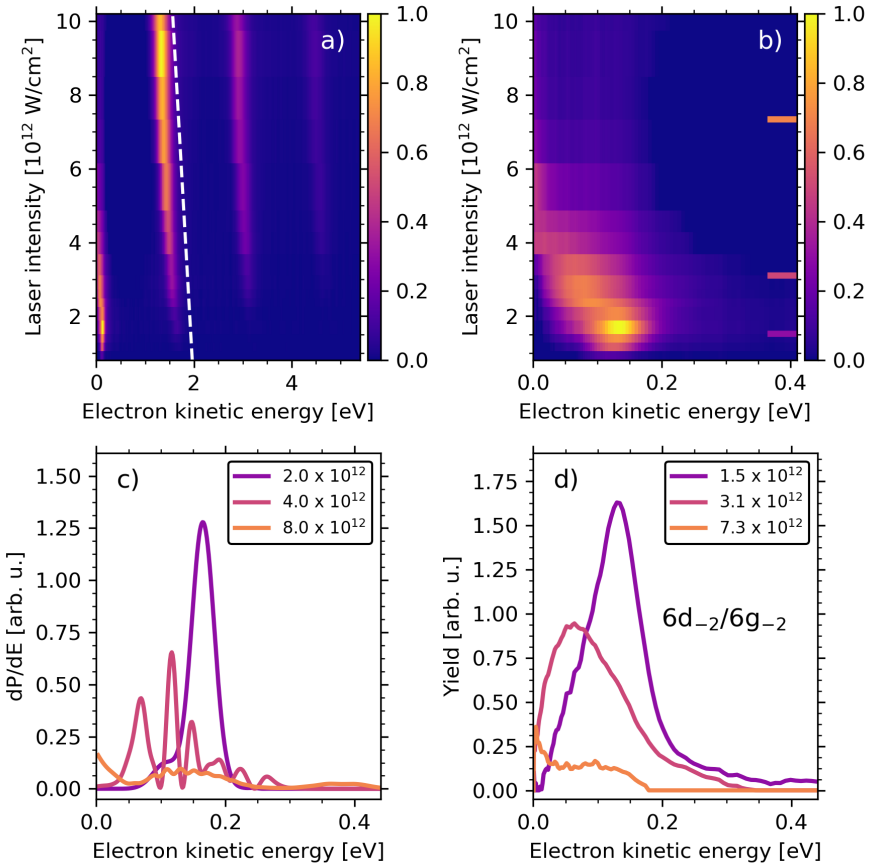

Figure 71: a) Kinetic energy distribution of the low energy electrons as a function of the laser intensity. b) Same as in a), but focusing on the MPI electron. c) shows line-outs of the 2D plots at different laser intensities. d) Photoelectron spectra calculated using TDSE. The XUV and NIR are counter-rotating and temporally separated. The wavelength of the optical laser is 784 nm. The scale of the color map in a) and b) is chosen to highlight all the important features. A white line indicating a linear shift in kinetic energy is shown in a), next to the ATI feature.

feature arises due to the two NIR photon $3p_{+1} - 4f_{+3}$ resonance. Comparing the calculated, using TDSE, (Fig. 70 c) and the measured (Fig. 70 d) photoelectron spectra, we find good agreement between the two. Channel closing appears around a laser intensity of $5 \cdot 10^{12}\,\mathrm{W/cm^2}$.

The spectra of MPI and ATI electrons for the counter-rotating case are shown in figure 71. The smooth shift to lower energies for the ATI electrons is seen in figure 71 a), as we already saw it in the co-rotating case (cf. Fig. 70 a). Another feature already observed in the case of overlapping pulses is that higher ATIs are more pronounced in the counter-rotating case at higher laser intensities. The shift of the MPI feature, displayed in figure 71 b) and c), is very gradually compared to other configurations and could be very well linearly approximated. Again multiple features are observed, of which some can be connected to Freeman resonances (cf. Fig. 71 c). The feature at 130 meV arises due to the three NIR photon resonant transitions $3p_{+1} - 6d_{-2}$ and $3p_{+1} - 6g_{-2}$ at $1.7 \cdot 10^{12}\,\mathrm{W/cm^2}$. The

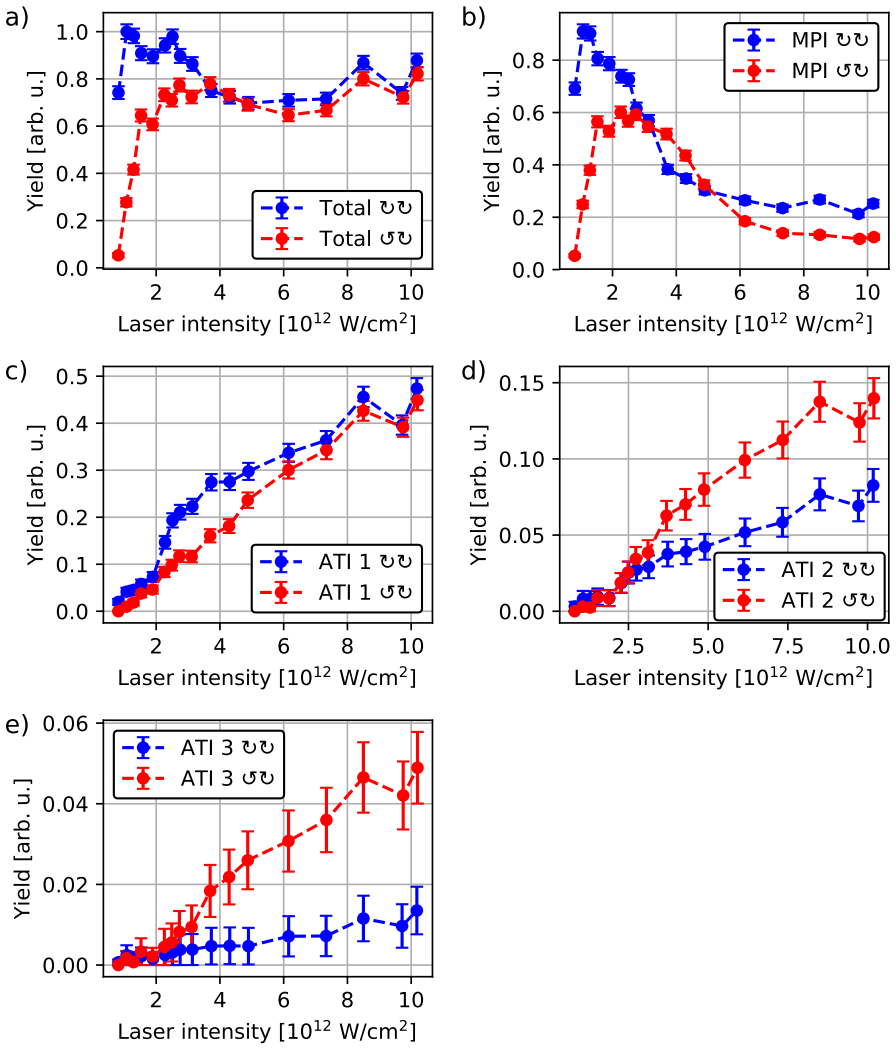

Figure 72: Yields of different electron lines as a function of the NIR intensity for temporally separated pulses. The blue curves show the yield in the case of co-rotating pulses, the red curves show the yield in the case of counter-rotating pulses. a) compares the total yield, while other figures focus on a specific line: b) MPI, c) ATI, d) ATI 2, e) ATI 3.

feature centered around 65 meV cannot be attributed to a certain resonance, at least not following the quasi-energy calculations in figure 66 a). Finally, above $3.5 \cdot 10^{12}\,\mathrm{W/cm^2}$, the tail of the resonance just below the ionization threshold appears, which is connected to the two NIR photon $3p_{+1} - 4f_{-1}$ resonance. At the highest laser intensities, most of the MPI feature shifts below the ionization threshold, which in turn enhances all the ATI features through high-lying Rydberg states in the region of higher laser intensity. Channel closing appears at a laser intensity of $8 \cdot 10^{12}\,\mathrm{W/cm^2}$, which is higher compared to the co-rotating case due to the additional AC-Stark shift of the $3p_{+1}$ resonance towards lower energies that is much more significant for the co-rotating case.

To understand the origin of the circular dichroism, we will first investigate how the yield of the electron lines changes as a function of the NIR intensity

in the co- and counter-rotating case. As in the case of overlapping laser pulses, the total amount of ionization in the co-rotating case is favoured at lower laser intensities (figure 72 a). From an intensity of $3.5 \cdot 10^{12}\,\mathrm{W/cm^2}$ on the yield of both polarization combinations is very similar and stays similar with further increasing laser intensity. In contrast to the situation where the laser pulses arrive at the same time, the yield in the co-rotating case does not drop, since the $3p_{+1}$ resonance is populated before the arrival of the NIR pulse. This way both, co- and counter-rotating laser pulse polarization, interact with the same amount of helium ions prepared in the $3p_{+1}$ state.
Considering the MPI yield in figure 72 b), the yield curves show a smoother behaviour compared to the situation when the laser pulses overlap temporally (cf. Fig. 68 b). In the case of co-rotating pulses, the yield has a maximum at $1 \cdot 10^{12}\,\mathrm{W/cm^2}$. With increasing laser intensity the yield decreases as the MPI feature shifts below the ionization threshold. If the XUV and NIR pulse counter-rotate, the maximum appears at a higher laser intensity of $2.7 \cdot 10^{12}\,\mathrm{W/cm^2}$ and is very broad. Compared to the co-rotating case the maximum appears at higher laser intensities due to the lower ionization probability at lower laser intensities and the shift of the MPI feature below the ionization threshold at higher laser intensities. At laser intensities far in the saturation regime, the yield in the counter-rotating case drops below the yield in the co-rotating case. The reason for this can be observed in the intensity dependent kinetic energy of the MPI feature for co-rotating pulses where the $4f_{+3}$ resonance near threshold is much more persistent, from $2 \cdot 10^{12}\,\mathrm{W/cm^2}$ to the highest laser intensity, compared to the $4f_{-1}$ resonance at threshold, from $3.5 \cdot 10^{12}\,\mathrm{W/cm^2}$ to $7 \cdot 10^{12}\,\mathrm{W/cm^2}$, for counter-rotating pulses (cf. Fig. 70 a).
For the ATI feature in figure 72 c), the yield increases linearly in the counter-rotating case. This is in contrast to the co-rotating case, where the yield strongly increases above a laser intensity of $2 \cdot 10^{12}\,\mathrm{W/cm^2}$, which is where the MPI feature starts to shift below the ionization threshold. In the counter-rotating case, the shift below threshold happens at a higher intensity, where saturation has set in.
The yield of the second ATI, shown in figure 72 d), increases as the MPI features shift below threshold. From there on the yield in the counter-rotating case surpasses the yield in the co-rotating case, which will lead to a strong circular dichroism. For the third ATI, shown in figure 72 e), the situation is similar. Again we can see the yield in the counter-rotating case surpassing the yield in the co-rotating case, showing that ionization via non-linear processes of higher orders is more efficient for counter-rotating pulses.

From the yields, the circular dichroism of the different electron lines can be calculated (73). The circular dichroism of the MPI feature is close to 1 at the lowest available laser intensity of $8 \cdot 10^{11}\,\mathrm{W/cm^2}$, due to the more effective ionization in the co-rotating case at lower laser intensities [48]. With increasing laser intensity the circular dichroism decreases and becomes negative at $3.8 \cdot 10^{12}\,\mathrm{W/cm^2}$, due to the earlier shift below threshold of the MPI feature for co-rotating pulses. From there on the circular dichroism recovers and even becomes positive again at an intensity of $6.2 \cdot 10^{12}\,\mathrm{W/cm^2}$, due to the saturation of the total electron yield in combination with the increased ionization probability for ATI features in the

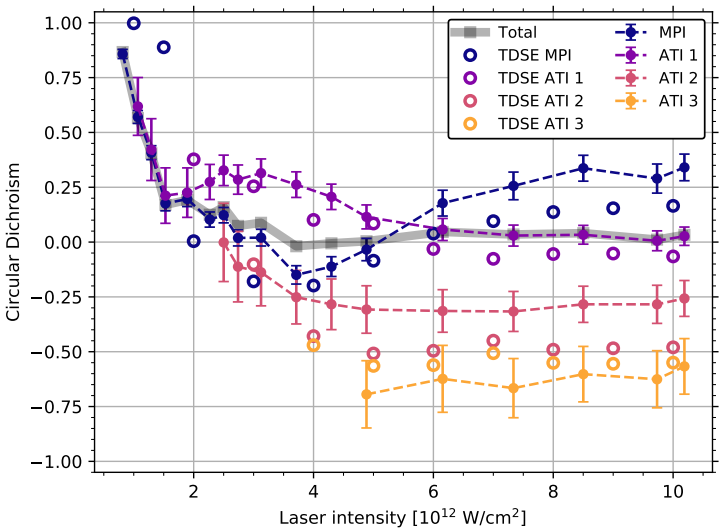

Figure 73: Circular dichroism of the four different lines of the electron spectrum, MPI, ATI, ATI 2 and ATI 3 for temporally separated pulses. The circles show results from TDSE calculations.

counter-rotating case compared to the co-rotating case and the more persistent resonance above threshold for co-rotating pulses. This recovery of the CD did not appear for overlapped pulses, where the CD at higher laser intensities is dominated by the population imbalance induced by the $3p_{+1}$ shift in the NIR laser field. Values from TDSE simulations (circles in figure 73) predict similar values for the circular dichroism of the MPI feature. Discrepancies can be the result of missing volume integration for the calculated spectra and the shorter pulse length in the calculation of 60 fs compared to the pulse length in the experiment of around 140 fs (FWHM). The CD values have been derived from separate calculations in regards to the calculated photoelectron spectra shown earlier.
The initial intensity dependence of the ATI circular dichroism at low laser intensities is similar to the MPI. Until a laser intensity of $1.5 \cdot 10^{12}\,\mathrm{W/cm^2}$ the CD decreases, since ionization in the counter-rotating case becomes more probable compared to the co-rotating case with increasing laser intensity. As the MPI feature drops below the ionization threshold, the ATI yield is enhanced for the co-rotating case due to ionization via high-lying Rydberg states, which leads to the CD increasing again. From $3 \cdot 10^{12}\,\mathrm{W/cm^2}$ on the CD starts to decrease again, as the MPI feature also shifts below threshold in the counter-rotating case and enhanced ionization via high-lying Rydberg increases the yield. As the laser intensity approaches saturation at $8 \cdot 10^{12}\,\mathrm{W/cm^2}$, the yield in both cases becomes similar, leading to a vanishing CD. That the plateau in the CD is not reproduced in the TDSE calculations might be related to the shorter pulse durations of the NIR used in the calculations.
The second ATI's CD starts at zero and decreases monotonously with increasing laser intensity until at $4.9 \cdot 10^{12}\,\mathrm{W/cm^2}$ the CD reaches a value of -0.30, from where the CD increases to -0.25 at the highest laser intensity. The CD of the third ATI is -0.70 at a laser intensity of $4.9 \cdot 10^{13}\,\mathrm{W/cm^2}$. With increasing laser intensity

the CD recovers slightly up to -0.55 at the highest laser intensity. The deviation of the CD predicted by TDSE calculations is more pronounced for the two highest investigated ATI features but the calculations agree with the overall trend of the CD. The calculations and the experimental results show that the higher the order of the non-linear ionization process involved, the more negative the CD becomes at the highest laser intensities.

The main differences in the CD for the temporally overlapped and separated laser pulses can be found when comparing the MPI and ATI features. At low laser intensities, where the AC-Stark shift of the eigen-energies is not so significant, the behaviour is very similar for the MPI. It starts out positive, close to one, and from there on decreases, due to the shift below the ionization threshold and due to the shift in energy of the $1s_0 - 3p_{+1}$ transition, which leads to less efficient population of the $3p_{+1}$ state. The latter is also the reason for the crossing of zero CD happening at lower laser intensities for temporally overlapped pulses, as these two effects decrease the CD, while for temporally separated pulses only one effect, which is the shift below threshold, decreases the CD.
As the pulses overlap, the CD of the first ATI decreases similarly to the MPI, due to the energy shift of the $1s_0 - 3p_{+1}$ transition. For separated pulses, the CD decreases with increasing laser intensity until a laser intensity of $1.5 \cdot 10^{12}\,\mathrm{W/cm^2}$ and then stagnates around 0.25 up to $4.0 \cdot 10^{12}\,\mathrm{W/cm^2}$, due to resonant ionization by high lying Rydberg states in the co-rotating case at lower laser intensities compared to the counter-rotating case. At the highest laser intensities, the CD goes to zero as saturation sets in.
The second and third ATI's CD is negative at most laser intensities, as they appear once saturation has set in and in saturation the counter-rotating case favours ionization into the higher ATI features, leading to negative CDs.

In conclusion, we have observed a circular dichroism in the photoelectron yield when ionizing the helium ion in the $3p_{+1}$ state by multi-photon ionization in an intense NIR laser field. In the previous experiment [48], it was argued that the intensity dependence of the CD originates from an imbalance in the population of the $3p_{+1}$ state from which the optical laser ionizes the helium ions. The origin of this imbalance in the population of the $3p_{+1}$ state was the helicity dependent AC-Stark shift of the $3p_{+1}$ state. While for counter-rotating pulses this shift is vanishingly small, it is significant for co-rotating pulses, leading to fewer electrons that could be ionized from the $3p_{+1}$ state via multi-photon absorption, which was assumed to be a contribution to the observed intensity dependent CD.
To entangle the influence of the population imbalance on the CD, we separated the laser pulses, so that the optical pulse arrives 500 fs after the XUV pulse, which allows to prepare the same amount of helium ions in the $3p_{+1}$ state independent of the polarization of the optical laser pulse. This led to differences in the CD for overlapped and separated XUV and NIR laser pulses, which are apparent for all the photoelectron features. For the MPI feature, the CD still decreases as the intensity of the optical laser increases, because the main driver is the increase of the ionization potential that leads to a shift of the MPI feature below the ionization threshold. For the MPI feature, this shift happens at already lower laser intensities

in the co-rotating case due to the additional shift of the $3p_{+1}$ state to lower energies. This shows that the population imbalance, that appears for overlapped pulses, is not the only contributor to the decrease in the CD.
The influence of the population imbalance clearly appears at higher laser intensities. Here the CD in the case of overlapped pulses stays negative, due to the population imbalance, while, surprisingly, for separated pulses, the CD becomes positive again. The reason for this is that at higher laser intensities only the photoelectron yield of resonances close to the ionization threshold contributes to the overall yield of the MPI photoelectrons. Where in the case of co-rotating pulses the $4f_{+3}$ resonance lies 10 meV above the ionization threshold at resonance, the $4f_{-1}$ resonance for counter-rotating pulses lies 10 meV below the ionization threshold. Due to the laser's bandwidth, photoelectrons can still be created, but the amount is limited compared to the co-rotating case, where the resonance is slightly above the ionization threshold.
Apart from the broader intensity dependence of the CD, we could observe Freeman-resonances ($4f_{+3}$, $6g_{+4}$ for the co-rotating case and $4f_{-1}$, $6d_{-2}$, $6g_{-2}$ for the counter-rotating case) in the intensity dependent photoelectron spectra and were able to match observed resonances to quasi-energy calculations. Additionally, we could measure the CD of ATI features, showing that higher-order ATI features are favored at higher laser intensities for temporally separated and overlapped pulses, leading to a negative CD. With this knowledge we will, in the next chapter, extend the investigation to an even higher intensity region at a slightly different wavelength.

9.7 CIRCULAR DICHROISM IN THE BARRIER-SUPPRESSION REGIME

After the discussion of the circular dichroism in the multi-photon regime of laser intensities, we will now investigate how the yield and circular dichroism change when the laser intensity is increased up to and above the regime of over-barrier-ionization (OBI). The laser intensity at which this is reached for an ionization potential of 6.05 eV (He^+ 3p) is $1.2 \cdot 10^{13}\,W/cm^2$. Here we reach laser intensities of up to $3 \cdot 10^{13}\,W/cm^2$. As observed before, saturation will play a significant role, especially for temporally overlapped NIR and XUV pulses. The central wavelength of the optical laser is slightly changed from 784 nm to 793 nm (1.56 eV), which was necessary to achieve a higher pulse energy of the optical laser pulses. We can expect that the earlier explanation of the observed features is not much affected, since the bandwidth of 22 nm covers the previous wavelength and the central photon energy is only slightly different with 18 meV. Therefore it is expected that the same resonances will play a role in the ionization at similar laser intensities. For resonant excitation to the 4p or 4f states after the absorption of two photons, an increase in energy of about 490 meV (520 meV for 784 nm) is required with respect to the energy levels assuming no AC-Stark shift. For the three-photon resonance with the 6d and 6g states, the corresponding increase in energy is about 160 meV (210 meV for 784 nm). Again disregarding the AC-Stark shift, the kinetic energy of all the features should decrease by 72 meV, which will affect the 4p and 4f resonances, as they lie energetically at, or just below the ionization threshold.

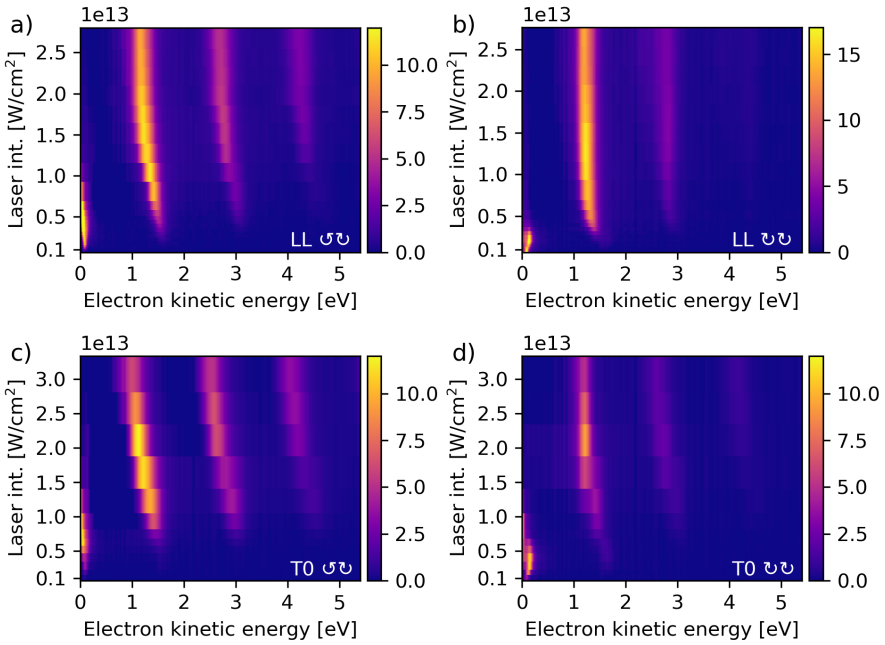

Figure 74: Intensity dependent photoelectron spectra for temporally separated pulses in the a) counter-rotating and b) co-rotating case and for temporally overlapped pulses in the c) counter-rotating and d) co-rotating case. The wavelength of the optical laser is 793 nm.

First of all the laser intensity dependent photoelectron spectra for the four different cases are shown in figure 74. The top row shows the result for temporally separated, the bottom row for temporally overlapped XUV and NIR pulses. On the left the results for counter-rotating, and on the right side for co-rotating XUV and NIR pulses are displayed.
There are different aspects that can be directly read off of this comparison. For increasing laser intensity, the kinetic energy shifts towards lower energies, which leads to the disappearance of the MPI feature. The MPI feature appears at lower laser intensities for the co-rotating case and also shifts below threshold at lower laser intensities compared to the situation with counter-rotating laser pulses. The appearance of higher ATI features is much more pronounced for counter-rotating pulses than for co-rotating pulses.
Saturation is at least expected to appear for temporally separated pulses because in this case the number of prepared helium ions is determined only by the properties of the XUV pulse. For co-rotating and temporally separated pulses (Fig. 74 b) the distribution is quite constant in terms of kinetic energies of the electrons above a laser intensity of $1.0 \cdot 10^{13}\,\mathrm{W/cm^2}$, which is where OBI is about to set in and the ionization probability is greatly enhanced. The prepared helium ions don't experience the further increasing laser intensity, because all prepared helium ions are already ionized during the temporal evolution of the laser pulses envelope. As a consequence, the kinetic energy doesn't shift any further, since the electrons never experience the ponderomotive potential created by the laser field above a certain laser intensity. The yield also stays rather constant with most of the yield concentrated in the ATI photoelectrons. With increasing laser intensity

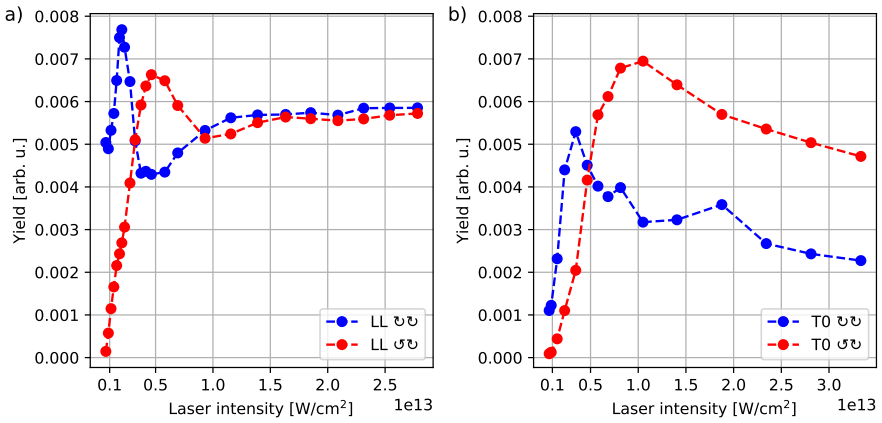

Figure 75: Total yield of all photoelectrons (MPI and ATI, ATI 2, ...) features for temporally a) separated and b) overlapped laser pulses and their polarization combinations. The laser's central wavelength is 793 nm.

the ratio between different features like ATI, ATI 2, etc. changes, but the total yield will stay constant as we will see later on.
For counter-rotating and temporally separated pulses (Fig. 74 a) the situation is similar but not as concise, due to the onset of the saturation at higher laser intensities of about $2.0 \cdot 10^{13}\,\mathrm{W/cm^2}$. But even here it is visible that the shift of the kinetic energy is reduced above this laser intensity and the yield of the individual features stays rather constant.
Looking at the intensity dependent photoelectron spectra for temporally overlapped pulses (Fig. 74 c, d), clear differences to the spectra for temporally separated pulses can be observed. The shift of the kinetic energies does not stop at a certain laser intensity for the counter-rotating case. At the highest intensity of $2.8 \cdot 10^{13}\,\mathrm{W/cm^2}$ for separated pulses the kinetic energy shift for overlapped pulses is 160 meV greater than for separated pulses indicating that the photoelectrons experience greater field strengths for temporally overlapped pulses. In contrast to the case of separated pulses, saturation due to the prepared helium ions is impossible because the preparation of the helium ions happens throughout the envelope of the NIR laser pulse. Another interesting aspect is the decrease of the yield at laser intensities higher than $2.3 \cdot 10^{13}\,\mathrm{W/cm^2}$. The reason for this could be that preparation of the helium ions could become less likely due to a shift of the helium ions 1s-3p resonance energy. The quasi-energy calculations [51] predicted that this energy should stay fairly constant at lower laser intensities, but this might not hold true for the laser intensities we reach in the experiment. A hint to this can be seen in figure 97 a), where the energy of the $3p_{+1}$ state crosses below the 1s + XUV energy with increasing laser intensity.

To get a better insight into our observations, the intensity dependence of the total yield of the MPI and ATI (ATI, ATI 2, ATI 3, ...) electrons for the four different scenarios is shown in figure 75. For separated pulses (Fig. 75 a) the yield increases to a maximum due to the increase in the MPI yield. The yield peaks and decreases then, due to the shift of the MPI below the ionization threshold. After this, the

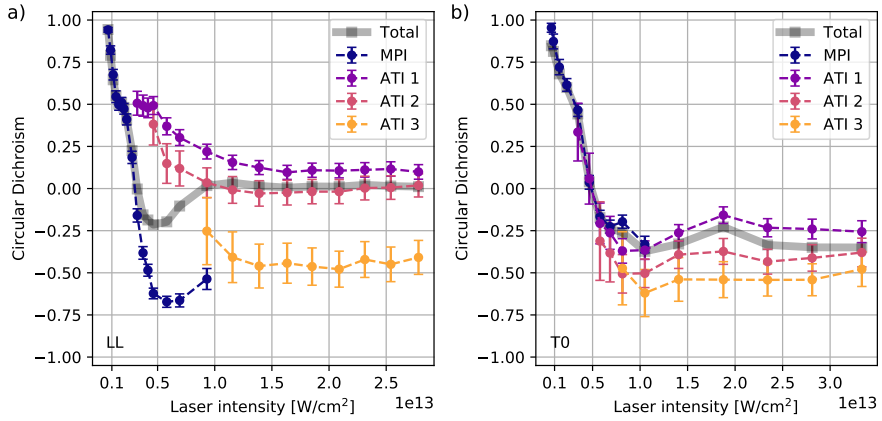

Figure 76: Intensity dependence of the circular dichroism for different features depending on the laser intensity for temporally a) separated and b) overlapped pulses. The laser's central wavelength is 793 nm.

yield increases again due to the increased yield of the ATI features. This behaviour is very similar for co- and counter-rotating pulses. For co-rotating pulses, the shift below threshold happens at a lower laser intensity and the ionization probability is decreased at low laser intensities. At high laser intensities, saturation is seen in the stagnation of the yield, which sets in around the intensity of OBI $1.2 \cdot 10^{13}\,\mathrm{W/cm^2}$. There is also nearly no difference in the yield between co- and counter-rotating pulses over a large range of intensities, showing that all the prepared helium ions have been ionized.
Looking at figure 75 b), the situation is similar in some ways and very different in others. The overall behaviour of the yield can still be explained by a strong increase of the yield due to the MPI feature and a decrease due to the shift below the ionization threshold. The complete decrease of the signal is prevented by the simultaneously increasing ATI yield. In contrast to the yield for separated pulses the yield for overlapped pulses does not flatten out and converge against a certain value for neither of the polarization combinations. The yield in the case of co-rotating pulses is lower by a factor of 2 at high laser intensities, due to the energetic shift of the 1s-3p resonance of the helium ion, than for counter-rotating pulses, where the energy of the 1s-3p resonance is predicted to change much less with increasing laser intensity.

The comparison of these CDs is shown in figure 76. For separated pulses, the main differences can be found in the CD of the MPI electrons and in the total CD. While the CD at 784 nm only drops to -0.15, the CD here drops to a CD of about -0.70 and it does not recover to positive values, which we will see in the upcoming section is due to the resonances at the ionization threshold. The CD of the ATI features is overall more positive for 793 nm than for 784 nm. The total CD converges towards zero with increasing laser intensity, as it did at 784 nm, due to saturation. For temporally overlapped pulses there is no difference to the CD at 784 nm at first sight. The CD of all features becomes negative as the intensity increases due to the AC-Stark shift of the $1s_0$-$3p_{+1}$ resonance for co-rotating pulses. Even the values of

the total CD at the highest laser intensities are very similar at around -0.3 to -0.35. In a similar experiment on lithium by De Silva et. al. [50], where the absorption of three NIR photons was sufficient to ionize lithium atoms prepared in the $2p_{+1}$ state, the CD was also measured as a function of the laser intensity. Their set-up corresponds to having separated pulses, as the preparation of the lithium ions was not influenced by the NIR field. Their analysis showed that the CD is very stable over a laser intensity range from $0.2 \cdot 10^{12}\,\mathrm{W/cm^2}$ to $1.2 \cdot 10^{12}\,\mathrm{W/cm^2}$. Compared to this the measured value of the CD in our experiment varies much more. In their data, only a slight trend toward a lower CD with increasing laser intensity is seen, which would match our observations.
In conclusion, the influence of high laser intensities is very well seen in a clear saturation effect in the case of separated pulses. For overlapped pulses, the energy shift of the helium ions 1s-3p resonance could clearly be seen in the comparatively low yield for co-rotating pulses compared to counter-rotating pulses. That even the yield in the counter-rotating case starts to decrease above a certain laser intensity shows that the 1s-3p resonance energy might also change for counter-rotating pulses if the laser intensities are high enough.

9.8 CIRCULAR DICHROISM AND DIFFERENT NIR WAVELENGTHS

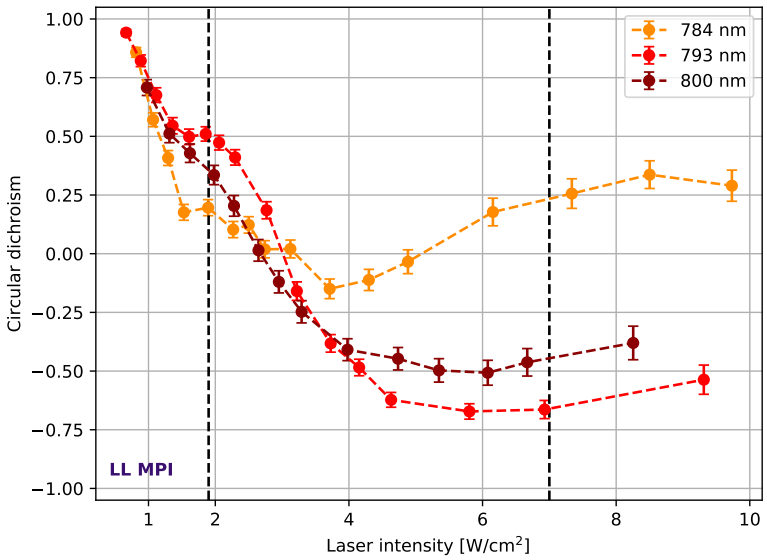

Figure 77: CD of MPI electrons for temporally separated pulses and three different wavelengths. Black lines highlight laser intensities where the CD behaviour will be discussed in more detail.

The influence of slightly different central wavelengths on the CD of the MPI and the ATI photoelectrons is discussed in the following. The wavelengths used are 784 nm (1.581 eV), 793 nm (1.563 eV) and 800 nm (1.550 eV). Because multiple photons are necessary for ionization, tiny variances in the photon energy can lead to significant differences in the ionization probability for the MPI photoelectron, which lies energetically just above the ionization threshold. How these differences

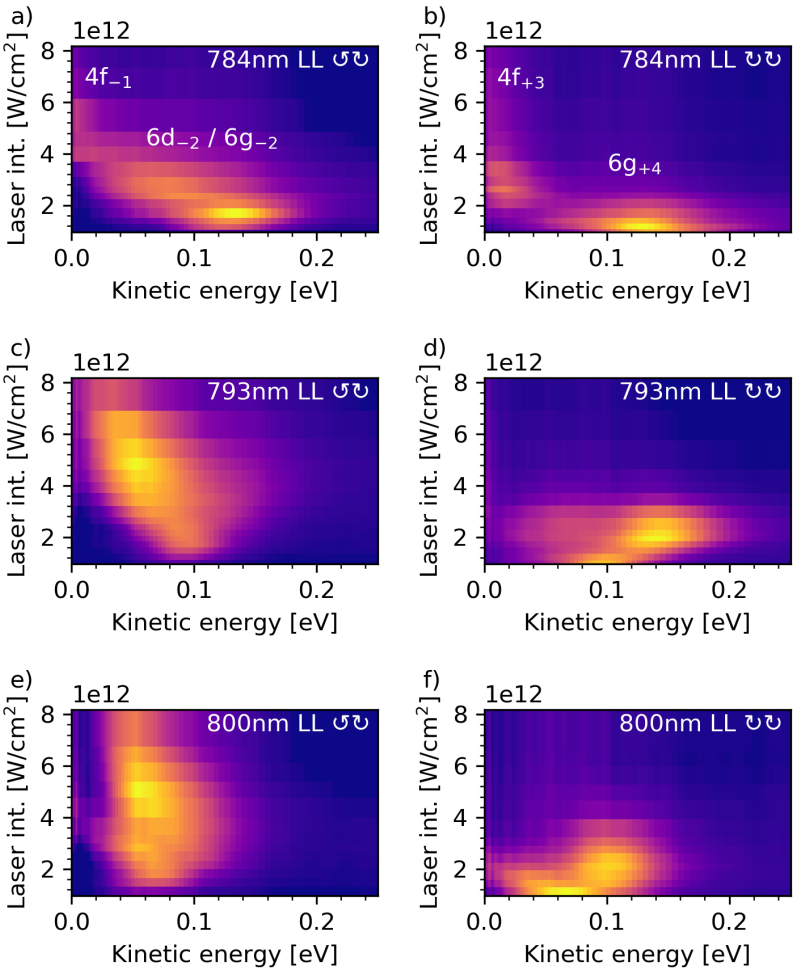

Figure 78: Intensity dependent photoelectron spectra of the MPI feature for three different wavelengths and the two polarization combinations. a) 784 nm counter-rotating, b) 784 nm co-rotating, c) 793 nm counter-rotating, d) 793 nm co-rotating, e) 800 nm counter-rotating, f) 800 nm co-rotating. Brighter colors correspond to higher values (blue to yellow). The colormap is normalized to the highest value in the section shown.

affect the CD of the MPI and ATI photoelectrons for temporally separated pulses is shown in figure 77.
The CDs of the MPI photoelectrons for separated pulses show an overall similar trend at laser intensities up to $3.3 \cdot 10^{13}\,\mathrm{W/cm^2}$ being positive for low laser intensities and then decreasing with increasing laser intensity and becoming negative. While the CD recovers to positive values for 784 nm, the CD at 793 nm and 800 nm stays negative with a slight upward trend. To examine what induces the change of the CD, we compare the intensity dependence of the CD to intensity dependent photoelectron spectra for the co- and counter-rotating case, shown in figure 78.

The deviation of the CDs at lower laser intensities of $1.3 \cdot 10^{12}\,\mathrm{W/cm^2}$ has its origin in a splitting of the $6g_{+4}$ resonance for 793 nm and 800 nm, which can be seen

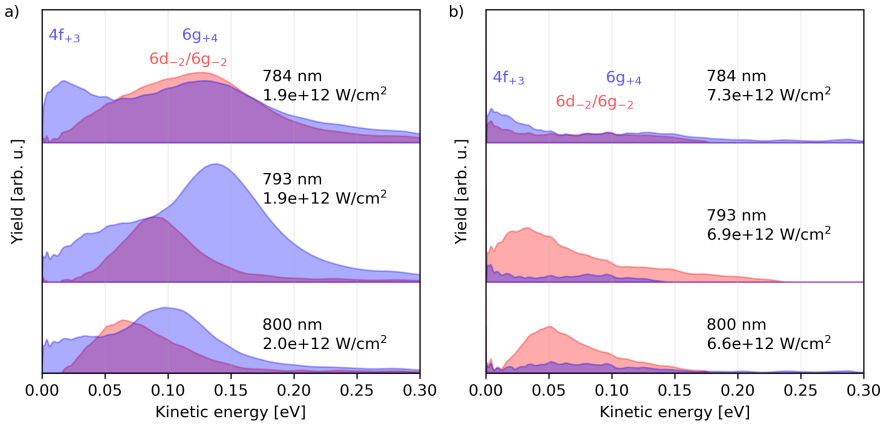

Figure 79: Photoelectron spectra of MPI photoelectrons for the three wavelengths at similar laser intensities around a), $1.9 \cdot 10^{12}\,\mathrm{W/cm^2}$, and b), $6.9 \cdot 10^{12}\,\mathrm{W/cm^2}$.

in figure 78 d) and f). This splitting and the increase in yield of the high kinetic energy feature counteracts the decrease of the MPI photoelectron yield, which is induced by the shift of the MPI feature below threshold, leading to a short plateau in the CD for 793 nm or a slight bump in the CD for 800 nm (cf. Fig. 77). As can be seen in the quasi-particle calculations (figure 97 b), this splitting might be due to an avoided crossing. For 793 nm (figure 78 d) the $6g_{+4}$ resonance is centered at 90 meV at a laser intensity of $1.0 \cdot 10^{12}\,\mathrm{W/cm^2}$ and then splits into two features with kinetic energies of 60 meV and 140 meV at a laser intensity of $1.4 \cdot 10^{12}\,\mathrm{W/cm^2}$, which is shown in more detail in figure 79 a. For 800 nm (figure 78 f) the $6g_{+4}$ resonance is centered around a lower kinetic energy of 65 meV at a laser intensity of $1 \cdot 10^{12}\,\mathrm{W/cm^2}$ due the lower photon energy. With increasing laser intensity this feature splits into two features with kinetic energies of 30 meV and 100 meV at a laser intensity of $2.0 \cdot 10^{12}\,\mathrm{W/cm^2}$, which is again shown in more detail in figure 79 a.

The deviation of the CDs between the different wavelengths at laser intensities above $4 \cdot 10^{12}\,\mathrm{W/cm^2}$ is induced by the lower photon energies, leading to the disappearance of the $4f_{+3}$ resonance below the ionization threshold, see figure 78 d) and e). At high intensities the line corresponding to the $4f_{+3}$ resonance at 784 nm is still above the ionization threshold and leads to the recovery of the CD to positive values, which is not the case for 793 nm and 800 nm. In the counter-rotating case the $4f_{-1}$ resonance is just below the ionization threshold and should also shift further below the ionization threshold, contributing less, if at all, to the yield for 793 nm and 800 nm, leading to a more positive CD. But as we can see in figure 78 c) and e) for 793 nm and 800 nm, the $6d_{-2}/6g_{-2}$ resonance shifts further towards the ionization threshold with increasing laser wavelength and contributes to the yield even at laser intensities of $4 \cdot 10^{12}\,\mathrm{W/cm^2}$ where the $6d_{-2}/6g_{-2}$ resonance does not significantly contribute to the yield any longer at a wavelength of 784 nm. For the co-rotating case the $6g_{+4}$ resonances shift below the threshold much faster, due to the $3p_{+1}$ shift to lower energies. Overall the combination of these effects prevents the CD to recover to positive values for 793 nm and 800 nm.

As we could see here, a slight change in the central wavelength can lead to large de-

viations in the CD of photoelectron features that are close to the ionization threshold. Such a change of the CD between different central wavelengths of the optical laser in multi-photon ionization has also been observed in a similar study by Da Silva et. al. [50]. For their experiment, they used lithium atoms in the $2p_{+1}$ state as the prepared species and used left- and right-circularly polarized light to ionize the atoms via multi-photon ionization. They also investigated the dependence of the CD on the central wavelength of the ionizing NIR laser pulse. Their results also show a strong variation of the CD between different wavelengths at the same laser intensity, which is also supported by theoretical calculations. They argue that the reason for this lies in the coherent population transfer between the initial and the intermediate, resonant, states. Due to Rabi oscillations, which are periodic population variations between the coupled, resonant states, the CD can be strongly influenced by small variations of the central laser wavelength.

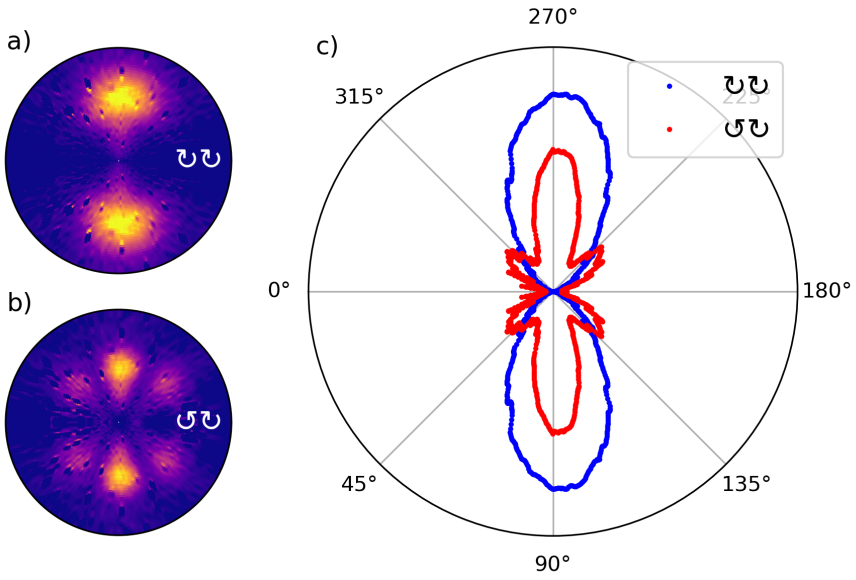

Figure 80: Angular distribution of the MPI feature for a) co-rotating and b) counter-rotating laser pulses. c) Radially integrated angular distribution for the co- (blue) and counter-rotating (red) case. The laser intensity is $1.8 \cdot 10^{12}$ W/cm^2 at a central laser wavelength of 784 nm of the optical laser.

9.9 ANGULAR DISTRIBUTION OF THE MPI PHOTOELECTRONS

The kinetic energy of the electrons that we investigated before is a reduced representation of the data acquired by the VMI. By using the VMI as an imaging spectrometer, access is also given to the emission direction of the electrons, which enables us to determine which final state partial waves contribute to the angular distribution. In particular, this will allow to investigate how transient resonances in the multi-photon ionization affect the angular distribution. The focus will lie on the ATI photoelectrons, since their angular distribution can be observed at all laser intensities.

To start off, the results from Ilchen et. al. [48] are compared to the results from the recent beamtime using the same configuration. In figure 80 a) and b) the PAD of the MPI feature is shown for the co- and counter-rotating case, respectively. In figure 80 c) the radially integrated angular distributions are presented for co- (blue) and counter-rotating (red) pulses. The linear radial axis in a) and b) corresponds to the kinetic energy of the electrons and goes from 0 meV to 261 meV. Since we will mainly discuss the angular distribution here, no axis is shown. The beam propagates from left to right through the polar images. In the co-rotating case (a) the angular distribution is simple and consists of two lobes perpendicular to the beam propagation axis. As we used the cylindrical symmetry around the beam axis in the transformation of the original detector images, the two lobes are a cut through the 3D momentum distribution. To get back to the 3D momentum distribution, the distributions shown in figure 80 a) and b) have to be rotated around the beam axis, which will result in a donut-shaped distribution for a) and a more complex distribution for b). The photoelectron angular distribution is determined by the

wave function in the continuum state, which can be expressed as a superposition of spherical harmonics $Y_{\ell,m}$ for different quantum numbers ℓ and m [80]. As we know from dipole transition rules for co-rotating pulses $\Delta\ell = +1$ and $\Delta m = +1$, there is only one continuum state for the MPI electron reachable with $\ell = 5$ and $m = 5$, due to the special ionization scheme (see figure 55). Following this, the angular distribution is proportional to the square of the spherical harmonic Y_5^5. The resulting distribution is shown in figure 81 a). The y-axis, displayed by the thick black line, is the propagation direction of the beam and the quantization axis. The detector plane of the VMI is parallel to the plane created by the x- and y-axis. Imagining the experiment, the detector would be on top of the distribution, with the z-axis being normal to the surface. In our experiment, we don't observe as many lobes, as the distribution is actually fully symmetric around the beam axis when taking into account the time evolution of the states and the change of direction of the electric field vector around the beam axis during ionization, which is shown in figure 81 d). The black curve at the bottom shows a slice through the 3D distribution in the x-y plane. In the experiment it is this distribution given by the black curve that we can calculate back to, using the Vrakking method [169] to invert the detector images. At first sight, this distribution is very similar to the one observed in the experiment, shown as the blue curve in figure 80 c). The black lines in figure 81 d) are actually squared associated Legendre polynomials $(P_\ell^m)^2$ with the corresponding quantum numbers to the spherical harmonics, as they equal the absolute of the rotationally symmetric squared spherical harmonics at an azimuthal angle of zero since the following relation holds [243]:

$$Y_\ell^m(\phi = 0, \theta) \propto P_\ell^m(\theta). \tag{51}$$

Here Y are the spherical harmonic functions, P are the associated Legendre polynomials, ϕ is the azimuthal angle and θ is the polar angle.

For the counter-rotating case, the situation is a little bit different and more complex. Through the combination of the positive and negative helicity, two final states can be reached. Starting from the $3p_{+1}$ state with quantum numbers $\ell = 1$ and $m = 1$, it is possible to reach states with ($\ell = 3$ and $m = -3$) as well as ($\ell = 5$ and $m = -3$) after absorption of a total of four photons. Thus the final angular distribution will be determined by the corresponding spherical harmonics of these two states and their interference [49]. As for the case of co-rotating pulses, the angular distribution of the square of the spherical harmonic and the radially symmetric distribution are shown in figure 81. Figure 81 b) and e) shows this for $Y_{3,-3}$ and c) and f) for $Y_{5,-3}$. Looking at the black curve in f) it becomes clear that the origin of the additional lobes in the angular distribution at roughly 45°, 135°, 225° and 315° (figure 80 c) is the continuum state with $\ell = 5$ and $m = -3$. Apart from the lobes at the sides, there are also two bigger lobes perpendicular to the beam propagation axis (figure 80 c), which mostly result from the continuum state with $\ell = 3$ and $m = -3$, because the part with $\ell = 5$ and $m = -3$ is too narrow and small, relative to the side lobes, to recreate the measured distribution on its own. For the resulting distribution, the wave functions of both final states can interfere,

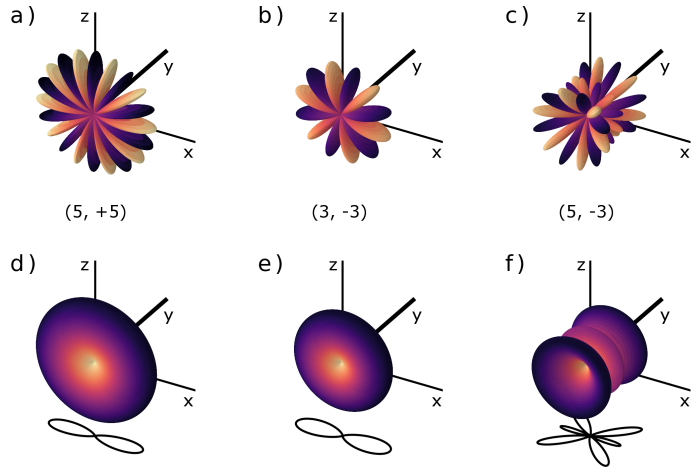

Figure 81: Spherical harmonics a) $|Y_{5,5}|^2$, b) $|Y_{3,-3}|^2$ and c) $|Y_{5,-3}|^2$. Spherical harmonics with beam axis symmetry (thick black line). The black curves below show a horizontal slice in the plane created by the x- and y-axis through the distributions shown in d) $|Y_{5,5}|^2$, e) $|Y_{3,-3}|^2$ and f) $|Y_{5,-3}|^2$.

depending on the phase relation between the two final states [244].

Knowing the shape of the angular distribution, we are able to compare it to simulations or other results. For a quantitative analysis, a series expansion of Legendre polynomials is used to fit the angular distribution of photoelectrons emitted in the multi-photon process. The sum has the following form:

$$I(\theta) = 1 + \sum_{n=1,2,\ldots}^{N} \beta_{2n} L_{2n}(\cos(\theta)). \tag{52}$$

Here N is the order of the multi-photon process. This form has a similar advantage to the series expansion of the wave function into spherical harmonics, i.e. the series can be truncated at low orders. The β_{2n} are the fit parameters and L_{2n} are associated Legendre polynomials of order 2n. A fit of the angular distributions and their β parameters is shown in figure 82 a) and b), respectively. Considering the solid lines in figure 82 a), we see that equation 52 can fit the experimental data very well with the use of only the first five parameters, up to β_{10}. In figure 82 b) the individual values of the β parameters for the two polarization combinations are displayed. Obviously, the simpler distribution in the co-rotating case (blue dots) also needs lower-order β parameters to fit the distribution. The distribution with only two lobes is already well approached by the two lowest order β parameters. For the distribution in the counter-rotating case all β parameters up to including β_8 contribute significantly. With this, the results of the former paper [48] regarding the angular distribution of the photoelectrons recovered and even extended.

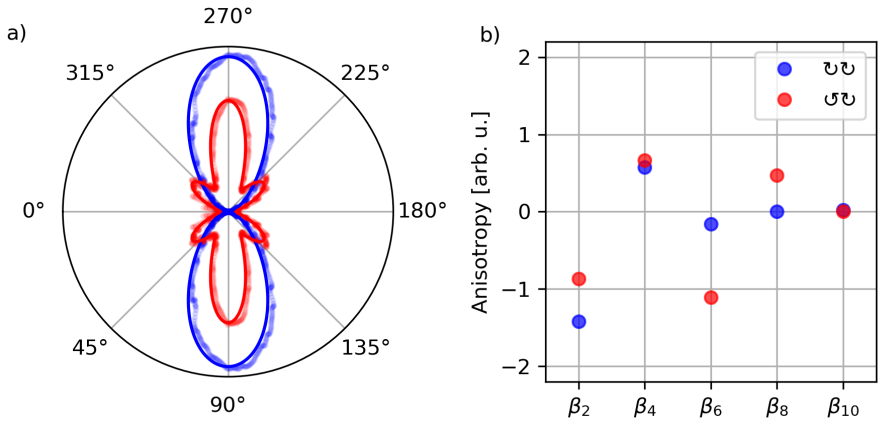

Figure 82: a) Angular distribution in co- (blue) and counter-rotating (red) laser fields at $1.8 \cdot 10^{12}\,\mathrm{W/cm^2}$ and a central wavelength of the laser of 784 nm. Faint circles are the measured distribution, the solid lines are the corresponding fits. b) β_{2n} fit parameters following equation 52.

To get a deeper insight into the ionization process, we investigate the intensity dependence of the angular distribution, in a similar way as it was done before for the circular dichroism. Since the MPI feature shifts below the ionization threshold above a certain laser intensity, we will mainly discuss the angular distribution of the first ATI electron, which is affected by the shift below threshold in kinetic energy, but is visible over the full intensity range once the signal of the feature is above the background.

The angular distribution of the possible continuum states of the ATI, shown in figure 83, is very similar to the MPI. The available states have quantum numbers $\ell = 6$ and $m = 6$ for the co-rotating case and $\ell = 4$ and $m = -4$, and $\ell = 6$ and $m = -4$ for the counter-rotating case. The biggest difference can be seen in the angular distribution of the state with $\ell = 6$ and $m = -4$, where the lobes are more narrow, in width, compared to the lobes of the continuum state with $\ell = 5$ and $m = -3$ for the MPI. Another aspect, which is not easily visible, is the angle at which the maxima of the non-perpendicular lobes appear. As long as $m = \pm(\ell - 2)$ and $\ell \geq 3$, the angular distribution will always have six lobes, two perpendicular to the beam propagation direction and four at other angles. Depending on the value of ℓ the angle at which the maximum of these lobes occur changes. The trend is that with increasing ℓ the lobes appear at higher angles, i. e. closer to the main, perpendicular lobes. Table 8 lists the angle at which the non-perpendicular lobes have their maximum. The values originate from the angular distribution of the squared associated Legendre polynomials, which are slices through the squared spherical harmonics to the corresponding quantum numbers. The angle is only given for one lobe, as it also defines the angle of the remaining three lobes.

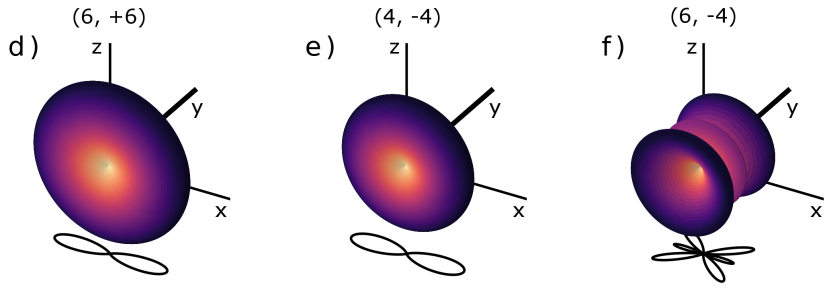

Figure 83: Spherical harmonics with beam propagation axis (thick black line) symmetry a) $|Y_{6,6}|^2$, b) $|Y_{4,-4}|^2$ and c) $|Y_{6,-4}|^2$. The black curve shows a horizontal slice through these 3D angular distributions.

ℓ, m	3,1	4,2	5,3	6,4	7,5	8,6
α [°]	31.0	40.7	46.9	51.2	54.4	56.9

Table 8: Angle of the first lobe of the squared associated Legendre polynomial $(P_\ell^m)^2$. The angle is chosen so that the angle is also relative to the beam propagation axis. The higher the angle, up to 90°, the closer the lobe is to being perpendicular to the beam propagation direction.

9.10 ANGULAR DISTRIBUTION WITH BALANCED INITIAL POPULATION

The goal of separating the XUV and NIR pulses temporally was to prevent the initial imbalance in the $3p_{+1}$ population for the two polarization scenarios from affecting the circular dichroism. The angular distribution of the photoelectrons is determined by the momentum and magnetic quantum numbers of the final state wavefunction and thus the only difference between temporally overlapped or separated pulses should arise due to the possibility of non-sequentially absorbing XUV and NIR photons for temporally overlapped pulses. At first, we will investigate the angular distribution of the ATI photoelectrons for temporally separated pulses, as we can complement the experimental findings with results from TDSE calculations.
There is only one continuum state reachable in the co-rotating polarization configuration, thus the angular distribution stays similar for all laser intensities, once the signal of the ATI is well above the background.

The intensity dependent angular distribution of the ATI photoelectrons for co-rotating pulses is depicted in figure 84. Shown are pairs of images, one of which shows the angular distribution and the dependence on the kinetic energy, while the other shows the angular distribution integrated over a certain kinetic energy region, which is marked by two white broken lines in the first image. Additionally, a fit to the angular distribution is shown using the series expansion given by equation 52. The intensity throughout these image pairs increases from left to right and top to bottom. As it is predicted by theory for the co-rotating case, all the angular distributions have to have the same shape, as only one continuum state with (ℓ = 6, m = +6) is accessible in first-order processes for the ATI feature. All the distributions show two major lobes perpendicular to the beam propagation axis, which is passing horizontally through the image from left (0°) to right (180°).

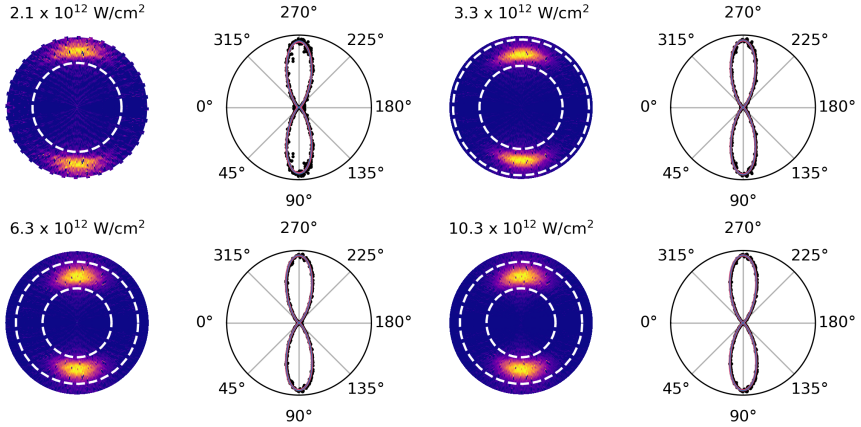

Figure 84: Intensity dependent angular distribution for a few selected intensities of the optical laser. Shown are pairs of images to one laser intensity. The left image shows a slice of the reconstructed 3D distribution, while the right image shows the energy-integrated angular yield. The integration borders are marked by the white circles in the left images. The XUV and NIR photons have the same helicity and the pulses are temporally separated. The central wavelength of the optical laser is 784 nm.

To quantify the angular distribution we use the series expansion in equation 52, which gives a set of beta parameters for every laser intensity that we can compare to sets of beta parameters that were obtained using TDSE calculations. The result of this is shown in figure 85. The beta parameters derived from the angular distribution calculated using TDSE are constant regarding changes in the laser intensity. This confirms the prediction from LOPT that, as there is only one final state ($\ell = 6$, $m = +6$) available, the angular distribution can't change. This weak intensity dependence of the beta parameters can also be observed by looking at the beta parameters derived from the experimental data. Although not as constant as the beta parameters from the TDSE calculations, the beta parameters derived from the experimental data also do not change a lot with increasing intensity of the optical laser, confirming the predictions from LOPT. Additionally, the agreement between the beta parameters from theory and experiment is quite well.

The angular distribution in the counter-rotating case is much more variable, as there are two final states with ($\ell = 4$, $m = -4$) and ($\ell = 6$, $m = -4$) available. The intensity dependence of the angular distribution of the ATI photoelectrons for the counter-rotating case for a few select laser intensities is shown in figure 86. With increasing laser intensity of the optical laser the angular distribution changes. At $2.1 \cdot 10^{12}\,\mathrm{W/cm^2}$ the angular distribution mainly consists of lobes perpendicular to the beam propagation direction with little side-lobes, which can only arise from the final state with ($\ell = 6$, $m = -4$). At the next higher laser intensity $3.3 \cdot 10^{12}\,\mathrm{W/cm^2}$ this final state is not significantly apparent anymore, as only the perpendicular lobes remain. This changes again at $6.3 \cdot 10^{12}\,\mathrm{W/cm^2}$, where the non-perpendicular lobes are the dominant contributors to the angular distribution. At the highest laser intensity of $6.3 \cdot 10^{12}\,\mathrm{W/cm^2}$ all lobes contribute equally to the angular distribution.

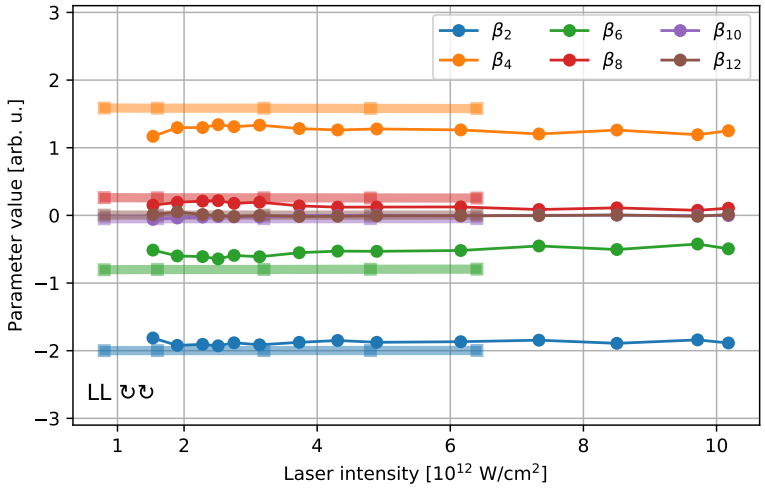

Figure 85: Beta parameter dependence on the intensity of the optical laser for temporally separated pulses in the co-rotating case, the central wavelength of the optical laser is 784 nm. Beta parameters from TDSE calculations are shown as faint squares with colors corresponding to a certain beta parameter.

This variability in the angular distribution with changing laser intensities of the optical laser is the consequence of having two final states available. Depending on the laser intensity there is a certain probability for the ATI electrons to end up in the ($\ell = 4$, $m = -4$) or ($\ell = 6$, $m = -4$) final state. Depending on the probability to end up in one or the other state, the angular distribution of the photoelectrons will change. Apart from this factor, which arises as a transition probability from the initial to the final state, the electron wave functions of the final states interfere. This means that the angular distribution is not just an addition of the two final state angular distributions, but, due to interferences, contributions in certain angular directions can also be suppressed.
To quantify which final state contributes how much to the angular distribution at a certain laser intensity, we use a formula adapted from Smith and Leuch [80] for the angular distribution $I(\theta)$:

$$I(\theta) = A^2 \cdot P_4^{-4}(\cos(\theta))^2 + B^2 \cdot P_6^{-4}(\cos(\theta))^2 \\ -2 \cdot |AB| P_4^{-4}(\cos(\theta)) P_6^{-4}(\cos(\theta)) \cos(\delta).$$

Here A and B are the amplitudes of the final states with ($\ell = 4$, $m = -4$) and ($\ell = 6$, $m = -4$), respectively. The P_4^{-4} and P_6^{-4} are the associated legendre polynomials to the two final states and δ is the phase between the two final state wave functions. To extract the total contribution of each of the final states to the overall angular distribution, the sums of $A^2 \cdot P_4^{-4}(\cos(\theta))^2$ for the ($\ell = 4$, $m = -4$) state and $B^2 \cdot P_6^{-4}(\cos(\theta))^2$ for the ($\ell = 6$, $m = -4$) state are calculated. The result of this for all intensities of the optical laser is shown in figure 87 a).

At the lower laser intensities up to $6.3 \cdot 10^{12}$ W/cm^2 the main contributor to the angular distribution is the ($\ell = 4$, $m = -4$) final state. Above this laser intensity the ($\ell = 6$, $m = -4$) final state is the dominant one and from $6.3 \cdot 10^{12}$ W/cm^2 on, the

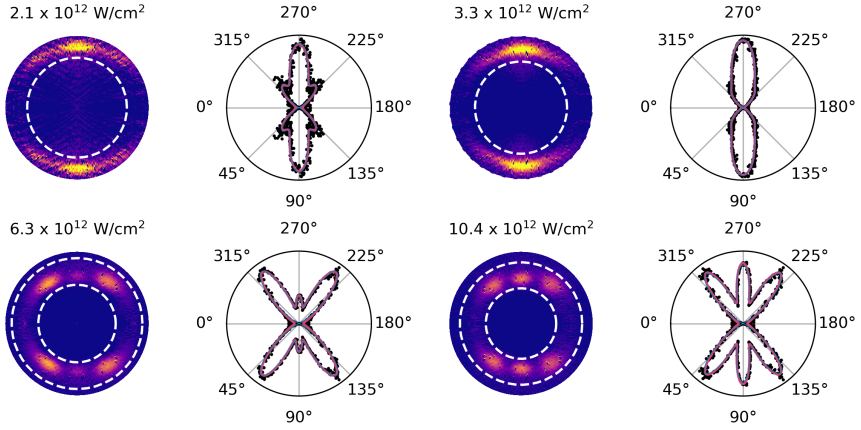

Figure 86: Intensity dependent angular distribution for a few selected intensities of the optical laser. Shown are pairs of images to one laser intensity. The left image shows a slice of the reconstructed 3D distribution, while the right image shows the energy-integrated angular yield. The integration borders are marked by the white circles in the left images. The XUV and NIR photons have opposing helicity and the pulses are temporally separated. The central wavelength of the optical laser is 784 nm.

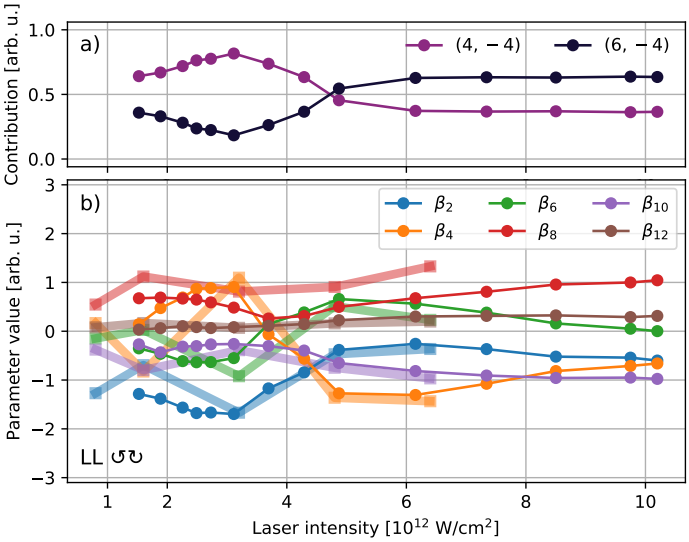

Figure 87: a) Relative contribution of (ℓ = 4, m = −4) and (ℓ = 6, m = −4) to the total fit. b) Value of the β-parameters used to optimally fit the angular distribution. The counter-rotating setup is used and the central wavelength of the optical laser is 784 nm. The XUV and NIR pulses are temporally separated.

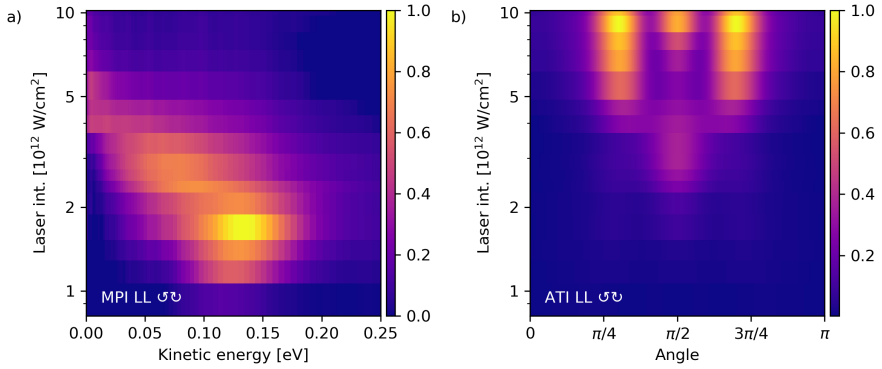

Figure 88: a) Colormap of the MPI photoelectrons intensity dependent kinetic energy distribution. b) Colormap of the ATI photoelectrons intensity dependent angular distribution. Only one side of the angular distribution is shown. Angles of 0 and π correspond to an emission against or with the propagation direction of the beam, while an angle of $\pi/2$ is perpendicular to the beam propagation direction. The laser pulses are temporally separated and the case is the counter-rotating. The central wavelength of the optical laser is 784 nm.

ratio of 1:2 regarding the ($\ell = 4$, $m = -4$) and ($\ell = 6$, $m = -4$) final states, respectively, does not change any longer.
That the ratio does not change anymore does not mean that the angular distribution does not change anymore, due to the variability of the phase between the two final states. This can be seen in the intensity dependence of the β parameters, which do not stagnate from a certain laser intensity onwards and one can also see that the angular distribution changes from $6.3 \cdot 10^{12}\,\mathrm{W/cm^2}$ to $1 \cdot 10^{13}\,\mathrm{W/cm^2}$ in figure 86. Compared to the co-rotating case, figure 85, the β parameter for the counter-rotating case vary a lot. Some of the parameters like β_4 and β_6 even change sign. The change of the β parameters with increasing laser intensity is also visible in the β parameters extracted from TDSE calculations, which again show an overall good agreement with the β parameters from the experimental data regarding the trend of the intensity dependence.

To investigate if a certain angular distribution is maybe connected to a certain transient resonance in the multi-photon ionization process, we compare the intensity dependent photoelectron spectrum of the MPI photoelectron, see figure 88 a), with the intensity dependent angular distribution of the ATI photoelectron, see figure 88 b). In figure 88 a) we can see the shift towards and below the ionization threshold with increasing laser intensity. The resonance feature from 50 meV to 200 meV is a result of resonant ionization via the $6d_{-2}/6g_{-2}$ resonance. Looking at the angular distribution of the ATI photoelectron in figure 88 b) we can see that in the intensity range, where ionization happens primarily via the $6d_{-2}/6g_{-2}$ resonance from $1 \cdot 10^{12}\,\mathrm{W/cm^2}$ to $3.3 \cdot 10^{12}\,\mathrm{W/cm^2}$, the angular distribution of the ATI photoelectron is dominated by the ($\ell = 4$, $m = -4$) final state. At higher laser intensities the multi-photon ionization is resonant via the $4f_{-1}$ resonance, see figure 66 a), which leads to the ($\ell = 6$, $m = -4$) final state becoming more dominant, which we could observe before in figure 87 a) and which can be seen in the dominant non-perpendicular lobes at a laser intensity of $6.0 \cdot 10^{12}\,\mathrm{W/cm^2}$ in figure 88

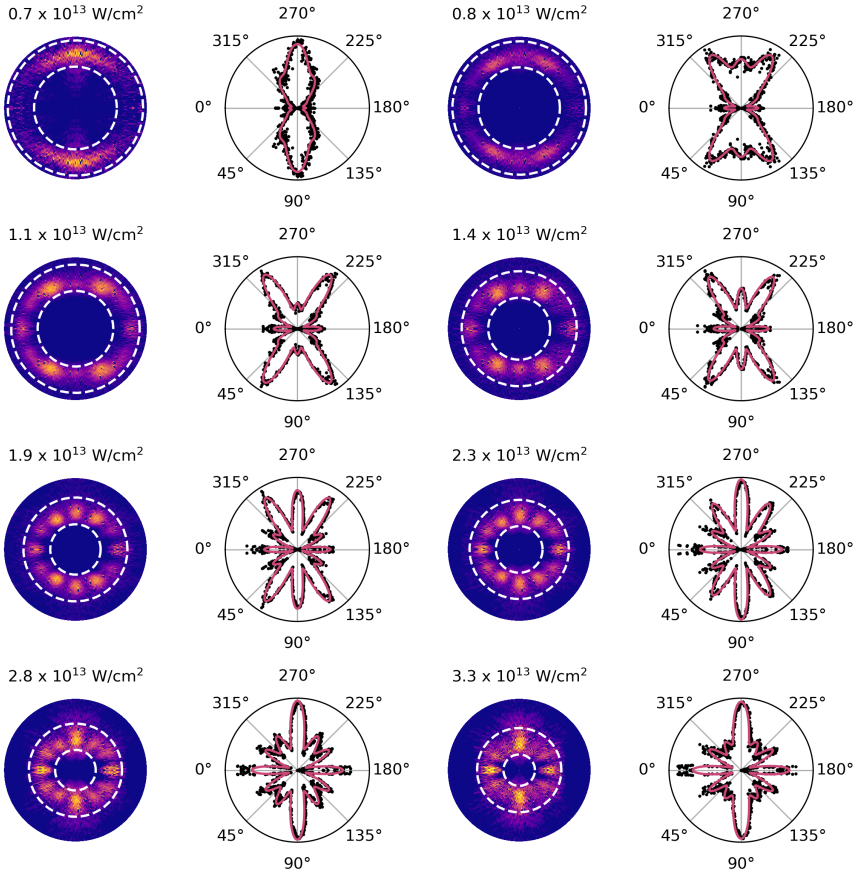

Figure 89: Intensity dependent angular distribution at 793 nm if the laser pulses are overlapped in time for the counter-rotating case. Shown are pairs of images to one laser intensity. The left image shows a slice of the reconstructed 3D distribution, while the right image shows the energy-integrated angular yield. The integration borders are marked by the white circles in the left images.

b). With further increasing laser intensity the phase between the two final states changes, leading to constructive interference in the lobe perpendicular to the beam propagation direction.
With the experimental investigation of the intensity dependent angular distribution for temporally separated pulses, we saw that the angular distribution is mainly determined by the available final states as predicted by LOPT. This observation was also supported by TDSE calculations. Furthermore, we could show that the angular distribution changes depending on the intensity of the optical laser due to transient resonances. In the upcoming section, we will investigate how the angular distribution behaves at even higher laser intensities, where one could expect deviations from the predictions by LOPT due to higher-order terms in the perturbation.

9.11 ANGULAR DISTRIBUTION IN THE BARRIER-SUPPRESSION REGIME

In the previous section, we saw that the intensity dependent angular distribution is determined by, following LOPT, the available final states and the combination of those. Here we will see that this does not have to be the case for temporally

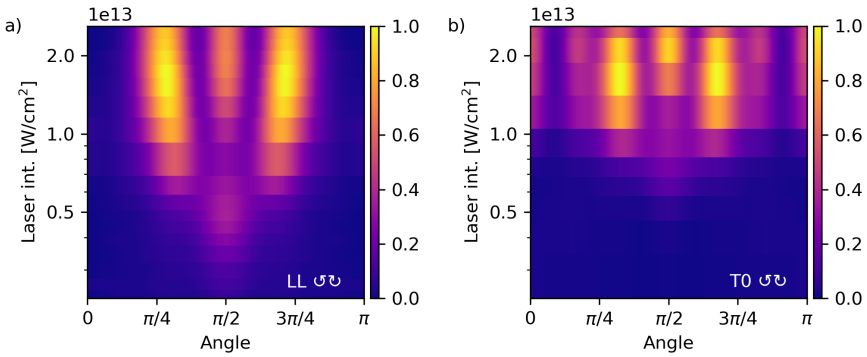

Figure 90: Intensity dependent top-half of the angular distribution for the counter-rotating case for temporally a) separated and b) overlapped pulses. For smoothness the angular distributions are fits to the experimental data using the β parameter series expansion, see equation 52.

overlapped pulses at laser intensities in the barrier-suppression regime, relative to the $3p_{+1}$ states ionization potential, while for the case of temporally separated pulses the angular distribution follows LOPT. As mentioned in the chapter about the circular dichroism, the central wavelength of the optical laser had to be shifted towards higher wavelengths to allow for higher laser intensities.
How different the angular distribution for temporally overlapped pulses in the counter-rotating case becomes with increasing laser intensities is shown in figure 89. Starting at the lowest laser intensity of $0.7 \cdot 10^{13}\,\mathrm{W/cm^2}$ we can see mainly two lobes with an indication of lobes to each side of the perpendicular lobes. In contrast to the previous observations, here we can see the formation of many more than six lobes with increasing laser intensity. For temporally overlapped pulses at a laser intensity of $1.1 \cdot 10^{13}\,\mathrm{W/cm^2}$ we can see the formation of additional lobes along the beam propagation direction and four additional lobes close to the beam propagation direction at angles of, which leads to a total of 12 lobes. With increasing laser intensity the shape of the angular distribution changes, but the amount of lobes stays the same. At the highest laser intensity of $3.3 \cdot 10^{13}\,\mathrm{W/cm^2}$ the angular distribution consists of 12 lobes, with the perpendicular ones being the most prominent.
Following LOPT not more than six lobes should appear, but apparently, the approximations within the LOPT do not support such high laser intensities. To investigate what could be the cause of these additional lobes, we investigate how the angular distribution changes at such high laser intensities in the case of temporally separated pulses. This comparison is shown in figure 90, where figure 90 a) shows a colormap plot of the intensity dependent angular distribution of the ATI photoelectrons for the counter-rotating case and temporally overlapped XUV and optical laser pulses, while 90 b) shows the same for temporally separated XUV and optical laser pulses.

Opposite to the case of temporally overlapped pulses, the angular distribution in case of temporally separated pulses consists of six lobes at most. Thus the appearance of additional lobes is related to the possibility of preparing helium ions and ionizing them throughout the pulse duration of the optical laser. The appearance of

additional lobes in the angular distribution for temporally overlapped pulses is a sign of additional final states becoming accessible, which might be due to second-order processes as they are already indicated by dotted lines in the co-rotating branch of the figure showing a schematic of the multi-photon ionization 55. Such second-order processes are for example the emission and absorption of a photon, leading to a photoelectron with the same magnetic quantum number, but with a different angular momentum quantum number. For example, from the (6, -4) state the (7, -3) state can be reached by emission of a circularly polarized optical photon. Then by absorbing another circularly polarized optical photon, a state with (8, -4) could be reached, which would correspond to an ATI photoelectron with an angular distribution that consists of ten lobes, see figure 91 b). The lobes that are missing here to have a total of twelve lobes, which we observe, are the lobes in the propagation direction of the beam and opposite to the propagation direction. The only associated Legendre polynomials that can produce any lobes along the beam propagation axis are polynomials with a magnetic quantum number of zero. To access such a final state from the prepared helium ions $3p_{+1}$ state, it is necessary to also allow transitions in which the angular momentum does not change, requiring the absorption of linearly polarized photons. Such a final state could be (6, 0), which is shown in figure 91 b). That these transitions become relevant only at higher laser intensities might be connected to a change in the polarization of the NIR laser pulses as they are less and less attenuated to reach the highest laser intensities.

Indications against the assumption of having a linear polarization component in the optical field are that the angular distribution for the counter-rotating case and that separated pulses do not show a sign of additional final states, see figure 91 a). This might be due to the onset of saturation before the linear polarization component appears at the higher laser intensities. Then one could still argue that the angular distribution for co-rotating and temporally overlapped pulses should show changes in the angular distribution, as, in principle, the ionization shouldn't be affected by saturation and hence the linear component could play a role and affect the angular distribution. Looking at the intensity-dependent angular distribution for the co-rotating case and temporally overlapped pulses, figure 98 in the appendix, we can see that also here the angular distribution does not show any extra features, like additional lobes at high laser intensities. Thus the appearance of additional lobes is unique for temporally overlapped pulses in the counter-rotating case.

Up to now, there are only speculations as to why these additional lobes appear, but what is certain is that additional final states become available at the highest laser intensities for temporally overlapped pulses in the counter-rotating case.

9.12 ANGULAR DISTRIBUTION FOR DIFFERENT NIR WAVELENGTHS

Here we investigate the influence of different central wavelengths of the NIR laser pulse on the angular distribution of ATI photoelectrons for temporally overlapped pulses in the counter-rotating case. The aim of doing this is to find out more about the origin of the multitude of lobes in the angular distribution of ATI photoelectrons in the counter-rotating case with temporally overlapped pulses at laser inten-

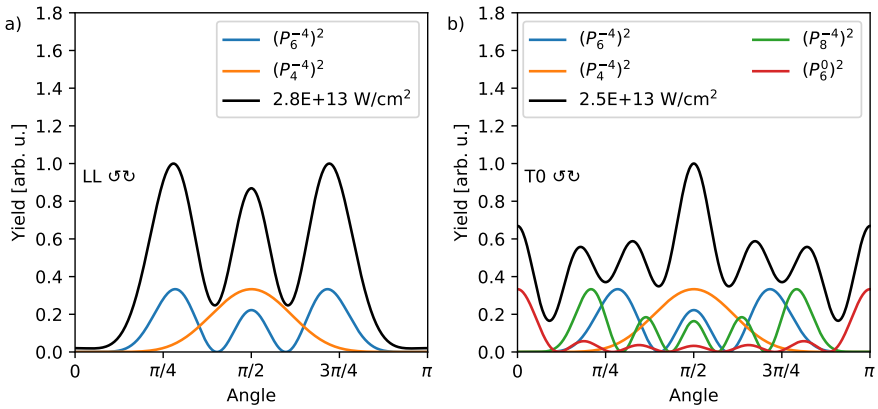

Figure 91: Top-half of the photoelectron angular distribution given by a fit with the β parameters series expansion (equation 52) around a laser intensity of $2.6 \cdot 10^{13}\,\mathrm{W/cm^2}$ (black curve) of the optical laser pulses for temporally a) separated and b) overlapped laser pulses in the counter-rotating case. The colored curves are associated Legendre polynomials P_ℓ^m to certain angular momentum ℓ and magnetic quantum numbers m. The central wavelength of the optical laser is 793 nm.

sities at and above $4.0 \cdot 10^{12}\,\mathrm{W/cm^2}$ for the three different central wavelengths.
A comparison of the intensity dependent angular distribution of ATI photoelectrons for the three central wavelengths of the optical laser of 784 nm, 793 nm and 800 nm is shown in figure 92. The angular distribution at 784 nm central wavelength of the optical laser has at most six lobes and can thus be mainly described via the two final states (4, -4) and (6, -4), as is predicted by LOPT. At laser intensities of $1 \cdot 10^{13}\,\mathrm{W/cm^2}$ the formation of lobes along the beam propagation direction becomes visible.
The intensity dependent angular distribution for a central wavelength of 793 nm of the optical laser leads to the formation of twelve lobes, which are well visible at a laser intensity of $11.0 \cdot 10^{12}\,\mathrm{W/cm^2}$ as is known from the previous section.
Interestingly the angular distribution at a central wavelength of 800 nm exhibits a stronger signal in lobes along the beam propagation direction at comparable laser intensities of $10.6 \cdot 10^{12}\,\mathrm{W/cm^2}$ compared to the central wavelength of 784 nm and 793 nm. With an increasing central wavelength of the optical laser additional lobes appear at already lower laser intensities. This might indicate that the appearance of the twelve lobes in the angular distribution in the counter-rotating case and temporally overlapped pulses is connected to the shift of the MPI feature below the ionization threshold, which happens at already lower laser intensities for larger central wavelengths. The small energy difference between different central wavelengths of 784 nm and 800 nm of 32 meV becomes a larger difference of 128 meV in the photoelectron kinetic energy after the absorption of four photons at the same laser intensities.

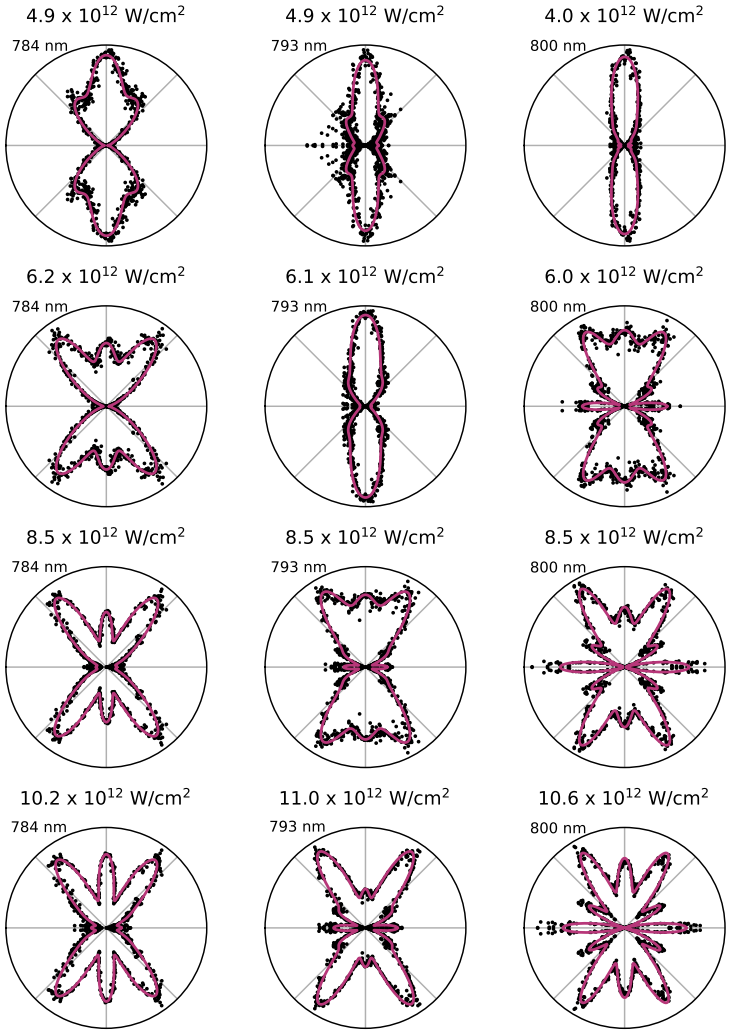

Figure 92: Intensity dependent angular distribution for the three different central wavelengths at similar laser intensities. The pulses are overlapped and counter-rotating. The left column shows the angular distribution at 784 nm, the middle column at 793 nm and the right column at 800 nm.

9.13 CONCLUSION

In the previous study [48], it could be shown that the $3p_{+1}$ can not be efficiently populated for the co-rotating case, leading to an imbalance in the population, which ultimately leads to the observed circular dichroism. A theoretical study using quasi-particle calculations [51] predicted that the $3p_{+1}$ state shifts in energy relative to the helium ions $1s_0$ state for co-rotating pulses, but much less so for counter-rotating pulses. With the recent experimental results, we could observe the AC-Stark shift of the $3p_{+1}$ state relative to the $1s_0$ state, confirming the predictions from quasi-particle calculations.
By separating the preparation of the helium ions and the multi-photon ionization step (temporally separated XUV and NIR laser pulses), we could prevent that an imbalance in the $3p_{+1}$ states population for the two polarization combinations will

affect the observed circular dichroism. With this setup we observed that the intensity dependent circular dichroism persists even without the population imbalance with the difference that at higher laser intensities the CD of the MPI photoelectron becomes positive again, due to enhanced ionization via the $4f_{+3}$ resonance at the ionization threshold for the co-rotating case. This recovery of the CD at higher laser intensity was previously prevented by the population imbalance of the $3p_{+1}$ state, leading to a negative CD. The appearance of such transient 'Freeman' resonances in the multi-photon ionization could be observed as distinct signatures in the intensity dependent photoelectron spectrum of the MPI feature.
Extending the study of the CD to photoelectron features from ATI, we found that the higher the order of the ATI feature, the lower the value of the CD at the highest laser intensities will be. Additionally, we compared predictions of the CD from TDSE calculations for the MPI and ATI features and found good agreement between the predicted and experimentally determined CD values.
Studying the CD at even higher laser intensities at a different wavelength of the optical laser of 793 nm, we could observe the depletion of helium ions prepared in the $3p_{+1}$ state, leading to an intensity independent circular dichroism.
Comparing the CD of the MPI photoelectron for three different central wavelengths of the optical laser 784 nm, 793 nm and 800 nm, we found that the CD does not recover to positive values for 793 nm and 800 nm, as it did for 784 nm. The reason being the shift of ionization via the transient $4f_{+3}$ resonance below the ionization threshold for 793 nm and 800 nm due to the decreased photon energy.
To further investigate the influence of these resonances we expanded the investigation to also include the angular distribution of the photoelectrons, which has previously been omitted by investigating the kinetic energy of the distinct photoelectron features.
We could show that the angular distribution of the MPI and ATI photoelectrons for temporally separated pulses in the co- and counter-rotating case at a central wavelength of 784 nm of the optical laser follows the predictions of LOPT. For the counter-rotating case a superposition of partial waves, given by associated Legendre polynomials according to the angular and momentum quantum numbers of the final states, could describe the angular distribution of the ATI photoelectrons at any of the laser intensities used in the experiment. Transient resonances influence the weight of each of the final states, thereby influencing and changing the angular distribution. Resonant ionization via the $6d_{-2}/6g_{-2}$ resonance favours the final state (4, -4) with a total of two lobes perpendicular to the beam propagation direction. At higher laser intensities resonant ionization via the $4p_{-1}/4f_{-1}$ resonance leads to an angular distribution that favours the final state (6, -4), which leads to a total of six lobes in the angular distribution. We found good agreement between the measured angular distributions of the ATI feature and the angular distribution determined by TDSE calculations.
To see if the predictions by LOPT hold true at higher laser intensities, we investigated the intensity dependent angular distribution of ATI photoelectrons for temporally overlapped pulses, to avoid saturation. To have access to these higher laser intensities, the central wavelength of the optical laser was set to 793 nm . At and above laser intensities of $8.5 \cdot 10^{12}\,\mathrm{W/cm^2}$ the angular distribution consists of twelve lobes, which is not supported by predictions from LOPT and hints at addi-

tional final states becoming available with different combinations of angular and magnetic quantum numbers. These final states had lobes along the beam propagation direction, which can in principle only appear if the polarization of the optical laser pulses has a linear component. That this linear component is not apparent at lower laser intensities might be the result of an intensity dependent linear polarization component, induced by the attenuation of the optical laser beam. In contrast to this, the angular distribution for co-rotating pulses exhibits no intensity dependence, showing that in the co-rotating case a linear polarization component either does not appear or that it has no influence on the angular distribution of the photoelectrons.

Further comparing the influence of different central wavelengths, 784 nm, 793 nm and 800 nm of the optical laser on the angular distribution of the photoelectrons showed that the appearance of additional final states at higher laser intensities for temporally overlapped pulses in the counter-rotating case is connected to the MPI feature shifting below the ionization threshold. This was concluded since, at a laser intensity of $8.3 \cdot 10^{12}\,\mathrm{W/cm^2}$ and higher, the lobes along the beam propagation were more pronounced, the longer the central wavelength of the optical laser is.

CONCLUSION AND OUTLOOK

The three major topics presented in this thesis deal with the interaction of atoms and molecules with intense femtosecond laser pulses of different colors.
In the first part, the XUV spectrum of a new semi-infinite gas cell in a laser laboratory at the EuXFEL was characterized regarding the gas pressure in the cell, the laser intensity and the position of the cell relative to the focal point of the driving beam. With a driving wavelength of 800 nm we were able to generate harmonics with a photon energy of up to 41.85 eV (27^{th} harmonic) in Argon. The XUV spectrum was characterized using the second harmonic with a wavelength of 400 nm to drive the high harmonic generation process. With this driving wavelength, we only obtained two harmonics at 21.7 eV (7^{th} harmonic) and 27.9 eV (9^{th} harmonic) with the former having a much higher yield. In this way, we essentially have a light source that mainly produces one XUV wavelength, which is very advantageous for photoelectron spectroscopy, as features in the photoelectron spectrum generated by different harmonics don't overlap. To demonstrate this capability, a photoelectron spectrum of molecular hydrogen using the XUV source driven by the second harmonic was measured and results were compared to literature values, resulting in a good agreement. In a future setup, the XUV source could be adapted to generate circularly polarized harmonics to allow for two-color pump-probe experiments on atomic systems or chiral molecules.
The investigations regarding the dissociation of molecular hydrogen in the laserlab at the EuXFEL in strong laser fields with central wavelengths of 800 nm and 400 nm showed the results known from literature, which confirmed that the newly commissioned experimental setup produces the expected results. With this, we moved on to the dissociation of methane using intense pulses with the same wavelengths used for the dissociation of molecular hydrogen. Compared to the hydrogen ion fragments of the hydrogen molecule, the hydrogen ion fragments from the dissociation of methane reached much higher kinetic energies, indicating higher degrees of ionization. This is also confirmed by the appearance of the triply charged carbon ion. The kinetic energy increase of some fragments originating from Coulomb-explosion channels with increasing photon energy indicates that higher laser intensities enable earlier ionization during an ongoing dissociation, leading to higher kinetic energies. One of the most striking aspects of the dissociation of methane was the formation of the molecular hydrogen ion, which had one high kinetic energy dissociation channel with a kinetic energy of 5.4 eV for all laser intensities after its appearance. In the ToF spectrum of the VMI indications for the formation of the trihydrogen ion could be found, but unfortunately not with enough statistics to allow for an investigation of its kinetic energy. At the shorter wavelength of 400 nm, the maximum kinetic energy of the fragments was overall lower, as was the yield of lighter fragments in the dissociation chain compared to the dissociation at 800 nm for similar laser intensities.
Using a delay-line VMI to record the angular distribution of the ions created in the dissociation, we had access to coincidence data of ions from the dissociation, which

clearly showed the coulomb-explosion channels of methane, as for example the dissociation of the methane di-cation, CH_4^{2+} into the molecular hydrogen ion, H_2^+, and the methylene ion, CH_2^+. The difference in the angular distribution of the hydrogen ions at 800 nm and 400 nm was in the appearance of multiple features at 800 nm, whereas only one feature was visible at 400 nm. The angular distribution of the low kinetic energy dissociation channels was more aligned towards the light's polarization at 400 nm than at 800 nm. Overall the observation is that the dissociation at 800 nm leads to more dissociation channels and fragments with higher kinetic energies at similar intensities, due to electron-recollision, which leads to higher excited states for 800 nm. Also, tunneling-ionization is more likely at 800 nm due to the period of the field being twice as long. As an outlook, it would be interesting to study the formation dynamics of H_2^+ in a pump-probe experiment, which could also shine a light on the dynamics that lead to the formation of H_3^+.
Lastly, the circular dichroism in multi-photon ionization of resonantly excited helium ions was investigated. For this, the intense circularly polarized XUV pulses provided by FERMI FEL at the LDM endstation were used to ionize and excite helium atoms into excited helium ions in the $3p_{+1}$ state by sequential ionization and excitation. Temporally overlapped NIR pulses with the same or opposite helicity as the XUV pulses then ionized the excited helium ions by MPI. For the MPI feature of the photoelectron spectrum, it was found that the CD is highly intensity dependent. It was suggested that this intensity dependence of the CD was due to a population imbalance in the $3p_{+1}$ state induced by the helicity-dependent AC-Stark shift of the $3p_{+1}$ resonance, leading to uneven populations. With the recent experiment, we could confirm this helicity-dependent AC-Stark shift and adapted the experimental setup so that the NIR pulses arrive 500 fs after the XUV pulses, making sure that the $3p_{+1}$ resonance is evenly populated for the different helicities of the NIR pulse. Additionally, the intensity dependence of the CD was measured over a larger range up to barrier-suppression intensities. Without the population imbalance, we still found a significant intensity dependence of the CD, as it decreases with increasing laser intensity from 1 to below zero and then increases again. We found that this behaviour of the CD is due to two factors. One is the combined AC-Stark and ponderomotive shift for the co-rotating case, whereas for the counter-rotating case the AC-Stark shift is negligible, leading to a strong decrease of the CD. That the CD recovers again at higher laser intensities is due to Freeman resonances involving the 4f state at the threshold, which is just above the threshold for co-rotating pulses and just below the threshold for the counter-rotating case, leading again to a positive CD. The CD of higher non-linear features such as the ATI, ATI 2 and ATI 3 photoelectrons show a similar behaviour in that the CD for each feature decreases with increasing laser intensity. Increasing the laser intensity further to over-barrier ionization intensities leads to saturation of the CDs' intensity dependence. Studying the CD for slightly different central wavelengths of the NIR pulses showed the relevance of the Freeman resonances for the CD, as in the case of longer wavelengths the 4f resonance is below the threshold for both polarization combinations and thus the CD of the MPI feature does not recover to positive values. A comparison with photoelectron spectra and CD values determined by TDSE calculations leads to a good agreement between the experiment and theory.

The angular distribution of the ATI feature revealed the partial wave contribution to the final states of the two polarization combinations. For the co-rotating case, only one final state was available, whereas two were available for counter-rotating pulses. For the co-rotating case, the PAD showed no intensity dependence, as only one final state was available. For the counter-rotating case, this was very different, as two final states can interfere. At lower laser intensities the (4, -4) state with two lobes was dominant, which changed as the MPI feature shifts below the ionization threshold and the (6, -4) state with six lobes becomes the dominant one. Apparently resonant ionization via high-lying Rydberg states favours the (6, -4) final state. Different wavelengths did not show significant differences in the intensity dependence of the CD, aside from the fact that for longer wavelengths the shift below the ionization threshold of the MPI photoelectrons happens already at lower NIR intensities. The intensity dependence of the ATI photoelectrons derived from TDSE calculations agrees well with the measured intensity dependence. A very interesting phenomenon was visible in the counter-rotating case for temporally overlapped XUV and NIR pulses at tunneling- and barrier-suppression ionization intensities, as the angular distribution developed a total of 12 lobes, which is not supported considering only the (4, -4) and (6, -4) final states. The exact reason for this is not clear yet.

In the future, it would be very interesting to observe the intensity dependence of the CD at higher laser intensities by using short NIR pulses to observe the intensity dependence of the CD over the whole range from the MPI regime to the tunneling and barrier-suppression regime and investigate if the results in the barrier-suppression regime match results from tunneling experiments on atomic ring-currents. Another interesting aspect could be to investigate the intensity dependence of the PECD in MPI of a chiral molecule with the wavelength of the radiation chosen so that transient resonances will appear by varying the intensity to study how this affects the PECD and the PAD.

APPENDIX

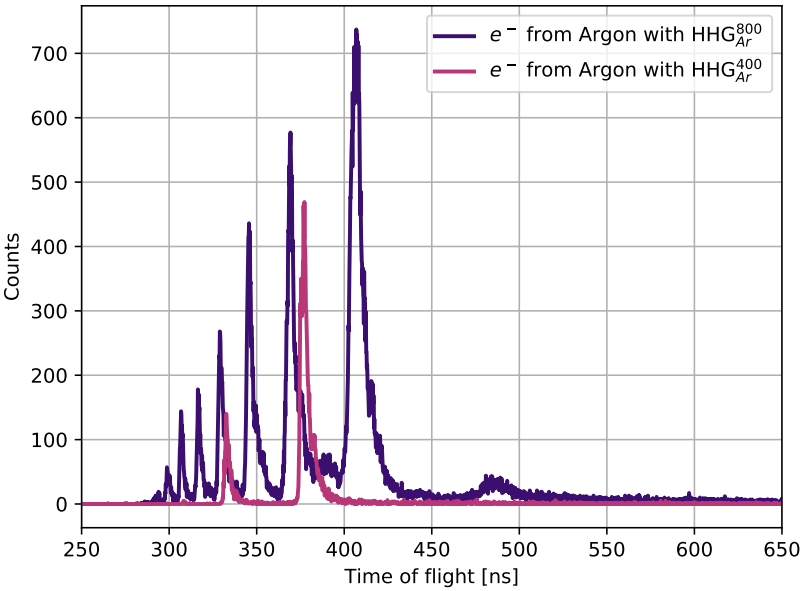

Figure 93: Time-of-flight spectra of photoelectrons from argon generated by HHG in argon driven by 800 nm and 400 nm.

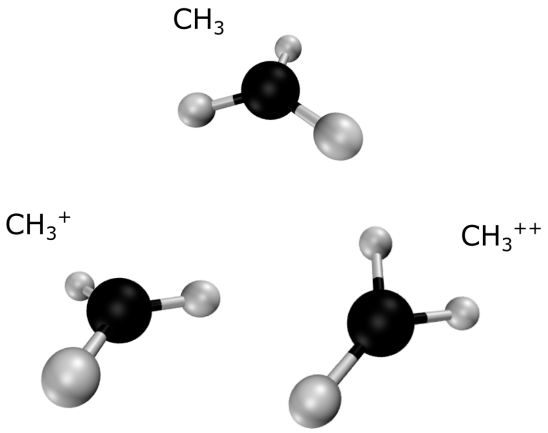

Figure 94: Geometry of methyl, the methyl ion and the methyl di-cation.

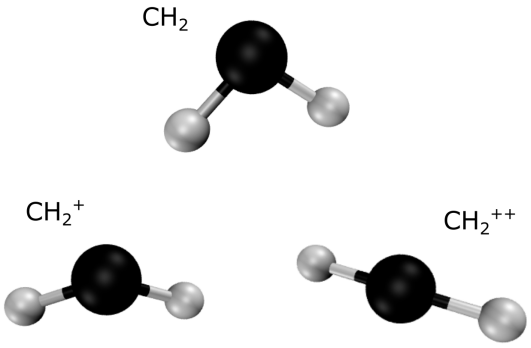

Figure 95: Geometry of methylene, the methylene ion and the methylene di-cation.

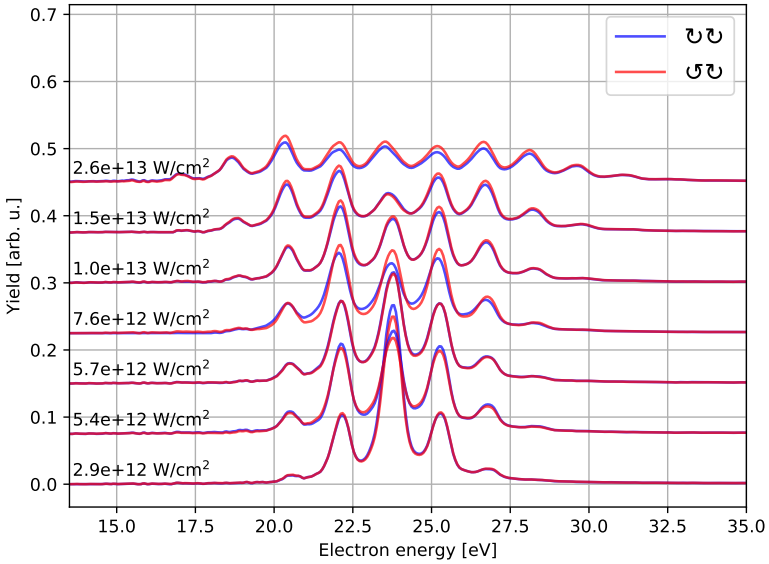

Figure 96: Comparison of co- and counter-rotating sideband spectra at similar laser intensities, for a range of different laser intensities.

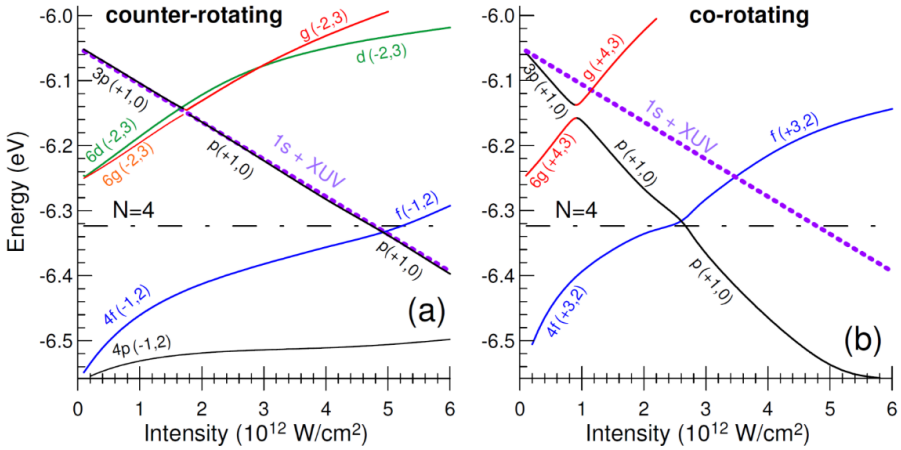

Figure 97: Shown are the quasi-energies of helium ion states depending on the NIR laser intensity relative to the helium ions 1s state for the a), counter-rotating and b), co-rotating case. The figure is taken from [51] and has been adapted.

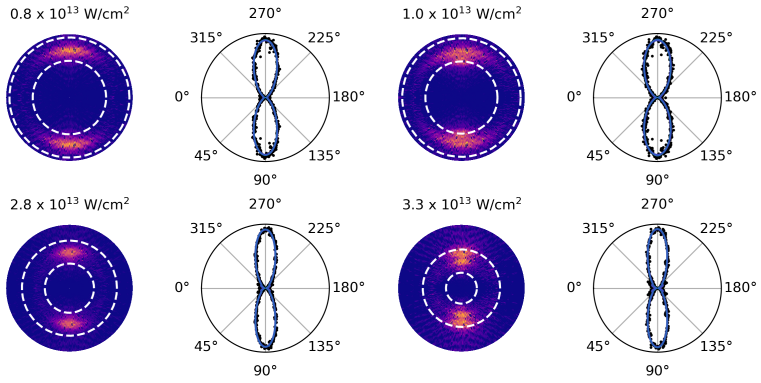

Figure 98: Intensity dependent angular distribution at 793 nm if the laser pulses are temporally overlapped for the co-rotating case. Shown are pairs of images to one laser intensity. The left image shows a slice of the reconstructed 3D distribution, while the right image shows the energy-integrated angular yield. The integration borders are marked by the white circles in the left images.

ABBREVIATIONS

CPA - chirped pulse amplification
MPI - multi-photon ionization
ToF - time-of-flight
VMI - velocity map imaging
HHG - high harmonic generation
XUV - extreme ultraviolet
FEL - free-electron laser
SASE - self-amplified spontaneous emission
UV - ultraviolet
CD - circular dichroism
PECD - photoelectron circular dichroism
PAD - photoelectron angular distribution
LDM - low density matter
NIR - near-infrared
ATI - above-threshold ionization
TDSE - time-dependent Schrödinger equation
MCP - multi-channel plate
CFD - constant fraction discriminator
PES - potential energy surface
DFT - density-functional theory
ATD - above-threshold dissociation
CREI - charge-resonance-enhanced ionization
KE - kinetic energy
KER - kinetic energy release
OBI - over-barrier ionization
REMPI - resonance-enhanced multi-photon ionization
CW - continuous-wave
FWHM - full-width half-maximum
SHG - second-harmonic generation
BBO - bariumborate
APT - attosecond pulse train
HGHG - high-gain harmonic generation
FROG - frequency-resolved optical gating
NIM - nuclear instrument standard
ADC - analog-to-digital converter
BS - bond-softening
VT - vibrational-trapping
FC - Franck-Condon
FAD - field-assisted dissociation
PIPICO - photoion-photoion coincidence
PEPICO - photoelectron-photoion coincidence

SIGC - semi-infinite gas cell
LOPT - lowest order perturbation theory
LINAC - linear accelerator

BIBLIOGRAPHY

1. Li, T., Senesi, A. J. & Lee, B. Small Angle X-ray Scattering for Nanoparticle Research. *Chemical Reviews* **116.** PMID: 27054962, 11128–11180 (2016).
2. Reinert, F. & Hüfner, S. Photoemission spectroscopy—from early days to recent applications. *New Journal of Physics* **7,** 97–97 (Apr. 2005).
3. Metcalf, H. J. & van der Straten, P. Laser cooling and trapping of atoms. *J. Opt. Soc. Am. B* **20,** 887–908 (May 2003).
4. Abbott, B. P. *et al.* Observation of Gravitational Waves from a Binary Black Hole Merger. *Phys. Rev. Lett.* **116,** 061102 (6 Feb. 2016).
5. Einstein, A. Über einen die Erzeugung und Verwandlung des Lichtes betreffenden heuristischen Gesichtspunkt. *Annalen der Physik* (Jan. 1905).
6. Strickland, D. & Mourou, G. Compression of amplified chirped optical pulses. *Optics Communications* **56,** 219–221. ISSN: 00304018 (1985).
7. Göppert-Mayer, M. Über Elementarakte mit zwei Quantensprüngen. *Annalen der Physik* **401,** 273–294 (1931).
8. Franken, P. A. *et al.* Generation of optical harmonics. *Physical Review Letters* **7,** 118–119. ISSN: 00319007 (1961).
9. Kaiser, W. & Garrett, C. G. B. Two-Photon Excitation in CaF_2: Eu^{2+}. *Phys. Rev. Lett.* **7,** 229–231 (6 Sept. 1961).
10. Mainfray, G & Manus, G. Multiphoton ionization of atoms. *Reports on Progress in Physics* **54,** 1333–1372 (Oct. 1991).
11. Keldysh, L. V. Ionization in the Field of a Strong Electromagnetic Wave. *Soviet Physics JETP* **20,** 1307–1314 (1965).
12. Chin, S. L., Yergeau, F & Lavigne, P. Tunnel ionisation of Xe in an ultraintense CO_2 laser field (10^{14} W/cm^2) with multiple charge creation. *Journal of Physics B: Atomic and Molecular Physics* **18,** L213–L215 (Apr. 1985).
13. Giusti-Suzort, A. *et al.* Dynamics of H_2^+ in intense laser fields. *Journal of Physics B: Atomic, Molecular and Optical Physics* **28,** 309–339. ISSN: 13616455 (1995).
14. Cornaggia, C. *et al.* Intensity dependence of the multielectron dissociative ionization of N_2 at 305 and 610 nm. *Phys. Rev. A* **42,** 5464–5472 (9 Nov. 1990).
15. Zewail, A. H. Laser Femtochemistry. *Science* **242,** 1645–1653 (1988).
16. Urbain, X. *et al.* Intense-laser-field ionization of molecular hydrogen in the tunneling regime and its effect on the vibrational excitation of H2+. *Physical Review Letters* **92,** 1–4. ISSN: 00319007 (2004).
17. Frasinski, L. J. *et al.* Manipulation of bond hardening in H2+ by chirping of intense femtosecond laser Pulses. *Physical Review Letters* **83,** 3625–3628. ISSN: 10797114 (1999).

18. Walsh, T. D., Ilkov, F. A. & Chin, S. L. The dynamical behaviour of H2 and D2 in a strong, femtosecond, titanium:sapphire laser field. *Journal of Physics B: Atomic, Molecular and Optical Physics* **30,** 2167–2175. ISSN: 09534075 (1997).

19. Xu, H. *et al.* Experimental observation of the elusive double-peak structure in R-dependent strong-field ionization rate of H2+. *Scientific Reports* **5.** ISSN: 20452322 (2015).

20. Boll, R. *et al.* X-ray multiphoton-induced Coulomb explosion images complex single molecules. *Nature Physics* **18,** 423–428. ISSN: 1745-2481 (Apr. 2022).

21. Hoshina, K. *et al.* Efficient ejection of H3+ from hydrocarbon molecules induced by ultrashort intense laser fields. *The Journal of Chemical Physics* **129,** 104302 (2008).

22. Okino, T *et al.* Ejection dynamics of hydrogen molecular ions from methanol in intense laser fields. *Journal of Physics B: Atomic, Molecular and Optical Physics* **39,** S515–S521 (June 2006).

23. Wu, C. *et al.* Laser-induced dissociation and explosion of methane and methanol. *Journal of Physics B: Atomic, Molecular and Optical Physics* **35,** 2575–2582. ISSN: 09534075 (2002).

24. Strohaber, J. *et al.* Observation of anisotropic fragmentation in methane subjected to femtosecond radiation. *Physical Review A - Atomic, Molecular, and Optical Physics* **89,** 2–7. ISSN: 10502947 (2014).

25. Jagutzki, O. *et al.* Multiple hit readout of a microchannel plate detector with a three-layer delay-line anode. *IEEE Transactions on Nuclear Science* **49,** 2477–2483 (2002).

26. Månsson, E. P. *et al.* Ultrafast dynamics of adenine following XUV ionization. *Journal of Physics: Photonics* **4,** 034003 (May 2022).

27. Zhong, S. *et al.* Attosecond electron–spin dynamics in Xe 4d photoionization. *Nature Communications* **11,** 5042. ISSN: 2041-1723 (Oct. 2020).

28. Rohde, G. *et al.* Ultrafast Formation of a Fermi-Dirac Distributed Electron Gas. *Phys. Rev. Lett.* **121,** 256401 (25 Dec. 2018).

29. Popmintchev, T. *et al.* Bright Coherent Ultrahigh Harmonics in the keV X-ray Regime from Mid-Infrared Femtosecond Lasers. *Science* **336,** 1287–1291 (2012).

30. Yang, Y. *et al.* Strong-field coherent control of isolated attosecond pulse generation. *Nature Communications* **12,** 6641. ISSN: 2041-1723 (Nov. 2021).

31. Kfir, O. *et al.* Generation of bright phase-matched circularly-polarized extreme ultraviolet high harmonics. *Nature Photonics* **9,** 99–105. ISSN: 1749-4893 (Feb. 2015).

32. Walker, R. P. Synchrotron radiation (1994).

33. Robinson, A. L. History of Synchrotron Radiation. *Synchrotron Radiation News* **28,** 4–9. https://doi.org/10.1080/08940886.2015.1059228 (2015).

34. Milton, S. V. *et al.* Exponential gain and saturation of a self-amplified spontaneous emission free-electron laser. *Science* **292,** 2037–2041. ISSN: 00368075 (2001).

35. Allaria, E. *et al.* Highly coherent and stable pulses from the FERMI seeded free-electron laser in the extreme ultraviolet. *Nature Photonics* **6,** 699–704. ISSN: 17494885 (2012).

36. Ackermann, W. *et al.* Operation of a free-electron laser from the extreme ultraviolet to the water window. *Nature Photonics* **1,** 336–342. ISSN: 1749-4893 (June 2007).

37. Decking, W. *et al.* A MHz-repetition-rate hard X-ray free-electron laser driven by a superconducting linear accelerator. *Nature Photonics* **14,** 391–397. ISSN: 1749-4893 (June 2020).

38. Bostedt, C. *et al.* Linac Coherent Light Source: The first five years. *Rev. Mod. Phys.* **88,** 015007 (1 Mar. 2016).

39. Allaria, E. *et al.* Control of the polarization of a vacuum-ultraviolet, high-gain, free-electron laser. *Physical Review X* **4,** 1–15. ISSN: 21603308 (2014).

40. Mazza, T. *et al.* Determining the polarization state of an extreme ultraviolet free-electron laser beam using atomic circular dichroism. *Nature Communications* **5,** 1–6. ISSN: 20411723 (2014).

41. Lutman, A. A. *et al.* Polarization control in an X-ray free-electron laser. *Nature Photonics* **10,** 468–472. ISSN: 17494893 (2016).

42. Meierhenrich, U. *Amino Acids and the Asymmetry of Life* (Springer, 2008).

43. Lux, C. *et al.* Circular Dichroism in the Photoelectron Angular Distributions of Camphor and Fenchone from Multiphoton Ionization with Femtosecond Laser Pulses. *Angewandte Chemie International Edition* **51,** 5001–5005 (2012).

44. Beaulieu, S. *et al.* Multiphoton photoelectron circular dichroism of limonene with independent polarization state control of the bound-bound and bound-continuum transitions. *The Journal of Chemical Physics* **149,** 134301 (2018).

45. Artemyev, A. N. *et al.* Photoelectron circular dichroism in the multiphoton ionization by short laser pulses. I. Propagation of single-active-electron wave packets in chiral pseudo-potentials. *The Journal of Chemical Physics* **142,** 244105 (2015).

46. Barth, I. & Smirnova, O. Nonadiabatic tunneling in circularly polarized laser fields: Physical picture and calculations. *Phys. Rev. A* **84,** 063415 (6 2011).

47. Eckart, S. *et al.* Ultrafast preparation and detection of ring currents in single atoms. *Nature Physics* **14,** 701–704. ISSN: 1745-2481 (2018).

48. Ilchen, M. *et al.* Circular Dichroism in Multiphoton Ionization of Resonantly Excited He+ Ions. *Physical Review Letters* **118,** 1–6. ISSN: 10797114 (2017).

49. De Silva, A. H. *et al.* Using Circular Dichroism to Control Energy Transfer in Multiphoton Ionization. *Physical Review Letters* **126,** 23201. ISSN: 10797114 (2021).

50. De Silva, A. H. N. C. *et al.* Circular Dichroism in Atomic Resonance-Enhanced Few-Photon Ionization. **053125,** 1–7. ISSN: 24699934 (2021).

51. Grum-Grzhimailo, A. N. *et al.* Two-color XUV plus near-IR multiphoton near-threshold ionization of the helium ion by circularly polarized light in the vicinity of the 3p resonance. *Physical Review A* **100,** 1–7. ISSN: 24699934 (2019).

52. Amusia, M. Y. in *VUV and Soft X-Ray Photoionization* (eds Becker, U. & Shirley, D. A.) 1 (Plenum Press - New York and London, 1996).
53. Sobota, J. A., He, Y. & Shen, Z. X. Angle-resolved photoemission studies of quantum materials. *Reviews of Modern Physics* **93,** 1–72. ISSN: 15390756 (2021).
54. Leißner, T. *et al.* Morphological tuning of the plasmon dispersion relation in dielectric-loaded nanofiber waveguides. *Physical Review Letters* **111,** 1–5. ISSN: 00319007 (2013).
55. Ilchen, M. *et al.* Site-specific interrogation of an ionic chiral fragment during photolysis using an X-ray free-electron laser. *Communications Chemistry* **4,** 1–14. ISSN: 23993669 (2021).
56. Heimann, P. A. *et al.* Helium and neon photoelectron satellites at threshold. *Physical Review A* **34,** 3782–3791. ISSN: 10502947 (1986).
57. Amusia, M. Y. *Atomic Photoeffect* 13 –25, 47 –54 (Plenum Press, New York, 1990).
58. Fließbach, T. *Quantenmechanik - Lehrbuch zur Theoretischen Physik III* 5th ed., 324–329 (Spektrum Akademischer Verlag, Heidelberg, 2008).
59. Bethe, H. A. & Salpeter, E. E. *Quantum Mechanics of One- and Two-Electron Atoms* 251–255, 295–303 (Springer-Verlag, Berlin, Heidelberg, 1957).
60. *Atoms, Molecules and Photons. An Introduction to Atomic-, Molecular- and Quantum Physics* 2nd ed. (ed Demtröder, W.) (Springer, Berlin, Heidelberg, 2010).
61. Manson, S. T. & Cooper, J. W. Photo-Ionization in the Soft x-Ray Range: 1Z Dependence in a Central-Potential Model. *Phys. Rev.* **165,** 126–138 (1 Jan. 1968).
62. Starace, A. F. in *Springer Handbooks of Atomic, Molecular and Optical Physics* (ed Drake, G. W. F.) 2nd ed., 379–388 (Springer, New York, Berlin, 2006).
63. Lindle, D. W. *et al.* Photoemission from Xe in the vicinity of the 4d Cooper minimum. *Phys. Rev. A* **37,** 3808–3812 (10 May 1988).
64. Cooper, J. W. Photoionization from outer atomic subshells. a model study. *Physical Review* **128,** 681–693. ISSN: 0031899X (1962).
65. Haglund, R. in *Springer Handbooks of Lasers and Optics* (ed Träger, F.) 2nd ed., 17 (Springer-Verlag Berlin Heidelberg, 2012).
66. H. J. Eichler, J. E. *Laser* 7th ed. (Springer-Verlag Berlin Heidelberg, 2010).
67. N. B. Delone, V. P. K. *Multiphoton Processes in Atoms* 2nd ed., 1–9 (Springer-Verlag Berlin Heidelberg, 2000).
68. Zheltikov, A. M. Keldysh parameter, photoionization adiabaticity, and the tunneling time. *Phys. Rev. A* **94,** 043412 (4 Oct. 2016).
69. Landsman, A. S. *et al.* Ultrafast resolution of tunneling delay time. *Optica* **1,** 343–349 (Nov. 2014).
70. Bucksbaum, P. H. *et al.* Role of the ponderomotive potential in above-threshold ionization. *J. Opt. Soc. Am. B* **4,** 760–764 (May 1987).
71. Crance, M. Nonperturbative ac Stark shifts in hydrogen atoms. *J. Opt. Soc. Am. B* **7,** 449–455 (Apr. 1990).

72. N. B. Delone, V. P. K. *Multiphoton Processes in Atoms* 2nd ed., 15–18 (Springer-Verlag Berlin Heidelberg, 2000).

73. McIlrath, T. J. *et al.* Above-threshold ionization processes in xenon and krypton. *Phys. Rev. A* **35,** 4611–4623 (11 June 1987).

74. Streibel, T. & Zimmermann, R. Resonance-enhanced multiphoton ionization mass spectrometry (REMPI-ms): Applications for process analysis. *Annual Review of Analytical Chemistry* **7,** 361–381. ISSN: 19361335 (2014).

75. Freeman, R. R. *et al.* Above-threshold ionization with subpicosecond laser pulses. *Physical Review Letters* **59,** 1092–1095. ISSN: 00319007 (1987).

76. Mevel, E. *et al.* Atoms in strong optical fields: Evolution from multiphoton to tunnel ionization. *Physical Review Letters* **70,** 406–409. ISSN: 00319007 (1993).

77. Freeman, R. R. & Bucksbaum, P. H. Investigations of above-threshold ionization using subpicosecond laser pulses. *Journal of Physics B: Atomic, Molecular and Optical Physics* **24,** 325–347. ISSN: 09534075 (1991).

78. Agostini, P. *et al.* Giant Stark shifts in multiphoton ionization. *Physical Review Letters* **63,** 2208–2211. ISSN: 00319007 (1989).

79. Li, M. *et al.* Selective enhancement of resonant multiphoton ionization with strong laser fields. *Physical Review A - Atomic, Molecular, and Optical Physics* **92,** 1–6. ISSN: 10941622 (2015).

80. Smith, S. J. & Leuchs, G. Angular correlation in multiphoton ionization of atoms. *Advances in Atomic and Molecular Physics* **24,** 157–221. ISSN: 00652199 (1988).

81. Hall, J. L. & Siegel, M. W. Angular Dependence of the Laser Photodetachment of the Negative Ions of Carbon, Oxygen, and Hydrogen. *The Journal of Chemical Physics* **48,** 943. ISSN: 00219606 (1968).

82. Cooper, J. & Zare, R. N. Angular Distribution of Photoelectrons. *The Journal of Chemical Physics* **48,** 942–943 (1968).

83. Manson, S. T. & Starace, A. F. Photoelectron angular distributions: Energy dependence for s subshells. *Reviews of Modern Physics* **54,** 389–405. ISSN: 00346861 (1982).

84. Reid, K. L. Photoelectron angular distributions. *Annual Review of Physical Chemistry* **54,** 397–424. ISSN: 0066426X (2003).

85. Faisal, F. H. M. *Theory of Multiphoton Processes* 1st ed., 89 –117 (Springer-Verlag US, 1987).

86. Rogers, D. M. *et al.* Electronic Circular Dichroism Spectroscopy of Proteins. *Chem* **5,** 2751–2774. ISSN: 24519294 (2019).

87. Barron, L. D. *Molecular Light Scattering and Optical Activity* 2nd ed., 2 (Cambridge University Press, 2004).

88. Brookes, J., Horsfield, A. & Stoneham, A. Odour character differences for enantiomers correlate with molecular flexibility. *Journal of the Royal Society, Interface / the Royal Society* **6,** 75–86 (Aug. 2008).

89. Nguyen, L., He, H. & Pham-Huy, C. Chiral Drugs: An Overview. *International journal of biomedical science : IJBS* **2,** 85–100 (June 2006).

90. Artemyev, A. N. *et al.* Photoelectron circular dichroism in the multiphoton ionization by short laser pulses. I. Propagation of single-active-electron wave packets in chiral pseudo-potentials. *The Journal of Chemical Physics* **142,** 244105 (2015).

91. Beaulieu, S. *et al.* Photoexcitation circular dichroism in chiral molecules. *Nature Physics* **14,** 484–489. ISSN: 17452481 (2018).

92. Ritchie, B. Theory of the angular distribution for ejection of photoelectrons from optically active molecules and molecular negative ions. II. *Physical Review A* **14,** 359–362. ISSN: 10502947 (1976).

93. Böwering, N. *et al.* Asymmetry in photoelectron emission from chiral molecules induced by circularly polarized light. *Physical Review Letters* **86,** 1187–1190. ISSN: 00319007 (2001).

94. Lux, C. *et al.* Circular dichroism in the photoelectron angular distributions of camphor and fenchone from multiphoton ionization with femtosecond laser pulses. *Angewandte Chemie - International Edition* **51,** 5001–5005. ISSN: 14337851 (2012).

95. Müller, A. D., Artemyev, A. N. & Demekhin, P. V. Photoelectron circular dichroism in the multiphoton ionization by short laser pulses. II. Three- and four-photon ionization of fenchone and camphor. *Journal of Chemical Physics* **148.** ISSN: 00219606 (2018).

96. Beaulieu, S. *et al.* Universality of photoelectron circular dichroism in the photoionization of chiral molecules. *New Journal of Physics* **18,** 1–8. ISSN: 13672630 (2016).

97. Herath, T. *et al.* Strong-field ionization rate depends on the sign of the magnetic quantum number. *Physical Review Letters* **109,** 1–5. ISSN: 00319007 (2012).

98. Barty, C. P. J. *et al.* Generation of 18-fs, multiterawatt pulses by regenerative pulse shaping and chirped-pulse amplification. *Optics Letters* **21,** 668. ISSN: 0146-9592 (1996).

99. Emma, P. *et al.* First lasing and operation of an ångstrom-wavelength free-electron laser. *Nature Photonics* **4,** 641–647. ISSN: 17494885 (2010).

100. Li, J. *et al.* Attosecond science based on high harmonic generation from gases and solids. *Nature Communications* **11,** 1–13. ISSN: 20411723 (2020).

101. Hirlimann, C. in *Femtosecond Laser Pulses* (ed Rullière, C.) 2nd ed., 1–23 (Springer Science+Media Business Media, Inc., 2005).

102. Maiman, T. H. Optical and microwave-optical experiments in ruby. *Physical Review Letters* **4,** 564–566. ISSN: 00319007 (1960).

103. Javan, A., Bennett, W. R. & Herriott, D. R. Population inversion and continuous optical maser oscillation in a gas discharge containing a He-Ne mixture. *Physical Review Letters* **6,** 106–110. ISSN: 00319007 (1961).

104. Patel, C. K. Continuous-Wave Laser Action on Vibrational-Rotational Transitions of CO2. *Physical Review* **136.** ISSN: 0031899X (1964).

105. Hargrove, L. E., Fork, R. L. & Pollack, M. A. Locking of He-Ne laser modes induced by synchronous intracavity modulation. *Applied Physics Letters* **5,** 4–5. ISSN: 00036951 (1964).

106. Haus, H. A. Mode-locking of lasers. *IEEE Journal on Selected Topics in Quantum Electronics* **6,** 1173–1185. ISSN: 1077260X (2000).

107. Morgner, U *et al.* Sub-two-cycle pulses from a Kerr-lens mode-locked Ti : sapphire laser (vol 24, pg 411, 1999). *Optics Letters* **24,** 920 (1999).

108. French, P. M. The generation of ultrashort laser pulses. *Reports on Progress in Physics* **58,** 169–262. ISSN: 00344885 (1995).

109. Hirlimann, C. in *Femtosecond Laser Pulses* (ed Rullière, C.) 2nd ed., 25–56 (Springer Science+Media Business Media, Inc., 2005).

110. Spence, D. E., Kean, P. N. & Sibbett, W. 60-fsec pulse generation from a self-mode-locked Ti:sapphire laser. *Optical Society of America* **16,** 42–44 (1991).

111. Eckardt, R. C. & Reintjes, J. Phase Matching Limitations of High Efficiency Second Harmonic Generation. *IEEE Journal of Quantum Electronics* **20,** 1178–1187. ISSN: 15581713 (1984).

112. Dharmadhikari, A. K. *et al.* Highly efficient white light generation from barium fluoride. *Optics Express* **12,** 695. ISSN: 1094-4087 (2004).

113. Couairon, A. & Mysyrowicz, A. Femtosecond filamentation in transparent media. *Physics Reports* **441,** 47–189. ISSN: 03701573 (2007).

114. New, G. H. & Ward, J. F. Optical third-harmonic generation in gases. *Physical Review Letters* **19,** 556–559. ISSN: 00319007 (1967).

115. Wildenauer, J. Generation of the ninth, eleventh, and fifteenth harmonics of iodine laser radiation. *Journal of Applied Physics* **62,** 41–48. ISSN: 00218979 (1987).

116. Johnson, A. S. *et al.* High-flux soft x-ray harmonic generation from ionization-shaped few-cycle laser pulses. *Science Advances* **4.** ISSN: 23752548 (2018).

117. Midorikawa, K. Ultrafast dynamic imaging. *Nature Photonics* **5,** 640–641. ISSN: 17494885 (2011).

118. Corkum, P. B. Plasma perspective on strong field multiphoton ionization. *Physical Review Letters* **71,** 1994–1997. ISSN: 00319007 (1993).

119. Lewenstein, M. *et al.* Theory of high-harmonic generation by low-frequency laser fields. *Physical Review A* **49,** 2117–2132. ISSN: 10502947 (1994).

120. Krause, J. L., Schafer, K. J. & Kulander, K. C. High-order harmonic generation from atoms and ions in the high intensity regime. *Physical Review Letters* **68,** 3535–3538. ISSN: 00319007 (1992).

121. Popmintchev, T. *et al.* Bright coherent ultrahigh harmonics in the kev x-ray regime from mid-infrared femtosecond lasers. *Science* **336,** 1287–1291. ISSN: 10959203 (2012).

122. Willner, A. *et al.* Efficient control of quantum paths via dual-gas high harmonic generation. *New Journal of Physics* **13.** ISSN: 13672630 (2011).

123. Zaïr, A. *et al.* Quantum path interferences in high-order harmonic generation. *Physical Review Letters* **100,** 1–4. ISSN: 00319007 (2008).

124. Constant, E. & Mével, E. in *Femtosecond Laser Pulses* (ed Rullière, C.) 2nd ed., 402–404 (Springer Science+Media Business Media, Inc., 2005).

125. Paul, P. M. *et al.* Observation of a train of attosecond pulses from high harmonic generation. *Science* **292,** 1689–1692. ISSN: 00368075 (2001).

126. Marceau, C. *et al.* Wavelength scaling of high harmonic generation for 267 nm, 400nm and 800nm driving laser pulses. *Journal of Physics Communications* **1.** ISSN: 23996528 (2017).

127. Pfeifer, T., Spielmann, C. & Gerber, G. Femtosecond x-ray science. *Reports on Progress in Physics* **69,** 443–505. ISSN: 00344885 (2006).

128. Heyl, C. *et al.* Introduction to macroscopic power scaling principles for high-order harmonic generation. *Journal of Physics B: Atomic, Molecular and Optical Physics* **50,** 013001 (Jan. 2017).

129. Kim, K.-J. Characteristics of synchrotron radiation. **565,** 565–632 (2008).

130. Kunz, C. in *Synchrotron Radiation* (ed Kunz, C.) 1st ed., 1 (Springer-Verlag Berlin Heidelberg, 1979).

131. Hwu, Y. & Margaritondo, G. Synchrotron radiation and X-ray free-electron lasers (X-FELs) explained to all users, active and potential. *Journal of Synchrotron Radiation* **28,** 1014–1029. ISSN: 16005775 (2021).

132. Huang, Z. & Kim, K. J. Review of x-ray free-electron laser theory. *Physical Review Special Topics - Accelerators and Beams* **10,** 1–26. ISSN: 10984402 (2007).

133. Bermúdez Macias, I. J. *et al.* Study of temporal, spectral, arrival time and energy fluctuations of SASE FEL pulses. *Optics Express* **29,** 10491. ISSN: 1094-4087 (2021).

134. Yu, L. H. *et al.* First Ultraviolet High-Gain Harmonic-Generation Free-Electron Laser. *Physical Review Letters* **91,** 89–92. ISSN: 10797114 (2003).

135. Yu, L.-H. *et al.* High-Gain Harmonic-Generation Free-Electron Laser. *Science* **289,** 932–934 (2000).

136. Zhao, Z. T. *et al.* First lasing of an echo-enabled harmonic generation free-electron laser. *Nature Photonics* **6,** 360–363. ISSN: 17494885 (2012).

137. Posthumus, J. H. The dynamics of small molecules in intense laser fields. *Reports on Progress in Physics* **67,** 623–665. ISSN: 00344885 (2004).

138. Loriot, V. *et al.* Laser-induced field-free alignment of the OCS molecule. *Journal of Physics B: Atomic, Molecular and Optical Physics* **40,** 2503–2510. ISSN: 09534075 (2007).

139. Scherrer, A. *et al.* On the mass of atoms in molecules: Beyond the born-oppenheimer approximation. *Physical Review X* **7,** 1–23. ISSN: 21603308 (2017).

140. Burke, K. Perspective on density functional theory. *Journal of Chemical Physics* **136.** ISSN: 00219606 (2012).

141. Neese, F. The ORCA program system. *WIREs Computational Molecular Science* **2,** 73–78 (2012).

142. Condon, E. A theory of intensity distribution in band systems. *Physical Review* **28,** 1182–1201. ISSN: 0031899X (1926).

143. Edvardsson, D *et al.* A photoabsorption, photodissociation and photoelectron spectroscopy study of NH_3 and ND_3. *Journal of Physics B: Atomic, Molecular and Optical Physics* **32,** 2583–2609 (Jan. 1999).

144. Bransden, B. H. & Joachain, C. J. *Physics of Atoms and Molecules* 1st ed., 438–448 (Longmann Publishing Group, 1982).

145. Giusti-Suzor, A *et al.* Dynamics of H2in intense laser fields. *Journal of Physics B: Atomic, Molecular and Optical Physics* **28,** 309–339 (Feb. 1995).

146. Shirley, J. H. Solution of the Schrödinger Equation with a Hamiltonian Periodic in Time. *Phys. Rev.* **138,** B979–B987 (4B May 1965).

147. Bucksbaum, P. H. *et al.* Softening of the H_2^+ molecular bond in intense laser fields. *Phys. Rev. Lett.* **64,** 1883–1886 (16 Apr. 1990).

148. Giusti-Suzor, A. *et al.* Above-threshold dissociation of H2+ in intense laser fields. *Physical Review Letters* **64,** 515–518. ISSN: 00319007 (1990).

149. Zuo, T. & Bandrauk, A. D. Charge-resonance-enhanced ionization of diatomic molecular ions by intense lasers. *Phys. Rev. A* **52,** R2511–R2514 (4 Oct. 1995).

150. Holzmeier, F. *et al.* Control of H_2 Dissociative Ionization in the Nonlinear Regime Using Vacuum Ultraviolet Free-Electron Laser Pulses. *Phys. Rev. Lett.* **121,** 103002 (10 Sept. 2018).

151. Posthumus, J. H. *et al.* Field-ionization, Coulomb explosion of diatomic molecules in intense laser fields. *Journal of Physics B: Atomic, Molecular and Optical Physics* **29,** 5811–5829 (Dec. 1996).

152. Pitzer, M. *et al.* Direct Determination of Absolute Molecular Stereochemistry in Gas Phase by Coulomb Explosion Imaging. *Science* **341,** 1096–1100 (2013).

153. Stoian, R. *et al.* Coulomb explosion in ultrashort pulsed laser ablation of Al_2O_3. *Phys. Rev. B* **62,** 13167–13173 (19 Nov. 2000).

154. Kaesdorf, S. *MANUAL Time-of-Flight Spectrometer for Electron and Ion Spectroscopy* ().

155. Ladislas Wiza, J. Microchannel plate detectors. *Nuclear Instruments and Methods* **162,** 587–601. ISSN: 0029-554X (1979).

156. *The RoentDek Constant Fraction Discriminators CFD8c, CFD7x, CFD4c, CFD1c and CFD1x* https://www.roentdek.com/manuals/CFD%20Manual.pdf. Accessed: February 22, 2022.

157. Ben-Itzhak, I., Ginther, S. & Carnes, K. Coincidence time-of-flight studies of molecular fragmentation. *Nuclear Instruments and Methods in Physics Research Section B: Beam Interactions with Materials and Atoms* **66,** 401–414. ISSN: 0168-583X (1992).

158. Mirsaleh-Kohan, N., Robertson, W. D. & Compton, R. N. Electron ionization time-of-flight mass spectrometry: Historical review and current applications. *Mass Spectrometry Reviews* **27,** 237–285 (2008).

159. Nibarger, J. P., Menon, S. V. & Gibson, G. N. Comprehensive analysis of strong-field ionization and dissociation of diatomic nitrogen. *Physical Review A - Atomic, Molecular, and Optical Physics* **63,** 12. ISSN: 10941622 (2001).

160. Kothe, A. *et al.* Time-of-flight electron spectrometer for a broad range of kinetic energies. *The Review of scientific instruments* **84 2,** 023106 (2013).

161. Chandler, D. W. & Houston, P. L. Two-dimensional imaging of state-selected photodissociation products detected by multiphoton ionization. *The Journal of Chemical Physics* **87,** 1445–1447. ISSN: 00219606 (1987).

162. Eppink, A. T. & Parker, D. H. Velocity map imaging of ions and electrons using electrostatic lenses: Application in photoelectron and photofragment ion imaging of molecular oxygen. *Review of Scientific Instruments* **68,** 3477–3484. ISSN: 00346748 (1997).

163. Ashfold, M. N. *et al.* Imaging the dynamics of gas phase reactions. *Physical Chemistry Chemical Physics* **8,** 26–53. ISSN: 14639076 (2006).

164. Gardiner, S. H. *et al.* Dynamics of the A-band ultraviolet photodissociation of methyl iodide and ethyl iodide via velocity-map imaging with 'universal' detection. *Physical Chemistry Chemical Physics* **17,** 4096–4106. ISSN: 14639076 (2015).

165. Preston, T. J. *et al.* Direct and indirect hydrogen abstraction in Cl + alkene reactions. *Journal of Physical Chemistry A* **118,** 5595–5607. ISSN: 15205215 (2014).

166. Karamatskos, E. T. *et al.* Molecular movie of ultrafast coherent rotational dynamics of OCS. *Nature Communications* **10,** 3364. ISSN: 2041-1723 (2019).

167. Kerbstadt, S. *et al.* Odd electron wave packets from cycloidal ultrashort laser fields. *Nature Communications* **10,** 1–8. ISSN: 20411723 (2019).

168. Sobottka, S. & Williams, M. Delay line readout of microchannel plates. *IEEE Transactions on Nuclear Science* **35,** 348–351 (1988).

169. Vrakking, M. J. An iterative procedure for the inversion of two-dimensional ion/photoelectron imaging experiments. *Review of Scientific Instruments* **72,** 4084. ISSN: 00346748 (2001).

170. Trebino, R. *et al.* Measuring ultrashort laser pulses in the time-frequency domain using frequency-resolved optical gating. *Review of Scientific Instruments* **68,** 3277–3295 (1997).

171. Rothhardt, J. *et al.* Enhancing the macroscopic yield of narrow-band high-order harmonic generation by fano resonances. *Physical Review Letters* **112.** ISSN: 10797114 (2014).

172. Popmintchev, T. *et al.* Phase matching of high harmonic generation in the soft and hard X-ray regions of the spectrum. *Optics InfoBase Conference Papers,* 1–6. ISSN: 21622701 (2009).

173. Sutherland, J. R. *et al.* High harmonic generation in a semi-infinite gas cell. *Optics Express* **12,** 4430. ISSN: 1094-4087 (2004).

174. Brichta, J. P. *et al.* Comparison and real-time monitoring of high-order harmonic generation in different sources. *Physical Review A - Atomic, Molecular, and Optical Physics* **79,** 1–6. ISSN: 10502947 (2009).

175. (2017), A. J. R. *Two-Color Photoionization Experiments with Ultrashort Light Pulses on Small Atomic Systems* PhD thesis (University of Hamburg, Germany).

176. Gullikson, E. *CRXO THE CENTER FOR X-RAY OPTICS* http://henke.lbl.gov/optical_constants/filter2.html. Accessed: 05.05.2020.

177. Henke, B. L., Gullikson, E. M. & Davis, J. X-ray interactions: photoabsorption, scattering, transmission, and reflection at E=50-30000 eV, Z=1-92. *Atomic Data and Nuclear Data Tables* **54,** 181–342 (1993).

178. Polyanskiy, M. *RefractiveIndex.INFO* https://refractiveindex.info. Accessed: 05.05.2020.

179. Werner, W. S., Glantschnig, K. & Ambrosch-Draxl, C. Optical constants and inelastic electron-scattering data for 17 elemental metals. *Journal of Physical and Chemical Reference Data* **38,** 1013–1092. ISSN: 00472689 (2009).

180. Weitzel, K.-M., Mähnert, J. & Penno, M. ZEKE-PEPICO investigations of dissociation energies in ionic reactions. *Chemical Physics Letters* **224,** 371 –380. ISSN: 0009-2614 (1994).

181. Higuet, J. *et al.* High-order harmonic spectroscopy of the Cooper minimum in argon: Experimental and theoretical study. *Physical Review A - Atomic, Molecular, and Optical Physics* **83,** 1–12. ISSN: 10502947 (2011).

182. Sorensen, S. L. *et al.* Argon 3s autoionization resonances. *Phys. Rev. A* **50,** 1218–1230 (2 Aug. 1994).

183. Watson, W. S. & Stewart, D. T. Photoelectron angular distributions for argon and krypton in the 0-20 eV electron energy range. *Journal of Physics B: Atomic and Molecular Physics* **7,** 3–7. ISSN: 00223700 (1974).

184. Samson, J. & Stolte, W. Precision measurements of the total photoionization cross-sections of He, Ne, Ar, Kr, and Xe. *Journal of Electron Spectroscopy and Related Phenomena* **123.** Determination of cross-sections and momentum profiles of atoms, molecules and condensed matter, 265 –276. ISSN: 0368-2048 (2002).

185. Brabec, T. & Krausz, F. Intense few-cycle laser fields: Frontiers of nonlinear optics. *Reviews of Modern Physics* **72,** 545–591. ISSN: 00346861 (2000).

186. Wörner, H. J. *et al.* Observation of electronic structure minima in high-harmonic generation. *Physical Review Letters* **102,** 1–4. ISSN: 00319007 (2009).

187. Popmintchev, D. *et al.* Ultraviolet surprise: Efficient soft x-ray high-harmonic generation in multiply ionized plasmas. *Science* **350,** 1225–1231. ISSN: 0036-8075 (2015).

188. Fangchuan, Z. *et al.* Spectral splitting of high-order harmonic emissions from ionizing gases. *Physical Review A - Atomic, Molecular, and Optical Physics* **65,** 6. ISSN: 10941622 (2002).

189. Cao, W. *et al.* Spectral splitting and quantum path study of high-harmonic generation from a semi-infinite gas cell. *Journal of Physics B: Atomic, Molecular and Optical Physics* **45.** ISSN: 09534075 (2012).

190. Wang, Y. *et al.* Spectral splitting in high-order harmonic generation. *Physical Review A - Atomic, Molecular, and Optical Physics* **62,** 063806–063801. ISSN: 10502947 (2000).

191. Nefedova, V. E. *et al.* Determination of the spectral variation origin in high-order harmonic generation in noble gases. *Physical Review A* **98,** 33414. ISSN: 24699934 (2018).

192. Gullikson, E. *CRXO THE CENTER FOR X-RAY OPTICS* http://henke.lbl.gov/optical_constants/atten2.html. Accessed: 05.05.2020.

193. Wacks, M. E. Franck-Condon Factors for the Ionization of H2, HD, and D2. *Journal of research of the National Bureau of Standards. Section A, physics and chemistry* **68A,** 631–633 (1964).

194. Ibrahim, H. *et al.* H2: The benchmark molecule for ultrafast science and technologies. *Journal of Physics B: Atomic, Molecular and Optical Physics* **51,** 42002. ISSN: 13616455 (2018).

195. Thompson, M. R. *et al.* One and two-colour studies of the dissociative ionization and Coulomb explosion of H2 with intense Ti:sapphire laser pulses. *Journal of Physics B: Atomic, Molecular and Optical Physics* **30,** 5755–5772. ISSN: 09534075 (1997).

196. Azarm, A. *et al.* Neutral dissociation of hydrogen molecules in a strong laser field through superexcited states. *Journal of Physics B: Atomic, Molecular and Optical Physics* **44.** ISSN: 09534075 (2011).

197. Alnaser, A. S. *et al.* Laser-peak-intensity calibration using recoil-ion momentum imaging. *Physical Review A - Atomic, Molecular, and Optical Physics* **70,** 1–6. ISSN: 10502947 (2004).

198. Chelkowski, S. *et al.* Dynamic nuclear interference structures in the Coulomb explosion spectra of a hydrogen molecule in intense laser fields: Reexamination of molecular enhanced ionization. *Physical Review A - Atomic, Molecular, and Optical Physics* **76,** 1–16. ISSN: 10502947 (2007).

199. Xu, H. *et al.* Observing electron localization in a dissociating H2+ molecule in real time. *Nature Communications* **8,** 1–6. ISSN: 20411723 (2017).

200. Peng, P. *et al.* Intensity-dependent study of strong-field Coulomb explosion of H_2. *Optics Express* **23,** 18763. ISSN: 1094-4087 (2015).

201. Saunois, M. *et al.* The growing role of methane in anthropogenic climate change. *Environmental Research Letters* **11.** ISSN: 17489326 (2016).

202. Demirbas, A. The importance of natural gas as a World fuel. *Energy Sources, Part B: Economics, Planning and Policy* **1,** 413–420. ISSN: 15567249 (2006).

203. Tobie, G., Lunine, J. I. & Sotin, C. Episodic outgassing as the origin of atmospheric methane on Titan. *Nature* **440,** 61–64. ISSN: 14764687 (2006).

204. Mumma, Michael J, Villanueva, G.L., Novak, R.E., Hewagama, T., Bonev, B.P., DiSanti, M.A., Mandell, A.M., Smith, M. Strong Release of Methane. *Science* **323,** 1041–1045. ISSN: 0036-8075. http://www.ncbi.nlm.nih.gov/pubmed/19150811 (2009).

205. Dresselhaus, M. S., Dresselhaus, G. & Jorio, A. *Group Theory. Application of the Physics of Condensed Matter* (Springer-Verlag Berlin Heidelberg, 2008).

206. Varvarezos, L. *et al.* Ionization – dissociation of methane in ultrashort 400 nm and 800 nm laser fields. *Chemical Physics Letters* **775,** 138687. ISSN: 00092614 (2021).

207. Guilhaus, M. Principles and Instrumentation in Time-of-flight Mass Spectrometry. *Journal of Mass Spectrometry* **30,** 1519–1532. ISSN: 1076-5174 (1995).

208. *Keldysh Parameter calculator* http://power1.pc.uec.ac.jp/~toru/keldysh/. Accessed: 15.03.2022.

209. Samson, J. A. *et al.* Ionization yields, total absorption, and dissociative photoionization cross sections of CH4 from 110-950 Å. *The Journal of Chemical Physics* **90,** 6925–6932. ISSN: 00219606 (1989).

210. Wang, S. *et al.* Dissociation of methane in intense laser fields. *Journal of Physical Chemistry A* **107,** 6123–6129. ISSN: 10895639 (2003).

211. Wu, Z. *et al.* Fragmentation dynamics of methane by few-cycle femtosecond laser pulses. *Journal of Chemical Physics* **126.** ISSN: 00219606 (2007).

212. Kong, F. *et al.* Explosive photodissociation of methane induced by ultrafast intense laser. *Journal of Chemical Physics* **125.** ISSN: 00219606 (2006).

213. Dujardin, G., Winkoun, D. & Leach, S. Double photoionization of methane. *Physical Review A* **31,** 3027–3038. ISSN: 10502947 (1985).

214. Dahl, D. A., Delmore, J. E. & Appelhans, A. D. SIMION PC/PS2 electrostatic lens design program. *Review of Scientific Instruments* **61,** 607–609 (1990).

215. Chelkowski, S. & Bandrauk, A. D. Two-step coulomb explosions of diatoms in intense laser fields. *Journal of Physics B: Atomic, Molecular and Optical Physics* **28,** 723–731. ISSN: 13616455 (1995).

216. Sharifti, M. *et al.* Experimental and theoretical investigation of high-power laser ionization and dissociation of methane. *Journal of Physical Chemistry A* **111,** 9405–9416. ISSN: 10895639 (2007).

217. Mathur, D. & Rajgara, F. A. Dissociative ionization of methane by chirped pulses of intense laser light. *Journal of Chemical Physics* **120,** 5616–5623. ISSN: 00219606 (2004).

218. Ekanayake, N. *et al.* Mechanisms and time-resolved dynamics for trihydrogen cation (H3+) formation from organic molecules in strong laser fields. *Scientific Reports* **7,** 4703. ISSN: 2045-2322 (July 2017).

219. Siegbahn, P. E. Double ionization of methane. *Chemical Physics* **66,** 443–452. ISSN: 03010104 (1982).

220. Williams, J. B. *et al.* Probing the dynamics of dissociation of methane following core ionization using three-dimensional molecular-frame photoelectron angular distributions. *Journal of Physics B: Atomic, Molecular and Optical Physics* **45.** ISSN: 09534075 (2012).

221. Vallance, C., Heathcote, D. & Lee, J. W. Covariance-Map Imaging: A Powerful Tool for Chemical Dynamics Studies. *Journal of Physical Chemistry A.* ISSN: 15205215 (2021).

222. Kukk, E. *et al.* Electronic state dependence in the dissociation of core-ionized methane. *Journal of Physics B: Atomic, Molecular and Optical Physics* **40,** 3677–3692. ISSN: 09534075 (2007).

223. Perelomov, A. M., Popov, V. S. & Terent'ev, M. V. Ionization of Atoms in an Alternating Electric Field. *Soviet Journal of Experimental and Theoretical Physics* **23,** 924 (Nov. 1966).

224. Ammosov, M. V., Delone, N. B. & Krainov, V. P. *Tunnel Ionization Of Complex Atoms And Atomic Ions In Electromagnetic Field* in *High Intensity Laser Processes* (ed Alcock, J. A.) **0664** (SPIE, 1986), 138 –141.

225. Martin, S. R. & Schilstra, M. J. Circular Dichroism and Its Application to the Study of Biomolecules. *Methods in Cell Biology* **84,** 263–293. ISSN: 0091-679X (2008).

226. Beyer, H. *et al.* 80% Valley Polarization of Free Carriers in Singly Oriented Single-Layer WS_2 on Au(111). *Phys. Rev. Lett.* **123,** 236802 (23 Dec. 2019).

227. Harp, G. R. *et al.* X-ray magnetic-circular-dichroism study of Fe/V multilayers. *Phys. Rev. B* **51,** 3293–3296 (5 Feb. 1995).

228. Macleod, N. A. *et al.* Structure, electronic circular dichroism and Raman optical activity in the gas phase and in solution: a computational and experimental investigation. *Phys. Chem. Chem. Phys.* **7,** 1432–1440 (7 2005).

229. Janssen, M. H. & Powis, I. Detecting chirality in molecules by imaging photoelectron circular dichroism. *Physical Chemistry Chemical Physics* **16,** 856–871. ISSN: 14639076 (2014).

230. Han, B. *et al.* Magnetic Circular Dichroism in Nanomaterials: New Opportunity in Understanding and Modulation of Excitonic and Plasmonic Resonances. *Advanced Materials* **32,** 1801491 (2020).

231. Allaria, E *et al.* The FERMI@Elettra free-electron-laser source for coherent x-ray physics: photon properties, beam transport system and applications. *New Journal of Physics* **12,** 075002 (July 2010).

232. Allaria, E. *et al.* Non-standard use of laser heater for FEL control and THz generation. *Proceedings of the 38th International Free-Electron Laser Conference, FEL 2017,* 566–568 (2017).

233. Svetina, C. *et al.* The Low Density Matter (LDM) beamline at FERMI: Optical layout and first commissioning. *Journal of Synchrotron Radiation* **22,** 538–543. ISSN: 16005775 (2015).

234. KIRKPATRICK, P. & BAEZ, A. V. Formation of optical images by X-rays. *Journal of the Optical Society of America* **38,** 766–774. ISSN: 00303941 (1948).

235. Lyamayev, V. *et al.* A modular end-station for atomic, molecular, and cluster science at the low density matter beamline of FERMI@Elettra. *Journal of Physics B: Atomic, Molecular and Optical Physics* **46.** ISSN: 09534075 (2013).

236. itnik, M *et al.* Lifetimes ofn1P states in helium. *Journal of Physics B: Atomic, Molecular and Optical Physics* **36,** 4175–4189 (Oct. 2003).

237. Glover, T. E. *et al.* Observation of Laser Assisted Photoelectric Effect and Femtosecond High Order Harmonic Radiation. *Phys. Rev. Lett.* **76,** 2468–2471 (14 Apr. 1996).

238. Owada, S. *et al.* Characterization of soft X-ray FEL pulse duration with two-color photoelectron spectroscopy. *Journal of Synchrotron Radiation* **27,** 1362–1365 (Sept. 2020).

239. Kramida, A. *et al. NIST Atomic Spectra Database* https://physics.nist.gov/asd. Accessed: Mon Jun 07 2021. National Institute of Standards and Technology, Gaithersburg, MD.

240. Gibson, G. N., Freeman, R. R. & McIlrath, T. J. Verification of the dominant role of resonant enhancement in short-pulse multiphoton ionization. *Physical Review Letters* **69,** 1904–1907. ISSN: 00319007 (1992).

241. McIlrath, T. J. *et al.* Above-threshold ionization processes in xenon and krypton. *Physical Review A* **35,** 4611–4623. ISSN: 10502947 (1987).

242. Verolaĭnen, Y. F. & Nikolaich, A. Y. Radiative lifetimes of excited states of atoms. *Soviet Physics Uspekhi* **25,** 431–447 (June 1982).

243. Bronstein, I. N. *et al. Taschenbuch der Mathematik* (Wissenschaftlicher Verlag Harri Deutsch GmbH, 2012).

244. Thini, F. *et al.* Photo-ionization of polarized lithium atoms out of an all-optical atom trap: A complete experiment. *Journal of Physics B: Atomic, Molecular and Optical Physics* **53.** ISSN: 13616455 (2020).

245. *Femtosecond Laser Pulses* 2nd ed. (ed Rullière, C.) (Springer Science+Media Business Media, Inc., 2005).

PUBLICATIONS

1. **René Wagner**, K. Bartschat, N. Douguet, M. Ilchen, D. E. Rivas, V. Music, P. Schmidt, J. Hofbrucker, C. Callegari, O. Plekan, M. Di Fraia, K. C. Prince and M. Meyer, Variability of the Circular Dichroism in Multiphoton Ionization of Resonantly Excited Helium Ions - *to be submitted*.

2. Rebecca Boll, Julia M. Schäfer, Benoît Richard, Kilian Fehre, Gregor Kastirke, Zoltan Jurek, Markus S. Schöffle, Malik M. Abdullah, Nils Anders, Thomas M. Baumann, Sebastian Eckart, Benjamin Erk, Alberto De Fanis, Reinhard Dörner, Sven Grundmann, Patrik Grychtol, Alexander Hartung, Max Hofmann, Markus Ilchen, Ludger Inhester, Christian Janke, Rui Jin, Max Kircher, Katharina Kubicek, Maksim Kunitski, Xiang Li, Tommaso Mazza, Severin Meister, Niklas Melzer, Jacobo Montano, Valerija Music, Giammarco Nalin, Yevheniy Ovcharenko, Christopher Passow, Andreas Pier, Nils Rennhack, Jonas Rist, Daniel E. Rivas, Daniel Rolles, Ilme Schlichting, Lothar Ph. H. Schmidt, Philipp Schmidt, Juliane Siebert, Nico Strenger, Daniel Trabert, Florian Trinter, Isabel Vela-Perez, **Rene Wagner**, Peter Walter, Miriam Weller, Pawel Ziolkowski, Sang-Kil Son, Artem Rudenko, Michael Meyer, Robin Santra and Till Jahnke: X-ray multiphoton-induced Coulomb explosion images complex single molecule. Nature Physics, 18(4):423–428, Apr 2022, ISSN 1745–2481.

3. Allum, Felix, Valerija Music, Ludger Inhester, Rebecca Boll, Benjamin Erk, Philipp Schmidt, Thomas M. Baumann, Gunter Brenner, Michael Burt, Philipp V. Demekhin, Simon Dorner, Arno Ehresmann, Andreas Galler, Patrik Grychtol, David Heathcote, Denis Kargin, Mats Larsson, Jason W. L. Lee, Zheng Li, Bastian Manschwetus, Lutz Marder, Robert Mason, Michael Meyer, Huda Otto, Christopher Passow, Rudolf Pietschnig, Daniel Ramm, Kaja Schubert, Lucas Schwob, Richard D. Thomas, Claire Vallance, Igor Vidanovic, Clemens von Korff Schmising, **René Wagner**, Peter Walter, Vitali Zhaunerchyk, Daniel Rolles, Sadia Bari, Mark Brouard und Markus Ilchen: A localized view on molecular dissociation via electron-ion partial covariance. Communications Chemistry, 5(1):42, Mar 2022, ISSN 2399-3669.

4. Lazaros Varvarezos, John T. Costello, Conor Long, Alexander J. Achner, **Rene Wagner**, Michael Meyer, and Patrik Grychtol, Ionization - dissociation of methane in ultrashort 400 nm and 800 nm laser fields. *Chemical Physics Letters* **755**, 138687. ISSN: 00092614 (2021).

5. T. Jahnke , R. Guillemin, L. Inhester, S.-K. Son, G. Kastirke, M. Ilchen, J. Rist, D. Trabert, N. Melzer, N. Anders, T. Mazza, R. Boll, A. De Fanis, V. Music, Th. Weber, M. Weller, S. Eckart, K. Fehre, S. Grundmann, A. Hartung, M. Hofmann, C. Janke, M. Kircher, G. Nalin, A. Pier, J. Siebert, N. Strenger, I. Vela-Perez, T. M. Baumann, P. Grychtol, J. Montano, Y. Ovcharenko, N. Rennhack, D. E. Rivas, **R. Wagner**, P. Ziolkowski, P. Schmidt, T. Marchenko,

O. Travnikova, L. Journel, I. Ismail, E. Kukk, J. Niskanen, F. Trinter, C. Vozzi, M. Devetta, S. Stagira, M. Gisselbrecht, A. L. Jäger, X. Li, Y. Malakar, M. Martins, R. Feifel, L. Ph. H. Schmidt, A. Czasch, G. Sansone, D. Rolles , A. Rudenko , R. Moshammer, R. Dörner, M. Meyer, T. Pfeifer, M. S. Schöffler, R. Santra, M. Simon, and M. N. Piancastelli, Inner-Shell-Ionization-Induced Femtosecond Structural Dynamics of Water Molecules Imaged at an X-Ray Free-Electron Laser. *Phys. Rev. X* **11**, 041044 (4 Dec. 2021).

6. Patrik Grychtol, Daniel E. Rivas, Thomas M. Baumann, Rebecca Boll, Alberto De Fanis, Benjamin Erk, Markus Ilchen, Jia Liu, Tommaso Mazza, Jacobo Montaño, Jost Müller, Valerija Music, Yevheniy Ovcharenko, Nils Rennhack, Arnaud Rouzé, Philipp Schmidt, Sebastian Schulz, Sergey Usenko, **René Wagner**, Pawel Ziołkowski, Holger Schlarb, Jan Grünert, Nikolay Kabachnik, and Michael Meyer, Timing and X-ray pulse characterization at the Small Quantum Systems instrument of the European X-ray Free Electron Laser. *Optics Express* **29** (Oct. 2021).

7. T. Mazza , M. Ilchen, M. D. Kiselev , E. V. Gryzlova , T. M. Baumann, R. Boll, A. De Fanis, P. Grychtol, J. Montaño, V. Music, Y. Ovcharenko, N. Rennhack, D. E. Rivas, Ph. Schmidt, **R. Wagner**, P. Ziolkowski, N. Berrah, B. Erk, P. Johnsson, C. Küstner-Wetekam, L. Marder, M. Martins, C. Ott, S. Pathak, T. Pfeifer, D. Rolles, O. Zatsarinny, A. N. Grum-Grzhimailo, and M. Meyer, Mapping Resonance Structures in Transient Core-Ionized Atoms. *Phys. Rev. X* **10**, 041056 (4 Dec. 2020).

8. Gregor Kastirke, Markus S. Schöffler, Miriam Weller, Jonas Rist, Rebecca Boll, Nils Anders, Thomas M. Baumann, Sebastian Eckart, Benjamin Erk, Alberto De Fanis, Kilian Fehre, Averell Gatton, Sven Grundmann, Patrik Grychtol, Alexander Hartung, Max Hofmann, Markus Ilchen, Christian Janke, Max Kircher, Maksim Kunitski, Xiang Li, Tommaso Mazza, Niklas Melzer, Jacobo Montano, Valerija Music, Giammarco Nalin, Yevheniy Ovcharenko, Andreas Pier, Nils Rennhack, Daniel E. Rivas, Reinhard Dörner, Daniel Rolles, Artem Rudenko, Philipp Schmidt, Juliane Siebert, Nico Strenger, Daniel Trabert, Isabel Vela-Perez, **Rene Wagner**, Thorsten Weber, Joshua B. Williams, Pawel Ziolkowski, Lothar Ph. H. Schmidt, Achim Czasch, Kiyoshi Ueda, Florian Trinter, Michael Meyer, Philipp V. Demekhin, and Till Jahnke, Double Core-Hole Generation in O_2 Molecules Using an X-Ray Free-Electron Laser: Molecular-Frame Photoelectron Angular Distributions. *Phys. Rev. Lett.* **125**, 163201 (16. Oct. 2020).

9. Gregor Kastirke, Markus S. Schöffler, Miriam Weller, Jonas Rist, Rebecca Boll, Nils Anders, Thomas M. Baumann, Sebastian Eckart, Benjamin Erk, Alberto De Fanis, Kilian Fehre, Averell Gatton, Sven Grundmann, Patrik Grychtol, Alexander Hartung, Max Hofmann, Markus Ilchen, Christian Janke, Max Kircher, Maksim Kunitski, Xiang Li, Tommaso Mazza, Niklas Melzer, Jacobo Montano, Valerija Music, Giammarco Nalin, Yevheniy Ovcharenko, Andreas Pier, Nils Rennhack, Daniel E. Rivas, Reinhard Dörner, Daniel Rolles, Artem Rudenko, Philipp Schmidt, Juliane Siebert, Nico Strenger, Daniel Trabert, Isabel Vela-Perez, **Rene Wagner**, Thorsten Weber, Joshua B. Williams, Pawel

Ziolkowski, Lothar Ph. H. Schmidt, Achim Czasch, Florian Trinter, Michael Meyer, Kiyoshi Ueda, Philipp V. Demekhin, and Till Jahnke, Photoelectron Diffraction Imaging of a Molecular Breakup Using an X-Ray Free-Electron Laser. *Phys. Rev. X* **10**, 021052 (2 June 2020).

10. U. Eichmann, H. Rottke, S. Meise, J.-E. Rubensson, J. Söderström, M. Agåker, C. Såthe, M. Meyer, T. M. Baumann, R. Boll, A. De Fanis, P. Grychtol, M. Ilchen, T. Mazza, J. Montano, V. Music, Y. Ovcharenko, D. E. Rivas, S. Serkez, **R. Wagner**, and S. Eisebitt, Photon-recoil imaging: Expanding the view on nonlinear x-ray physics. *Science* **369**, 1630–1633 (2020).

ACKNOWLEDGEMENTS

The time spent doing the Ph.D. was an incredible ride that taught me a lot.

I am very thankful for my supervisor Dr. Michael Meyer for giving me the opportunity to experience science at the EuXFEL. It was a pleasure to work in such an international environment at one of the brightest x-rays sources in the world. Many thanks also to Dr. Patrik Grychtol for all the help and guidance in the laser lab, as well as for the pep talks in times when making progress seemed impossible.
The time in the laser lab at the EuXFEL was very enjoyable, as there were many people around who you could always ask about science, set-ups, or the latest music releases. Thank you Alexander Achner for showing me the laser lab and for all the fun we had building set-ups and measuring things in the laser lab. Many thanks also to Michael Diez for fruitful talks about science, safety and many other enjoyable things. As in a laser lab there are sometimes issues with electronics, I was lucky to be able to ask Nils Rennhack who always made some time to fix the issues I had or that I created. Thanks alot!
Thanks to Dr. Markus Ilchen and Dr. Michael Meyer I could be part of beamtimes at the EuXFEL, FLASH and at FERMI FEL, where I got an insight into the world of FEL science. The discussions about the data with Dr. Markus Ilchen, Dr. Michael Meyer, Dr. Nicolas Douguet, Prof. Dr. Klaus Bartschat and Prof. Dr. Alexei Grum-Grzhimailo were very fruitful and helped a lot.
The time spent in the office was always a good one and many laughs were shared, thanks to my office colleagues Jacobo Montaño and Dr. Yevheniy Ovcharenko.
In general, I would like to thank the SQS group of EuXFEL for helping me in all kinds of ways.

Thanks to the SFB925 and the University of Hamburg for funding my work at the EuXFEL. The SFB925 seminars were always fun and connected me with people outside of my own scientific bubble. I would like to especially thank Prof. Dr. Klaus Sengstock, my university supervisor, for discussing matters outside of the EuXFEL and thereby giving another perspective on scientific topics.

The social Ph.D. events with Christina, Michael, Tae, Karina and many more were always a highlight. I won't forget the numerous hikes along Alster in the name of 'Kohltour'. Neither will I forget the countless days on 'Elbstrand', the barbecue events and the cocktail nights.
In times of corona it was at times difficult to stay sane, but thanks to Katharina and Tae and our regularly culinary adventures in the Hamburg west area, it was a lot easier to keep a clear mind. Special thanks also to Marv for the nice times swimming and everything else.
Shout out also to the people from the 'Hamburger Kanu Club', who always had an open ear for my troubles and with whom I collected many kilometers on the

Alster river. For the times off, it was a pleasure to go on surfing adventures to France and Morroco or just to meet somewhere with Isi, Henne and Max. I can't wait for the next adventures with you guys! And thank you Lena for being there and around.

Finally, I would like to thank my parents for their unending and unconditional support throughout all these times. You are always there for me.

EIDESTATTLICHE VERSICHERUNG

Hiermit versichere ich an Eides statt, die vorliegende Dissertationsschrift selbst verfasst und keine anderen als die angegebenen Hilfsmittel und Quellen benutzt zu haben.

Hamburg, den

René Marcel Leopold Wagner